Normal conducting RF structure development for CLARA

Louise Sophie Cowie

This thesis is submitted for the degree of
Doctor of Philosophy

Department of Engineering
Lancaster University
November 2021

Declaration

This thesis is my own work and has not been submitted in support of an application for another degree at this or any other university. For all work done in collaboration the contribution of others is clearly indicated.

Louise Cowie

Abstract

This thesis covers three RF structures that form part of the linear accelerator for the CLARA Free Electron Laser test facility project. The first structure is the RF photoinjector. The design, tuning, low power testing and work towards the RF conditioning of the structure are presented. The design includes a novel coupler and automated parametric optimisation of the cavity structure. The tuning was performed via trimming the length of each cell before brazing, and the chapter presents pre- and post-braze RF measurements. The RF conditioning chapter includes the design of a program for unmanned RF conditioning of not only the photoinjector but all CLARA RF structures.

The second structure is the first CLARA linac. It is a 2 m travelling wave structure, and the RF envelope evolves as it travels through the structure due to RF dispersion. A method to predict the pulse evolution using Fourier methods is presented. The method requires two inputs to calculate the dispersion: the group velocity as a function of cell number, and the phase advance. Attenuation is included in the model with the addition of a third input: the cavity Q_0. The model is tested on the first CLARA linac and shows good agreement with measurements of the rf pulse. The model can also be used to predict the beam momentum and this too shows good agreement with measurements from CLARA.

The third structure is the CLARA transverse deflecting cavity. This is a dipole mode structure that is part of a diagnostic system to measure the longitudinal characteristics of the electron bunch. The structure will require field-profile tuning after fabrication. Tuning requires a method to take RF measurements and find the relative detuning of each cell. Two types of tuning method are presented, a commonly used perturbation theory based method and a novel method that finds the pseudoinverse of a matrix of measured values. Two variations of each method type are tested using 3D RF simulation results and the results compared.

Acknowledgements

I would like to thank all of the members of the CLARA and 400-Hz photoinjector teams at Daresbury for making this work possible. Accelerator research and design requires a great amount of teamwork by a great many people, more than I can list here by name.

Thank you to my supervisor and colleague, Graeme Burt, for so many ideas, discussions and a great deal of advice, as well as his contribution the 400-Hz photoinjector and TDC designs.

Thank you to Peter McIntosh and Alan Wheelhouse for allowing me time during my work at ASTeC for this PhD.

Thank you to Philippe Goudket for sharing his knowledge with me when I started at ASTeC, and for his his contribution to the 400-Hz photoinjector and TDC designs.

Thank you to Julian McKenzie for his his contribution to the 400-Hz photoinjector, for his help taking measurements of the beam momentum from linac 1, and for being there in the office to advise and share his knowledge.

Thank you to Duncan Scott, without whom my vision for the NO-ARC program would not be a reality.

Thank you to Boris Militsyn for leading the 400-Hz photoinjector design.

Thank you to Thomas Jones for his his contribution to the 400-Hz photoinjector design.

Thank you to James Jones for the simplex optimiser which I used many times, and the Superfish cavity optimiser.

Thank you to Bill Kyle for the beam simulations of the effect of dipole component in the photoinjector.

Thank you to Hannah Kockelbergh for the breakdown detection neural net.

Thank you to Stefano Benedetti for providing data from the TULIP BTW structure.

And finally thank you to my parents for always encouraging me, and to my partner Stephen Burgess whose support I could not have done without.

Contents

List of Figures

List of Tables

Chapter 1

Project introduction

1.1 Free Electron Lasers

A Free Electron Laser (FEL) is a 4th generation synchrotron light source. A bunch of electrons is accelerated in a linear particle accelerator, and then passed through an alternating polarity magnetic field. The field causes the electron bunch to oscillate transversely to the direction of propagation. The change in velocity from the field causes synchotron radiation, which co-propagates with the electron bunch. The transverse motion of the electron bunch allows it to couple to the transverse electric field of the radiation. This causes the electrons to micro-bunch, that is, to form smaller bunches longitudinally within the main bunch. This microbunching coherently enhances the emission from the electrons. This continues as a positive feedback loop, giving exponential growth to the radiation [1].

The result of this is very bright, coherent, very short pulse radiation, with a tunable wavelength and control of the polarisation. This is useful in many areas of science, including structural biology, atomic and molecular physics, photochemistry and materials science [1]. FELs operate in the far-IR to hard X-ray wavelength region. The short pulses are usually in the order of fs, and the high brightness is around 8-9 orders of magnitude higher than previous generation light sources. Together these allow the study of phenomena occurring on very fast timescales, such as molecular structure dynamics, using a table-top laser pump and FEL probe [2]. X-ray FELs can use scattering techniques to achieve atomic level spatial resolution [3]. Overall FELs are a powerful and unprecedented tool for studying the structure and dynamics of matter.

1.2 Linear electron accelerators

Linear accelerators use linear RF structures called linacs to accelerate bunches of electrons to high energies in the MeV to GeV range. A linac is a metallic vacuum RF (radio frequency) structure made up of multiple coupled resonant cells. The RF in the structure resonates, and the electron bunch travels through each cell when the electric field in that cell is in the positive longitudinal direction. This increases the energy of the electron bunch. Early accelerators used DC fields, but higher fields can be reached, and thus more efficient acceleration, by using RF fields. This is because RF fields can achieve higher accelerating fields without vacuum breakdown (arcing) occurring. Linacs can be either normal- or super-conducting. This thesis will concentrate only on normal conducting RF technology.

A linear electron accelerator will start with an electron source, this can use RF or DC acceleration, and photoemission or thermionic electron emission, and will produce bunches of electrons with charge usually in the pC to nC range. The electron bunches will then be accelerated to the design energy using linacs. The electron bunches can be focused with quadrupole magnets and steered with dipole magnets along the length of the accelerator. Diagnostics such as Faraday cups and scintillator screens give information about the electron bunches, such as location, transverse shape and charge. Longitudinal shape or length measurements can be performed by transforming longitudinal electron position to a transverse offset using a dipole-mode RF deflecting structure. The electron bunches at the end of the accelerator can be used for a variety of purposes: as the gain medium in a FEL or for user experiments such as electron diffraction or particle physics experiments.

To act as the injector for a FEL, a linear electron accelerator must produce bright electron bunches. This requires the energy spread and transverse emittances to be small, and the current to be high. For high average brightness the time between bunches should be small, and for high peak brightness the bunch length should be small. The FEL wavelength is inversely proportional to the square of electron beam energy for the same undulator parameters. For CLARA, the values of these parameters are given in Table 1.1.

Table 1.1: Beam parameters for CLARA operating modes [4]

Parameter	Seeding	SASE	Ultra-short
Max Energy (MeV)	250	250	250
Macropulse Rep Rate (Hz)	1−100	1−100	1−100
Bunch Charge (pC)	250	250	20100
Peak Current (A)	125−400	400	1000
Bunch length (fs)	850−250 (flat-top)	250 (rms)	<25 (rms)
Norm. Emittance (mm-mrad)	≤ 1	≤ 1	≤ 1
rms Energy Spread (keV)	25	100	150

1.3 CLARA

CLARA is the Compact Linear Accelerator for Research and Applications, designed at Daresbury Laboratory. CLARA was designed to test FEL schemes in four key areas: ultrashort pulses; temporal coherence; stability and power; and tailored pulses. The Conceptual Design Review [4] was published in 2013, and CLARA is being built with a phased approach as funding for each phase becomes available, the phases can be seen in Figure 1.1. This approach allows the design to be iterated as phases are built, allowing the design to evolve to respond to developments in the design and testing of FELs worldwide. The operating wavelength for the FEL is 100 to 400 nm, allowing FEL concepts to be tested at a much lower beam momentum of 250 MeV/c than a multi-GeV/c X-ray FEL user facility.

CLARA is sited next to the existing Versatile Electron Linear Accelerator (VELA) beam-line, a 5 MeV/c electron beam-line built as a facility for industrial applications. The first CLARA phase includes a photoinjector and a 2 m travelling wave linac which allows a beam momentum of approximately 50 MeV/c to be reached. There are attendant beam diagnostics including a

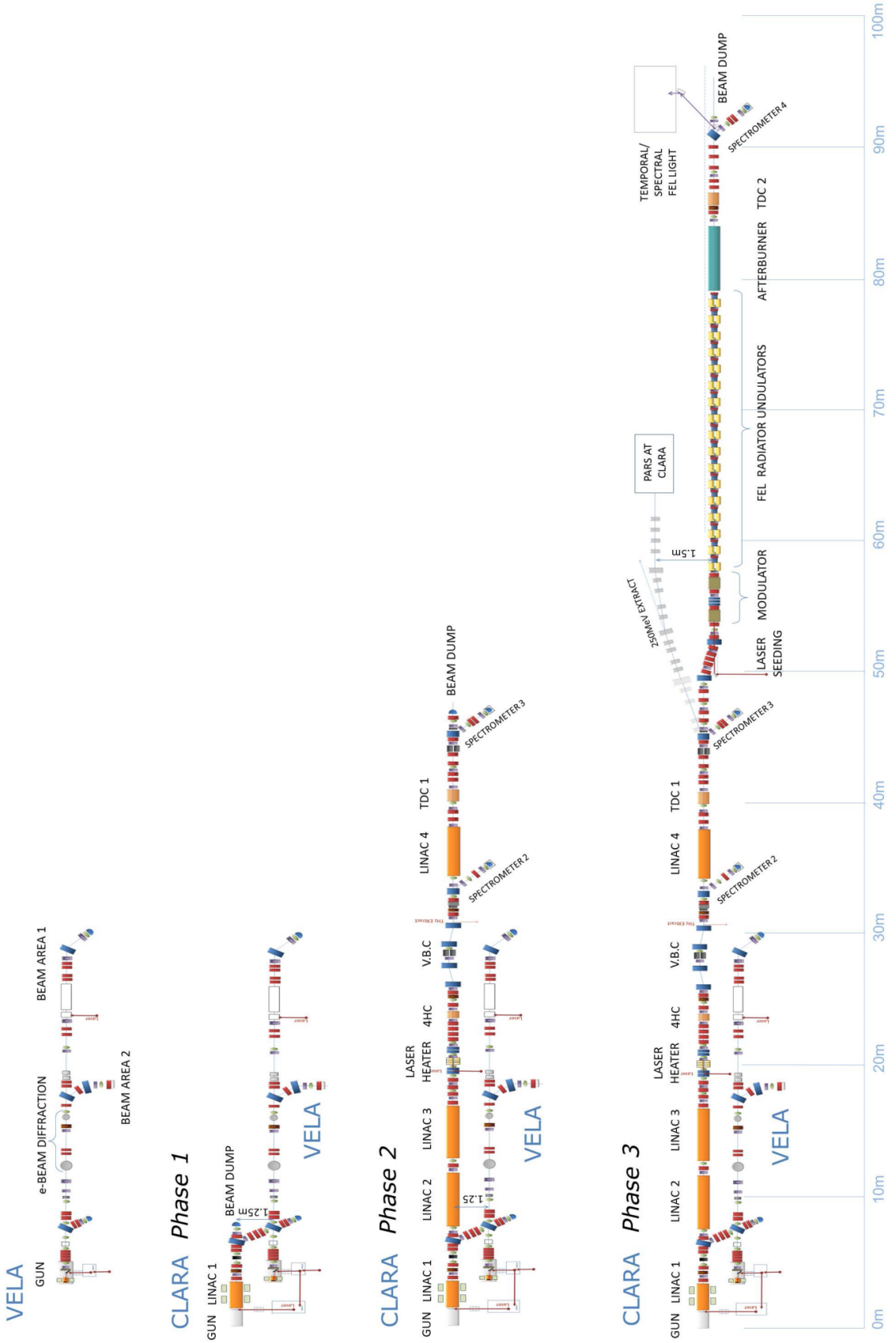

Figure 1.1: Schematic layouts of the build phases for CLARA, including the existing VELA line.

dipole spectrometer line for momentum measurement. Phase 2 adds three more travelling wave linacs, each 4 m long to reach a beam momentum of 250 MeV/c. Phase 2 also includes a fourth harmonic linearising structure and magnetic variable bunch compressor to achieve a short bunch of less than 100 fs. To measure the bunch length and longitudinal profile a dipole mode transverse deflecting cavity is included in Phase 2. Phase 3 is the FEL section, the original design included laser seeding, a modulator section, the undulator radiating section, an afterburner and a second transverse deflecting cavity. As mentioned, this may evolve to test new FEL schemes. The RF structures covered by this thesis are described in the sections below.

1.3.1 Photoinjector

The photoinjector is the first element in the CLARA design. It will consist of a metal replaceable photocathode, which will be illuminated by a pulsed laser with wavelength 266 nm, that will produce bunches of electrons inside the first half-cell of an accelerating RF structure. The structure will operate at S-band, and have a peak accelerating electric field of 120 MV/m. The laser and the RF will be pulsed at 100-400 Hz. The bunches will be accelerated by the RF, and will be focused with a solenoid that surrounds the RF structure. Chapter 2 focuses on the design of the RF photoinjector cavity, and includes a literature review of normal conducting RF photoinjectors. Chapter 3 describes the field profile and frequency tuning of the structure, and the measurements of the structure at low power both in the lab and when installed in the CLARA hall. Once installed, the photoinjector requires RF conditioning to increase the RF field that can be sustained without vacuum breakdown. Chapter 4 describes the process of automating the RF conditioning for this structure, including a literature review, description of the conditioning program including beta-testing, and the first data from conditioning the photoinjector itself.

1.3.2 First linac

The first CLARA linac is a 2 m long S-band travelling wave RF structure, with an accelerating field of 25 MV/m. The RF pulse in the linac experiences frequency-dependent dispersion as it travels, and the shape of the pulse changes due to the superposition of the frequency components. Chapter 5 describes a new mathematical model to predict the pulse envelope distortion based only on the structure group velocity and phase advance values along the structure. The addition of the value of the quality factor allows attenuation to be calculated. The method is used to predict the pulse distortion in the first CLARA linac and this is compared to measurements of the RF. The acceleration of an electron bunch depending on the injection time is predicted and compared to experimental data from CLARA.

1.3.3 Transverse deflecting cavity

As mentioned in Section 1.2, dipole mode RF structures can be used as diagnostics to study the longitudinal bunch profile, including measuring the bunch length. A transverse deflecting cavity has been designed for CLARA, and once manufactured requires tuning to give a constant peak deflecting field in each cell. Chapter 6 defines 4 tuning methods and tests them using 3D electromagnetic simulation of detuned structures.

1.4 Introduction to the thesis

This thesis covers work on RF structures for CLARA, and comprises this introductory chapter, Chapters 2-6 which contain the technical work and are described in detail below, and Chapter 7 which is a brief conclusion. Relevant literature is reviewed in the chapter where it is pertinent, to enable each chapter to be understood individually.

1.4.1 Chapter 2: 400 Hz photoinjector design

An RF photoinjector is a resonant RF structure, within which a photocathode is illuminated by a pulsed laser, exciting electrons from the surface which form an electron bunch. The high voltage RF fields in the structure, which can be up to 120 MV/m at the cathode, accelerate the electrons to close to the speed of light within the structure. This can provide a short, high charge electron bunch, with favourable properties for use in a FEL. Chapter 2 begins with a literature review of normal conducting RF photoinjectors, covering the development from the first RF photoinjector design up until 2013 when the design process for the CLARA photoinjector began. All the major decisions in designing the RF photoinjector cavity are discussed. The chapter then describes the specification and design of the RF photoinjector for CLARA. This covers a parametric optimisation of the cavity structure, the design of a novel dual-feed coaxial coupler and the addition of a probe and load-lock cathode to the RF design. The power handling and design of the water cooling channels is briefly described. Finally simulations of the integrated design in different modelling software are compared and the sensitivity of the frequency and field flatness of the structure to the variation in cavity parameters is simulated to inform the mechanical design tolerances.

1.4.2 Chapter 3: 400 Hz photoinjector tuning and low power tests

In order to achieve the highest acceleration possible whilst staying within surface field limits, multi-cell resonant RF structures often require tuning. This ensures all cells resonate at the same frequency, so that the peak accelerating electric field is equal in all cells. The 400 Hz photoinjector has 1.5 cells, and these must be tuned to the same frequency. This is often performed on normal-conducting structures using specialised tuning pins that can be used to slightly deform the RF structure, however in the case of the 400 Hz photoinjector this was not possible due to the water channels that were built into the structure walls for cooling. Chapter 3 describes the tuning of the 400 Hz photoinjector cavity for both overall frequency and field balance via a novel method of cell length trimming at the pre-braze stage. The amount to trim was based on low power RF measurements of the clamped structure taken at the manufacturers premises. The tuning process was successful, achieving a frequency only 100 kHz from the nominal frequency of 2998.5 MHz, and a ratio of 99.99% peak electric field between the two cells. The structure was then brazed and the final power coupling tuned with a gasket in the coaxial line. Measurements were performed of the structure post-braze both in the laboratory setting, allowing bead-pull measurements, and on the VELA beam line with the load-lock cathode system installed.

1.4.3 Chapter 4: RF conditioning automation for the 400 Hz photoinjector

Resonant RF structures cannot sustain high surface fields immediately after manufacture. This is due largely to a phenomenon called RF breakdown, which is current arcing inside the structure.

This can damage the structure so care is taken to minimise it. The field in the structure is slowly increased to build up the field that can be sustained. This can be done manually, or in a more controlled way by a computer program. Chapter 4 begins with a discussion of high gradient phenomena and RF conditioning, including RF gradient limits and the effect of magnetic field on breakdown. Relevant literature is summarised. The chapter then goes on to detail the motivation and operation of the unmanned RF conditioning program NO-ARC. This includes a description and flow chart of the program operation, the details of the VELA and CLARA photoinjector RF systems and how RF breakdowns are detected. The program was tested by using it to condition the current CLARA photoinjector, and the results of this conditioning are described, including several interesting phenomena encountered in the process. These include the effects of the emittance compensating solenoid on the conditioning cavity vacuum pressure, and a low power multipactor band. The program was then used to begin to condition the 400 Hz CLARA photoinjector, and similar low power multipactor effects were seen. These are considered in more detail and the results of a multipactor simulation are shown, showing multipactor in the cathode region.

1.4.4 Chapter 5: Analytical model of dispersion in travelling wave linacs

Frequency dispersion is the effect of different frequencies propagating with different speeds. In a travelling wave linac an RF pulse travelling through the structure is subject to dispersion, and different frequencies contained within the pulse bandwidth travel at different group velocities. These frequency components then interact via superposition, changing the shape of the pulse envelope. Chapter 5 introduces a new model for predicting RF dispersion in travelling wave linacs. Knowing only the phase advance and group velocity, it allows the evolution of the shape of the RF envelope to be predicted. This is useful as it does not require the full 3D structure model, and can be computed for turn-key linacs about which the full internal design is unknown. With an additional piece of information, Q_0, the attenuation along the structure can be added to the model. The model is used to predict the effect of dispersion on a pulse in CLARA linac 1, and the expected beam momentum when varying beam injection time. These are compared to RF and beam measurements from CLARA and show good agreement. Beam loading is discussed, and the limits of the model and validity of approximations are tested.

1.4.5 Chapter 6

As described in Section 1.4.2, multi-cell RF structures can require tuning to ensure the resonant frequency is the same in all cells. Whilst the field profile can be measured with laboratory techniques, it can be difficult to tell which cell is out of tune for standing wave linacs with 3 or more cells. This is because the structure is made up of coupled resonators, and a frequency error in one cell can have an effect on the field in the cells coupled to it. Often the frequency error is calculated from the field profile using a multi-cell monopole mode equivalent circuit model of the structure. Chapter 6 discusses the applicability of this model to a dipole mode structure, in this case the CLARA transverse deflecting cavity. Alterations of the model are suggested to increase its accuracy for dipole mode structures. Another possible method for dipole mode structure tuning is developed, which is based on matrix inversion using the pseudoinverse from singular value decomposition. The matrix to be inverted consists of the simulated effect of detuning each cell in turn on the field profile. This then can be used to calculate the frequency detuning from the field profile. The effect of frequency detuning of each cell on the cavity power coupling factor can be

optionally added to the matrix. Four methods- the unmodified circuit model, the modified circuit model, the pseudoinverse based model and the pseudoinverse based model with the coupling factor are described. These four models are tested on 20 simulations of randomly detuned versions of the transverse deflecting cavity. The results of the tests are described and the models compared using statistical tests.

Chapter 2

400 Hz photoinjector design

2.1 Literature review of RF photoinjectors

2.1.1 Introduction

An RF photoinjector (or gun) is a device that uses a pulsed laser to excite electrons from a cathode via the photoelectric effect. The bunch of electrons is then accelerated using an RF linearly accelerating cavity. The first significant RF photoinjector was designed at Brookhaven National Lab (BNL) in 1988 [5] and can be seen in Figure 2.1. RF, as mentioned in Section 1.2, is advantageous over a DC field as a higher voltage can be sustained. Variations on this design have been developed and built to provide electrons for particle accelerators and other experiments around the world ever since. While all designs include a cathode and an RF cavity there are several major modifications that have been made. These include different RF coupling designs; single or multi-cell RF cavities, including the use of half-cells; different cathode types; and the use of bucking coils and emmitance compensating solenoids.

Different accelerators and experiments require different beam properties. High beam brightness is one property that RF photoinjectors are particularly well suited to provide. Beam brightness is defined as the particle density in 6D phase space. There are two defined brightnesses; peak and average. Peak brightness can be described by the equation

$$B_{peak} \propto \frac{I_{peak}}{\epsilon_x \epsilon_y \sigma_z}, \tag{2.1}$$

here it can be seen the bunch must have a high peak current I_{peak} and small transverse emittances $\epsilon_{x,y}$, to have a high particle density in 4D phase space. For the same overall bunch charge a smaller longitudinal length σ_z gives a brighter beam. Conversely for the average brightness the length of individual bunches is unimportant. This brightness is driven by the average current, given by the bunch charge Q and repetition rate, R.

$$B_{av} \propto \frac{RQ}{\epsilon_x \epsilon_y}, \tag{2.2}$$

As mentioned in Chapter 1 FELs require electron bunches with high peak current, small energy spread and small transverse emittance to operate effectively [1], therefore RF photoinjectors are well suited as electron sources for these machines.

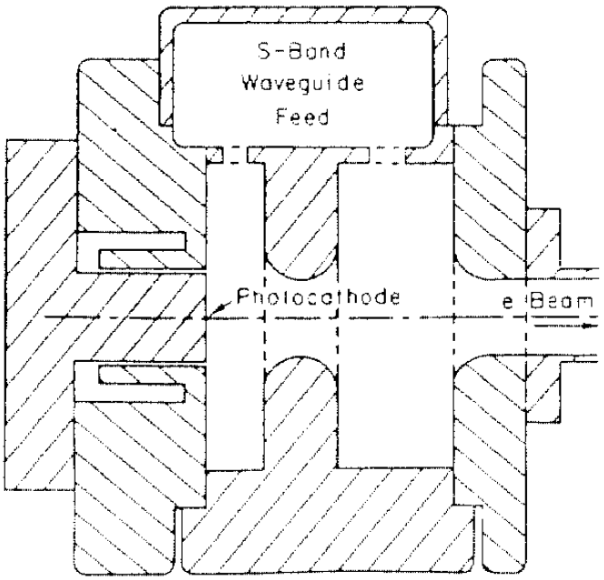

Figure 2.1: Cross-sectional view of the first Brookhaven National Laboratory photoinjector. Reproduced from [5].

2.1.2 Beam parameters

The use of a pulsed laser to excite the electrons from the cathode allows a high repetition rate, for example the EU XFEL injector [6] can provide up to 2700 electron bunches in a single 650 ns RF flat top. However these pulses and bunch-trains occur only every 10 Hz; the duty cycle of normal conducting RF structures is limited by the average Ohmic heating, that is, the heating due to the currents in the metal RF structure. If electron bunches must be equidistant in time the bunch repetition rate is currently limited to 100 Hz.

The laser pulse can also provide a short pulse length, down to sub-picosecond bunches [7], and a high degree of control over the shape of the bunch. Short pulses can be achieved by operating in the "blow out" regime, which applies an ultra-short laser pulse (around 50 fs rms) [7] to the cathode, causing the initial beam to resemble a flat disc. The high transverse space charge forces result in an ellipsoid bunch [8]. The bunch is ideal in that it has approximately uniform charge density and linear space charge forces, and therefore linear beam dynamics. Such a bunch can be compressed to a greater degree than a bunch with nonlinear space charge forces.

Photocathodes can deliver high current densities, giving a high charge beam. The RF cavity means a much higher gradient at the cathode is available than in a DC gun. The effect of this high gradient is to limit space charge effects and thus keep the emittance of the accelerated bunch small. These effects can be combined in an RF gun to give a high brightness electron source, but of course a photoinjector can be adapted to optimise a single one or any combination of these parameters, depending on the experiment.

The transverse emittance of the electron beam is determined not only by the laser spot size, but also growth mechanisms within the photoinjector. The first mechanism is the time dependence of the RF field. The electrons at different longitudinal positions in the cavity experience different RF focusing as the RF field varies with time, due to the transverse electric and magnetic fields which are zero on axis but increase with radius. This gives rise to a radial force and an increase in emittance. The second mechanism is space charge. Coulomb repulsion between the electrons causes emittance growth at low energy, before the electrons reach highly relativistic speeds at which

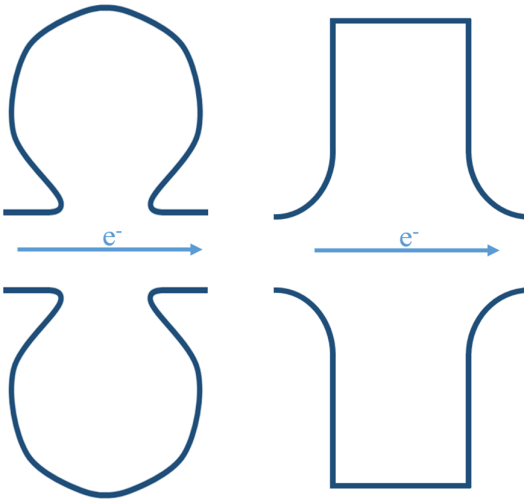

Figure 2.2: Re-entrant (left) and pillbox (right) cell shapes

the induced magnetic field cancels the electric field force, reducing the space charge forces as $1/\gamma^2$. Space charge is more problematic at higher bunch charges. Space charge forces can be compensated by a focusing solenoid, which transfers the electrons' angular momentum to a focusing force. The third mechanism is thermal effects, where the electrons have a spread in energy due to thermal energy held by the electrons. The thermal emittance originates during the photoemission process and depends on the temperature and roughness of the cathode surface.

The uncorrelated energy spread of the electron bunch is the range of energies of particles within that bunch, once any correlated energy chirp has been removed. For FEL operation this must be less than the FEL induced energy modulation [1]. Uncorrelated energy spread in photoinjectors is dominated by the space charge contribution [9] which emerges from the transverse variation of the longitudinal space charge field. Photoinjectors have an intrinsically low uncorrelated energy spread in comparison to other electron sources for example DC injectors [10].

2.1.3 Cell Shape

There are two main categories of cell shape: pillbox (cylindrical) and re-entrant. Re-entrant cells have a nose-cone at the iris and elliptical side walls to create a region of more concentrated axial electric field [11]. Figure 2.2 shows these shapes. The re-entrant shape increases the shunt impedance, where shunt impedance is defined as

$$R_s = \frac{V_0^2}{P} \tag{2.3}$$

where V_0 is the accelerating voltage and P is the power loss [11]. Re-entrant shaping also improves the average power dissipation of the structure due to the larger surface area. Because of these advantages, it is commonly used at low (<1 GHz) frequencies in high duty factor guns, for which the limit on gradient is often average power dissipation or RF power coupler limitation [10]. At higher frequencies the limiting factor on the gradient tends to be RF breakdown, and the re-entrant cell shape has no advantage over the pillbox when it comes to the peak surface electric field. The re-entrant cell shape must by design have long beam-pipes between the cells, and this leads to a longer structure to reach the same beam energy [10], and therefore possibly a lower

shunt impedance per unit length defined, given $V_0 = E_0 L$, as

$$R = \frac{E_0^2}{P/L} \tag{2.4}$$

where E_0 is the accelerating electric field and L is the structure length.

Both shapes can be further optimised, but this inevitably requires trade-offs. The main figures of merit are shunt impedance R_s or effective shunt impedance R_z and Q_0, which can be combined into the useful parameter, R/Q [11]. Here

$$R_z = R_s T^2 \tag{2.5}$$

where T is the transit time factor, which is a scaling factor that takes account of the RF field changing in time as the particle passes through at a finite speed. Also

$$Q_0 = \omega U/P \tag{2.6}$$

where U is the stored energy in the cavity and P is the power lost in the walls. The structure design must be optimised for the chosen figure of merit, whilst keeping the surface electric field low enough to avoid breakdown and the surface magnetic field low enough to avoid thermal stress or, in high duty factor guns, to limit the average heating.

2.1.4 Number of cells

Photoinjectors have been built with anything from 1 to 10.5 cells. Most modern photoinjectors have 1.5 or 2.5 cells, where the nominal half cell is the first cell, whose length is in fact optimised and is often up to 0.6 of the full cell length.

For many years, 1.5 cell photoinjectors were the norm. The original BNL injector paper says that the cathode cell may be followed by as many cells as power limitations will allow. The obvious advantage of more cells is a higher integrated accelerating voltage. The advantage of fewer accelerating cells is a larger mode separation between the desired accelerating mode and those adjacent to it. Fewer cells also give a higher degree of phase precision for short bunches. Acceleration through more cells gives a larger phase error off crest: if the photoinjector is operated at a phase other than crest phase it will be accelerated by a lower gradient, and arrive at later cells at a phase that is not synchronous with the RF. There is therefore less scope for operating at different phases as the number of cells increases.

2.1.5 RF Coupling methods

The ideal photoinjector is a perfectly axially symmetric, simple cavity with no areas of high field or small gaps where multipacting could occur. Unfortunately the RF must be introduced into the cavity through a coupler, inevitably bringing complication and in some cases asymmetries. A variety of couplers have been designed to introduce the RF into the cavity with a maximum power, while minimising the detrimental effects. The main two coupler types are waveguide and coaxial couplers, and they are discussed in detail below, along with some more uncommon solutions.

Waveguide couplers

The BNL injector, and many that came after it, can be described as 'waveguide coupled': the RF power is introduced to the cavity through one or more rectangular waveguides that attach directly to the sides of the RF cavity cells. The field in the waveguide is a rectangular travelling TE_{10} wave, and the impedance match into the cavity is determined by a narrowing of the waveguide as it enters the cell. In the original BNL design [5][12], a single waveguide coupled directly both cells of a 1.5 cell cavity. The waveguide fields match the field required in the cells for π mode acceleration, so the coupling scheme effectively supresses the zero mode (the mode with cell length equal to the RF wavelength).

Multipole components of the on axis field should be considered. The magnetic field near the axis can be expanded

$$B_\phi(r,\phi,z) \approx A_0(z)r + \sum_{n=1}^{\infty} A_n(z)\cos(n\phi)r^{n-1}, \tag{2.7}$$

where the A_n refer to the multipole components and are generally complex, with A_1 referring to the dipole and A_2 the quadrupole components and so on [13]. This single waveguide coupling scheme causes an increase in the dipole component of the operating monopole mode, distorting the field and giving rise to emmitance growth.

This coupler design was adapted by the BNL/SLAC/UCLA collaboration in 1995 [14] to a single waveguide coupling only into the full cell of a 1.5 cell cavity. The coaxial scheme was chosen to limit the transverse emittance increase due to the dipole component of E_z. The coupling to the half cell was achieved through the beam iris, whose diameter was increased to improve the coupling. This change also increased the mode separation between the zero and π modes so that supression of the zero mode was not deemed necessary. Figure 2.3 shows a drawing of the gun. The waveguide coupler was symmetrised by the addition of a dummy port on the opposite side of the cell. However as this now has two-fold symmetry it increases the quadrupole component instead, which varies quadratically with radius and hence is less harmful than the dipole component. This coupling method does not completely cancel the dipole component as the flow of the RF is still asymmetric. Azimuthal (θ) coupling (coupling with an RF coupling hole elongated azimuthally) was chosen to minimise the excitation of the quadrupole component. Many other designs use this coupling regime including BNL/KEK/SHI, SPARC, and PEGASUS [15, 16, 17].

In 2005 LCLS developed this design further [19]. Instead of a symmetrising the RF feed with a dummy port, a second RF feed was employed. This dual feed scheme was designed to eliminate any transverse RF field asymmetry. The shape of the full cell was changed, a "racetrack" shape was chosen, as this shape corrects for quadrupole fields introduced by the dual feed. This cell shape complicated the machining of the cell, as it cannot be accomplished via a lathe and could only be achieved with a computer controlled milling machine. This change meant the azimuthal coupling was not needed to minimise the quadrupole mode. This was changed to z-coupling (with the coupling hole elongated longitudinally), and the radius of the edges of the rectangular coupling port were increased, to reduce the pulsed heating that would be caused by the planned 120 Hz operation. The iris shape was changed; it was made larger in diameter to increase the 0 and π mode separation to 15 MHz, reducing the zero mode excitation to 3% of the π mode. The coupling and racetrack shaping is shown in Figure 2.4 This coupler design was also used on the 2.5 cell SwissFEL and PAL photoinjectors [20, 21].

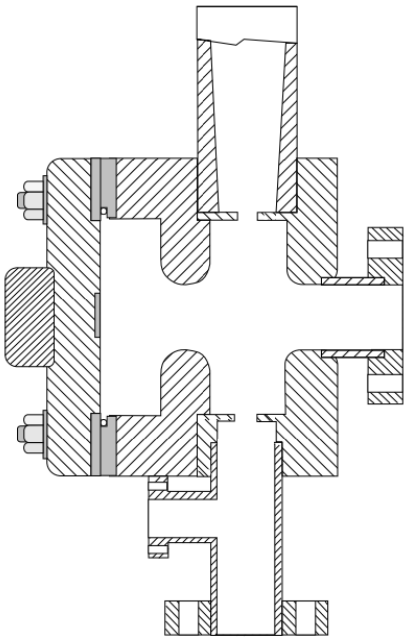

Figure 2.3: Cross-sectional drawing of the BNL/SLAC/UCLA collaboration photoinjector cavity. Reproduced from [18].

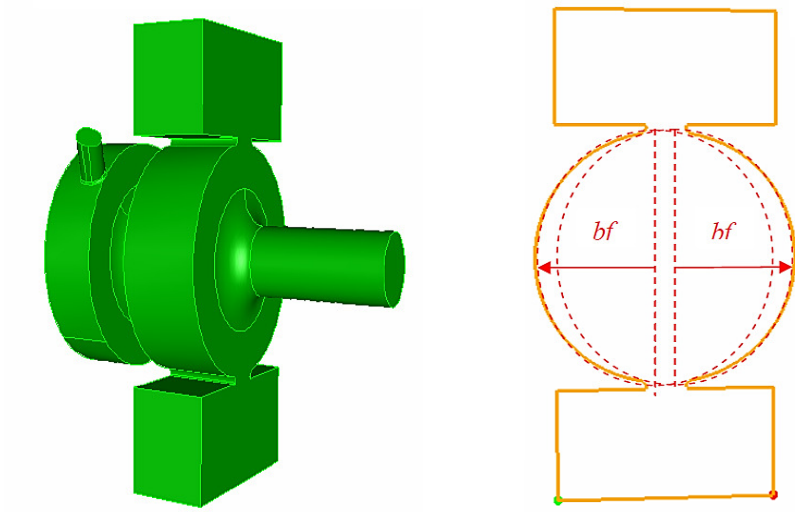

Figure 2.4: Racetrack shaping and dual z-coupling on LCLS redesigned photoinjector. Reproduced from [19].

Coaxial couplers

In 1997, a radically different input coupler was presented by Dwersteg et al. [22] as part of the gun design for the TESLA FEL, later renamed FLASH, at DESY. The RF enters the gun via a coaxial line, positioned around the forward beam-line of the gun, that couples to the cavity on the cavity axis. A "doorknob" coupler is required to couple the TE_{10} mode in the waveguide to the TEM mode in the coaxial line. The gun itself has 1.5 cells, and the power is coupled to the half cell through the iris. This can be seen in Figure 2.5. The advantage of this design over the contemporary single feed side coupled coupler is symmetry. Dwersteg et al. cite a value of emittance contribution due to the

asymmetry of the side coupler design of more than 1π mrad mm. This scheme strongly suppresses asymmetric mode configurations, by a factor of at least $1/Q_0$. Any dipole modes generated at the doorknob transition can be damped in the coaxial line if the dipole cut-off frequency is above the operating frequency. A large outer coaxial line diameter avoids multipacting. Other advantages of this scheme include complete freedom of placement for the emmitance compensating solenoid, and facilitated cooling channel construction as the coupler connects to the gun at an area of low magnetic field, and therefore low heat deposition.

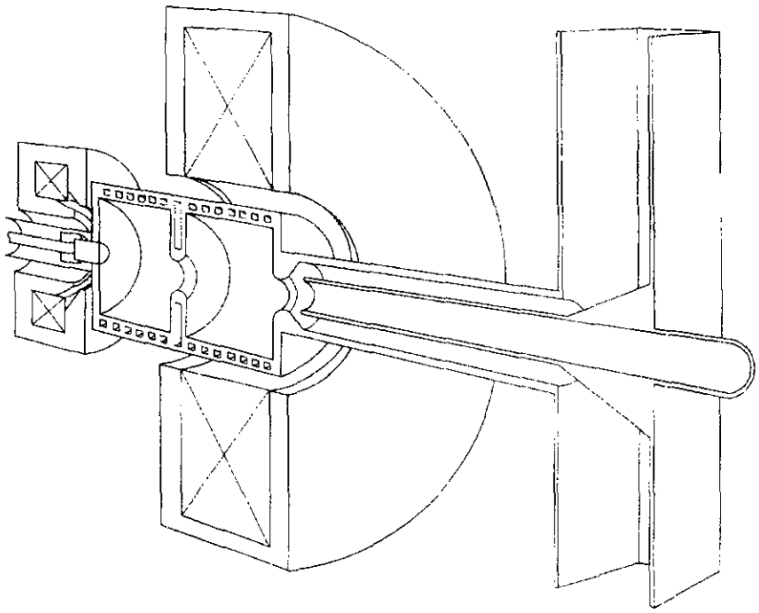

Figure 2.5: Cross-sectional view of the TESLA/FLASH photoinjector cavity. Reproduced from [22].

The disadvantage of this scheme is the unavoidable complication to the coupler design and to the fabrication of the gun. Other issues associated with this design include a possible dipole RF component at the end of the coaxial line, reported at PITZ [23]. This coupling design is used in the EUXFEL photoinjector [24] and the Alpha-X photoinjector designed at LAL [25].

Cell to cell coupling and iris shape

The original BNL gun design included a Fourier analysis of the RF fields, which was used to calculate an optimised iris geometry to limit transverse fields and therefore emittance growth due to the RF fields. The optimum geometry was a hyperbola with $r \to \infty$, which was found to be sufficiently approximated by a 20 mm radius circular iris [12]. The BNL/SLAC/UCLA [14] collaboration injector was the first to couple to a single cell, necessitating power coupling between this and the half cell. The iris radius was increased to 12.49 mm, while keeping the shape circular, to improve the coupling, which, as mentioned above, also increased the separation between the π and zero modes. The mode separation in this gun is 3.4 MHz, giving a zero-mode amplitude of approximately 10% of the π mode in the half cell, which has a significant detrimental effect on the emittance. The circular shape was also used by the DESY design [22], again with an increased radius. This was found to increase the thermal conductance of the iris, as well as increasing the cell-to-cell coupling, resulting in an improved field stability at the cost of a reduced shunt impedance.

In the reports on the design on the LCLS gun [19, 26] changes to the BNL/SLAC/UCLA iris design are described. The aim of the changes was twofold: to increase the mode separation to nullify the effect of the zero mode mentioned above, and also to improve the surface fields to solve a problem with RF breakdown. To improve mode separation the iris was increased further to 14.85 mm, the iris length reduced from 22.05 to 19.05 mm to maintain the same value of shunt impedance: 49 MΩ m^{-1}. To decrease the electric surface fields the shape of the iris was changed to elliptical. This had the effect of reducing peak electric surface field from 11 % higher than that on the cathode to 2% lower. The Alpha-X photoinjector designed at LAL [27] and the DLS [28] photoinjector also employ elliptical irises for this reason.

Coupling factor

The RF coupling factor β_c for an RF cavity can be defined as the ratio of the power lost from the coupler P_{ext} to power lost in the cavity walls P_0 when RF sources are turned off. This is equal to the ratio of the unloaded Q, Q_0, to the external Q, Q_{ext}

$$\beta_c = \frac{P_{ext}}{P_0} = \frac{Q_0}{Q_{ext}} \tag{2.8}$$

To minimise the RF power that is reflected from a standing wave cavity in steady state the β_c should be equal to 1 in cases where beam-loading is negligible. However Figure 2.6 shows the transient reflections seen during filling of an arbitrary standing wave structure, and it can be seen that an overcoupled cavity will fill faster than a matched cavity, albeit with higher steady state reflections.

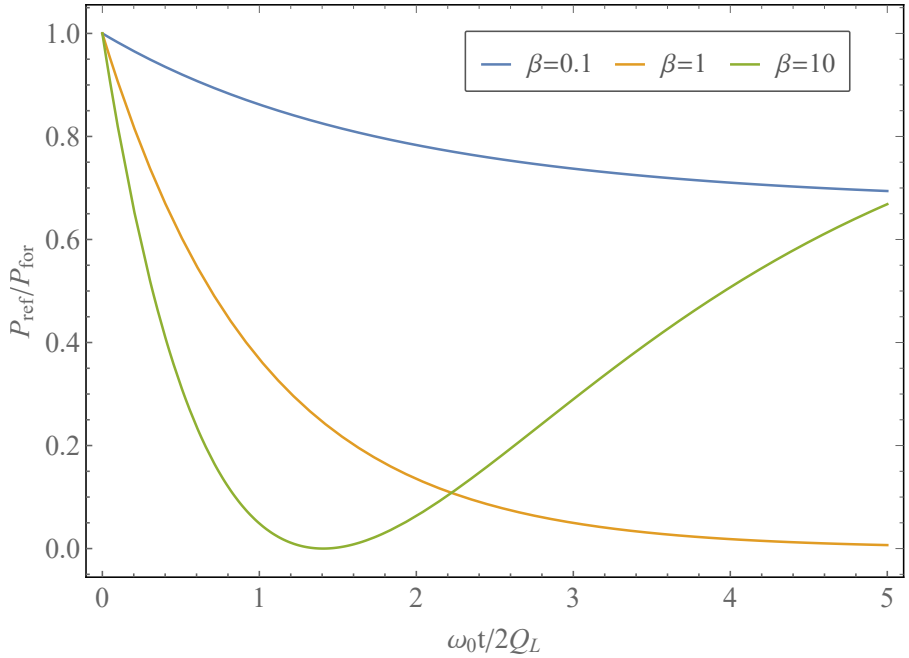

Figure 2.6: Transient reflection ratio in the undercoupled ($\beta_c = 0.1$), matched ($\beta_c = 1$), and overcoupled ($\beta_c = 10$) cases.

A number of modern photoinjectors [19, 21, 20] use this fact to minimise the average power dissipated in the cavity. The cavity is overcoupled, with a coupling factor of up to 2, and thus fills faster, allowing the pulse length to be decreased. This method does require a large overhead on input RF power to produce a flat-top, which can be costly.

2.1.6 Cathode

With regard to the cavity design, there are two main types of cathode: those that can be replaced under vacuum and those that cannot. Simple photoinjectors use the copper back plane of the first half cell, and this can be removable [25], or not [29]. However to remove or replace the full back plane the cavity must be brought up to air, which necessitates vacuum baking and re-conditioning of the cavity. Some modern photoinjectors [30, 31] have implemented a "load-lock" system. This entails a system of vacuum chambers and transfer arms that allow small (10 mm diameter) cathode plugs to be removed and replaced entirely under vacuum. The plug and its socket must be carefully designed to limit the peak surface fields. An RF spring is used to provide electrical contact between the cathode plug and the cavity body [30].

A load-lock cathode system is useful as photocathode quantum efficiency decays over time: the cathode can be replaced with minimal machine down-time. Additionally the system is favoured by groups with an interest in cathode material science, as multiple cathodes can be tested in a short period of time, and the cathodes do not have to be exposed to air after preparation, which can cause oxidation of the surface and change the properties.

2.1.7 Average power handling

Average power in photoinjectors can vary hugely depending on the needs of the accelerator. Duty factor (RF pulse length/period) can vary from 1% or below [32] to 100% (continuous wave (CW) operation) [33], and gradient (as the cathode voltage V_0 is commonly referred in photoinjectors) can vary from 7 MV/m [33] to 120 MV/m [19]. There is usually a trade-off between these two parameters due to the average heating.

Pulse length requirement can vary due to structure filling time. The filling time is inversely proportional to cavity frequency, however over-coupling can lower the filling time at the expense of RF power, as mentioned in Section 2.1.5. Some accelerators have only a single electron bunch per pulse, however others operate with trains of bunches within the same pulse, which can require longer pulses. Generally a higher repetition rate (lower period) is preferred as it increases the statistics of any end-user science for the same length of machine time, however some accelerators may not have this requirement.

To increase the average power handling, the heat from the resistive heating, (due to the current flow from the magnetic field) must be removed. Water pipes are often built into the structure walls for this purpose [33, 28]. As previously mentioned, a re-entrant cell shape can benefit average power handling due to the large surface area, however the nose-cones can make cooling the irises between cells with water pipes impossible, so the shape must be carefully optimised. High frequency operation >3 GHz can also make cooling the irises with water pipes difficult or impossible.

2.1.8 Overview

Figure 2.7 shows a diagram categorising major photoinjectors that exist worldwide.

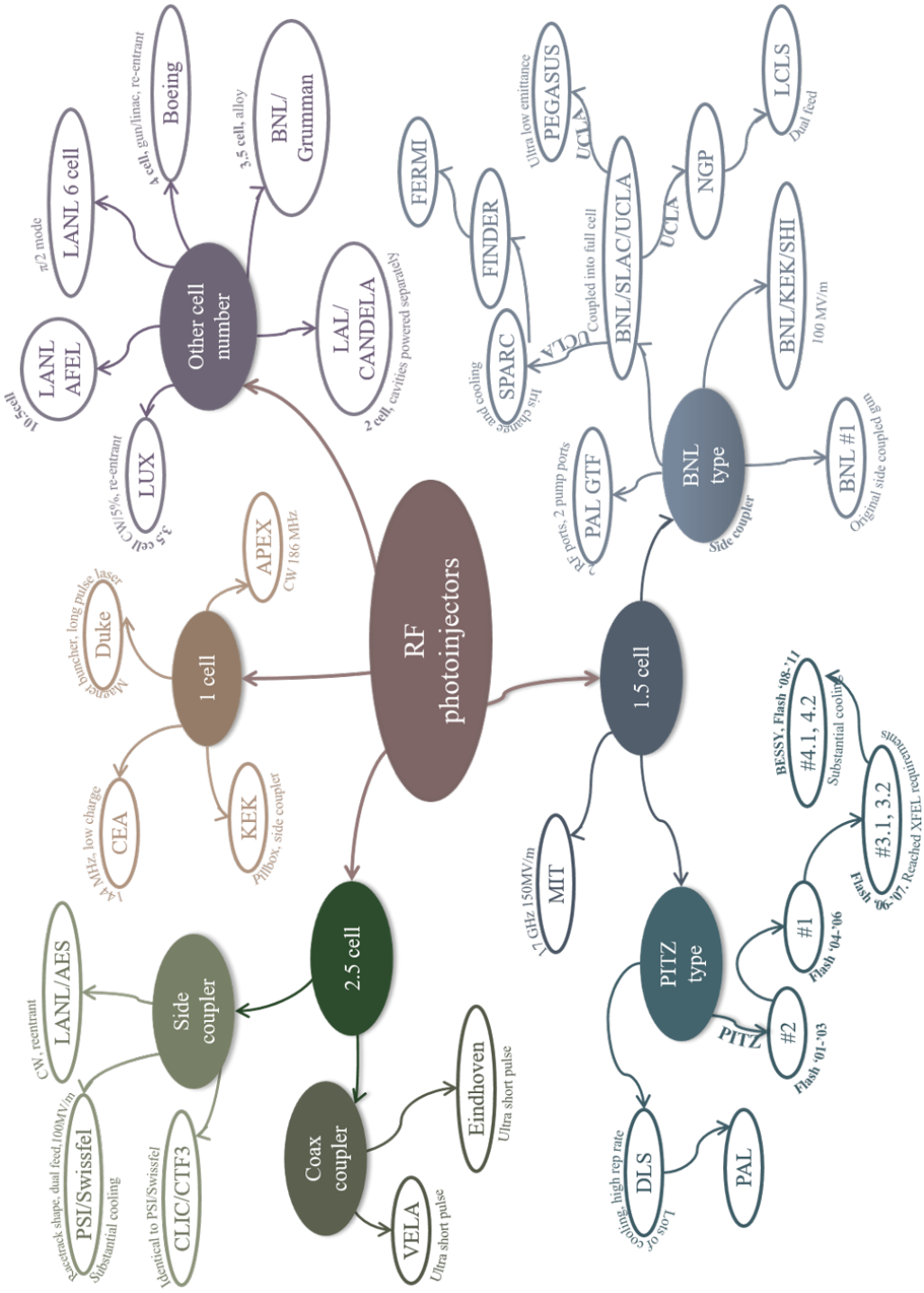

Figure 2.7: Diagram categorising RF photoinjectors worldwide.

2.2 400 Hz photoinjector RF optimisation and simulations

2.2.1 Introduction

CLARA requires an RF photoinjector operating at a frequency of 2.9985 GHz and a repetition rate of up to 400 Hz in some modes of operation. It is required to deliver a very short and low transverse emittance beam, particularly in 100 Hz modes of operation. It is also required to operate at gradients up to 120 MV/m in order to meet challenging electron bunch requirements. The following results are the simulations and optimisation performed for the cavity structure RF design. The mechanical design is not described except where it impacts on the RF performance.

2.2.2 Specification

The photoinjector will be required to meet stringent bunch length and emittance requirements for operation on the CLARA accelerator, and operate in different modes to meet the needs of the different FEL regimes given in Table 1.1. The specification is given in Table 2.1.

Table 2.1: RF and bunch requirements for the CLARA photoinjector

	Units	100 Hz Mode	400 Hz Mode
Gun field	MV/m	120	80/100
Repetition rate	Hz	100	400
Beam energy	MeV	4-6	4-6
Bunch charge	pC	20-250 pC	250 pC
Slice rms transverse emittance	mm.mrad	$\leq$1	-
Slice rms energy spread	keV	25-150	-
Field amplitude stability	%	0.01	0.1
Field phase stability	degree	0.1	1
Photocathode		Metal interchangeable	Metal interchangeable
RF feedback		Required	-

These requirements are discussed in detail in the CLARA Conceptual Design Report [4]. The bunch must have a 250 fs 400 A flat top to reach saturation at 100 nm in a compact undulator section, and a 250 pC bunch charge allows enough charge contingency to achieve this flat top with the expected rise and decay. The 20 pC lower charge requirement stems from the need for very short ($\leq$ 25 fs) bunch length in the ultra-short operating mode. The stability specifications come from the requirement that the energy jitter in the electron bunch should be low enough that the rms FEL wavelength jitter is less than half the SASE bandwidth. The transverse emittance at the FEL should be $\leq$ 4 mm.mrad according to the equation $\epsilon_n < \lambda_r\gamma/4\pi$, where ϵ_n is the transverse emittance, λ_r is the resonant wavelength, and γ is the Lorentz factor. However a lower emittance will increase the FEL performance and help to reduce the saturation length [34]. The beam energy is of less importance, and the specification value is simply a consequence of the field requirement and expected cavity length.

Higher accelerating field gradient leads to lower emittance, as described in Section 2.1.2, and a higher repetition rate gives a higher FEL repetition rate which leads to more statistics for

experimental results in a shorter time. For CLARA the repetition rate and gun field are traded off against each other in the different modes of operation to moderate the average power, and are as high as was thought practical based on a review of current photoinjectors. Even so, the most challenging aspect of the requirements is the power handling capability of the photoinjector. The high repetition rate in the 400 Hz mode and 100 MV/m gradient give a high average power of 6.8 kW, compared to 2.6 kW for the 100 Hz mode. The klystron available has a peak RF power output of 10 MW, which may limit the achievable gradient. A 1.5 cell structure was chosen to limit the overall average heat load, which was estimated to be close to double the given values for a 2.5 cell structure [35].

2.2.3 Gun cavity shape optimisation

A review of similar guns led to the investigation of two options. One was a design similar to the DESY/PITZ/Strathclyde/DLS type of gun with a coaxial coupler at the front end of the gun, another was investigating the possibility of coupling the power from the back of the gun cavity. Initial investigations on the back coupled design were promising, but due to time constraints it was decided to focus effort onto the classical front-coupling scheme. The general characteristics of that design include coaxial power coupling from the front of the gun with a doorknob conversion to waveguide. A coaxial coupler was chosen over side-coupling in order to preserve symmetry of the fields in the cavity and to minimise the effects of the dipole component. This also allows a solenoid to be placed around the cavity itself, rather than after, which is desirable from a beam dynamics standpoint. The cells are cylindrical with rounded edges to allow for a better distribution of the peak fields and heat load. Integral water-cooling will be required due to the high average power levels, and will be provided by water channels cut into the bulk of the copper. The cathode will be a plug that is inserted into the back-plate of the first cell. The gun operating frequency is European S-band at 2.9985 GHz to match the CLARA and VELA RF frequencies. An optimisation was carried out in conjunction with beam physics studies to define the optimal dimensions for the CLARA operating parameters. Starting from a basic coaxial gun cavity, the first cell length, iris radius, iris minor/major radii, and edge rounding radii were optimised by varying the parameters shown in Figure 2.8.

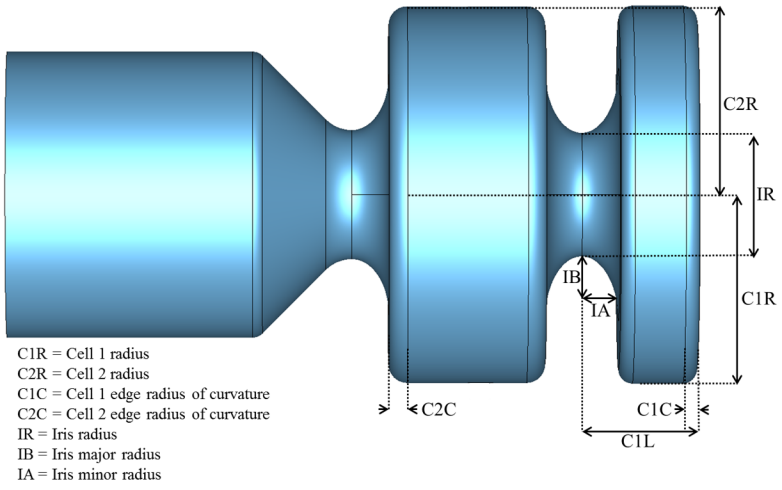

Figure 2.8: The basic gun design showing parameters to optimise.

A Mathematica [36] front-end for Superfish [37] was developed to my specification by J.K. Jones, which I then used to optimise the cavity shape. The front-end allowed each parameter to be varied individually, and optimised the radii of both cells to compensate for any changes in frequency or field flatness. In principle, a higher field in the cathode vicinity is desirable as this reduces the beam emittance by limiting space charge effects as described in Section 2.1.2. However, assuming we are limited to a peak electric field of 120 MV/m, as this is the highest gradient previously reached in an S-band photoinjector [26], having a higher field in the first cell over the second cell just reduces the final beam energy. Thus the cavity was kept field-flat, and should have the same peak field in each cell to within 1% in the RF design.

First cell length

The first parameter to determine was the first cell length. The lengths were defined as fractions of the full cell length, defined from iris to iris, and equal to 50 mm. Superfish models of guns with a first cell length ranging from 0.4 to 0.6 of the full cell were created and optimised using the Mathematica frontend. For each gun created, the RF phase and solenoid settings were optimised for minimum transverse emittance after the first linac section of CLARA as described in [35] by J. McKenzie and summarised here. A peak on-axis electric field of 120 MV/m at the cathode was assumed in all cases. The optimisation was carried out at bunch charges of 25, 100, and 250 pC to cover the CLARA operational range. The biggest effects are seen for higher charges. Figure 2.9 shows that going for a longer first cell, there is a reduction in transverse emittance and an increase in beam energy from the gun. However, looking at the longitudinal properties, there is a clear optimum cell length for minimising bunch length and longitudinal emittance. Figure 2.10 shows that for longer cell lengths there is more curvature in the longitudinal phase space of the beam. This makes the beam more difficult to manipulate further down in CLARA to provide the required bunch length for the Free Electron Laser (FEL). Given that there is no requirement to extend the beam energy above 6 MeV, the transverse emittance in all cases meets the requirements for the CLARA FEL, a first cell length of 0.5 times that of the full cell provides optimum longitudinal beam properties.

Iris radius

The next parameter to optimise was the iris radius. A larger iris radius results in a weaker accelerating field along the beam axis. It can be seen in Figure 2.11 that for a larger iris radius less field is concentrated near the beam axis, reducing the shunt impedance. This result can be seen in the plot of simulated R/Q in Figure 2.12. This is the R/Q without the inclusion of a Transit Time Factor (TTF). The actual value will be around half the value shown here, depending on the electron starting phase.

Changing the radius has little effect on the maximum surface fields, leading to a 3 % change in maximum surface magnetic field across the whole range and a 2 % change in maximum surface electric field for a fixed gradient. Both increase with increasing radius. For these parameters, a smaller radius is preferable, however the mode separation between the zero and π modes decreases as the iris radius is decreased, so there is a limit on how small the radius can be made. This can be seen in Figure 2.13.

The lower limit for mode separation was decided to be a conservative value of 20 MHz. This was based on a bandwidth calculation and results from the LCLS gun design where a mode separation

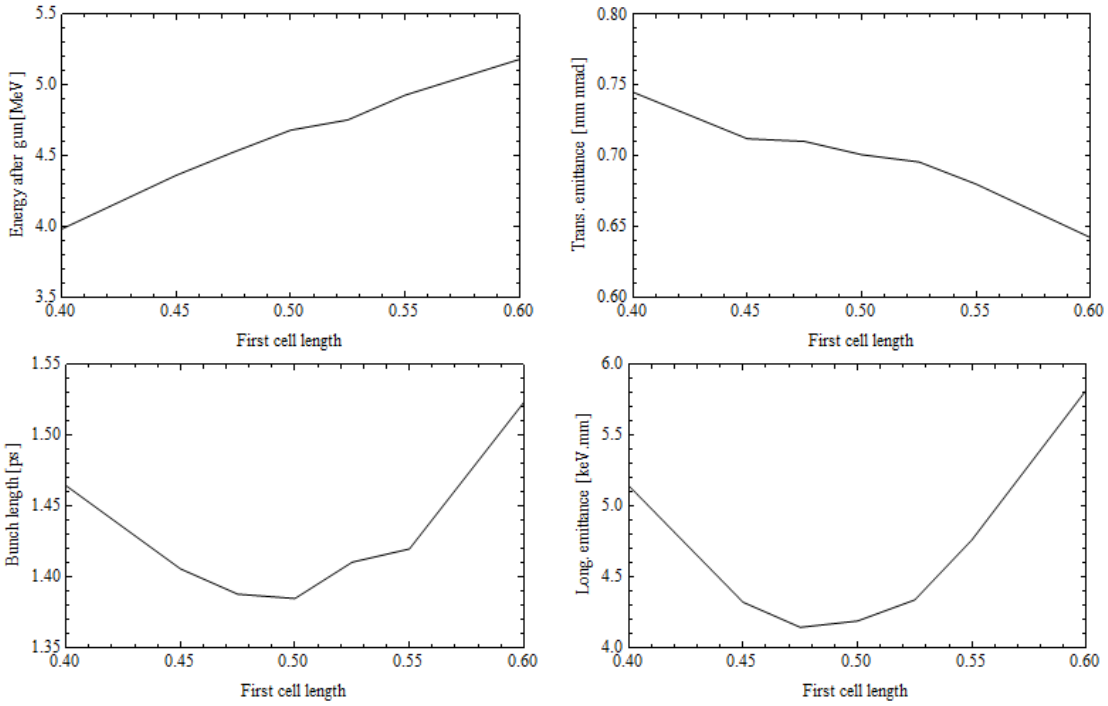

Figure 2.9: Variation of beam parameters for a 250 pC bunch after first linac on varying length of first cell of photoinjector. Simulation in Superfish and ASTRA. Reproduced from [35]

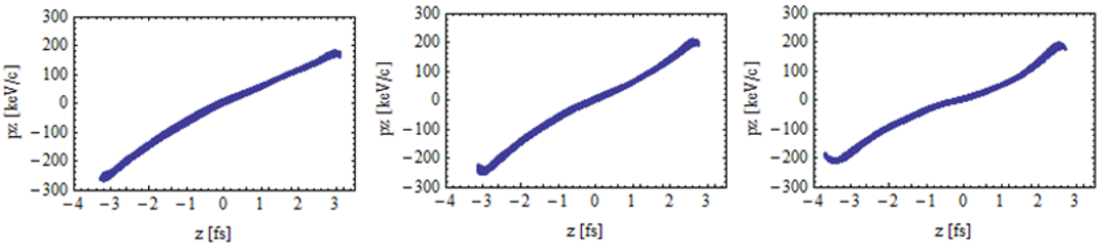

Figure 2.10: Longitudinal phase spaces for the optimised beams after linac 1 for first cell lengths of 0.4, 0.5 and 0.6 (left to right) of the full cell length.Reproduced from [35]

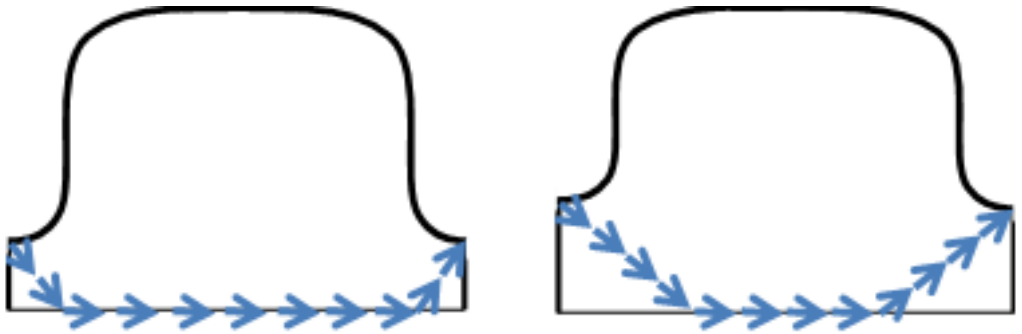

Figure 2.11: Schematic of two half-cells showing the influence of iris radius on accelerating field on the beam axis.

of 15 MHz greatly reduced beating between the modes [26]. From this requirement, the iris radius was chosen to be 13.7 mm.

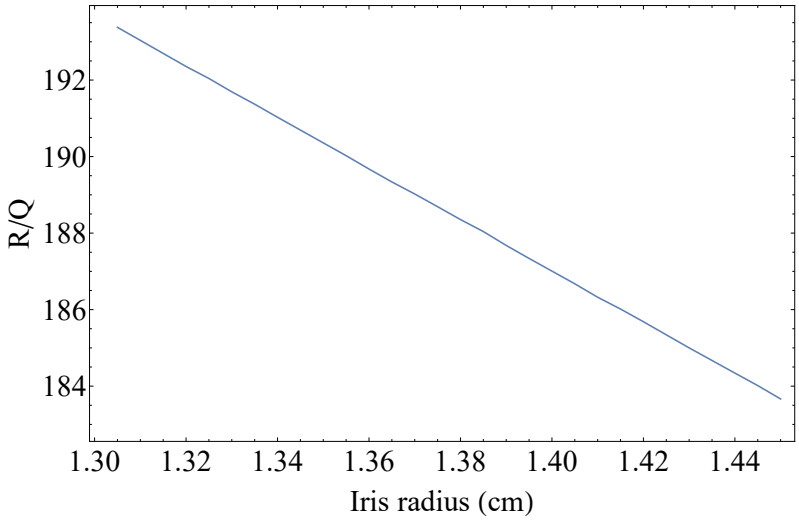

Figure 2.12: The effect of iris radius on R/Q

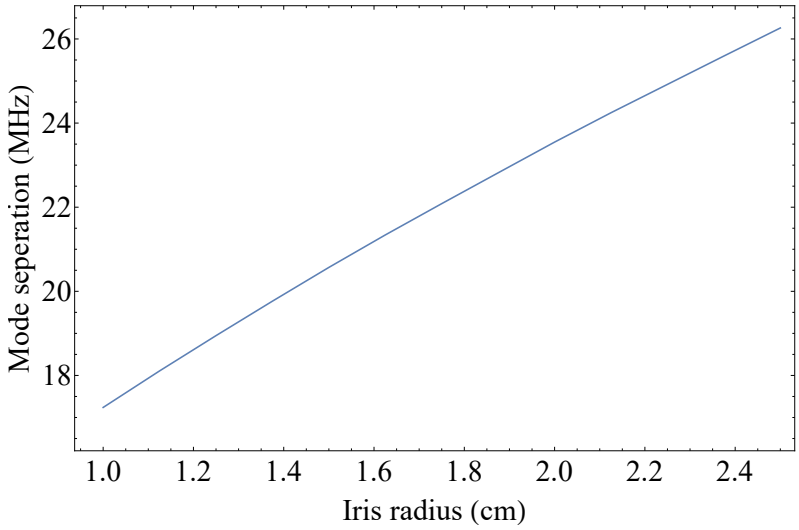

Figure 2.13: The effect of iris radius on mode separation

Iris Ellipticity

The minor radius of the iris ellipse was briefly investigated, but due to cooling constraints it was determined that it could not be made shorter, whereas making it longer would decrease the amount of field on axis, so it was left at 8 mm. Ellipticity is here defined as the major radius/minor radius. Changing the major radius while keeping the iris radius and minor radius the same is equivalent to varying the ellipticity of the iris. As expected the ellipticity had a large effect on the surface electric field, the larger the ellipticity the lower the peak E field on the iris. At an ellipticity of 1.75 the curve flattens, as the peak E field on the cell to cell iris becomes equal to that on the cell to coupler iris. This can be seen in Figure 2.14. The value at this point is 113 MV/m, 0.94 times the cathode field. As this value is acceptable, there is no need to alter the iris any more so an ellipticity of 1.75 corresponding to a major iris radius of 14 mm was chosen. This does decrease the R/Q, and increase the surface magnetic field, but both changes are by less than 1%. It also increases the mode separation to 22 MHz as can be seen in Figure 2.14, meaning the iris radius can be further reduced.

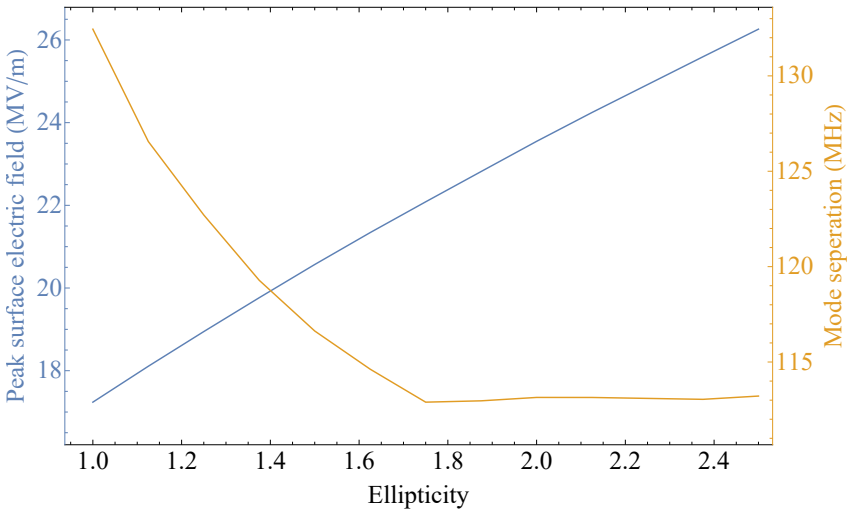

Figure 2.14: The effect of iris ellipticity on maximum surface electric field and mode separation.

Iris Radius (2nd iteration)

With a higher ellipticity, the iris radius can be further reduced to 13.4 mm and still have 20 MHz mode separation, as seen in Figure 2.15

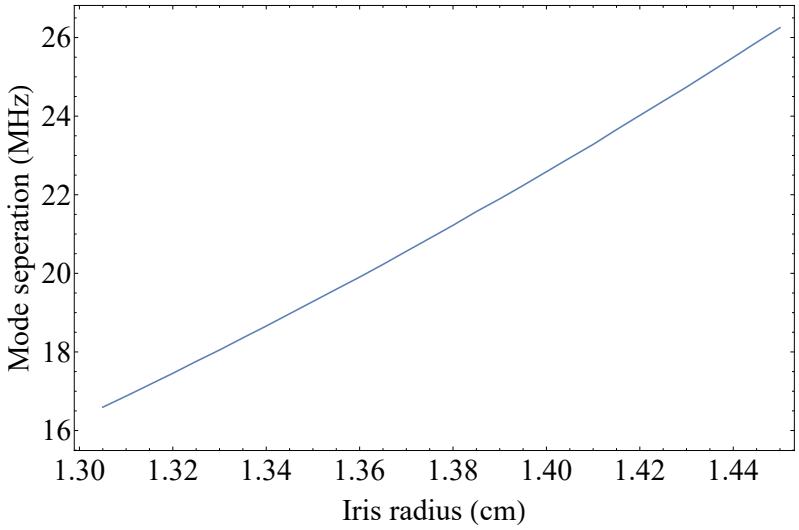

Figure 2.15: The effect of iris radius on mode separation with ellipticity 1.75

Cell Edge Radii

The effect of the radius on the cell edge on surface magnetic field was investigated by using the Mathematica frontend to optimise gun cavities in Superfish with a range of radii. These models were then simulated in CST [38]. The H fields along a curve on the surface, shown in Figure 2.16, were then plotted and compared, as seen in Figure 2.17. Is should be noted that the 0.5 mm radii result includes some non-physical values due to poor mesh quality. These have been ignored.

The conclusion drawn from this is that the peak field is the same in each case, but for a smaller edge radius the path length is longer. This means the area heated in the gun will be larger, so there will be more integrated heating the smaller the radius. However, the effect of this is not

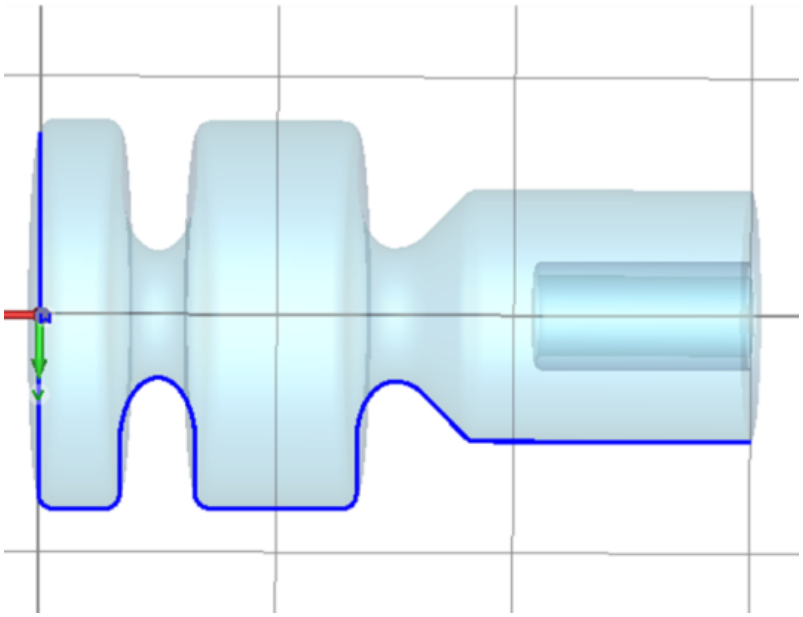

Figure 2.16: The curve over which the surface H field was calculated

large, and mechanical constraints, due to water cooling, mean the radius cannot be larger than 3 mm on the first cell. The cell edge radii were chosen to be 3 mm on the first cell and 4 mm on the second.

Cavity design results from Superfish

The initial 2.5D optimisation yields the results seen in Table 2.2. The on-axis electric field is shown in Figure 2.18.

Table 2.2: RF results for the Superfish design of the CLARA photoinjector cavity

Stored Energy	6.23 J
Maximum Surface H	221 kA/m
Ratio of cathode E field to maximum surface E field	1.065
Field flatness	0.99987
Operating Mode Frequency	2998.498 MHz
Zero Mode Frequency	2978.414 MHz
Q0	13768.8
Cell to cell coupling (k)	0.00686
Mode Separation	20.09 MHz
Integrated Axis field	6.69 MV
R/Q (no Transit Time factor)	222.24
R (no Transit Time factor)	3.06 MΩ

2.2.4 RF probe

The RF probe design is described in [39] by P. Goudket and will be summarised here. The photoinjector requires an RF probe for fast feed-forward power compensation. The feed-through

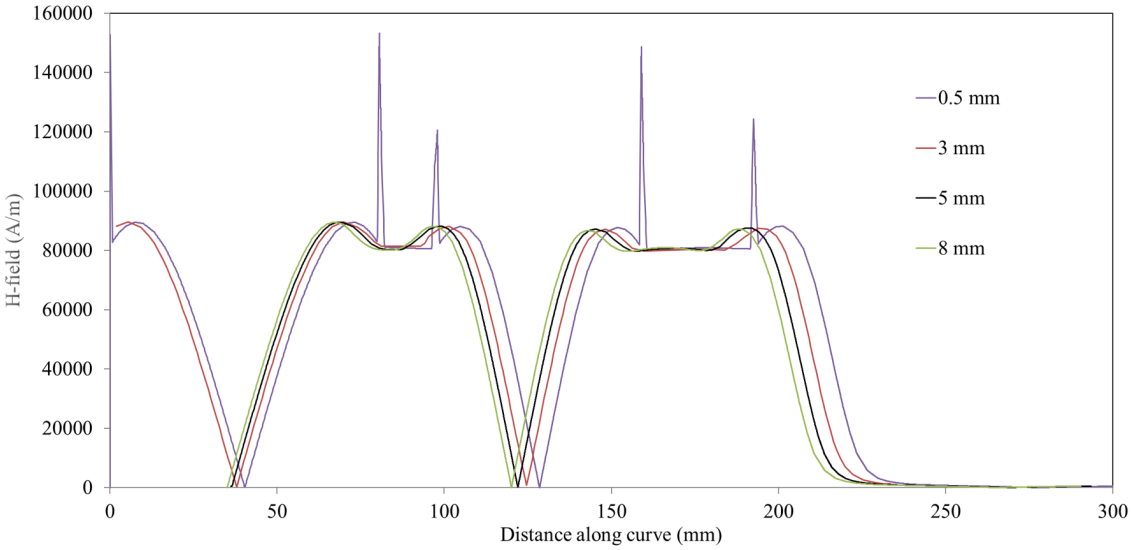

Figure 2.17: H-field on curve for varying edge radii. The spikes are due to meshing issues and can be ignored.

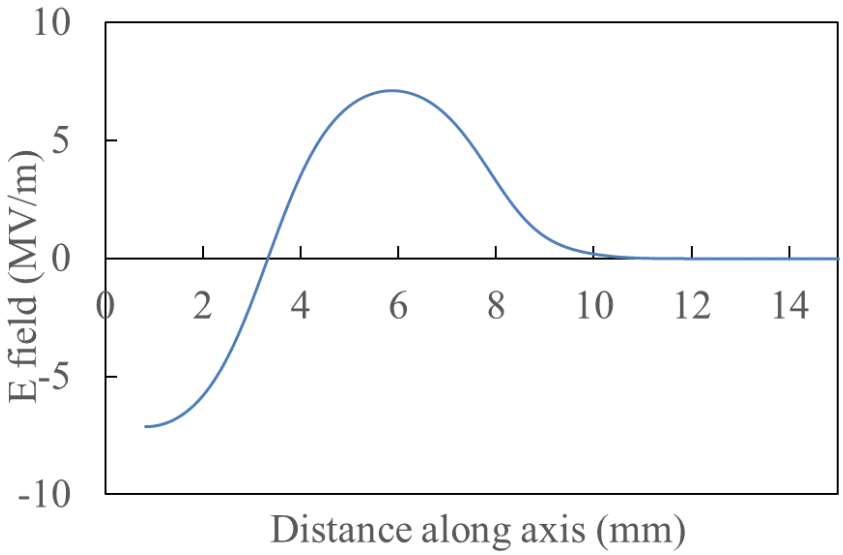

Figure 2.18: On-axis electric field in initial 2.5D optimised design

central pin has a diameter of 0.8 mm. In order to ensure clearance of the pin it was chosen that the probe aperture would have a diameter of 1.5 mm.

The probe design was performed in parallel with the design of the cooling channels for the structure. The probe was placed in the full cell, 3 mm from the mid-line of the cell to fit with the cooling channels. The position of the probe can be seen in Figure 2.19.

The outer wall of the cavity before the addition of the probe has surface currents of up to 173 kA/m. To calculate the instantaneous surface temperature rise T_s in this region we can use the Equation 2.9 [40]

$$T_s = \frac{R_s H^2 \sqrt{\tau}}{\sqrt{\pi \rho k c_\epsilon}} \tag{2.9}$$

where R_S is the surface resistance, H is the peak magnetic field in the region, τ is the pulse length, and ρ, k and c_ϵ are the density, heat conductivity and specific heat respectively of oxygen free

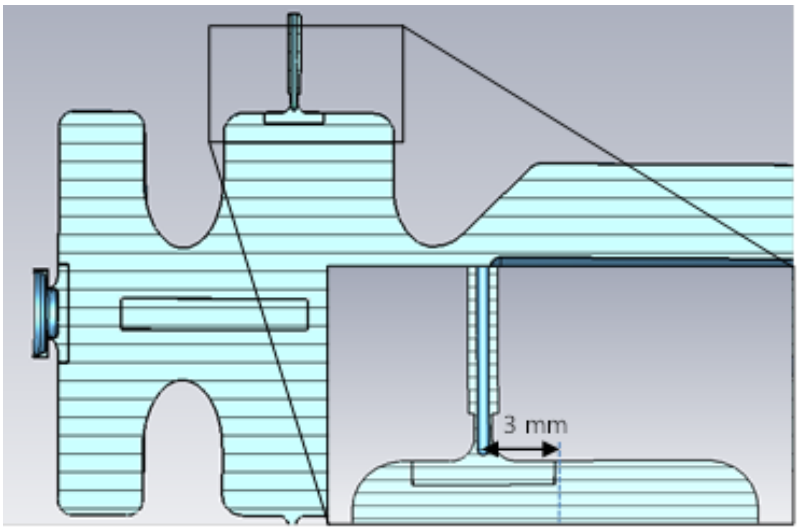

Figure 2.19: Position of the RF probe in the cavity. The figure shows the internal vacuum space of the cavity.

copper. The maximum T_s in the outer wall is 11.2 K for a 3 μs pulse.

The probe aperture will cause field enhancement, therefore a rounded aperture edge is required to limit surface heating that would otherwise cause metal fatigue and damage. A curvature with radius 2 mm is mechanically feasible and is sufficient to limit the surface current to 227 kA/m and the instantaneous temperature rise during a 3 μs RF pulse to 19.2 K. The limit over which temperature damage can be expected is 40 K [41].

To ensure field symmetry, a 1 mm deep dimple with the same aperture size and curvature of the probe was added to the design on the opposite side of the cell. The radius of the cell was adjusted by 1 μm to compensate for the changes and restore the field flatness. The effect of manufacturing error on the aperture radius of curvature was studied, and found that an error of 0.5 mm affects the field flatness by less than 0.1%.

Simulation shows that for the coupling factor to be -70 dB, the inner pin of the probe will need to be recessed in the aperture by approximately 1.5 mm. The pin will be left intentionally longer until RF transmission measurements are performed on the manufactured cavity, and then the pin can be trimmed to length before brazing.

It was verified that the electric field was not measurably distorted by the addition of the probe. The variation in the magnitude of the E-field on an azimuthal curve with a 3.2 mm radius in the centre of the second cell is less than 0.02%.

2.2.5 Photocathode

The photocathode design is described in [39] by P. Goudket and will be summarised here. The photocathode will be inserted into the gun through the back-plate. RF contact between the insert and the cavity body will be ensured by spring fingers shown in the Figure 2.20. It was verified that the spring design does not lead to a concentration of field in the open region. Adding the cathode plug also perturbs the field in the first cell. The LBNL/FNAL modification of the previous DESY/LASA plug design was chosen, as the former has a reduced diameter tip. This limits the size of the aperture and the perturbation to the fields in the first cell. The cathode plug profile was optimised to maximise the peak field in the centre of the cathode, while reducing the peak

field away from the cathode (caused by the edge effect of the cathode plug opening). An elliptical shape falling back to 0.6 mm from the cathode face was found to be the optimum plug shape. The optimisation curve in Figure 2.22 shows the ratio of peak field in the cathode centre divided by the peak field on the edge. The flat central section of the cathode has a 6 mm diameter.

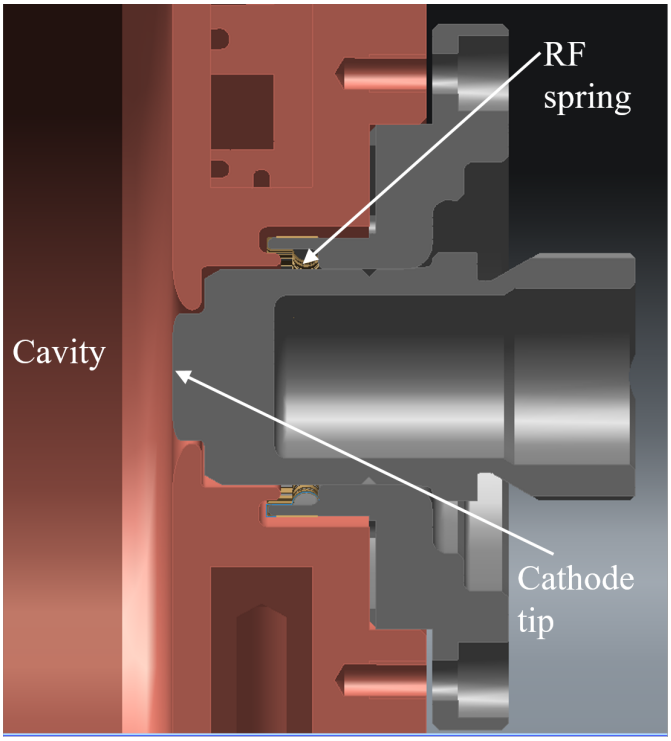

Figure 2.20: The design of the cathode region showing RF spring fingers

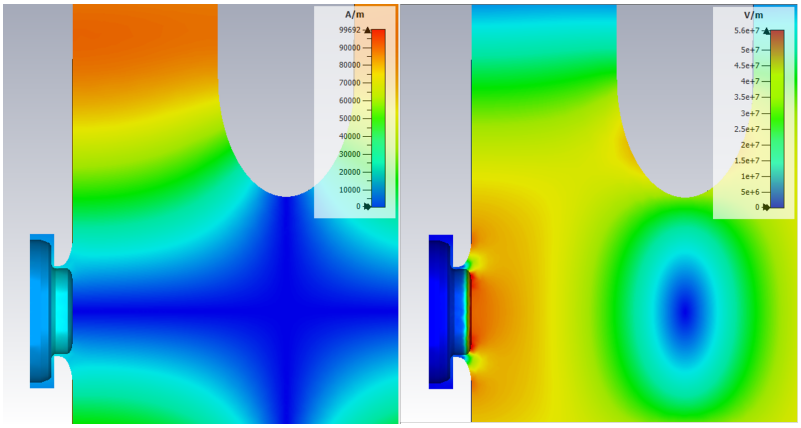

Figure 2.21: The H-field (left) and E-field (right) in the cathode region

Some field is unavoidable in the gap between the cathode plug and the cavity body. If the peak field is 120 MV/m, the field in the plug may reach 7 MV/m. This is much higher than multipactor levels, but there will also necessarily be some lower fields that may be susceptible to multipacting further inside the gap. Multipactor simulation in this area is unreliable due to the comparatively small volume of the area, but should multipactor prove to be a limiting factor, grooves on the plug could be implemented as a countermeasure. There is a requirement for the cathode to be removed and replaced with different cathodes for cathode characterisation purposes thus a study was performed to determine the effect of cathode misalignments during this process. If the cathode

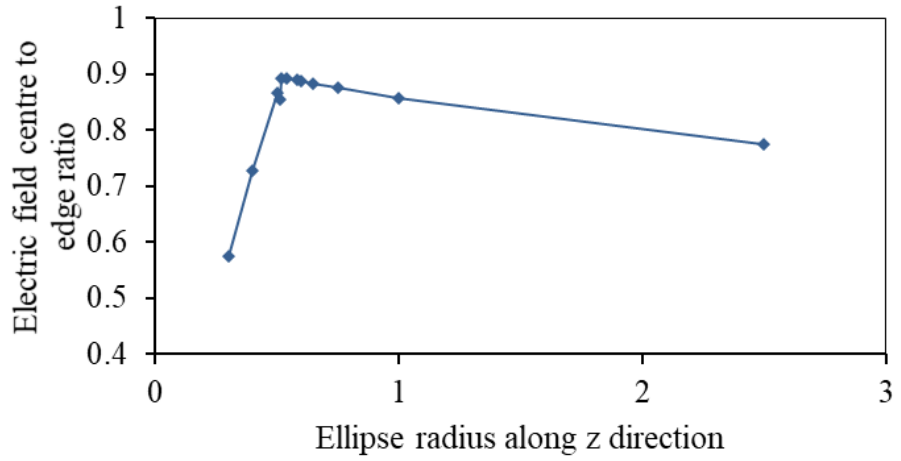

Figure 2.22: The optimisation curve for the elliptical rounding of the cathode edge

penetrates too far or too little into the cavity, the effect on the cavity frequency is small, less than 200 kHz for a 100 m error, which could be corrected for by adjusting the water temperature. The effect on the field flatness is less than 2%. If the cathode is tilted 2 degrees from vertical the effect on the fields is negligible, the change in frequency is 4 kHz, and the field flatness changes by 0.3%. The results can be seen in Figures 2.23 and 2.24.

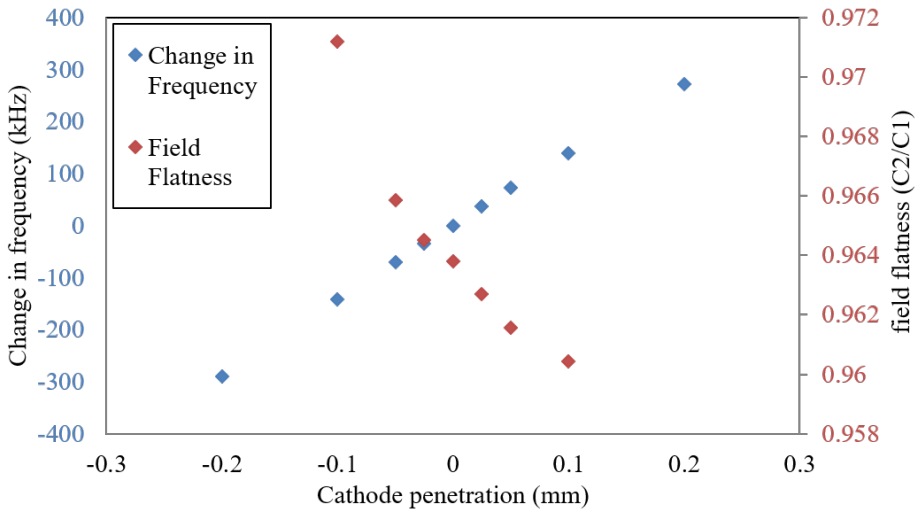

Figure 2.23: Effect of cathode penetration on cavity frequency and field flatness

2.2.6 Coupler design

The initial design of the coupler is described in [39] by G. Burt and will be summarised here. A coaxial type coupler was chosen to minimise the field asymmetry in the structure, and to provide full freedom for the placement of the gun solenoids. However studies carried out on single-feed designs show that they lead to a dipole mode with cut-off a frequency of 2.946 GHz, calculated from

$$f_c = \frac{c}{\pi(R+r)} \tag{2.10}$$

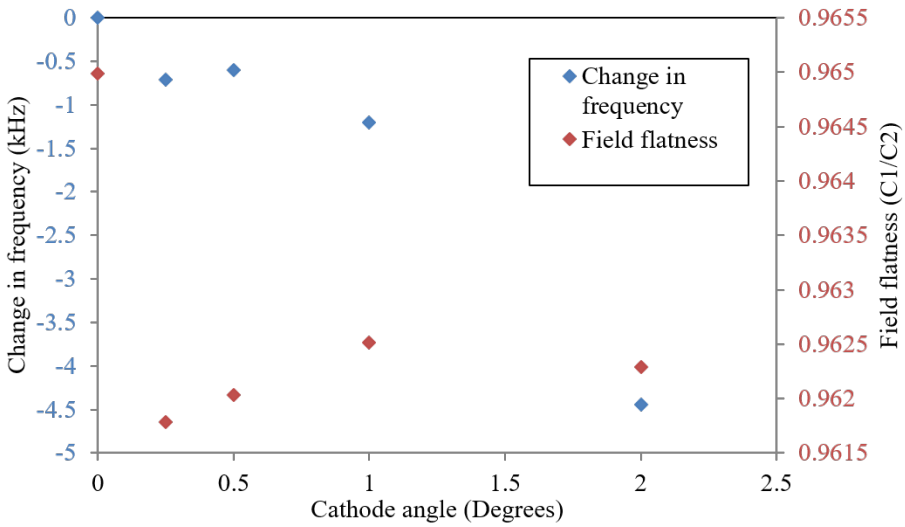

Figure 2.24: Effect of cathode angle on cavity frequency and field flatness

with outer radius $R = 22.39$ mm and inner radius $r = 10$ mm. The TE_{11} mode can propagate to the cavity. It is estimated that up to 25% of the forward power can be converted to a TE_{11} mode rather than the desired TEM mode. This could cause a 50 kV transverse kick to the beam and cause asymmetric heating, coupler mismatch and multipactor conditions.

In order to allay that risk, it was decided to use a dual-feed system whereby the RF arrives to the cavity symmetrically, and the dipole modes excited by each feed cancel. A capacitive match at the doorknob is the solution commonly chosen for similar designs. However, it is a risk in terms of multipactor and breakdown due to its geometry. An inductive iris would allow matching while removing the additional vulnerabilities presented by the capacitive coupling. A design solution for an inductive iris is shown in Figure 2.25.

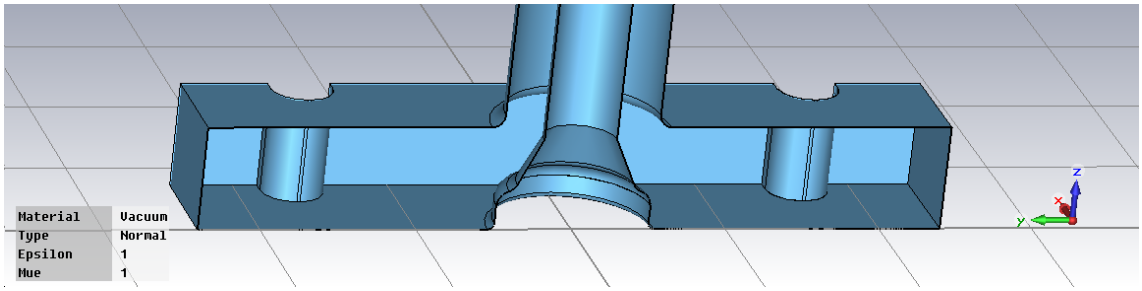

Figure 2.25: Design for an inductive iris

The inductive design iris is does not allow for tuning the match, and access for vacuum pumps is restricted. In order to allow the coupler to be tuned to achieve the best possible match, an alternative, capacitively coupled "H-feed" design was chosen. The coupler is shown in Figure 2.26. Movable shorts allow for tuning of each arm separately, allowing compensation of phase errors in the two arms as well as the overall match of the transition. The shorts also give good access for vacuum pumping. A sensitivity study was performed on various dimensional parameters (including the inner and outer coaxial line radii, the shape of the doorknob cone and the waveguide dimensions) and all were found to be cause a change of under 20 dB for a dimensional change of 100 μm.

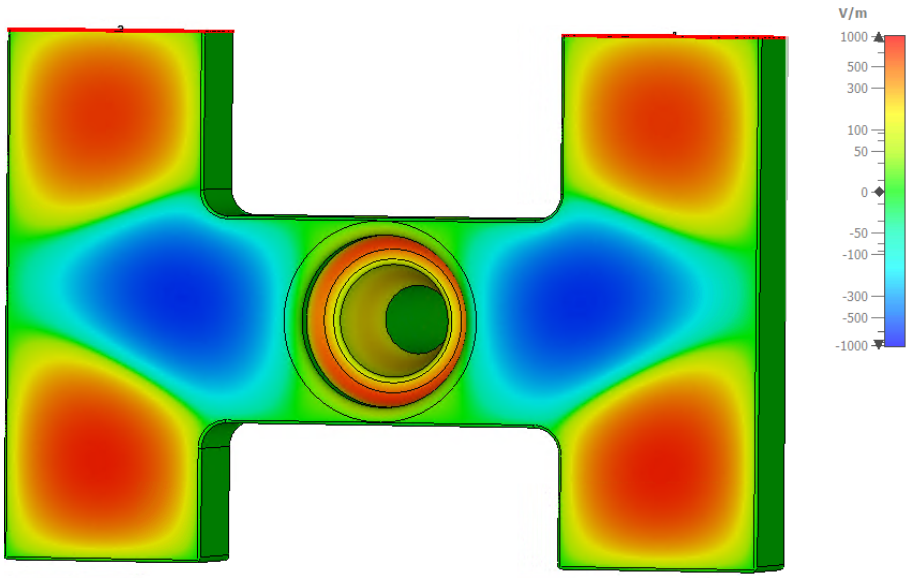

Figure 2.26: H-coupler design showing amplitude of electric field in z direction

Dipole component simulations

I studied the effect of a phase difference between the two RF inputs into the coaxial line, to further understand the tolerances and tuner ranges required in the H-coupler arms. CST simulations were performed on the gun model with the H-coupler. The phase difference between the input ports on the H-coupler was varied between 0 and 130°, corresponding to a length offset of 0 to 50 mm on one arm (1 mm=2.6°). Figure 2.27 shows the absolute electric field coupling into the cavity for an offset of 10 mm. It can be seen that the phase front reaches one side of the end of the coaxial line first. The field then sweeps across the coupler iris of the cavity. This is due to the superposition of the TEM and TE_{11} in the coaxial line.

Figure 2.28 shows the fields in the z-y plane at the approximate phase that the beam will pass through the coupler iris. The left figure shows the electric field in the x direction, and the right figure shows the magnetic field in the y direction.

Figure 2.29 shows the magnitude of the E field in the -x direction and H field in the -y direction over a range of phase offsets. The magnitude is scaled to 100 MV/m on the cathode.

The longitudinal FWHM of the dipole component fields seen at the exit of the cavity is approximately 20 mm. This was used to calculate the kick voltage from the electric field and the equivalent kick voltage from the magnetic field for electrons with velocity c. The kicks from the two fields are in opposite directions, in the x and -x directions for the electric and magnetic fields respectively. Figure 2.30 shows the kick voltage as a function of coupler arm offset. Assuming the kicks cancel as they are in opposite directions, the offset would need to be 110° of phase or 42 mm to approximate to the 50 MV/m kick from the single-feed option. For zero offset the combined kick is 130 V.

The 3D fields were exported from CST and GPT [42] simulations were performed for the 0 offset, 1 mm offset and 10 mm offset by W. Kyle [43]. The simulations follow the beam up through the first linac. They are very briefly summarised here. The dipole component causes a transverse beam offset in both x and y. Using standard machine parameters the transverse beam offset is small, less than 0.3 mm, and mostly damped by the exit of the first linac for the 1 mm case but is very large, up to 1.8 mm and maintained along the beam line in the 10mm case. This is changed little

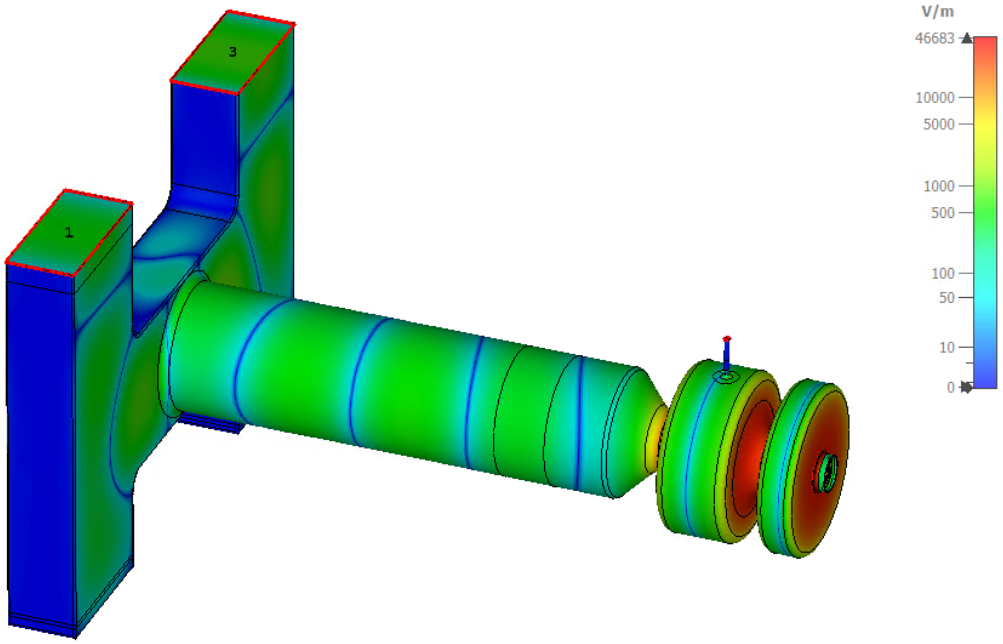

Figure 2.27: Absolute E field in the coupler and gun for an offset coupler.

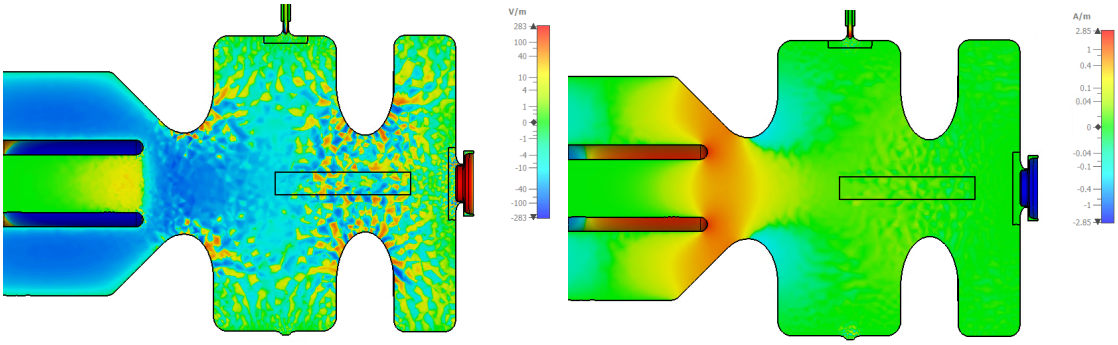

(a) E_z in the z-y plane

(b) H_y in the z-y plane

Figure 2.28: E_z (left) H_y (right) fields in the z-y plane for an offset coupler.

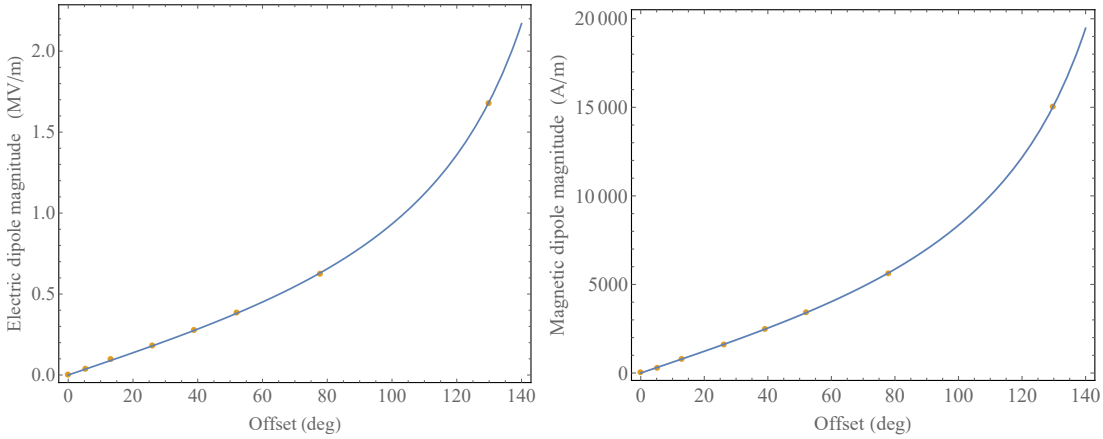

Figure 2.29: E_x (left) and H_y (right) dipole component magnitude scaled to 100 MV/m on the cathode as a function of coupler arm offset

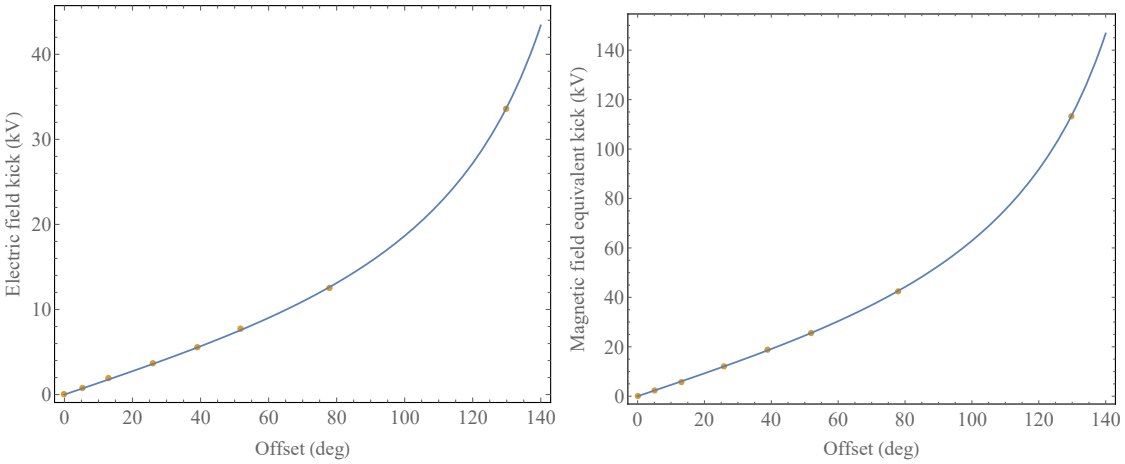

Figure 2.30: Electric (left) and magnetic (right) dipole component equivalent kick voltage scaled to 100 MV/m on the cathode as a function of coupler arm offset

by re-matching the machine parameters for each case. There is a significant increase in transverse bunch size as the dipole component increases when using the standard machine parameters but this can be almost entirely negated by adjusting the solenoid strengths. The transverse emittance shows a significant increase only for the 10 mm case, but again this can be negated by re-matching the machine parameters.

In conclusion, the presence of a phase difference in the two RF inputs to the coaxial coupler has no lasting detrimental effect for up to 1 mm (2.6°) offset.

It is interesting to note that a similar dipole component was discussed in the PITZ RF gun [23]. The H-coupler design is a solution to this problem.

Matching

There is 10 MW peak power available from the klystron, from which it is expected a maximum of 7 MW will reach the photoinjector cavity after transmission line losses. Figure 2.31 shows the predicted gradient for a given input power. It can be seen that 7 MW is insufficient to reach 120 MV/m and a klystron upgrade will be required to meet the specification.

Whilst, particularly for such a high repetition rate, over-coupling the cavity would be highly beneficial and would decrease the average power by decreasing the filling time, it is not currently feasible due to the low peak power available. This is a possible upgrade path however.

For these reasons, and as beam-loading is negligible, the design is optimised for a matched coupler, $\beta_c = 1$. An inner conductor distance of 10.56 mm from the iris is calculated to give an Q_{ext} of 14280, which is equal to the Q_0 value given by CST Simulation Suite Frequency Domain solver [38]. As the Q_0 of the manufactured cavity may vary from this, the cavity coupling can be tuned via a gasket in the outer conductor, shown in Figure 2.32, which has the effect of adjusting the penetration of the tip of the inner conductor and therefore the Q_{ext}.

Multipactor

Multipactor is a phenomenon that is caused by secondary electron emission that is in resonance with the RF field, it can lead to operational issues and should be avoided at the design stage where possible. Multipactor is described in more detail in Section 4.1.1 The simulations of multipactor in

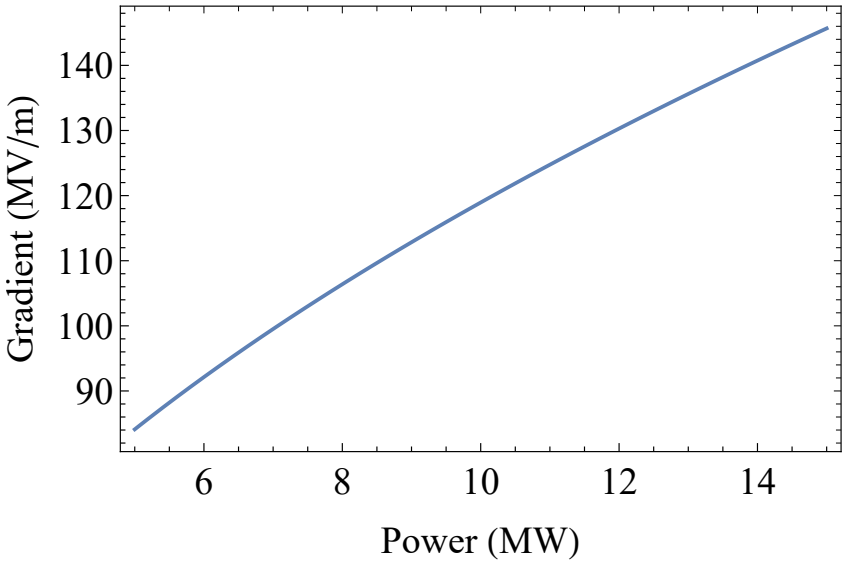

Figure 2.31: Predicted gradient for a given input power, scaled from CST simulation.

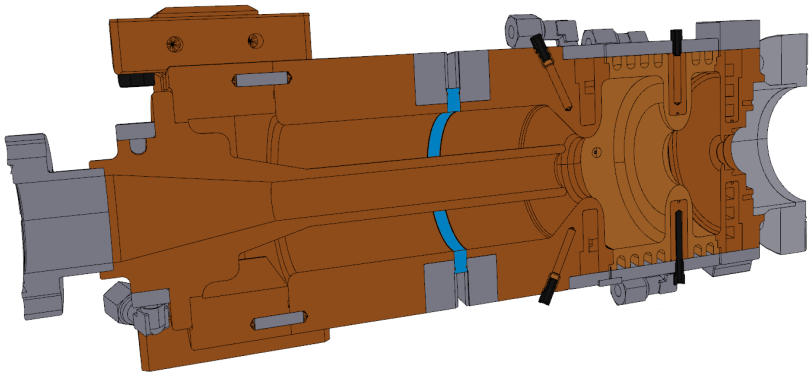

Figure 2.32: The gasket in outer conductor of coaxial line is shown in blue. Different gasket lengths allow the inner conductor penetration into the cavity to be adjusted.

the coaxial line are described by G. Burt in [39] and are summarised here. Multipactor in coaxial lines can be predicted by the general rule [44]

$$P \propto (\omega R_o)^4 Z \tag{2.11}$$

where P is the onset power of the multipactor, ω the RF frequency, R_o the radius of the outer coaxial wall, and Z the coaxial impedance.

The multipactor was simulated in the CST Studio Suite Tracking solver [38]. The inner coaxial wall has a radius of 12 mm, and the effect of outer wall radius on multipactor was studied and chosen to be 31 mm giving an impedance of 56.9 Ω. For this outer wall radius the onset of multipactor is over 18 MW.

Another multipacting trajectory was found at the transition between the coaxial and rectangular waveguide, at a power of 4-8 MW, the trajectories can be seen in Figure 2.33. This region has high surface fields. The coaxial aperture is limited to 31 mm, as increasing above this radius would require increasing the rectangular waveguide width from the standard WR284 dimensions. This constraint meant it was not possible to design out the multipactor, however the cavity is planned to be operated with an emittance-compensating solenoid, whose magnetic field will affect

the multipactor. A static magnetic field oriented parallel to the coaxial line was introduced in the simulation. Magnetic fields below 100 mT had no effect on the multipactor, and fields above 500 mT eliminated it entirely. It is estimated that the CLARA solenoid field will be approximately 250 mT. At this magnetic field level the multipactor is largely suppressed, but one narrow band is seen at 5 MW. This should be taken into account during RF conditioning and machine operation.

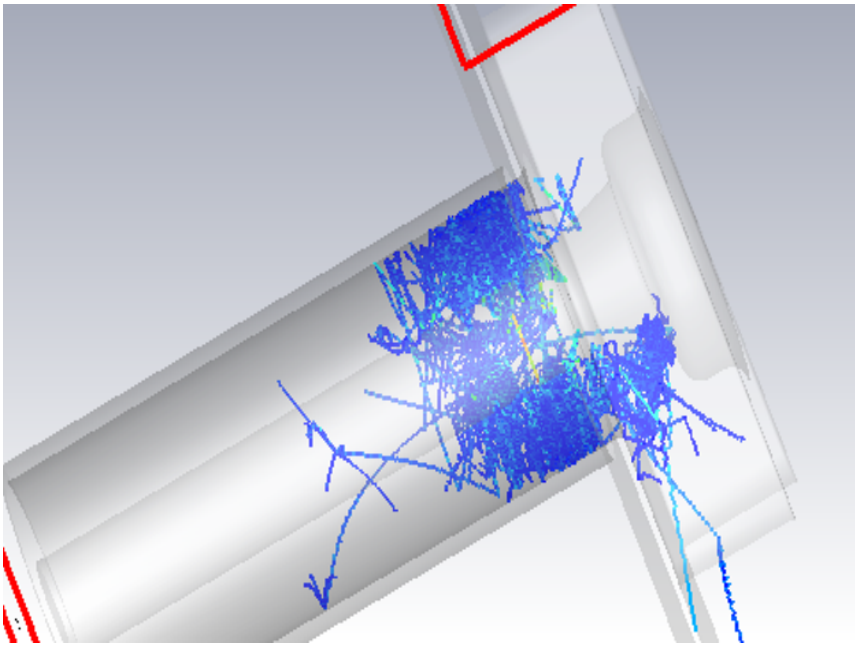

Figure 2.33: Multipactor trajectories in the coaxial region (low mesh evaluation)

2.2.7 Power handling

The cooling design is described in [35] by T. Jones and will be briefly summarised here. The cavity will be cooled by multiple water channels surrounding the cavity. The cooling channels from the Diamond Light Source S-band gun design [28] were used as a baseline, and modified to fit the cavity geometry and accommodate the RF probe. The magnetic fields on the surface were taken from the CST RF model and the heat flux calculated for each region. The total average heat load for the cavity was estimated to be 6.8 kW at 100 MV/m cathode field and 400 Hz repetition rate, which is the highest average power mode of operation. Computational fluid dynamics simulations were implemented with ANSYS. For a water temperature of 40°C and a pressure drop of 0.3 Bar across all channels the average temperature increase is 16°C. The iris region has a relatively high magnetic field, causing a temperature increase of 17°C. The highest magnetic field regions are the probe region and its symmetrising dimple, here the temperature increase is 22°C. The cooling channels and the surface temperature rise are shown in Figure 2.34.

2.2.8 Integrated design

The overall design was simulated in order to verify that all of the components interface correctly. Frequency domain simulations have verified that the coupler is matched and that the cavity remains at the correct frequency. The calculated Q_0 for this cavity is 14280 (measured from S21 bandwidth with matched coupler). The reliability of the design was benchmarked using a number of codes. It is worth noting that this cavity was initially optimised in Superfish which is known to be reliable.

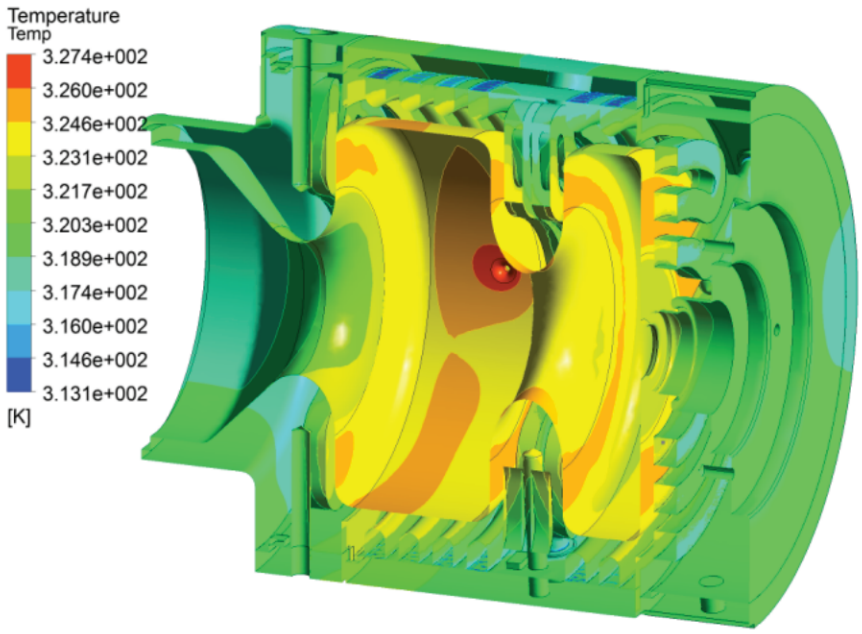

Figure 2.34: Temperature profile with the proposed cooling system with the gun operating at 100 MV/m at a 400 Hz repetition rate. Reproduced from [35]

CST simulations of the Superfish results have shown that the results lead to the correct frequency and flatness, both in Eigenmode solvers and Frequency domain solvers. A COMSOL verification of the overall geometry has been done to confirm the RF parameters. The RF parameters across the different codes are given in Table 2.3. The cavity only results are on the cavity shape with no probe, cathode or inner coaxial coupler line, optimised for field flatness. The full structure results are on the entire structure with all ports and couplers. The significant RF dimensions and sensitivity study are given in Table 2.2.8. The sensitivity study is important to inform the machining tolerances that should be allowed.

Table 2.3: RF results for frequency, field flatness and Q_0 for different codes and solvers.

	Cavity only			Full structure		
	Frequency (GHz)	Field flatness	Q_0	Frequency (GHz)	Field flatness	Q_0
Superfish	2.99849	0.9987	13768	-	-	-
CST Eigenmode	2.99814	0.9997	13717	2.9982	0.966	13805
CST Frequency Domain	-	-	-	2.99850	0.970	14280
COMSOL Eigenmode	2.99817	1.0002	-	-	-	-
COMSOL Frequency Domain	-	-	-	2.99856	0.961	-

Table 2.4: Major cavity dimensions at operating temperature, frequency and field flatness sensitivity, and temperature adjustment required per μm error to correct the frequency.

	Nominal dimension (mm)	Frequency sensitivity (MHz/mm)	Temperature correction (K/m)	Field flatness sensitivity (%/mm)
Radius of cell 1	40.979	-26.7	-0.535	398
Radius of cell 2	40.848	-52.8	-1.055	-386
Length of cell 1	17.000	-3.9	-0.078	54
Length of cell 2	34.000	-3.7	-0.074	-16
Iris curvature minor radius	8.000	2.8	0.056	-11
Iris curvature major radius	14.000	3.7	0.074	-13
Radius of the iris between cells 1 and 2	13.400	15.3	0.306	-56
Equatorial radius of cell 1	3.000	4.1	0.082	-59
Equatorial radius of cell 2	4.000	5.3	0.106	39
Coupler iris to coupler coax distance	10.800	0.4	0.008	0
Added penetration of cathode plug into cavity	0.000	1.4	0.028	-6
Angle from vertical of cathode plug (°)	0	-0.002	0.000	N/A
Coupler iris curvature minor radius	8.000	0.2	0.004	17
Coupler iris curvature major radius	12.000	0.2	0.004	13
Coupler iris radius	14.000	0.6	0.013	46

Chapter 3

400 Hz photoinjector tuning and low power tests

3.1 Tuning

3.1.1 Introduction

The CLARA photoinjector will operate at a high average power of 6.8 kW and as such will require significant cooling. This is achieved by building in water channels in the cavity body. This makes frequency and field flatness tuning with studs practically unfeasible. The cavity structure was fabricated at Research Instruments GmbH [45]. The frequency and field flatness of the cavity were tuned by taking pre-braze clamped low power RF measurements and using the data to trim the cavity cells to the optimum length. Each cell was manufactured with extra length to give a tuning range that would cover the frequency spread possible due to the radial tolerances. The extra length for each cell was proportional to its length, keeping the field amplitude in each cell of the design cavity equal. The extra length on cell 1 was 200 μm and on cell 2 422 μm

The cavity was measured and the amount to trim to achieve the operating frequency and field flatness was calculated. The trimming was planned to take place in a four steps covering 25% of the required frequency correction each, with coordinate-measuring machine (CMM) and RF measurements taken after each step. The nominal number of trims was 4, however the minimum possible amount that could be trimmed due to technological limitation was 50 μm, so contingencies were decided upon in the case that the value to trim was less than 200 μm. The contingencies for trimming can be seen in the flowchart in Figure 3.5. All trimming and all CMM measurements were performed by Research Instruments GmbH [45].

It should be noted that the it is more important to achieve the correct field-flatness during this tuning process than overall cavity frequency. This is because the overall frequency can be adjusted by adjusting the water temperature. The coefficient of linear expansion for copper is 16.7×10^{-6} °C^{-1} [46], multiplying by the operating frequency of 2.9985 GHz gives a temperature tuning rate of 50.08 kHz/°C. Tuning range is therefore limited by reasonable temperature ranges (a variation of 10°C either way is reasonable, leading to a 500 kHz tolerance in frequency).

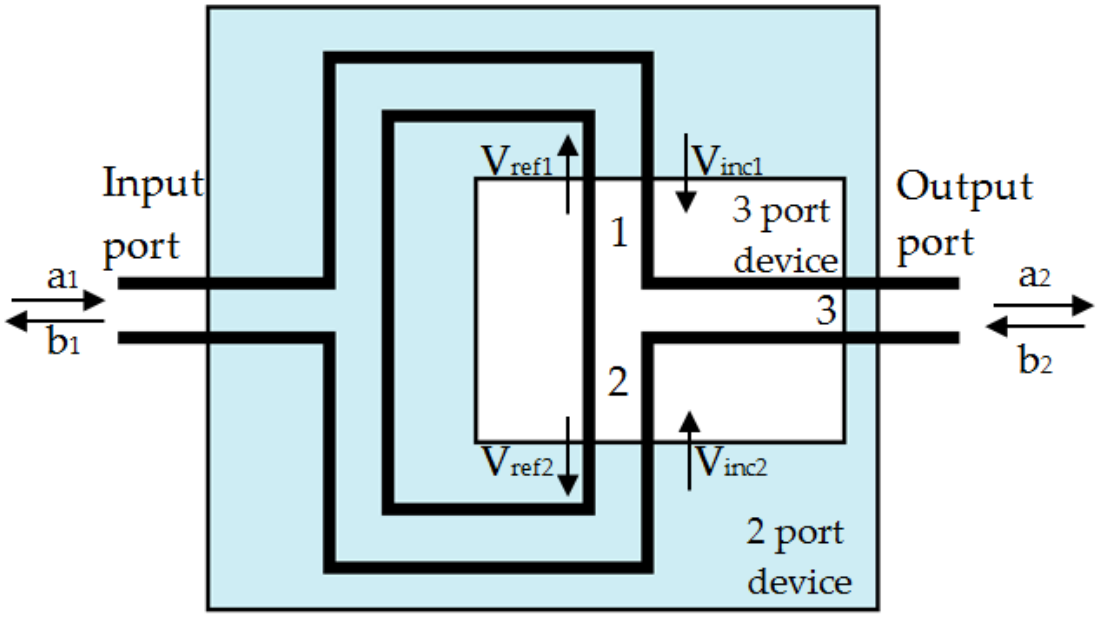

Figure 3.1: A schematic model of the gun cavity showing the correspondence between the ports of the 2 and 3 port devices

3.1.2 Measurement methods

Frequency

The frequency of the cavity was measured using a Vector Network Analyser to perform a measurement of the coefficient of reflection of the cavity. The cavity was excited through the power coupler and transmission measurements taken from the probe. Because there are two input ports, the coefficient of reflection of a theoretical 2 port device, as shown in Figure 3.1 was calculated [47].

For our purpose we would like to define the reflected signal from the input port of our theoretical 2 port device. This is by definition

$$\Gamma = \frac{b_1}{a_1} \tag{3.1}$$

where a_1 and b_1 are the normalized forward and reflected complex voltages at the input port, therefore

$$\Gamma = \frac{V_{ref}}{V_{inc}} \tag{3.2}$$

The input port of our 2 port device is a combination of ports 1 and 2 of the 3 port device, so

$$V_{inc} = V_{inc1} + V_{inc2} \tag{3.3}$$

$$V_{ref} = V_{ref1} + V_{ref2} \tag{3.4}$$

If you assume symmetry of the input ports then

$$V_{inc1} = V_{inc2} = V_{inc}/2. \tag{3.5}$$

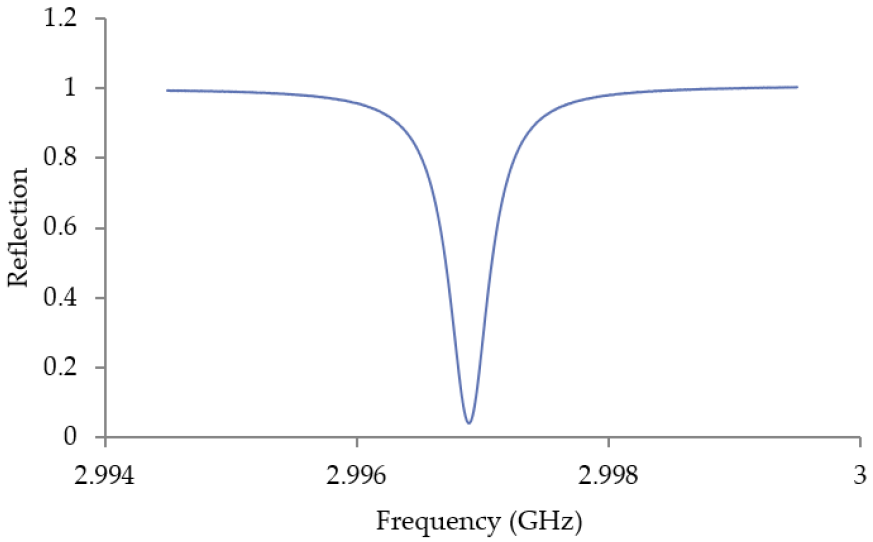

Figure 3.2: Dependence of cavity reflection on frequency

and the reflected voltages are

$$V_{ref1} = S_{11}V_{inc1} + S_{21}V_{inc2} = (S_{11} + S_{21})\frac{V_{inc}}{2} \tag{3.6}$$

$$V_{ref2} = S_{22}V_{inc2} + S_{12}V_{inc1} = (S_{22} + S_{12})\frac{V_{inc}}{2} \tag{3.7}$$

where the S-parameters are those of the 4-port device and can therefore be measured with a 2 port VNA. S11 = S22 due to symmetry and S21 = S12 , therefore $V_{ref1} = V_{ref2}$ and

$$V_{ref} = V_{ref1} + V_{ref2} = (S_{11} + S_{21})V_{inc} = (S_{22} + S_{21})V_{inc} \tag{3.8}$$

The input port reflection coefficient for our 2 port device is then

$$\Gamma = \frac{V_{ref}}{V_{inc}} = S_{11} + S_{21} = S_{22} + S_{21} \tag{3.9}$$

We therefore need to combine S11 and S21 to obtain the reflection coefficient for the full input coupler. The frequency value for which the reflection coefficient is minimal is taken as the resonant frequency f_0. An example can be seen in Figure 3.2.

The frequency of the cavity is then scaled to operating conditions using the measured room temperature, humidity and air pressure and the program CONVERTF [45]. The combined reflectance result can also be used to judge the symmetry of the H-coupler. The phase and magnitude of the reflection coefficient calculated from S11 and S21 and that calculated from S22 and S21 can be compared. In Figure 3.3 it can be seen that the signals vary very little , therefore tuning the coupler balance using the flexure tuners located on the shorts of the H- coupler was not required.

Field flatness

The field flatness, defined as a ratio of amplitude of the electric field in cell 2 to the amplitude of the electric field in cell 1 was determined using a bead-pull technique. A 0.2 mm nylon string was strung through the centre axis of the cavity, through a 0.5 mm diameter hole in the cathode. On the

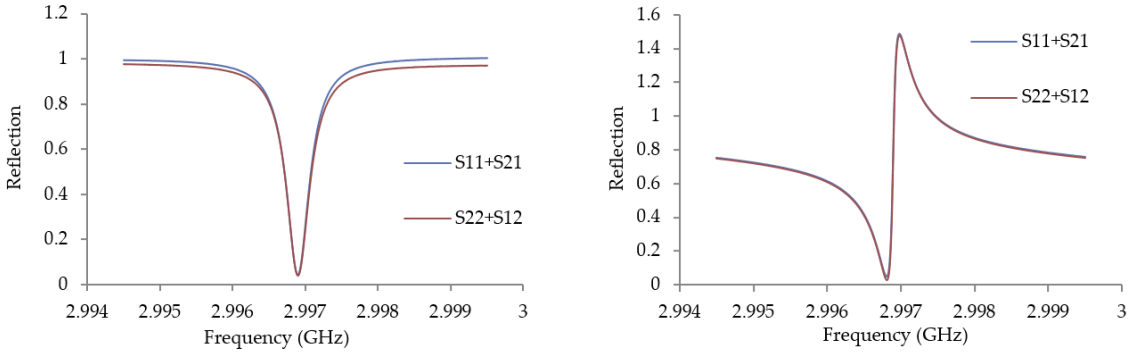

Figure 3.3: Symmetry of reflection coefficient measurement. Magnitude is shown on the left and phase on the right

string was a small cylindrical dielectric bead approximately 2mm in length and 1 mm in diameter. The bead was pulled through the cavity and the change in combined S11 phase measured. For the removal of a volume ΔV in a cavity volume V the Slater perturbation theorem [2] describes the shift in the resonant frequency ω_0 :

$$\frac{\Delta\omega_0}{\omega_0} = \frac{\int_{\Delta V}(\mu_0 H^2 - \epsilon_0 E^2)dV}{\int_V(\mu_0 H^2 + \epsilon_0 E^2)dV} = \frac{\Delta U_m - \Delta U_e}{U} \tag{3.10}$$

where $U = \frac{1}{4}\int_V(\mu_0 H^2 + \epsilon_0 E^2)dV$ is the total stored energy of the unperturbed field with amplitudes H and E. $U_m = \frac{1}{4}\int_{\Delta V}\mu_0 H^2 dV$ and $U_e = \frac{1}{4}\int_{\Delta V}\epsilon_0 E^2 dV$ are the time averages of the stored magnetic and electric energy removed respectively.

Modelling the bead as a spherical dielectric with volume ΔV the frequency shift is given as a function of the unperturbed electric field amplitude E at location of the bead:

$$\frac{\Delta\omega_0}{\omega_0} = -\frac{3\Delta V}{4U}\frac{\epsilon_r - 1}{\epsilon_r + 2}\epsilon_0 E^2 \tag{3.11}$$

The phase of the signal near the resonance changes linearly with the frequency as can be seen in Figure 3.3. The frequency shift can be given in terms of phase shift by

$$\frac{\Delta\omega_0}{\omega_0} = \frac{\Delta\phi}{2Q} \tag{3.12}$$

therefore $\Delta\phi \propto E^2$. This result means that the change in phase due to the presence of the bead in the cavity can be measured to find the field on axis normalised to the peak field in the second cell. In practice this is preferable to measuring the frequency change as the measurement can be done at a single continuous wave frequency. An example of the normalised field on axis is shown in Figure 3.4.

The cathode hole size was chosen to have a minimal effect on the field flatness and resonance frequency. Simulations of a 0.5 mm diameter hole show it shifts the frequency by 10 kHz, and has a negligible effect on the field profile when compared to a cathode with no hole. Close to the cathode the field perturbed by the bead is composed of both the unperturbed electric field and the additional field caused by the image charge of the bead on the cathode face. The unperturbed on axis field was extracted by fitting a cos^2 curve to the normalized electric field curve.

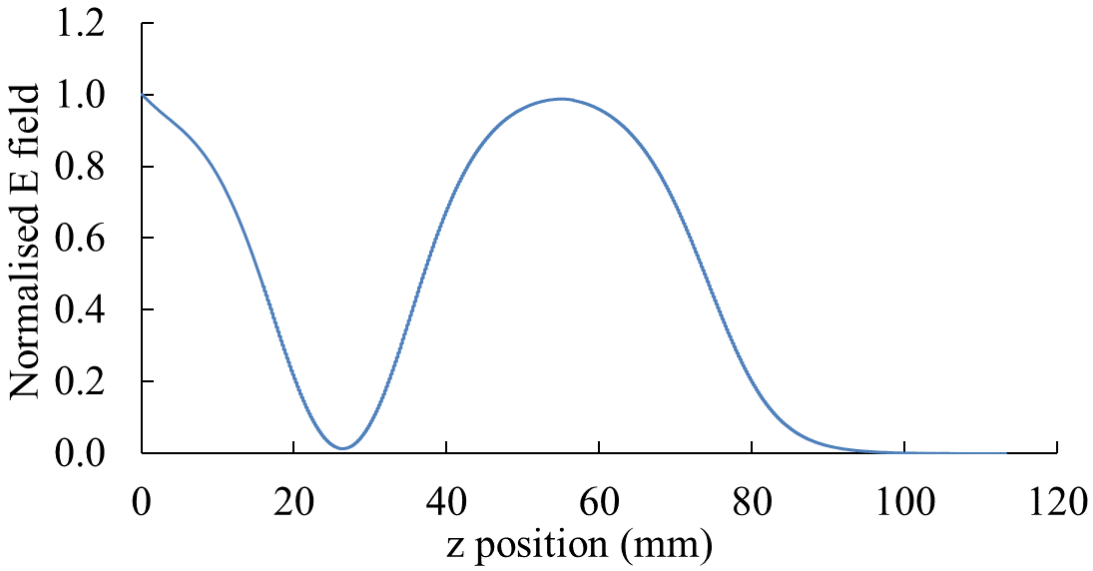

Figure 3.4: Normalised electric field along the axis of the cavity

Power coupling

The power coupling figures of merit β_c, Q_{Ext} and the cavity quality factor Q_0, related via $\beta_c = Q_0/Q_{Ext}$, were determined. As described in Section 2.2.7 the aim for β_c is 1 as there is no beam-loading. β_c was determined from the minimum and maximum values of the magnitude of the reflection coefficient, Γ_{min} and Γ_{max}

$$\beta_c = \frac{\Gamma_{max} - \Gamma_{min}}{\Gamma_{max} + \Gamma_{min}} \tag{3.13}$$

Q_L was determined from the transmission signal to the probe which is defined, analogously to the reflection signal, as S31+S32 . The output port is the probe port, an antenna was used to weakly couple to the cavity field and measure the bandwidth, B,

$$Q_L = \frac{f_0}{B}. \tag{3.14}$$

Q_0 can then be calculated from Q_L and β_c

$$Q_0 = (1 + \beta_c)Q_L. \tag{3.15}$$

3.1.3 Results

Frequency

The cavity was clamped and the frequency measured then unclamped. This was repeated three times. The frequencies measured differed by a maximum of 91 kHz. The average measured frequency of the structure with the full trimming length (200 µm on the first cell and 422 µm on the second cell) was 2996.53 MHz. This can be compared to the value predicted for a perfect cavity with such trimming lengths: 2996.21 MHz, a difference of 320 kHz, and the value predicted using the CMM measurements of the cell radii: 2996.63 MHz, a difference of 100 kHz. This 100 kHz is likely due to other non-conformities of the cavity geometry to the ideal. The flowchart in Figure 3.5 was used to perform the trimming steps. Three trim steps were carried out. The nominal

length for each trim and the actual trim measured on the CMM are given in Table 3.1. Each was within the 250 kHz frequency limit of the value predicted using the ideal trimming amount. The length of each cell was measured with the CMM and the adjusted predicted frequency calculated. The results are presented in Figure 3.6. All frequency results are scaled for temperature, air pressure and humidity to expected operating conditions for easy comparison using the program CONVERTF[45], except for the final measurement which was performed with 50°C water in the cooling pipes but was corrected for air pressure and humidity.

Table 3.1: Amount to trim nominal values and actual amount trimmed measured measured values for both cells over the three trimming steps.

Trim number	Trim cell 1 nominal (μm)	Trim cell 1 measured (μm)	Trim cell 2 nominal (μm)	Trim cell 2 measured (μm)
1	59	53	155	154
2	58	42	128	142
3	76	58	87	97

The final frequency was 2998.4 MHz. The operating frequency will be 2998.5 MHz; the cathode hole for the bead-pull causes a 10 kHz error so the frequency aim was 2998.49 MHz. The cavity is $-90\pm$ 100 kHz off frequency; the worst case of which can be corrected by a < 4°C water temperature change.

Field flatness

The field flatness repeatability with re-clamping was found to be 1%. The measured field flatness of the structure with the full trimming length (200 μm on the first cell and 422 μm on the second cell) was 98.9 %. This is exceptionally good for a cavity that has not been tuned. This meant that practically all that was needed was to keep the field flatness this high whilst tuning the frequency. Unfortunately the accuracy of the length trimming was such that there was some degradation of field flatness, although this was corrected by the end of the tuning process. After 2 steps a thinner gasket was used to optimize the cavity coupling β_c. This affected the field flatness by approximately 1%. For the final tuning step the aim was to have the cavity field flat with the thinner gasket as this is closer to what will be used in operation. The results of the field flatness tuning are presented in Figure 3.7. The final field flatness is 99.9 ± 1% using the thin gasket.

Coupling

The coupling of the cavity was the least repeatable of the measured values. It varied by over 10% with re-clamping. The accuracy of this measurement was 0.1. Coupling increased slightly as the cavity was trimmed to the correct length. This can be seen in Figure 3.8. It was adjusted using the copper gasket in the outer conductor of the coaxial line, as described in Section 2.2.7 and shown in Figure 2.32. The original gasket thickness was 6 mm. A thinner gasket was tested after the second trim to increase coupling, this was 4.41 mm. The target coupling was 0.87 as it is expected to increase when the cavity is brazed. The gasket may require further thinning but due to the uncertainty in the measurements and therefore the predicted increase in coupling, it was decided to wait until the cavity was brazed. It should be noted that the conflat flange knife-edges were not fully depressed into the gasket and as such the effective gasket length will be slightly thinner.

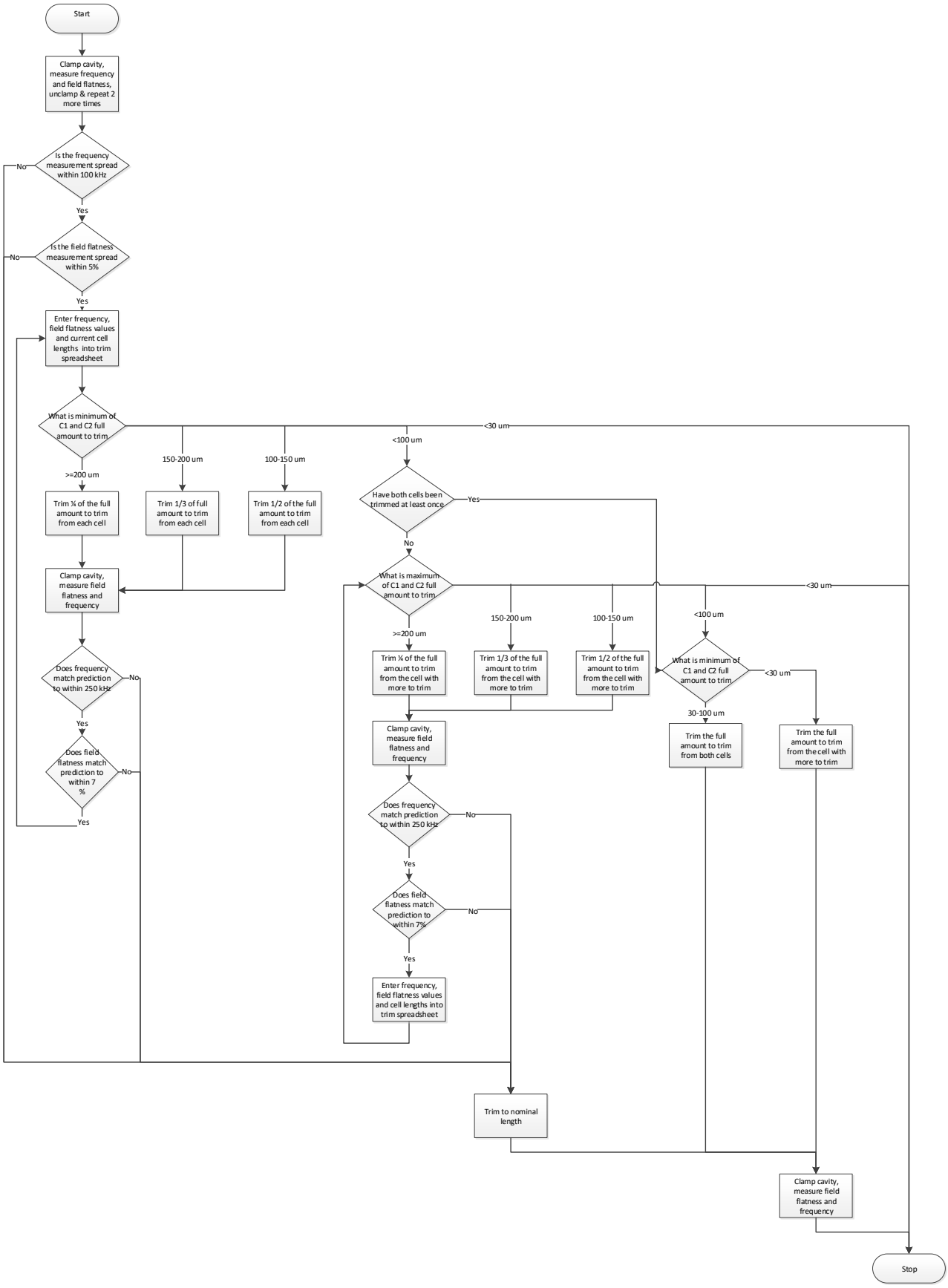

Figure 3.5: Logic flowchart for tuning procedure.

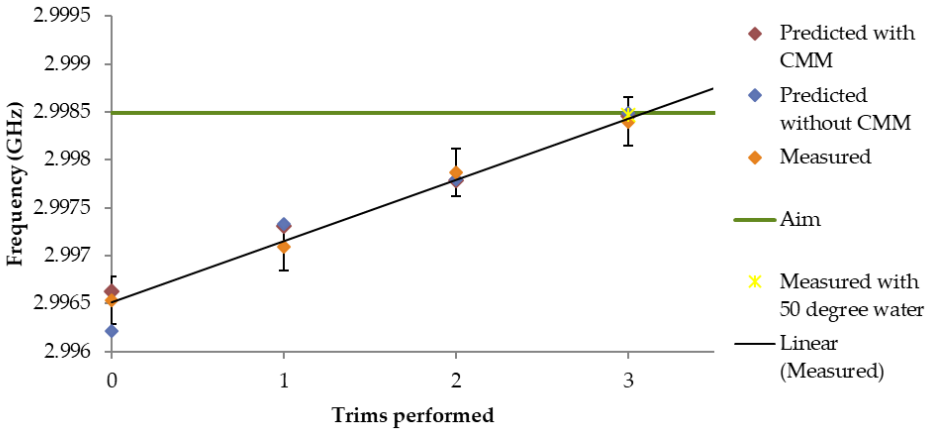

Figure 3.6: Measured frequency value with performed trims. The bars show the acceptable frequency range.

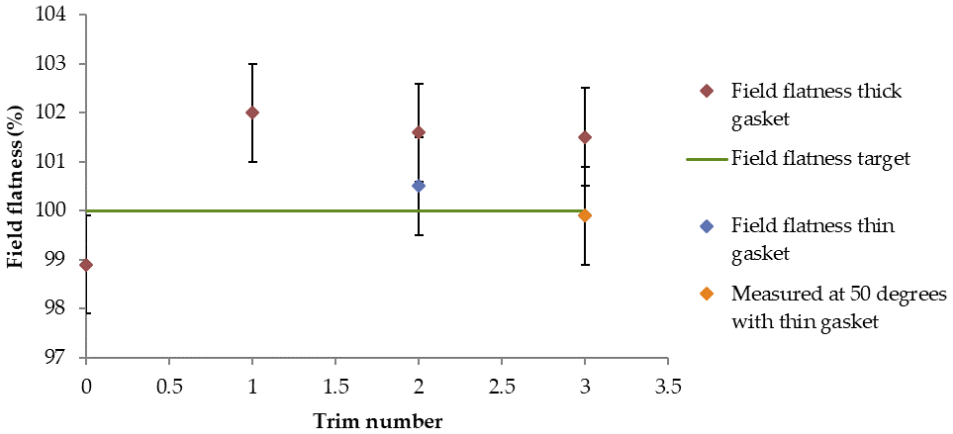

Figure 3.7: Measured field flatness with performed trims. The bars show the error on the measurement.

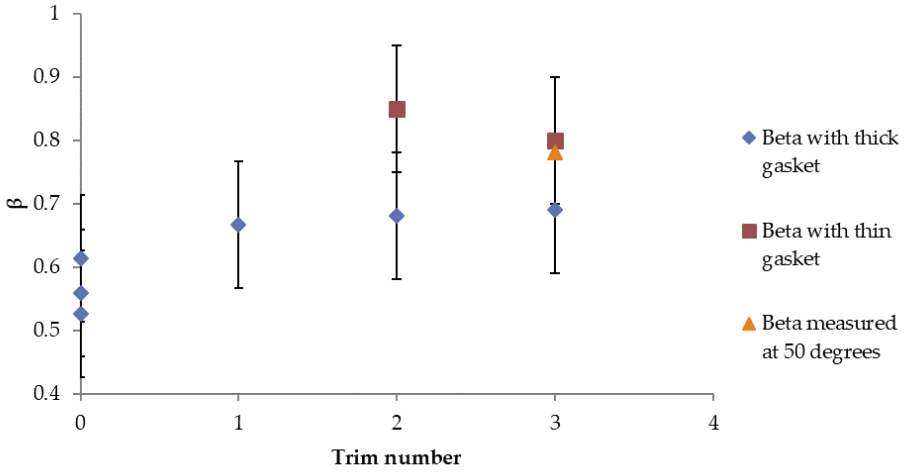

Figure 3.8: Measured β_c with performed trims. The bars show error on the measurement.

The Q_L was measured to be 7623±500 for all trim values. This uncertainty is due to the difficulty of measuring the transmission with an antenna. As the Q_0 is calculated from Q_L and the error propagates. The average Q_0 is 12923.25±2000, any trend will not be meaningful with such a large error. The Q_0 is predicted to increase when the cavity as brazed and the error in measurement should decrease when the antenna probe is in place.

3.1.4 Pre-braze Tuning Summary

The pre-braze tuning of the photoinjector was successful, with a final field flatness of 99.9% and a final frequency of 2998.4 MHz, measured to a tolerable accuracy. A less than 2°C change in the water temperature should be sufficient to tune the cavity. The coupling and quality factor values proved harder to measure on the clamped cavity, although the values measured were encouraging. Tuning of coupling will be performed after the cavity is brazed when the final Q_0 of the structure is known.

3.2 Low power measurement after brazing

3.2.1 Introduction

The cavity was brazed at Research Instruments GmBh [45] and the optimum coupling gasket length after brazing was found by Research Instruments to be 3 mm, tightened to give a 1.1 mm gap between the cavity body and the coupler body [48]. The brazed structure was then shipped to Daresbury Laboratory for low power RF measurements in the RF laboratory.

3.2.2 Preliminary measurements with copper cathode

The resonant frequency of the operating mode, the resonant frequency of the other mode in the passband, and the coupling characteristics of the cavity as delivered were measured using the same methods detailed in Section 3.1.2. The cavity at this point employed the copper bead-pull cathode with a hole, and the water channels were connected to a chiller with 50 °C water. The measured frequency of the operating mode was 2997.71 MHz under nitrogen, which scales to 2998.49 MHz at vacuum pressure. This can be seen in Figure 3.9.

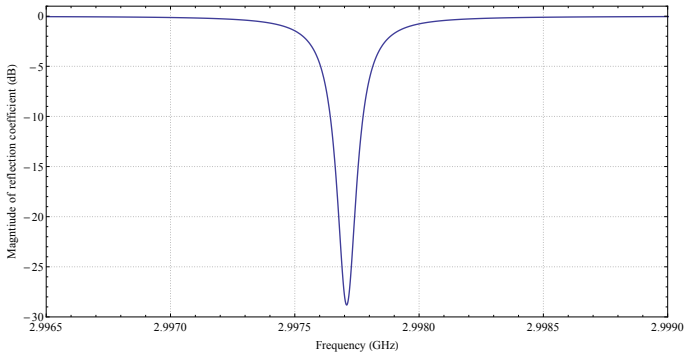

Figure 3.9: Measured reflection coefficient at $\frac{1}{3}$ psi positive nitrogen pressure at 50°.

The frequency of the other passband mode was 2977.72 MHz under nitrogen. A gap of 20 MHz between the operating mode and the next mode in the passband is sufficient to ensure negligible power loss and beating [26].

The coupling factor β_c measured 0.97 ± 0.05. Q_L measured from the transmission was 6400 ± 100. The Q_0 is calculated to be 12508 ± 400.

3.2.3 Measurement of on axis fields

The field on axis was measured using the perturbation measurement technique and image charge compensation described in Section 3.1.2. The result is shown in Figure 3.10. The field flatness of the structure was 98 ± 1 %.

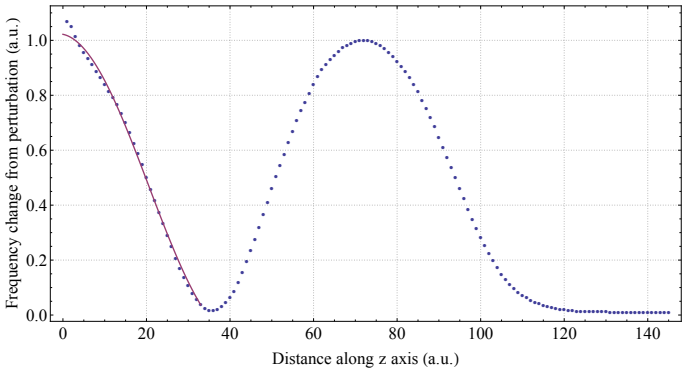

Figure 3.10: Measured reflection coefficient at $\frac{1}{3}$ psi positive nitrogen pressure at 50°.

3.2.4 Comparison of measurement results

Table 3.2 shows a comparison of the RF measurement results from simulation, pre-braze measurements and post-braze measurements.

Table 3.2: RF parameters from Frequency Domain CST simulation, pre-braze measurements with 4.41 mm gasket, and post-braze measurements with 3 mm gasket.

	Simulation	Pre-braze measurement	Post-braze measurement
Frequency (MHz)	2998.5	2998.4 ± 0.1	2998.49 ± 0.001
Field-flatness (%)	97.0	99.9 ± 1	98.0 ± 1
β_c	1	0.8 ± 1	0.97 ± 0.05
Q_0	14280	12923 ± 2000	12508 ± 400

It can be seen that the frequency and field flatness change from the clamped pre-braze measurements was very small, within the 0.1 MHz measurement error on the frequency and twice the 1% measurement error of the field Flatness. The Q_0 is much lower than the simulated Q_0 from the simulation result for both the pre- and post-braze measurements. This is not unusual as the simulation uses ideal pure copper with perfectly smooth surfaces. It should also be noted that in later measurements described in Section 3.2.6 with different cathodes and a gold-coated cathode spring, higher Q_0s were measured so it is possible the bead-pull cathode used for both pre- and post- braze measurements allowed some RF leakage from the cathode region. Q_0 was expected to rise after brazing due to the unimpeded current flow in the brazed structure in comparison to imperfect RF connection of the clamped faces, but this was not seen. One explanation for this may be that the surface flatness and roughness of the clamped faces was good enough to achieve a very good RF connection. The β_c cannot be directly compared, as different gaskets were used for

the two measurements, however it can be noted that as the Q_0 was expected to rise so was the β_c so a shorter gasket than expected was required to achieve a match.

3.2.5 Measuring the phase balance of the coupler

As discussed in Section 3.1.2 the reflection coefficient Γ for a three-port system can be calculated from $S11 + S21$ and equivalently from $S22 + S12$ where ports 1 and 2 are the symmetrical phase-matched input ports [47]. Figure 3.11 shows how $S11 + S21$ and $S22 + S12$ vary as the input phase to port 1 is varied in simulation. This is equivalent to adjusting the path length of the coupler half the distance via the phase tuner. The minimum of $S11 + S21$ is seen to become higher with more detuning, as the match worsens, the TE_{11} modes no longer fully cancel and a dipole component occurs in the cavity as described in Section 2.2.6.

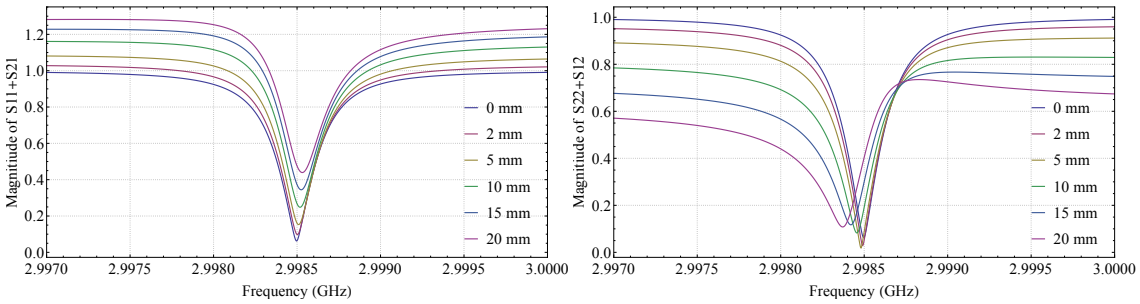

(a) S11 + S21 (b) S22 + S12

Figure 3.11: Simulation of reflections from the cavity to each port as port 1 input phase is varied.

The tuning range of the coupler is ±0.5 mm on each flexure tuner. The H-coupler is illustrated in Figure 3.12. The match was initially very good. The flexure tuners were tested and had the predicted effect. Tuning will be performed after installation on the beamline after the addition of the pumping ports to the H-coupler.

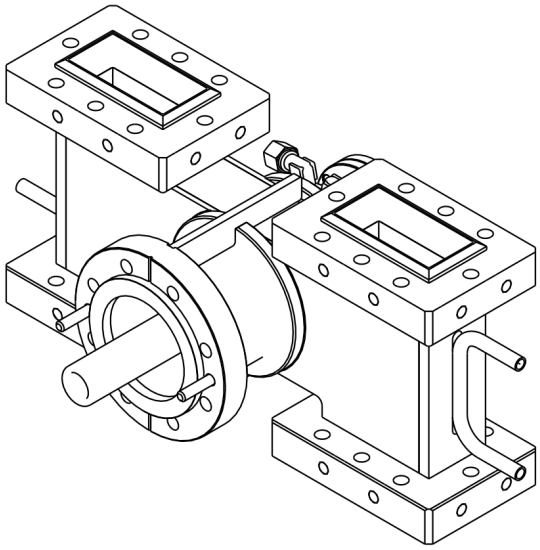

Figure 3.12: Mechanical drawing of the photoinjector H-coupler. Input ports 1 and 2 are shown at the top. The flexure tuners are on the underside.

3.2.6 Cathode measurement

RF measurement

Repeatability tests were performed with all cathodes. This was to quantify the repeatability of the RF cavity properties when removing and replacing the same cathode, as during operation the cathodes will be replaced under vacuum using the load-lock system. Whilst the cavity parameters can be estimated from the high power RF signals during operation, there will be little recourse for troubleshooting if it is found that cathode replacement does measurably alter the RF cavity properties, without venting and dismantling the system.

The cathodes were held in place by a steel plate bolted to the back of the cavity with eight molybdenum coated bolts incrementally tightened to 2 Nm in sequence. The cathodes tested were the copper bead-pull cathode and 6 molybdenum cathodes. The tests were performed with a plain copper RF spring and with a gold coated spring with rhodium interstitial. For the copper spring repeatability was poor. Standard deviation of the measured cavity frequency and β_c for each cathode was calculated. For frequency measurement the mean standard deviation across all the cathodes was 21.82 kHz and for β_c was 0.041. With the gold-coated spring repeatability improved. The mean standard deviation in the measured frequency was 3.02 kHz and for β_c was 0.011.

The RF properties of the cavity were different with each cathode. The standard deviation on the average frequency for each cathode is 18.5 kHz for the copper spring. For the same spring the standard deviation of the average β_c for each cathode is 0.070. The average β_c for the copper cathode is higher than the molybdenum cathodes. The standard deviation of the molybdenum cathode β_cs only is 0.029. For the gold-coated spring the standard deviation of the frequencies decreases to 6.9 kHz and β_cs decreases to 0.021, for the molybdenum cathodes the standard deviation is 0.007.

Table 3.3 shows the average RF parameters measured with each cathode with the plain copper spring, and the standard deviation of those measurements. Table 3.4 shows the same data with the gold coated spring. The molybdenum cathodes are named M1-6 and the copper cathode C1.

Table 3.3: RF parameters and their standard deviations measured with each cathode and a plain copper spring

Cathode	$f(GHz)$	$\sigma f(Hz)$	β_c	$\sigma\beta_c$	Q_L	σQ_L	Q_0	σQ_0	Q_{ext}	σQ_{ext}
M1	2.998442	5053	0.917	0.017	5875	66.7	11265	218.2	12281	70.8
M2	2.998462	46900	0.885	0.045	5791	142.0	10924	512.4	12326	199.3
M3	2.998448	19410	0.825	0.070	5503	282.0	10064	892.2	12146	172.2
M4	2.998424	24387	0.865	0.037	5767	165.6	10766	510.4	12423	153.8
M5	2.998444	13312	0.881	0.054	5846	266.8	11011	811.8	12460	174.8
M6	2.998433	12376	0.898	0.054	5908	256.4	11227	800.9	12469	182.4
C1	2.998400	31317	1.065	0.011	6422	222.0	13265	485.3	12448	415.2

Table 3.4: RF parameters and their standard deviations measured with each cathode and a gold coated spring

Cathode	$f(GHz)$	$\sigma f(Hz)$	β_c	$\sigma\beta_c$	Q_L	σQ_L	Q_0	σQ_0	Q_{ext}	σQ_{ext}
M1	2.998410	2943	1.072	0.003	6484	5.7	13437	11.1	12530	23.3
M2	2.998416	5760	1.053	0.026	6491	131.1	13332	430.7	12654	187.1
M3	2.998428	707	1.067	0.015	6484	129.4	13401	351.4	12562	120.5
M4	2.998412	4189	1.070	0.015	6489	24.4	13431	145.0	12556	52.3
M5	2.998418	3681	1.076	0.001	6456	28.7	13401	59.5	12459	55.7
M6	2.998411	3858	1.062	0.012	6369	56.4	13136	177	12366	79.3
C1	2.998430	0	1.125	0.006	6697	4.2	14230	297	12650	38.4

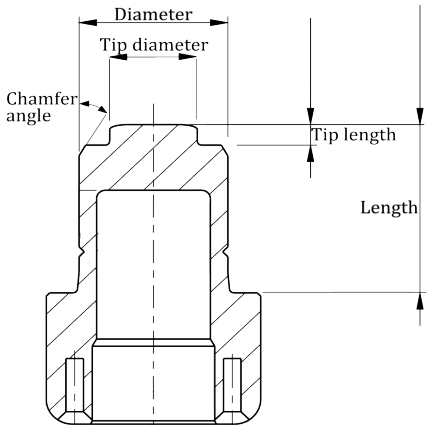

Figure 3.13: Dimensions of cathode.

Table 3.5: Dimensional measurements of cathodes. Out of tolerance dimensions are shown in red.

Dimension	Length	Tip length	Chamfer angle	Diameter	Tip diameter
Unit	mm	mm	°	mm	mm
Nominal	20.5	2.5	30	17	10
+Tol	0.01	0.05	0.25	0	0.05
-Tol	-0.01	0	-0.25	-0.05	-0.05
M1	20.518	2.542	-	16.958	9.985
M2	20.524	2.540	29.186	16.972	10.018
M3	20.500	2.521	29.364	16.953	10.012
M4	20.512	2.553	29.359	16.979	10.037
M5	20.523	2.546	29.064	16.963	10.037
M6	20.535	2.549	30.517	16.953	10.026
C1	20.489	2.493	29.103	16.981	-

There is not a single cathode with no dimension out of tolerance. The chamfer angle results are not too concerning, but all but one of the lengths being out of tolerance could cause variation in the cavity frequency. The simulated sensitivity of cavity frequency to cathode penetration is 1.4 MHz/mm.

Correlations between the cathode dimension changes and RF measurements were calculated but the low number of data points and large spread meant there were no strong correlations.

With the plain copper spring β_c is much higher for the copper cathode than the molybdenum cathodes, implying there is poor RF contact between the molybdenum cathodes and the spring. This was confirmed by measuring the field leakage behind the cathode with an antenna. The transmission to the antenna was around -70 dBm for the molybdenum cathodes with the plain copper spring. There was no measurable field leakage with the copper cathode.

With the gold coated spring there was no measurable leakage for all cathodes. The gold coated spring increases the RF contact and prevents leakage.

Summary

The most important result from the cathode measurement is that the gold coated spring increases the RF contact with the cathodes and the repeatability of the RF parameters on replacement, especially for the harder molybdenum cathodes, and should be used in operation. Additionally the data can be used to choose the cathodes for operation. Cathode M3 was chosen for first operation as it has the least out of tolerance dimensions, achieved the closest frequency to the specified frequency, and the most repeatable frequency result.

3.2.7 Measurement of dipole component

The flexure tuners were fully detuned to give a phase offset of 2 mm, and the field on axis was measured with a bead-pull technique to determine if the dipole component discussed in Section 2.2.6 can be measured. Γ calculated via $S11 + S21$ and $S22 + S12$ are shown in Figure 3.14.

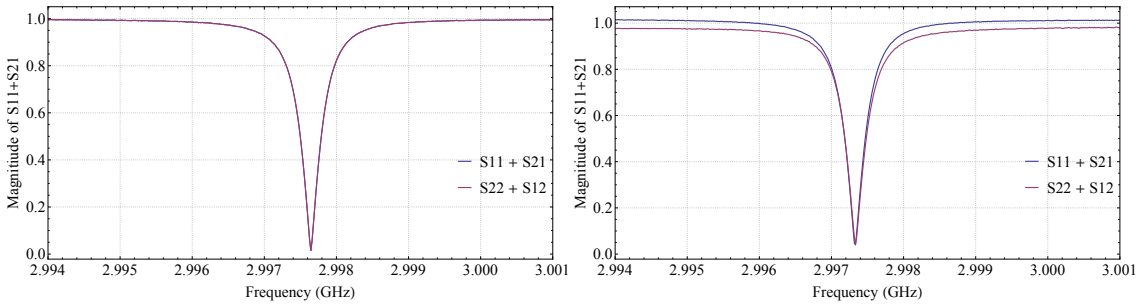

(a) Tuned (b) Detuned

Figure 3.14: Reflections for tuned flexure tuners and fully detuned flexure tuners

Four different beads were used. A metal disk and a plastic disk, each 5.7 mm diameter and 0.5 mm thick. A metal and a plastic spherical bead, each 2 mm in diameter. Metal will perturb both E and H field, whilst dielectric only perturbs E field. The spherical beads will perturb all field directions equally. The disks, which are threaded with the face in the axial direction will perturb the field in the x and y directions more than that in the z.

The on axis field is always dominated by the E field in the z direction. Every measurement of the perturbation is dominated by this. The dipole field has both an E and an H component, but both are small (less than 1%) with respect to the E field in the Z direction. No significant difference is seen in any of the bead-pull measurements after detuning the flexure tuners.

In the future a phase offset could be added to the incoming field in each port of the H-coupler in order to create a dipole component that is measurable.

3.2.8 Final laboratory measurements

A new gold coated spring was installed in the cavity ready for operation. The final off-line measurements of the cavity were performed with cathode M1. The frequency scaled to 50 °C and vacuum conditions was 2.99856 GHz ± 17 kHz. An operating temperature of 47.2 °C is required for operation at 2.9985 GHz. The coupling β_c is 1.071 ± 0.008. The Q values were as follows: Q_L was 6356 ± 1; Q_0 was 13167 ± 52; Q_{ext} was 12288 ± 43. The mode separation is 20.3 MHz. The measured reflection Γ from the cavity shown in Figure 3.15.

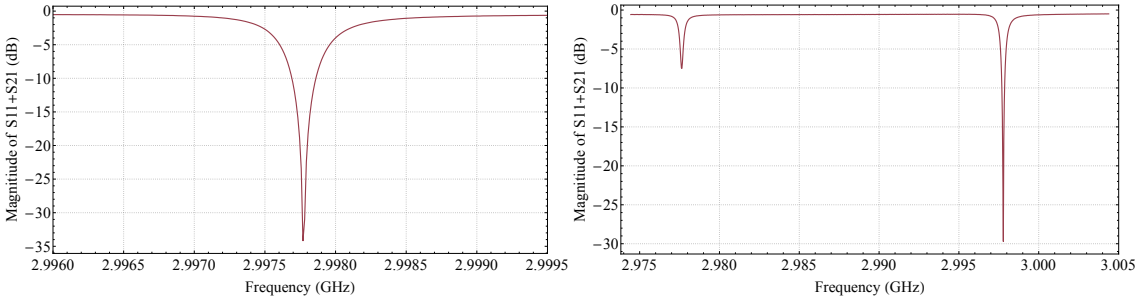

(a) Operating Mode

(b) Full passband

Figure 3.15: Reflection coefficient measured in final off-line measurement

3.2.9 Measurements after installation on the VELA beam-line

The cavity was installed on the VELA beam-line for initial conditioning and high-power characterisation. The VELA beam line photoinjector position shares an RF source with the CLARA beam-line, and has diagnostics that will be useful for characterisation such as a transverse deflecting cavity that enables longitudinal beam profile measurements.

First measurement after installation

The cavity was measured with cathode M3 held in place with the same steel plate. The cavity was at air and was heated to 50 °C with water from the chiller. The operating frequency was measured as 2998.53 ± 0.1 MHz The large error is due to the unknown humidity in the cavity. The β_c measured 1.07 ± 0.03.

Load Lock Cathode System

The cavity was measured with the cathode held in place by the load lock system. Repeatability tests were performed for removing and replacing the cathode and whilst the frequency was very repeatable (down to 10s of kHz) there was some variation in the measured β_c. The load lock system uses a magnet to move a transfer arm holding the cathode to load the cathode into the cavity. This magnet can be used to exert force on the back of the cathode and hold it in place or it can be left free. The standard deviation on the measurement of β_c was 0.026 without any force and 0.0048 with force applied. The stop on the arm has been placed in the optimal position and the magnet should be held in place against the stop. A sprung mechanism is being designed for this purpose, and will include interlocked switches to confirm the arm is in place.

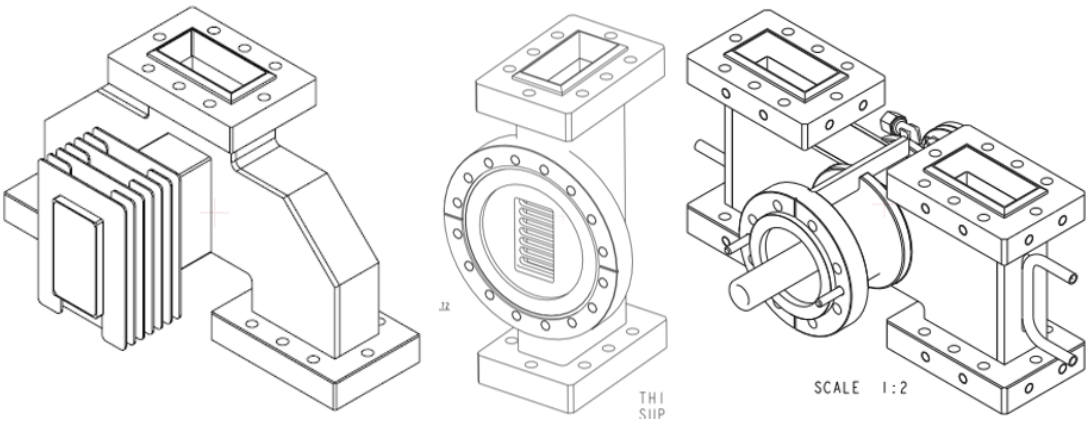

Figure 3.16: Magic tee, pumping waveguide section and H-coupler with coaxial doorknob.

H coupler tuning

The photoinjector cavity power coupling system design consists of a magic tee, a four-port, 180 degree hybrid power divider, which divides the power into two identical waveguide sections with pumping ports, each feeding one arm of the H-coupler which couples the power into the gun through the coaxial line. The components are shown in Figure 3.16.

The two waveguide sections with pumping ports were installed and the H coupler tuned with the S-parameters measured from the top of the waveguide sections. However it was subsequently discovered that the waveguide sections were not symmetrical and as such the magic tee did not fit. The decision was made to install the magic tee directly on to the H-coupler and then a single pumping section above that. The H-coupler was re-tuned using the flexure tuners on the base, with the S-parameters measured from the input ports of the H-coupler. The phase difference between the two output ports of the magic tee was measured, before installation, to be $0.89° \pm 0.08$. As concluded in Section 2.2.6 this is low enough to have a negligible effect on the beam. As such no correction was applied to the flexure tuners. The tuning result is shown in Figure 3.17, measured from the input ports of the H-coupler.

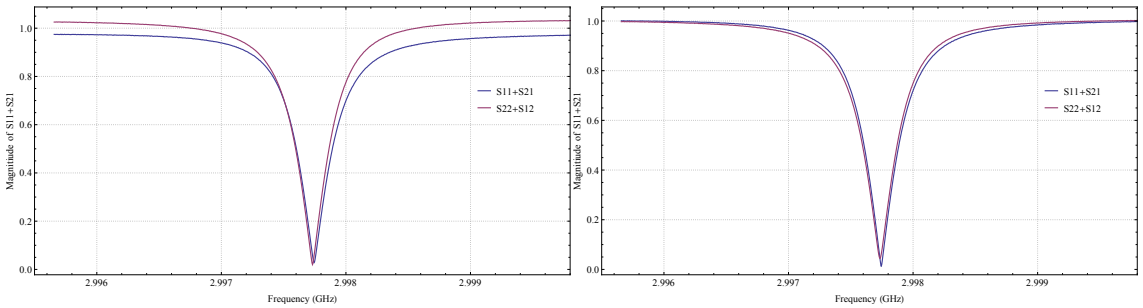

(a) Reflection measurements before re-tuning.

(b) Reflection measurements after retuning.

Figure 3.17: Retuning of the H-coupler.

Final installation and bake

The Magic Tee was installed, and then the pumping port and the vacuum window. The cavity was measured at each stage and all RF characteristics were as expected. The cavity was baked

at 150°C for 72 hours. After the bake the frequency at vacuum at 48.8°C was 2998.554 MHz, suggesting a required running temperature of 49.8 °C. The β_c was 1.077 and the mode separation was 20.07 MHz. The coupling to the probe was -69.14±0.1 dB. The S-parameters are shown in Figure 3.18.

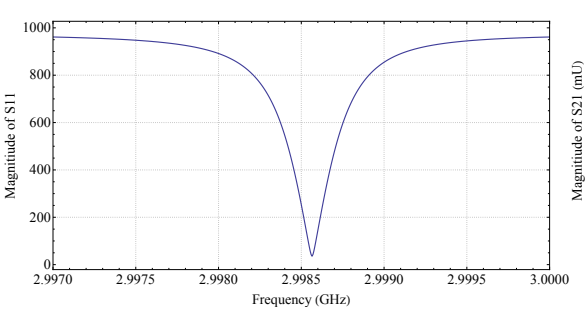

(a) S11 after bake from above the window.

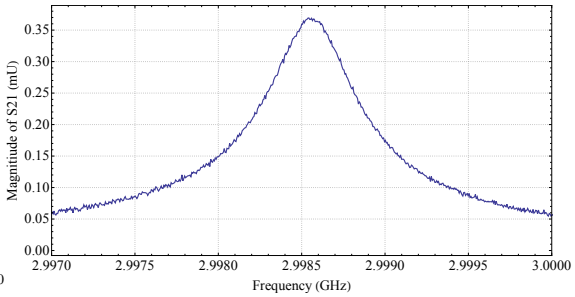

(b) S21 after bake from above the window to the probe.

Figure 3.18: S parameters after bake.

Chapter 4

High power conditioning program development for 400 Hz Photoinjector

4.1 Introduction

4.1.1 High power RF phenomena and conditioning

Once an RF structure is fabricated and low power measurements have confirmed it conforms to the design, it must be conditioned with high power RF to prepare the internal surfaces to sustain the high fields required. The limit on the surface fields is caused almost entirely by one phenomenon: RF breakdown, and high power conditioning involves slowly increasing the surface fields in the structure that can be sustained without, or more realistically with minimal, RF breakdowns.

There are however two other high field phenomena that are of interest, these are field emission and multipactor.

Field emission

In the presence of large surface electric fields, electrons from the surface of a material can be liberated from the surface into a vacuum, this is field emission. Also known as Fowler-Nordheim emission, this is a quantum mechanical process whereby the potential barrier holding the electrons in the conductive layer is weakened by the surface electric fields, increasing the probability of these electrons tunneling through to the vacuum [49]. An important parameter is the field enhancement parameter β_e, which relates the local electric field to the macro-scale electric field. The field emission current density J depends exponentially on β_e. It can be approximated for copper as [50]

$$J = 0.342\beta_e^2 E^2 e^{4.91} e^{-(28.37/(\beta_e E))}. \tag{4.1}$$

The β_e factor is empirical, but is related to the geometry of surface features and the surface roughness, and is typically in the range 30-100.

Field emission is not damaging by itself, however it can be a precursor to multipactor and RF breakdown. Additionally field emission can be a problem during beam operation as it can

be accelerated with the core bunch and spoil the quality of the bunch, or damage accelerator components such as undulator magnets in FELs [51].

Multipactor

Multipactor is a resonant phenomenon by which a large number of electrons can build up, absorbing the RF power [52]. Electrons from field emission can cause secondary electron emission when they impact the surface of the RF structure. If these secondary electrons are directed to the surface of the structure by the RF fields with sufficient energy, further secondary electrons are created. If this process continues in resonance with the RF fields, and the secondary electron yield (the average number of secondary electrons created by one primary electron impact) is greater than 1, an avalanche effect can occur.

Multipactor can absorb the RF power supplied to a structure, making it impossible for the RF fields to be increased by increasing the incident power. Some multipactor can be processed through, this is thought to be due to the multipacting impacts cleaning the surface and reducing the secondary emission yield below 1. Some multipactor however, cannot be processed through. Careful RF design can be used to try to avoid the possibility of strongly resonant electron trajectories. If multipactor that cannot be processed through is encountered during RF conditioning, one strategy that can be employed is to switch off the RF to stop the multipactor, and then switch on again at a step-change higher power, skipping the field range where multipactor occurs. This increases the likelihood of RF breakdown.

RF breakdown and conditioning

RF breakdown is a type of vacuum plasma arc. It has been studied for several decades, and although it is not fully understood, there are three steps thought to be important to the process, which repeat, allowing the breakdown to grow.

1. Field emission occurs. Electrons are liberated from the structure surface.
2. Neutral atoms evaporate. Neutral atoms evaporate from the surface due to the strong electric field, electron transport and high temperatures [53], and are ionised by field emitted electrons.
3. Bombardment. The ions are accelerated into the surface, causing a sputtering effect which releases atoms from the surface. This is one of the main sources of the gas that is required to sustain the plasma of the arc.

Eventually, the breakdown will grow to such an extent (usually on the order of ns) that the conductive plasma in the structure will affect the resonant frequency. In standing wave structures such as photoinjectors, the inductive match of the coupler will be lost, and any incoming RF will simply reflect from the coupler. The arc itself can damage RF components.

While research is still ongoing on the physical mechanisms at play, it is currently thought there are two different conditioning regimes at distinct RF gradients. The first phenomenon takes place at lower gradients and is somewhat dependent on the quality of the internal RF surfaces of the structure. In this regime, contaminants are removed. The cleanliness of structure preparation has been found to affect the number of breakdowns during conditioning, but not the ultimate performance [54], which implies that this regime is not required for sufficiently clean surfaces. For insufficiently clean surfaces some breakdowns may be required to achieve a contaminant-free surface.

The second phenomenon occurs at high field gradients, and in contrast to the low gradient

regime, on reviewing statistical data from a number of conditioning processes, it was suggested by the authors of [55] that this process does not depend on the number of RF breakdowns, but rather is dependent on the number of RF pulses just below the conditioned field level. Empirically, it has been found that the strong dependence of the breakdown rate on the surface electric field can be described by the equation

$$E_s^{30}\tau_p^5 \propto \mathrm{BDR} \tag{4.2}$$

where τ_p is the RF pulse length, E_s is the surface electric field, and BDR is the breakdown rate in breakdowns per pulse [50]. In recent years a dominant theory has developed as to the process, known as the dislocation model, this theory posits that the onset of breakdown is associated with crystal defects within the metal surface, and it is the rate of formation of vacancies under the stress of the electric field that determines the breakdown rate. This result is written as

$$\mathrm{BDR} \propto e^{\epsilon_0 E^2 \Delta V / k_B T} \tag{4.3}$$

where ΔV is the relaxation volume of the defect, ϵ_0 is the vacuum dielectric constant, k_B is Boltzmann's constant and T is the temperature.

One possible mechanism linking vacancies to breakdowns is dislocation-induced slip along crystallographic planes, causing mass transport and leading to field emitting tip formation. Conditioning is therefore considered to be a process of material hardening as the dislocation density increases and new dislocations are prevented from nucleating. Due to this it has been suggested that making structures from hard copper, rather than the currently used annealed copper, could reduce the asperity creation and therefore the need for conditioning. In practice this is difficult as any brazing or bonding procedure used to join the machined structure pieces currently requires high temperatures, so clamped [56] or open (structures with a gap in a low field region) [57] are under study.

The process of conditioning must be closely controlled. Breakdown events can damage the structure surface [58]. Figure 4.1 shows an Scanning Electron Microscope (SEM) image of breakdown damage in a DC system. The energy in the arc can cause craters, and these craters then become breakdown sites themselves, causing a cycle that can severely damage an RF structure. Breakdowns should therefore be limited, and the aim during the conditioning process is to clean up and harden the structure surface by slowly increasing the power, with the minimum breakdown events possible. In practise this can be difficult to achieve, as it is not possible to know the ideal power increase rate in advance.

4.1.2 Gradient limits

An RF structure will always have an upper gradient limit that can be reached before conditioning cannot continue due to repeated breakdown events. For many years this was thought to be limited by the surface electric field only, and RF structure design focused on structure geometries that minimise this. The Kilpatrick criterion is an empirical relation based on breakdown measurements in the 1950s [59] that related maximum electric field to the structure frequency, the Boyd formalism of which is:

$$f = 1.64\mathrm{MHz}\left(\frac{E}{E_0}\right)^2 e^{-8.5E_0/E} \tag{4.4}$$

where E is the surface electric field, f is the structure frequency and E_0 is 1 MV/m.

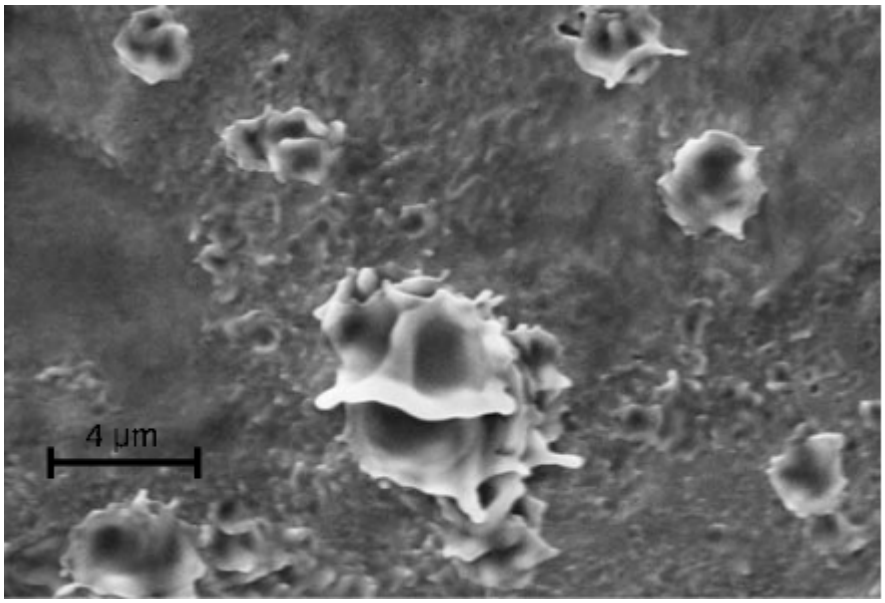

Figure 4.1: SEM image of breakdown damage craters from a DC system. Reproduced from [58]

For many years RF structure design used this as the electric field limit. As manufacturing processes improved, particularly with regard to surface finish and cleanliness, this criterion was found to be conservative, and structures were designed with electric fields that exceeded this limit, often many times over.

More recently, it has been found that the maximum surface electric fields achieved in modern structures vary more than would be expected were this the only factor involved in the onset of RF breakdown. This prompted the idea that it is the power flow which limits the achievable gradient. The power flow model [60] proposed a scaling law, which was found to fit the data better than surface electric field alone:

$$P\tau_p^{1/3} \propto C \tag{4.5}$$

where P is the total power flow and τ_p is the pulse length, and C is the minimum iris circumference of the structure. This model however cannot explain the concept for RF breakdown in standing wave structures as there is no net power flow in these structures.

Grudiev et al.[50] postulated that power flowing through field emitters and causing local pulsed heating is the cause of RF breakdown. The field-emitted current caused by electric field E flows through a field emitter (modeled here as a cylinder with a domed tip, with radius 20 nm) and, by resistive heating, the temperature of the tip increases. The field emission current induces a local magnetic field

$$H_{FN} = \frac{I_{FN}}{2\pi d} \tag{4.6}$$

where I_{FN} is the field emission current and d is the distance from the tip. In this way a power flow is created which transfers energy from the vicinity of the tip along the tip and into the outer volume. This power flow density can be described by the Poynting vector

$$S_{FN} = E \times H_{FN}. \tag{4.7}$$

There is one source of power at the surface of the RF structure, the RF source, with associated

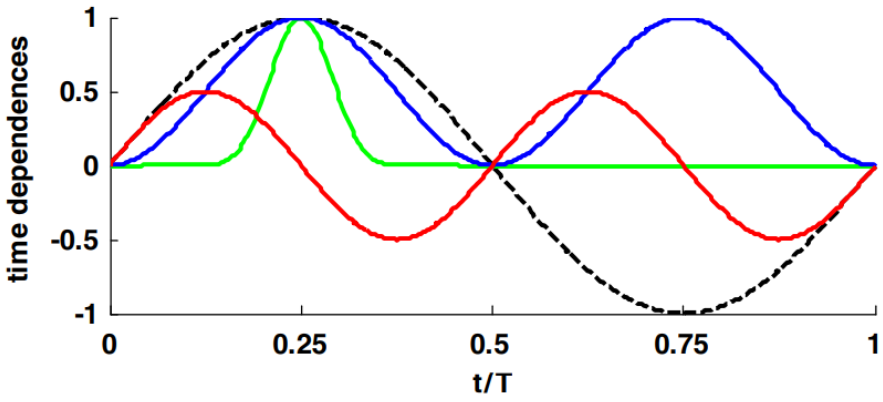

Figure 4.2: Time dependences of electric field (dashed black line), active power flow (blue), reactive power flow (red), and field emission power flow (green) are shown. Figure reproduced from [50]

Poynting vector

$$S_{rf} = E \times H_{rf} \tag{4.8}$$

which must provide the power for the field emission and subsequent heating.

The power transferred to the field emission power flow P_{FN} can be up to the value of the RF power flow P_{rf}. The resistive losses P_{loss} are significantly lower than the field-emitted power loss due to the low resistivity of copper, so a significant amount of power is required to cause heating.

$$P_{loss} \ll P_{FN} \leq P_{rf} \tag{4.9}$$

When considering the correlation in time the RF power can be split into two parts. The first is the active flow of power along the structure, the second is the reactive power flow which describes the oscillation between electric and magnetic stored energy on each RF cycle. The active power flow only exists where there is a travelling wave. The field emitted power is found to be highly non-linear and in phase with the active RF power. The time dependencies of each power can be seen in Figure 4.2.

It can be seen from Figure 4.2 that the field emission power flow is in phase with the active power flow and π out of phase with the reactive power. The active power flow is therefore more efficient in providing power for field emission. This can be quantified using the active and reactive parts of P_{rf}

$$g_c = \frac{\int_0^T |P_{rf}^{\text{reactive}}| \cdot P_{FN} dt}{\int_0^T P_{rf}^{\text{active}} \cdot P_{FN} dt}. \tag{4.10}$$

In practice frequency domain simulation codes are used for RF structure design, so the above considerations were adapted to the complex Poynting vector $\vec{S}$ which is simple to calculate in any of these codes. Similarly to the above, $\vec{S}$ has a real part, which is the active power flow, and an imaginary part, which is the reactive power flow. The new local field quantity,

$$S_c = |\text{Re}\{\vec{S}\}| + g_c|\text{Im}\{\vec{S}\}| \approx |\text{Re}\{\vec{S}\}| + \frac{1}{6}|\text{Im}\{\vec{S}\}| \tag{4.11}$$

called the "modified Poynting vector" was proposed for finding the high gradient limit in an accelerating structure. This quantity is a better fit to the measured high gradient limits in the data.

There are some limitations to the modified Poynting vector as a predictor for breakdowns. It has been found that [61] the modified Poynting vector does not always correctly predict the location of breakdowns, additionally it cannot explain or predict DC breakdown in steady state, where there is no power flow.

Paszkiewicz [61] posits that the electric and magnetic fields are not interchangeable as they are considered in Equation 4.11, and that consideration should be given to the transient effect of the nascent breakdown on the local surface electric field. During the onset of breakdown, the induced electric field from field emission destructively interferes with the electric field from the RF source, leading to a decreased surface electric field. This is termed "breakdown loading" and the new surface field is given by

$$E_{surf} = E_{rf} - R_{bd}I \tag{4.12}$$

where E_{rf} is the electric field from the RF source, R_{bd} is the real part of the coupling impedance between the tip and the RF source, and I is the current flowing in the antenna. At the same time, the current emitted from the tip increases as a monotonic function of the surface electric field, which can be fitted to a power law equation

$$I = kE_{surf}^{n} \tag{4.13}$$

where I is the current emitted from the tip and n and k are fitting parameters.

The intersection of these two functions is an equilibrium point where the system will settle. It is the surface electric field at this point, termed E^* that can be used as a threshold value during structure design. This model seeks to determine if there is enough power available at the equilibrium point to sustain the evolution to a full breakdown. Comparisons to travelling wave structure breakdown locations and maximum gradients were encouraging.

This model, by taking the real part of the coupling impedance in Equation 4.12, does not take into account stored energy in the structure. It is therefore not applicable to standing-wave RF structures. Another option for the impedance quantity, using $\sqrt{\int_0^\infty R_{bd}^2(f)df}$ instead of R_{bd} was proposed to correct this. This impedance quantity includes the dependence on frequency, which, due to discharging of stored energy involving a finite bandwidth, might result in an equilibrium E^* that is sensitive to the stored energy. This proposed quantity has not been well validated.

In conclusion, it is clear that the power flow at a breakdown site is an important quantity to take into account to predict breakdown, but it also seems that there is a distinction to be made between unperturbed fields and fields during the breakdown process, which are loaded by the current flow. Work is ongoing to advance our understanding of breakdown phenomena.

4.1.3 Effect of external magnetic field on breakdown rate

Typically, RF photoinjectors use a solenoid to compensate for emittance increase due to space charge. The field strength of the solenoid can be up to 0.5 T . In the case of coaxially coupled photoinjectors, the main solenoid can be placed directly around the accelerating structure. This adds an additional magnetic field to the system, which has been anecdotally found to cause an increase in breakdown rate as well as more damaging breakdowns which take longer for the system to recover from [62]. This effect has been seen during previous manual photoinjector conditioning at Daresbury [63].

A similar effect has been seen in muon ionisation cooling channels [64, 65, 66]. These beam-

lines consist of a very tightly spaced lattice of RF accelerating structures and magnetic focusing solenoids, such that the magnetic fields overlap with the RF structures. The magnetic fields are often very strong, up to 4 T. In dedicated experiments with 805 MHz structures, it was found that in a pillbox cavity the maximum stable gradient was limited by an applied axial magnetic field, with higher magnetic fields leading to lower maximum gradients [64]. It should be noted that the gradients studied in these experiments were far lower (up to 40 MV/m) than the typically $\geq$100 MV/m gradients seen in photoinjectors and in the X-band structures in which much of the above breakdown studies were performed.

Two theories of this phenomenon have been proposed, of which the second has a better fit to experimental data. The first is the "twist" model [65]. This models a field emitting asperity as a cone, and is predicated on the idea that breakdown occurs when the local tensile stresses on an asperity become greater than the material tensile strength. The current I in a field emitting tip, when combined with an external magnetic field create a force $\vec{F} = \vec{I} \times \vec{B}$, which is a torque on the tip and increases the tensile stress, leading to breakdown at lower electric field strengths.

The second theory [66] proposes that the magnetic field focuses field emitted electrons onto small regions of the structure, causing localised heating and leading to mechanical fatigue and surface damage. The molten metal at these spots is then pulled from the surface by electrostatic forces, where it is exposed to field emission leading to vaporisation and ionisation, and consequently breakdown. Simple simulations of this process along with an approximate treatment of the surface temperature rise were found to offer a reasonably good fit to the maximum gradient vs applied magnetic field data.

Of the numerous suggested solutions to this problem in muon ionisation cooling channels [66] (including lowering the electric field, and using high pressure hydrogen filled structures), few are applicable to photoinjectors. Building high quality surface structures with low initial field enhancement parameters is one suggested solution, and the 400-Hz photoinjector has been fabricated with an average roughness of 100 nm, which should be sufficient for this purpose. This should limit breakdowns in the low gradient regime, however as mentioned in [66] a single breakdown that leaves splashes of copper or craters could lead to a repeating cycle of breakdowns. Additionally this does not account for asperities produced in the high gradient regime by dislocation effects, although if the structure is conditioned well before applying the magnetic field, these asperities could be minimised, or using a hard copper structure could minimise their creation. One method suggested for creating these high quality surfaces is atomic layer deposition [66], which is being studied for superconducting structures, however it has been found that the quality of the substrate directly affects the quality of the film surface [67], so the benefit is not clear. Another option is to design the structure in such a way that high surface electric field regions are parallel to the applied magnetic field, however adding this further optimisation constraint to the structure design would be highly likely to limit the performance.

An external magnetic field was found to have no effect on the breakdown rate in a high DC field [68], regardless of the magnetic field orientation. This finding is inconsistent with the "twist" model as this model would hold true for DC fields, however as the field emission density from the DC cathode that reaches the cathode is unknown, no conclusions can be drawn with respect to the model based on the focusing of field emitted electrons.

4.2 NO-ARC

4.2.1 Motivation

CLARA will have 8 or more RF structures, and each of these will require high power RF conditioning. Automating this process to run unmanned will save time, and the cost of operators. For high gradient structures such as the 400 Hz photoinjector, automation also lowers the risk of gradient limitation due to damage from breakdowns.

4.2.2 NO-ARC introduction

No Operator Automatic RF Conditioner (NO-ARC) is an in-house program designed to be used, unmanned, with the CLARA control system (EPICS [69]) and LLRF systems (Libera I-tech [70]) to condition RF structures. The program was of my design and I made all technical decisions related to its operation, however all code was written and structured by D. Scott, with contributions by A. Gilfellon.

The aim of NO-ARC is to increase the RF power fed to the RF structure, whilst keeping the breakdown rate below a user chosen value. On first consideration, it seems as though a higher allowed breakdown rate should result in conditioning finishing in fewer pulses, however breakdowns slow the conditioning slightly by decreasing the power, and breakdowns can lead to structural damage which gives rise to more breakdowns. Essentially above a certain breakdown rate the conditioning rate is limited by the structure rather than the algorithm. Additionally, and importantly, allowing too many breakdowns may damage the structure and permanently limit the achievable gradient and therefore the structure performance.

The operation of the program is largely based on the program developed for conditioning structures in the the CLIC XBOXs at CERN [71] however its architecture is different. The XBOX program uses LabView [72], whereas NO-ARC is coded in C++ and python. The fast C++ code includes controllers and readers for the RF and other machine systems, and pulse-to-pulse breakdown detection. The python modules include the main flow of the program, data logging and front-end.

The basic flow of the program is shown in the flowchart in Figure 4.3. All numerical values can be user configured. In short, for each RF pulse the program checks for a breakdown, and if a breakdown has occurred switches off the RF, before the next pulse, for a user configured period of time, and then switches the RF back on, as long as the vacuum pressure has returned below a given value. When switching the RF back on during breakdown recovery there is an optional logarithmic ramp of the RF power back up. If no breakdown is detected, the power is increased, by increasing the LLRF amplitude, after a given number of normal pulses, as long as the vacuum and breakdown rates are within their given limits. This is repeated until the maximum power is reached, and then the pulse length must be increased. This is currently done manually using a look-up table, but is planned to be added to the program in its next version.

The program has been designed to work with any RF structure that uses the CLARA control system and Libera I-tech low level RF (LLRF), this chapter however, will focus on conditioning of the 400 Hz photoinjector.

4.2.3 Modularity

NO-ARC has a modular design, which allows for easy refactoring and extension.

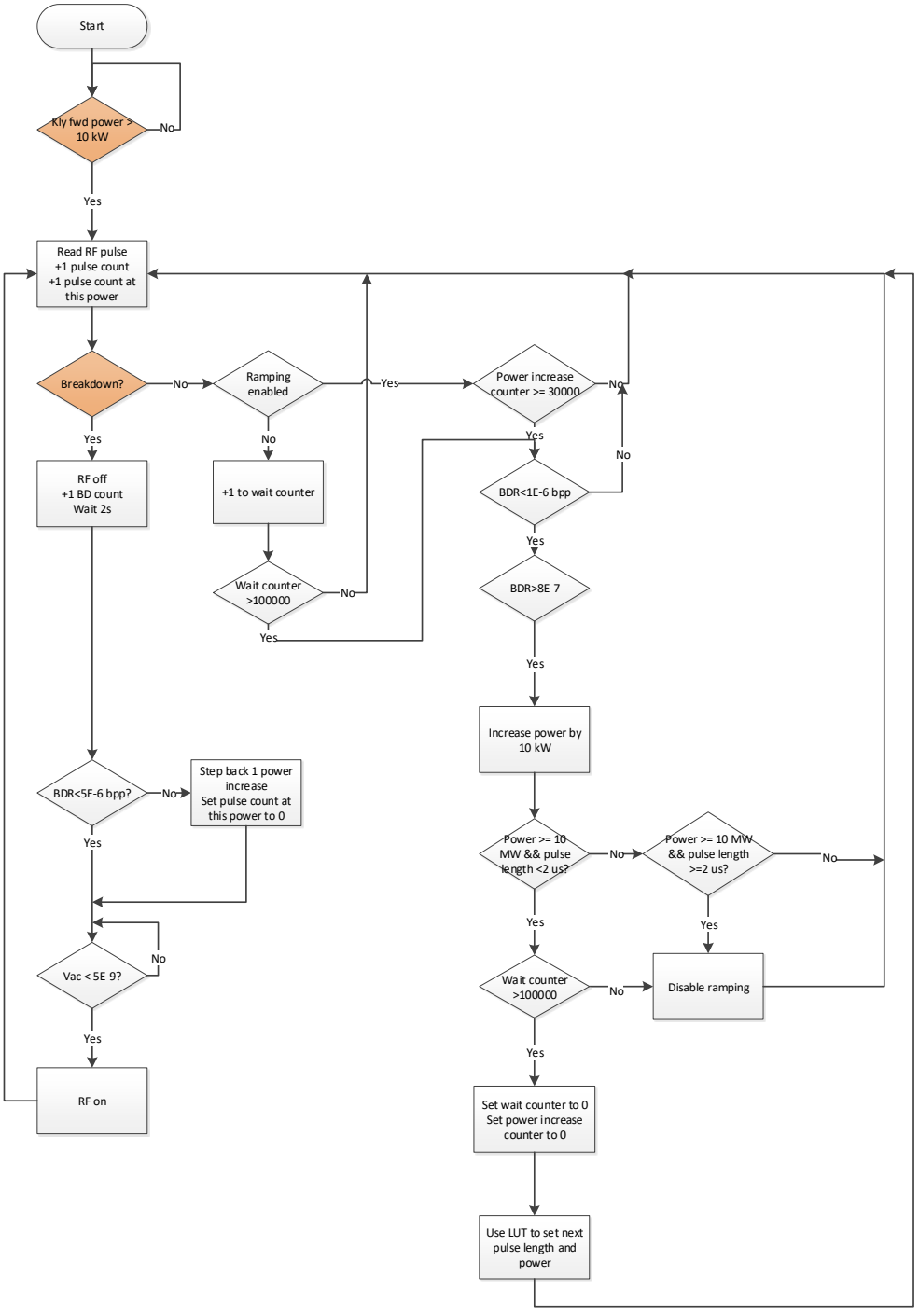

Figure 4.3: The basic logic of the NO-ARC conditioning program

Figure 4.4 shows the interaction between the modules. The modules are:

- Main Controller. This class holds all the objects and controls the flow of the program.
- Data. This module holds a dictionary with all the single valued data collected.
- Configuration file reader. This module holds the configuration file and puts the input data into dictionaries, which are then available to other classes
- Data logger. This module writes all output files.
- C++ hardware controllers. These are a group of c++ sub-programs that interact with the hardware.
- Base. This is a utility class that holds lower level classes and general functions that can be used for higher lever classes.
- GUI. The graphical user interface.

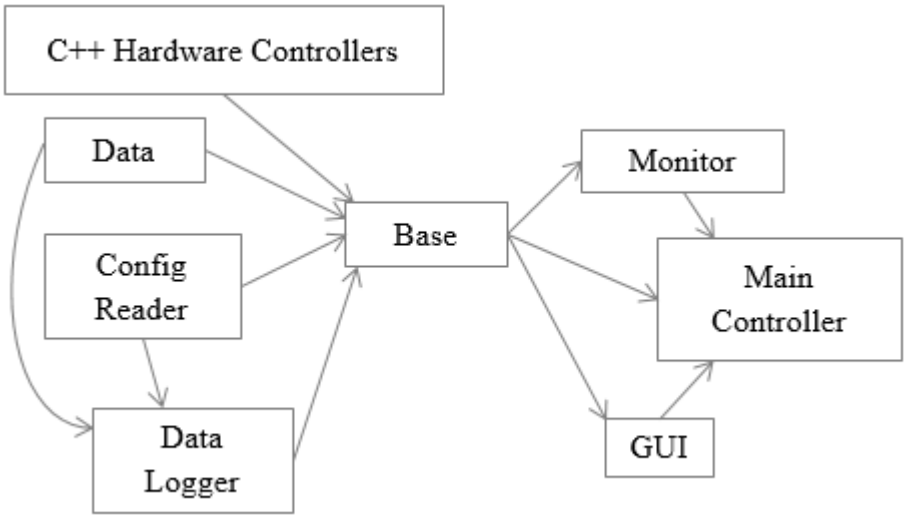

Figure 4.4: The modular design of the NO-ARC program

4.2.4 CLARA/VELA photoinjectors

CLARA and VELA are two electron beam-lines that sit next to each other. The photoinjector positions on each line are fed from the same RF system, sharing SF_6 filled waveguide up to an elbow that must be manually removed and replaced in a different orientation to alter which position the RF is sent to. Previously a high power waveguide switch was employed, however after repeated SF_6 leaks and breakdowns, it became clear that the switch was not fit for purpose and it was removed.

The shared infrastructure includes the Libera I-tech low level RF (LLRF) system, high voltage (HV) modulator, 10 MW klystron, ferrite waveguide circulator, and klystron-end directional coupler (which sits between the klystron and circulator). Each photoinjector position has its own structure-end directional coupler. The layout of the RF system is shown in Figure 4.5.

The RF traces available are therefore the amplitude/power and phase of:

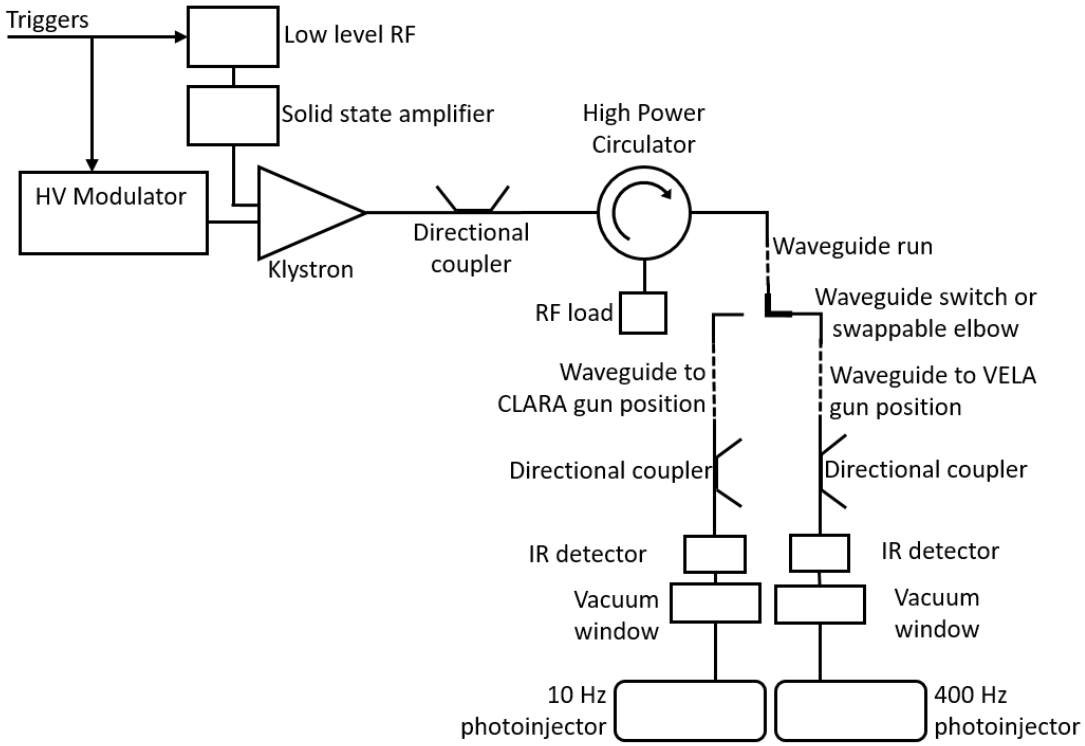

Figure 4.5: High power RF system serving the CLARA and VELA gun positions

- Klystron forward signal for CLARA/VELA
- Klystron reverse signal for CLARA/VELA (circulator between structure and coupler means this signal is negligable and trace is dominated by cross-talk of the forward power)
- Cavity forward signal for CLARA
- Cavity reverse signal for CLARA
- Cavity forward signal for VELA
- Cavity reverse signal for VELA
- Cavity probe signal 400 Hz photoinjector

Currently the 400 Hz photoinjector is installed on the VELA beam-line, and an older photoinjector, the 2.5 cell 10 Hz ALPHA-X style gun [25] on loan from the University of Strathclyde, is installed and operated on CLARA. The 10 MW klystron provides approximately 7 MW at the VELA position and 6.5 MW at the CLARA position after waveguide losses. This is not enough to reach 120 MV/m operation of the 400 Hz photoinjector. Replacement of the 10 MW klystron with a 20 MW klystron is planned for 2022. The 400 Hz photoinjector will then need further conditioning to a higher power.

The surface electric field and modified Poynting vector distributions in the 10 Hz photoinjector are shown in Figure 4.6, and in the 400 Hz photoinjector in Figure 4.7. The high electric field regions can be expected to have higher field emission, and, as discussed in Section 4.1.2 the modified Poynting vector may play a role in the onset of RF breakdown, although experimentally it has been shown that it is not a good predictor for breakdown location. It should be noted that the

Poynting vector during steady state operation of both photoinjectors is entirely imaginary, it is the reactive power flow.

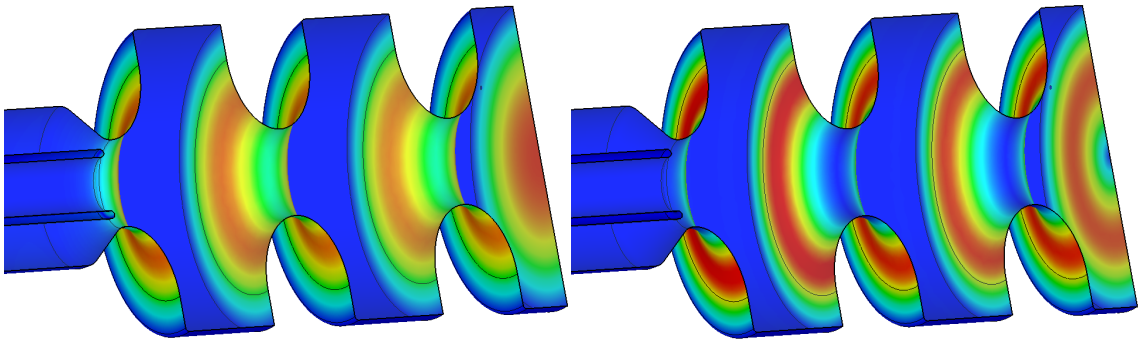

Figure 4.6: Surface electric field (left) and modified Poynting vector (right) distributions in the 10 Hz photoinjector.

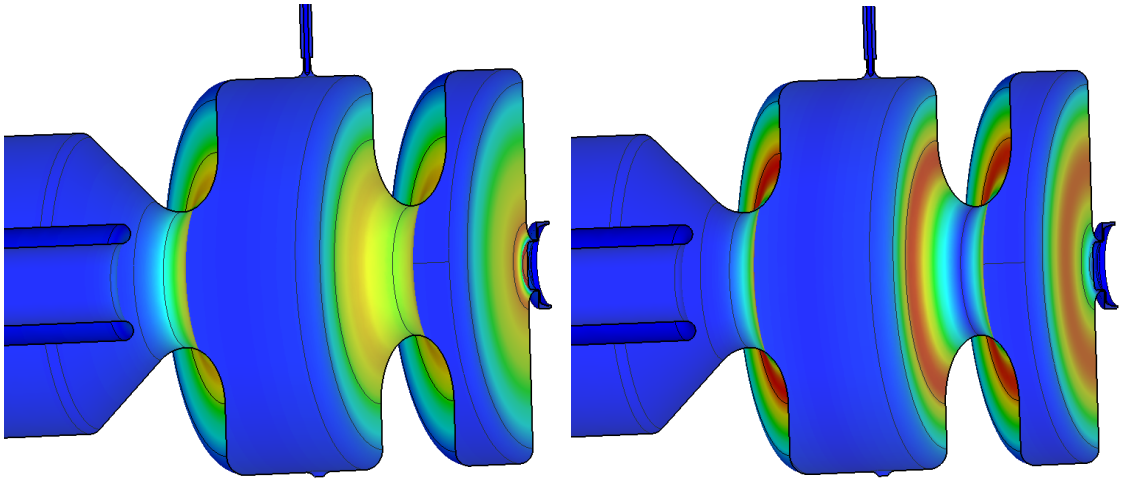

Figure 4.7: Surface electric field (left) and modified Poynting vector (right) distributions in the 400 Hz photoinjector.

4.2.5 Breakdown detection

Possible breakdown detection methods include the measurement and analysis of:

- RF pulse shape
- Structure internal vacuum pressure
- Dark current
- Acoustic signals
- Optical light
- Ionising radiation

NO-ARC currently uses RF pulse shape analysis as its main breakdown detection mechanism, with internal vacuum measurements as a back up mechanism, as well as for measuring outgassing.

Dark current analysis is not currently utilised but is possible for the gun positions on CLARA and VELA due to wall current monitors (WCM) immediately following the photoinjector in the lattice. Acoustic, optical and ionising radiation signals are not currently measured on CLARA or VELA.

RF pulse shape analysis

Measurement of RF pulse shapes from an RF structure is commonly done using waveguide directional couplers or RF probes. This signal is demodulated by the LLRF to give the amplitude and phase envelopes which are then used in analysis.

Detection of breakdown from the RF pulse shape depends on the structure type. Travelling wave structures make breakdowns easy to detect, as the reflected power is negligible in normal operation, but spikes when a breakdown occurs. A simple maximum measurement of this signal is all that is required to detect a breakdown (although other signals such as transmitted pulse shape, as the transmission becomes suppressed in the event of a breakdown, are useful for more detailed analysis, such as determining location of breakdowns [73]). In standing wave structures, such as the 400 Hz photoinjector, determining if a breakdown has occurred is more involved, and must entail a comparison of the measured RF pulse signal to previous non-breakdown signals.

The reflected amplitude signal from a standing wave structure has a characteristic shape, consisting of an immediate peak at the beginning of the pulse, which decreases as the structure fills, and then a second peak when the incoming RF signal ends as the structure empties. The phase of the signal will be constant during structure filling, and will change to a different constant value for emptying. An example is shown in Figure 4.8. If a breakdown occurs both signals will be disrupted. If the breakdown occurs during structure filling a spike in reflected amplitude is seen, if the breakdown occurs when the structure is emptying the power remaining in the structure will be transferred to the arc and a drop is seen.

Some structures may also have an RF probe to measure the RF pulse shape of the stored energy in the structure. The amplitude of this signal, increases to maximum slowly and then drops as the structure empties. An example is shown in Figure 4.8. If a breakdown occurs this signal will drop to zero. The phase of this signal is constant during the pulse, but will vary wildly when a breakdown occurs.

The RF pulses can vary over short timescales (pulse to pulse) due to both timing and amplitude/phase jitter, mainly from the HV modulator, and over long timescales (on the order of seconds or minutes) due to slowly changing real-world variables (eg. SF_6 pressure in the transport line, small temperature fluctuations of the structure, klystron or transport line). These long timescale variable effects can be large, but the average pulse shape is calculated as a rolling average over a much shorter time period (typically 5 pulses) and the effect of these variables on the RF pulse during this timescale is very small. It should be noted however that these effects can alter the gradient achieved in the structure for a given input power, so they should be tightly controlled in order to accurately control the ramp up of the structure gradient.

To accept any variations a region around the rolling averaged pulse shape in which the new pulse shape may be labelled as "normal" must be defined, as done for the conditioning of the ELI-NP S-band gun [56]. NO-ARC allows for user set upper and lower bounds of this region, an absolute value in phase and the choice of either an absolute or a percentage value for the amplitude, which of course increases throughout the conditioning. The upper bound must be set such that the programmed increases in amplitude do not exceed the allowed region. This is not an issue as any spike that exceeds the upper bound must necessarily break the lower bound as it drops. The

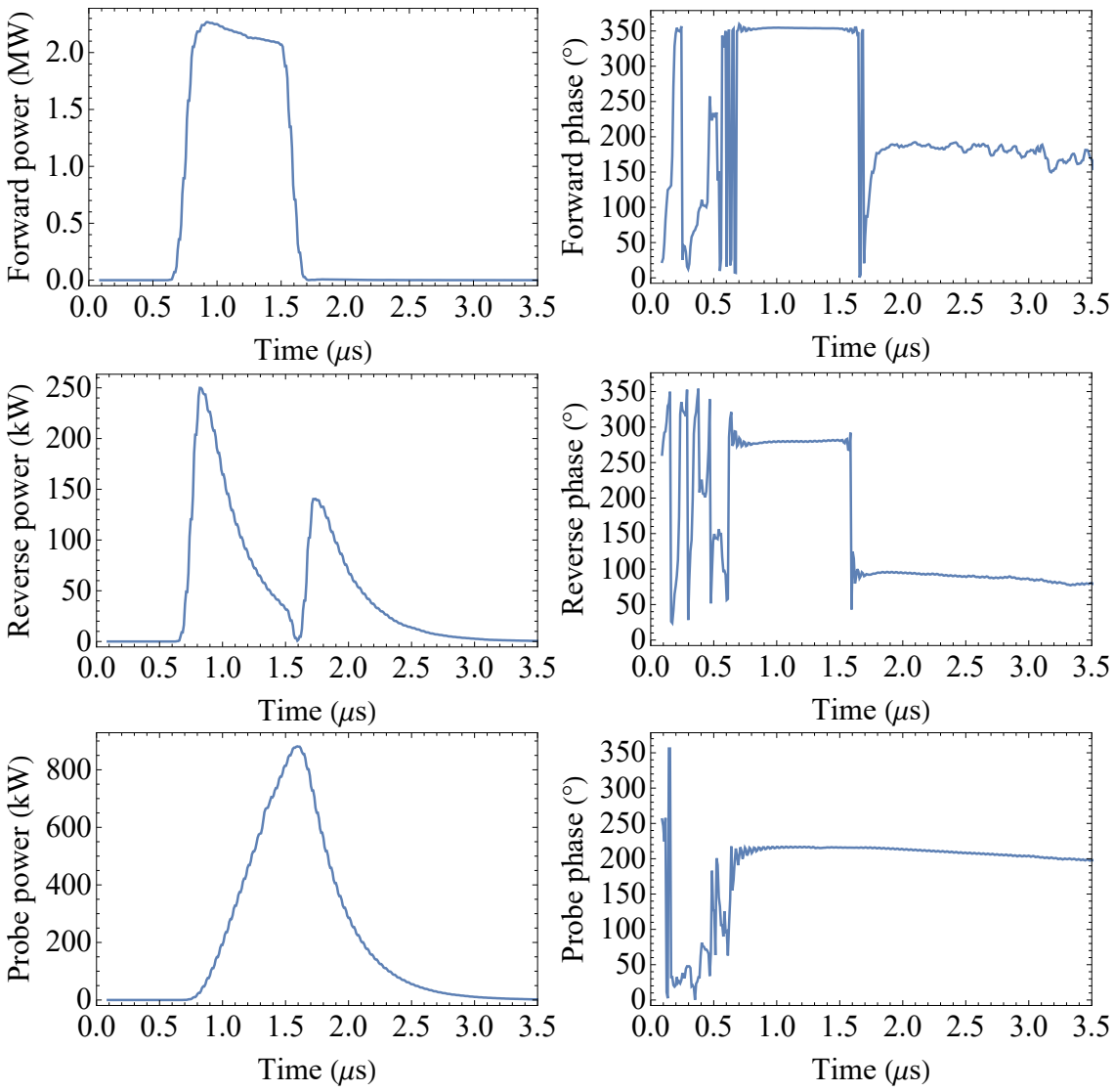

Figure 4.8: Forward power and phase, reverse power and phase, and probe power and phase for a standing wave structure in normal operation

start and end bounds of the allowed region are user set, as is a lower bound which should be set at the noise level. The reflected power signal of a normal and a breakdown pulse is shown in Figure 4.9, if the signal enters the blue region, as seen for the breakdown pulse in orange, it is labelled as a breakdown.

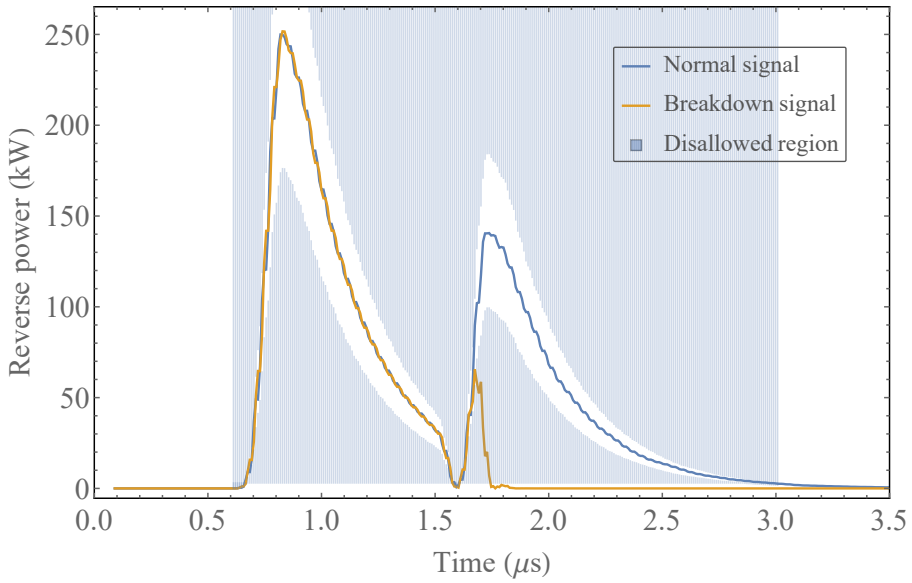

Figure 4.9: The reflected power for a normal pulse and a breakdown pulse. If the signal enters the blue region it is labelled as a breakdown.

The phase measurements are far more sensitive to breakdown events than the amplitude, so most breakdowns are detected in these signals. Because of this, more false-positive breakdown detections are seen with this method, for example multipactor can be mis-identified as a breakdown.

This method brings with it certain scope for issues, such as in the event that the first pulse analysed by the program on starting is a breakdown pulse. In this case the "normal" pulse for comparison will be misshapen and all future normal pulses may be labelled breakdowns. In this case the program must be restarted. This is one reason why it is best practice not to stop and start the program, but rather to let it run continuously.

As breakdown detection from RF pulse shapes is a shape-detection problem, it is an ideal candidate for a neural network. Neural networks can perform automatic feature extraction and classification simultaneously. Work is ongoing at Daresbury to train a model and adapt it to work in real time as a NO-ARC module, this is discussed in [74] by H. Kockelbergh and will be briefly summarised here. A network trained on on half the data from the gun-400 conditioning period and tested on the other half has 99.7% accuracy and 99.0% breakdown recall, where

$$\text{accuracy} = \frac{\text{pulses correctly identified}}{\text{number of traces}} \tag{4.14}$$

and

$$\text{breakdown recall} = \frac{\text{number of breakdowns identified}}{\text{number of true breakdowns}}. \tag{4.15}$$

Vacuum pressure

The internal vacuum pressure of the structure is used as a backstop method of breakdown detection, in the event that other methods fail. The vacuum pressure is measured by inverted magnetron gauges (IMGs). The vacuum pressure data is only collected at 1 Hz so, if conditioning at 100 Hz

for example, 100 pulses could be allowed after the breakdown pulse before the RF is switched off, if depending only on this method. This would allow "follow-up breakdowns" [75] and increase the possibility of damage.

NO-ARC allows the user to set the breakdown detection threshold as either a pressure increase from the average of the previous 5 measurements, or an absolute value threshold. One issue with the pressure increase method is that if the pressure rises over a number of seconds, what might be a large overall change in pressure is split between several data points, and may not be large enough to trigger a breakdown detection. Breakdown events should in theory cause a rapid increase in pressure however, so a slow increase of this kind is more likely to be some other effect, for example outgassing.

The internal vacuum pressure is also used to monitor outgassing, which may be increased by higher RF powers, multipactor, or external solenoid fields. NO-ARC allows the user to set a lower vacuum pressure limit at which the RF power will no longer be increased, but rather will stay constant until the vacuum pressure falls. This allows the structure to release absorbed gas before continuing the conditioning process.

Dark current

On CLARA and VELA the current from the photoinjector is constantly monitored by a wall current monitor (WCM) placed at the exit of the photoinjector. The WCM can be used to detect the electron bunch when the photoinjector is operational, or the dark current (current not caused by the photoinjector laser) from the structure during RF only operation such as RF conditioning. The baseline dark current during conditioning is from field emission, in the 10 Hz photoinjector this has been shown to come mostly from the cathode and the region around the cathode, as the electrons produced in these regions are accelerated out of the structure [76]. RF breakdown is accompanied by high currents, which cause a spike in the dark current measurement. NO-ARC has the option of using this signal to detect breakdowns, however it has not been required. Manual data analysis has found dark current spikes which occur at the same time breakdowns are detected.

A secondary method for dark current detection is available on CLARA, which could be implemented in NO-ARC in the future, and in fact has great potential for localising breakdowns. Fibre based optical beam loss monitors detect the Cherenkov radiation caused by electrons hitting RF structures or beam pipes. These monitors were not integrated into the CLARA control system at the time of writing. The current system of longitudinal fibres allows for sub-meter longitudinal loss resolution [77], but the same fibres could be used in different orientations such as wrapped around cavity cells to gain further insight into breakdown position.

4.2.6 Machine protection

As NO-ARC is designed to be used unmanned, it had to have robust machine safety protections. The CLARA control system already has machine safety protections that switch off the high power RF by setting the HV modulator to standby when certain values of machine parameters are breached- for example if the vacuum pressure in an RF structure becomes too high. A separate program was written that is operated within the CLARA control system. This application returns the high power RF system to operation after a machine protection interlock trips the RF off. The program does not return the RF power on if the same tripping interlock is triggered more than 3 times in 30 minutes, as this could indicate a larger issue that should be assessed by an operator.

If the HV modulator is left in standby for this or any other reason for 30 minutes the program will switch the klystron filament heater off to protect the klystron.

Operation of the RF without NO-ARC would mean no breakdown detection, and would increase the likelihood of runs of breakdowns, which could cause structure damage. To avoid operation of the high power RF without NO-ARC, for example in the event of a crash or computer or network failure, NO-ARC sends a signal to the control system every second. If this signal is not received for 30 seconds, a machine protection interlock is triggered and the high power RF turned off.

4.2.7 Front-end

The front-end of NO-ARC has very little user input. The program is configured using a plain-text YAML file, which allows a very high degree of customisation. This design choice was made so that any operator can use NO-ARC once it has been set up, but only RF specialists can edit the configuration file. A planned upgrade is to allow changes to the configuration settings during operation by adding a password-protected "expert panel" pop-out to the front-end.

The front-end, shown in Figure 4.10, has three user input buttons. These buttons:

- Enable or disable ramping of RF power, allowing the user to begin active conditioning or pause at the current power.
- Shut down the RF power e.g. in case of emergency.
- Copy the current values shown on the front-end to the clipboard.

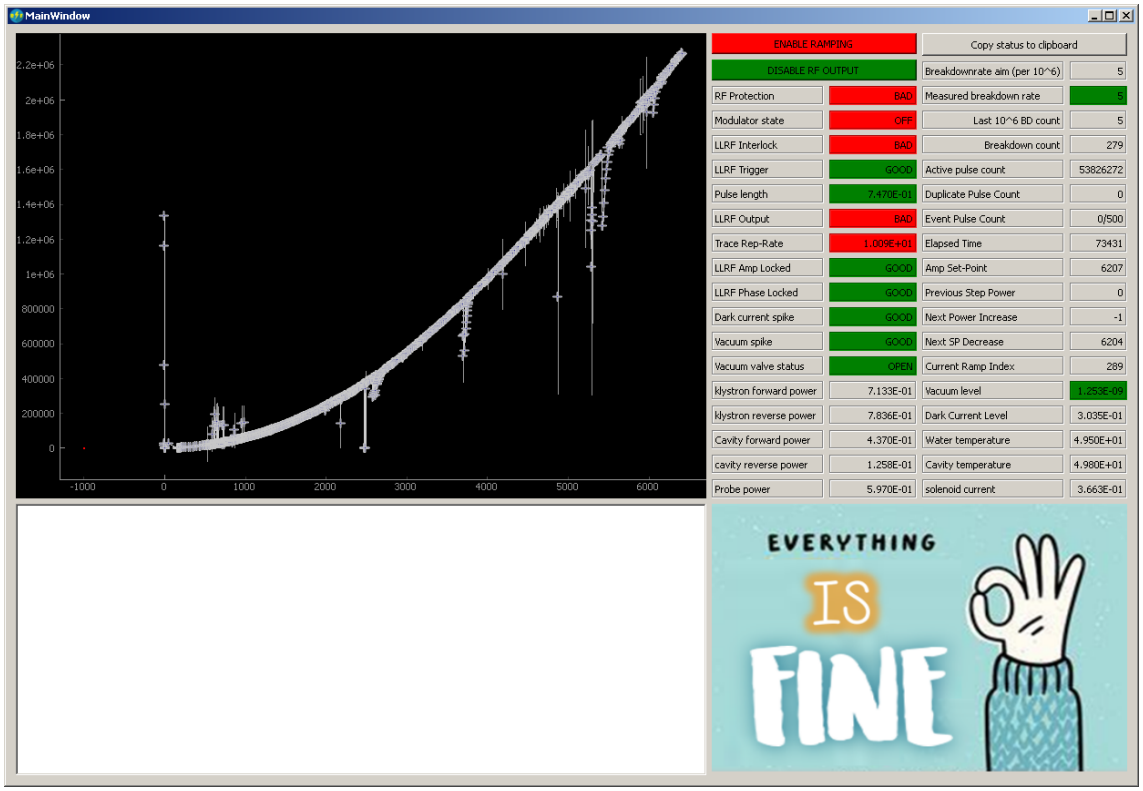

Figure 4.10: Graphical User Interface for NO-ARC, including plot of LLRF set-point against forward power from the klystron

The read-outs on the right are updated at 1 Hz and show RF and program data, as well as breakdown rate. The breakdown rate readout shows green or red dependent on whether the

breakdown rate exceeds the preset value. The values on the bottom left show the state of various parameters in the system and show green if they are within operational limits. The plot on the left shows the RF power at the structure achieved for a given LLRF set point. Past data is used to predict the LLRF set point required for the next power step.

4.2.8 Beta test

NO-ARC was tested by conditioning the 10 Hz photoinjector cavity currently on the CLARA beam line. It is a 2.5 cell photoinjector cavity that is run at approximately 70 MV/m. This photoinjector has been conditioned previously manually multiple times [63]. The structure required reconditioning because it had been vented to atmospheric pressure, and under a nitrogen flow, the cathode removed and replaced. The cathode is the entire back-plate of the structure, a not insignificant proportion of the internal surface, and experiences high fields. The new cathode was diamond turned and had good surface quality.

In Figure 4.11 the cathode and the first half-cell of the structure can be seen. Structure surface pitting and discoloration from damage during previous conditioning can be seen. Investigation with an endoscope has shown the other cells to have similar surfaces, as well as green/blue discoloration around the braze joins at the cavity equator.

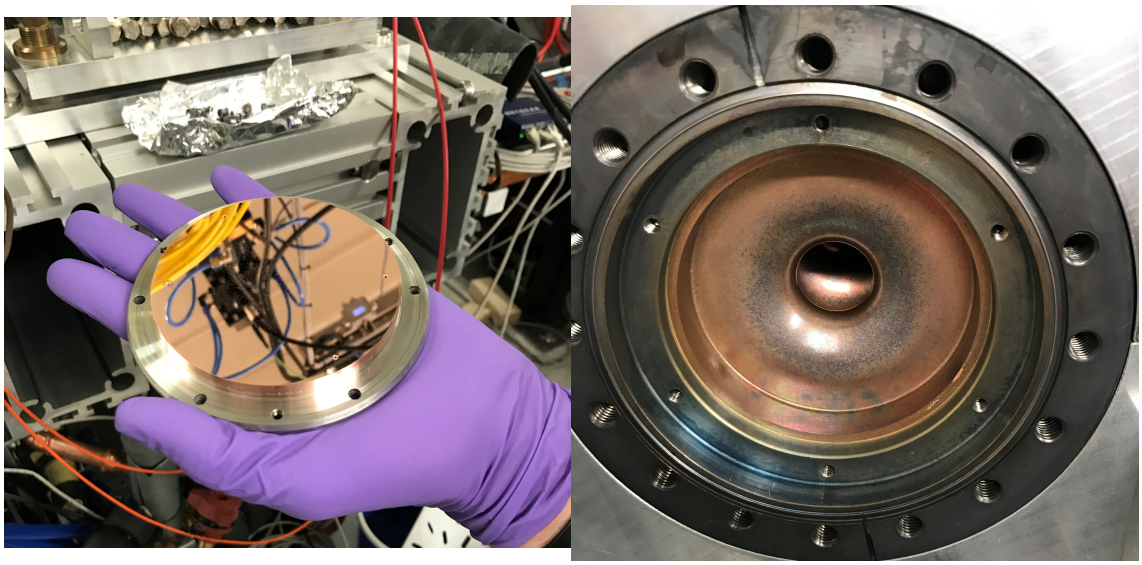

Figure 4.11: New cathode (left) and first half-cell (right) of gun-10 during cathode replacement for the beta test.

The damage to this structure could be expected to provide copious field emission and breakdown points, however it has been recently conditioned and as such any breakdown points have been smoothed. The 400 Hz photoinjector, in contrast, has a smooth, well finished internal surface, but has never been conditioned before, and will be conditioned to a much higher gradient of 120 MV/m.

This was the first test of NO-ARC, and as such the program was developed as conditioning progressed, having never been tested at high power before. The program increases the RF power at a set rate. If a breakdown occurs the RF power is switched off for 5 seconds, and then switched back on. There is a set breakdown rate limit of breakdowns per pulse. If the measured breakdown rate is above this the RF power will not be increased. This state will continue until the breakdown

rate drops below the limit. Any breakdowns that occur in this state will cause the power to come back on one ramp step lower.

The set breakdown rate was 100 per million pulses (10 times higher than recommended for Gun-400, as time was limited and the cavity had been conditioned before). The ramp rate was 10 W/pulse to begin with, but was increased on 22/02/18 at 14:30 to 20 W/pulse due to minimal breakdown activity. For the majority of conditioning the power was raised in steps of 20 kW every 1000 pulses.

Conditioning took approximately 2.1 million active pulses, equalling 60 active hours. Figure 4.12 shows the cavity forward power versus the pulse number. Marked on the plot is the solenoid status, and a number of points of interest which are elaborated on below. Figure 4.13 shows the same data plotted against time, to show the frequency with which the program had to be stopped and re-started.

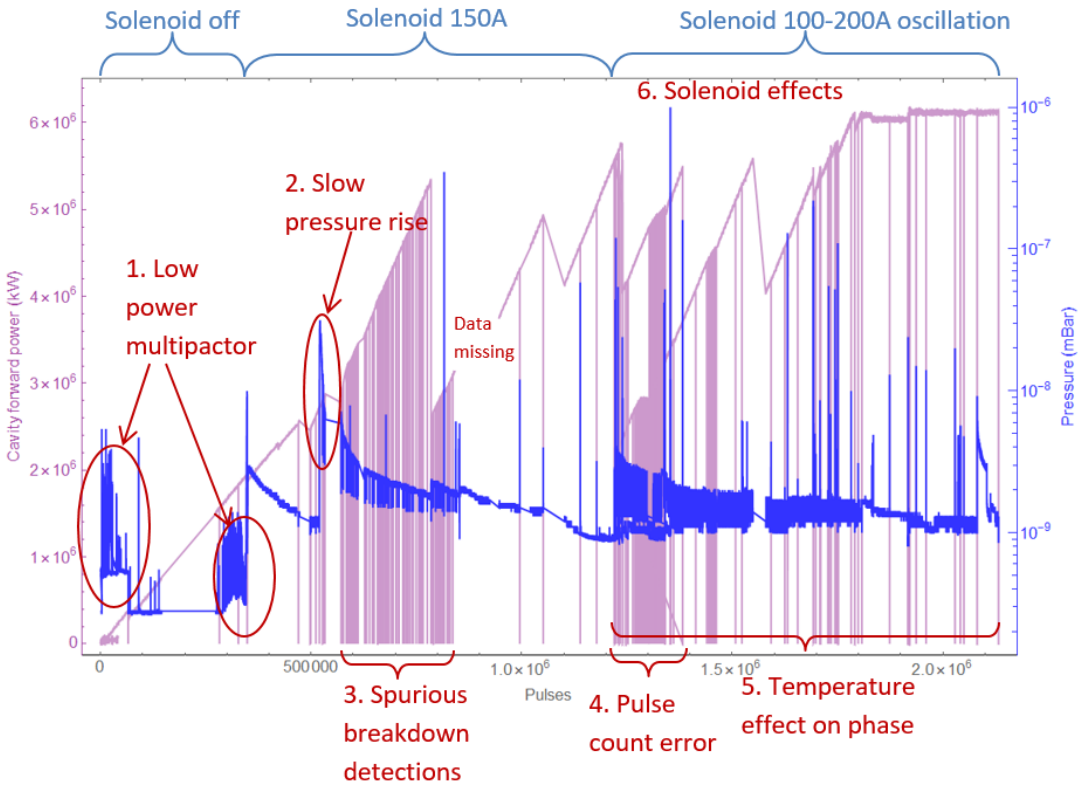

Figure 4.12: An overview of the conditioning process of the 10 Hz photoinjector cavity showing forward power measured at the cavity-end directional coupler and vacuum pressure level against number of pulses

Low power multipactor

When the peak forward power reached 80 kW cavity activity was detected by NO-ARC, both in the cavity reflected RF phase and the vacuum. The cavity reflected power and phase during one of these events can be seen in Figure 4.14. It can be seen that the phase of the reflected RF power from the cavity has a sharp rise at 1.8 s. This is 0.6 µs after the forward power pulse is switched off. A slight drop in the reflected power can also be seen at this point.

The pressure in the cavity spiked during these events. The baseline pressure was 6×10^{-10} mBar, and the spikes were up to 2.5×10^{-9}mBar. This is a very small spike by cavity conditioning

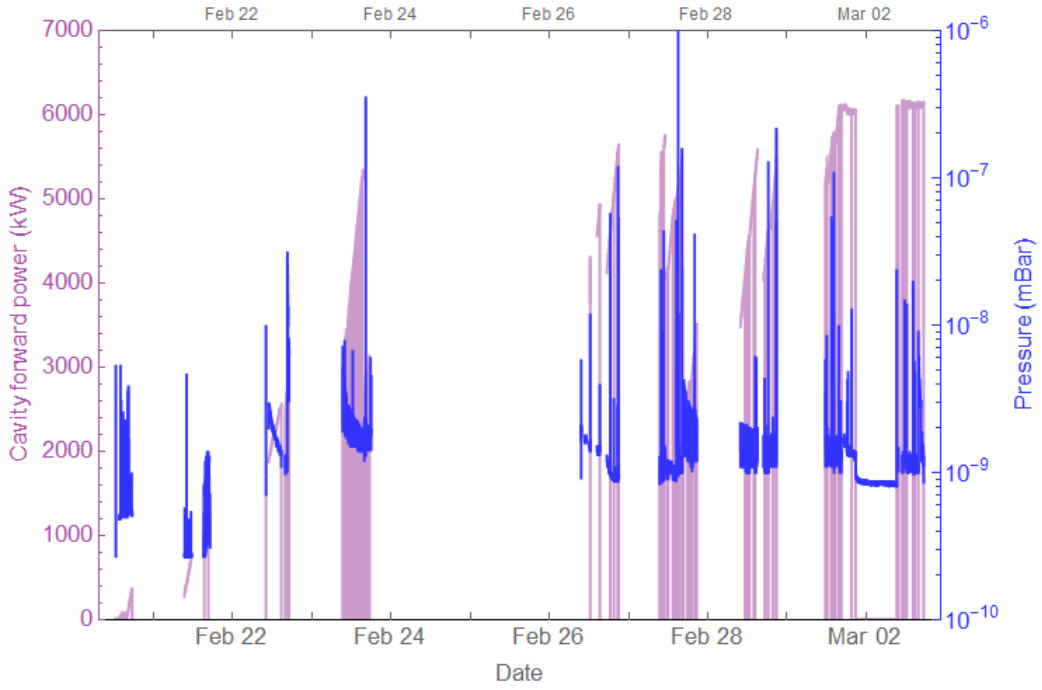

Figure 4.13: An overview of the conditioning process of the 10 Hz photoinjector cavity showing forward power measured at the cavity-end directional coupler and vacuum pressure level against time

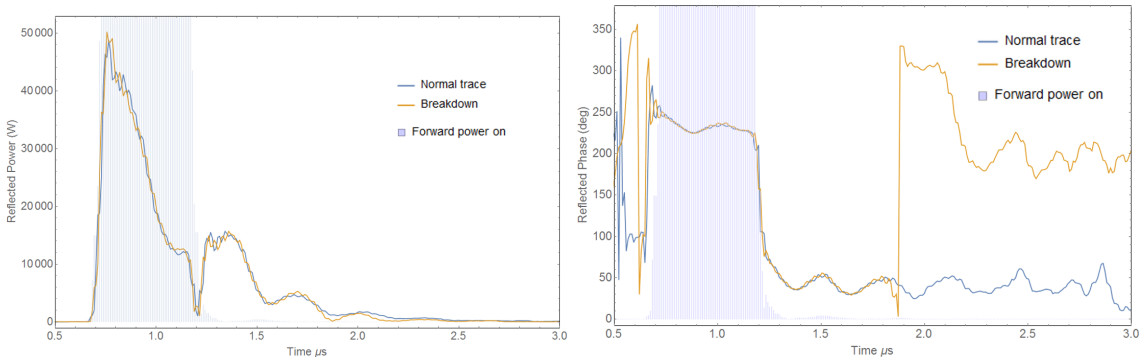

Figure 4.14: Effect of low power multipactor on the reverse power and phase from the structure.

standards. The spikes did not even exceed the specification for normal pressure when running with beam. The vacuum spikes along with the cavity forward power can be seen in Figure 4.15. This shows the NO-ARC detecting the spike or phase event, and switching the RF power off.

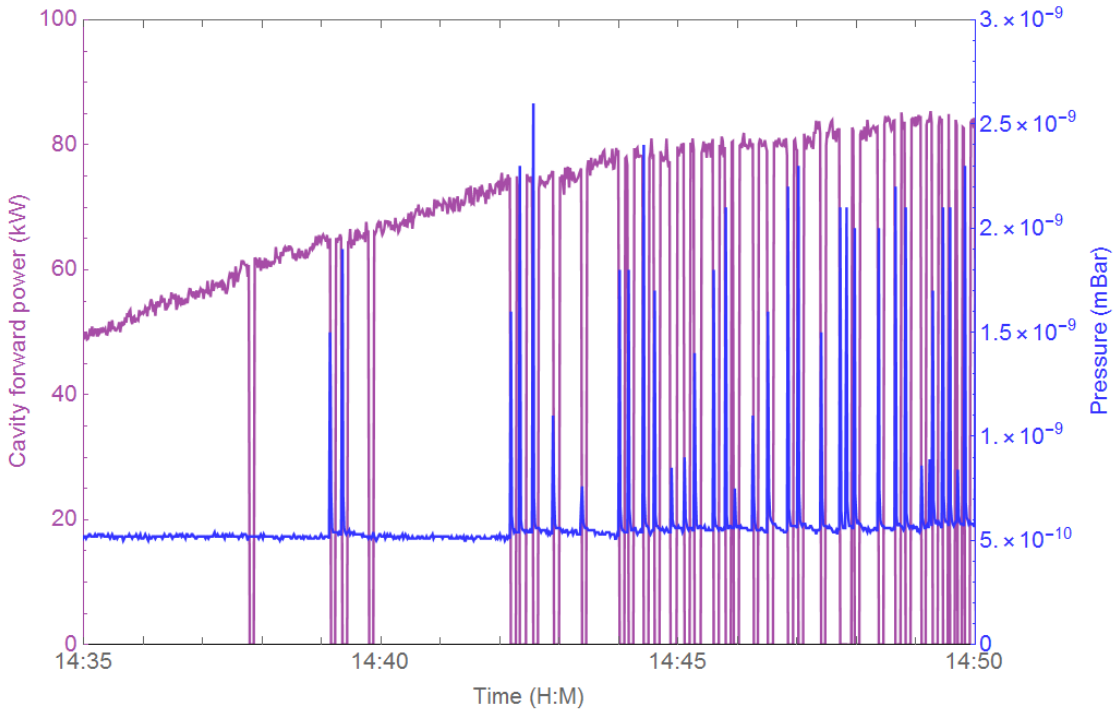

Figure 4.15: Forward power measured at the cavity-end directional coupler and vacuum pressure spikes in the low power multipactor band, showing NO-ARC switching off the power at each spike.

Multipactor is the obvious conclusion for this effect. It is interesting however that the multipactor occurs only when the cavity is emptying, and only at specific forward power levels. This behaviour was seen at forward powers of between 80 and 150 kW, and again between 1.5 and 1.9 MW. The first band of multipactor occurs at approximately 5000 W reflected power (which approximates cavity power in this region), but the power decay in the cavity must pass through this power at all cavity powers higher than 5000 W, so why does multipactor only occur at certain forward power bands, and why only on the power decay and not the rise? One explanation could be that higher power is required to seed the multipactor with dark current, and then the multipactor band multiplies this seed. Additionally the cavity filling is faster than the decay in the power regions where multipactor is seen, so the multipactor has longer to build. This is illustrated for clarity in Figure 4.16, the time spent in the light green region where multipactor occurs is longer as the cavity empties. The scaling laws and results for multipactor in a coaxial line given by Somersalo [44] can be used to show that the coupler dimensions are far too large for two-point multipactor to occur and too small for single-point multipactor to occur. It is concluded that the multipactor is not in the coaxial coupler.

It was decided to ignore these very low power effects as the risk of cavity damage was low, and, as described in Section 4.1.1 multipactor can often be processed through. The multipactor was not affecting the peak field achieved and was therefore not a concern. The algorithm was therefore set to not label these events as breakdowns, or turn off the power when they occurred. Figure 4.17 shows the cavity forward power and cavity pressure as the power was increased through the first band. The events stopped occurring at 150 kW cavity forward power. It should be noted that

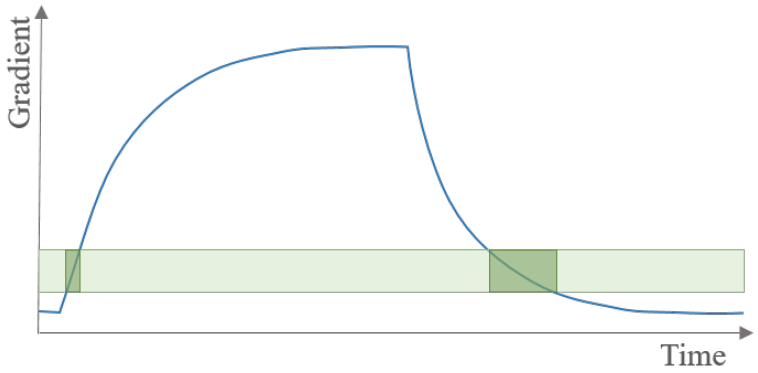

Figure 4.16: Illustration of time spent in gradient region of interest during filling and emptying.

on returning to this power range later in the conditioning process no events were seen. The effect conditioned away. This effect is discussed further in Section 4.3.3.

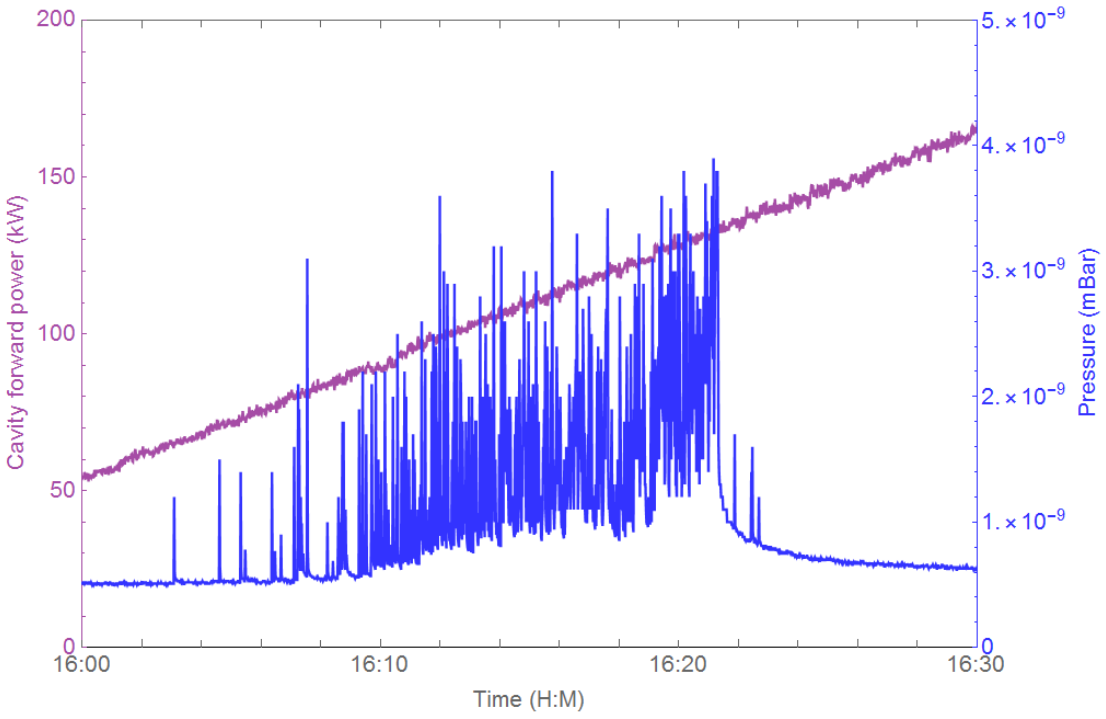

Figure 4.17: Forward power measured at the cavity-end directional coupler and vacuum pressure spikes in the low power multipactor band after NO-ARC was set to ignore low power multipactor.

Slow pressure rise

Another low power effect that was seen on one occasion was the vacuum behaviour shown in Figure 4.18. There were two small vacuum spikes, 6 seconds apart (5×10^{-9} and 7×10^{-9} mBar respectively) each with no change in the RF detected. After another 7 seconds the cavity pressure began to rise slowly, reaching 3×10^{-8} mBar after approximately 3 minutes. This is quite a high pressure considering no change was seen in the RF throughout. A possible explanation is that this is neutral gas outgassing, but it seems quite unlikely at this magnitude.

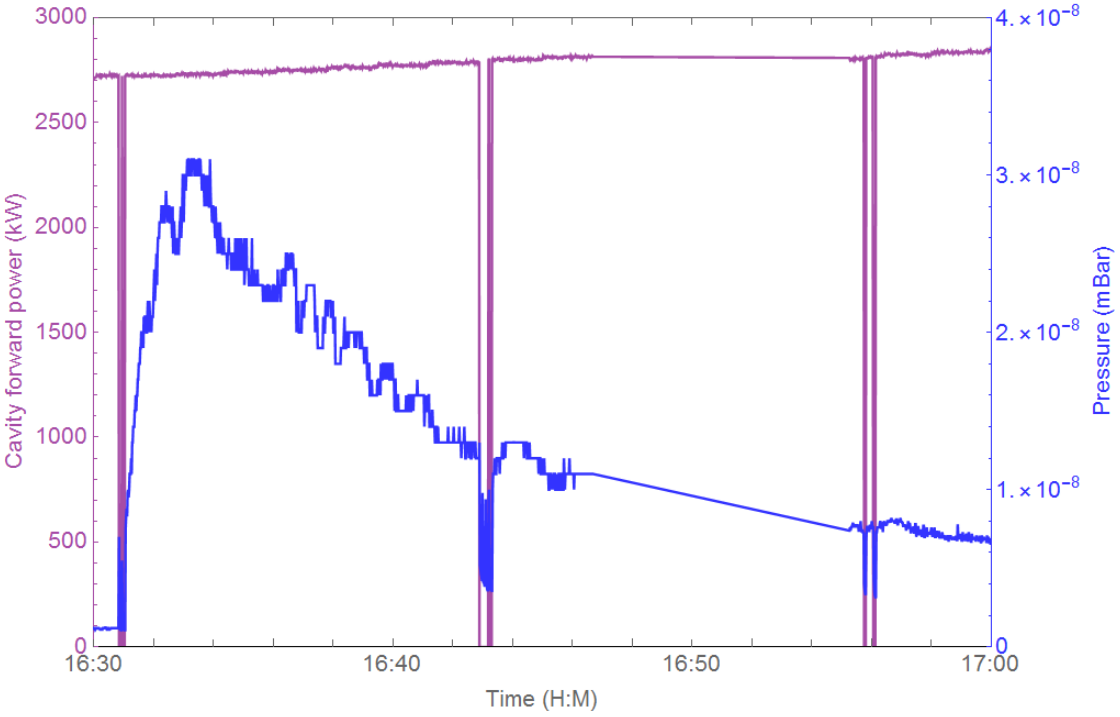

Figure 4.18: Unexplained slow pressure rise

Spurious breakdown detections

Spurious breakdowns have been occurring since Jan 2018 when we began to test the program. These occur when the acquired forward power drops to zero. This seems to be a problem with acquisition. This effect got worse on Feb 24th when the RF trigger was switched from the RF master oscillator to the laser trigger. It was noticed that the drops were more likely to occur when the LLRF setpoint was changed by the python program, and a change in the method for this change within the python alleviated this problem somewhat.

Subsequently the upgrade to the Libera LLRF system described in 4.2.9 allowed a pre-check of the forward power pulse to excluded pulses where the forward power is zero from breakdown detection analysis.

Pulse counting errors

When the pulse length was changed it was necessary to manually re-set the pulse breakdown count log, which keeps track of the pulse number and the number of breakdowns. This lead to errors in the pulse count and the data overlaps seen in Figure 4.12. The pulse length change procedure will be improved for the next conditioning run.

Effect of temperature on reflected phase

At pulse lengths higher than 2 µs, the reflected phase was seen to vary towards the end of the pulse length. Figure 4.19 shows the measured reflected phase from the cavity-end directional coupler at two times a few minutes apart. In one the phase decreases and the other it increases. This correlates with temperature changes in the cavity. Over the 10 minutes in which these plots were taken the cavity temperature stabilisation water temperature varied up to 1°C. The

water fluctuation occurred due to the conditioning program misdiagnosing the phase changes as breakdowns and repeatedly turning the power off.

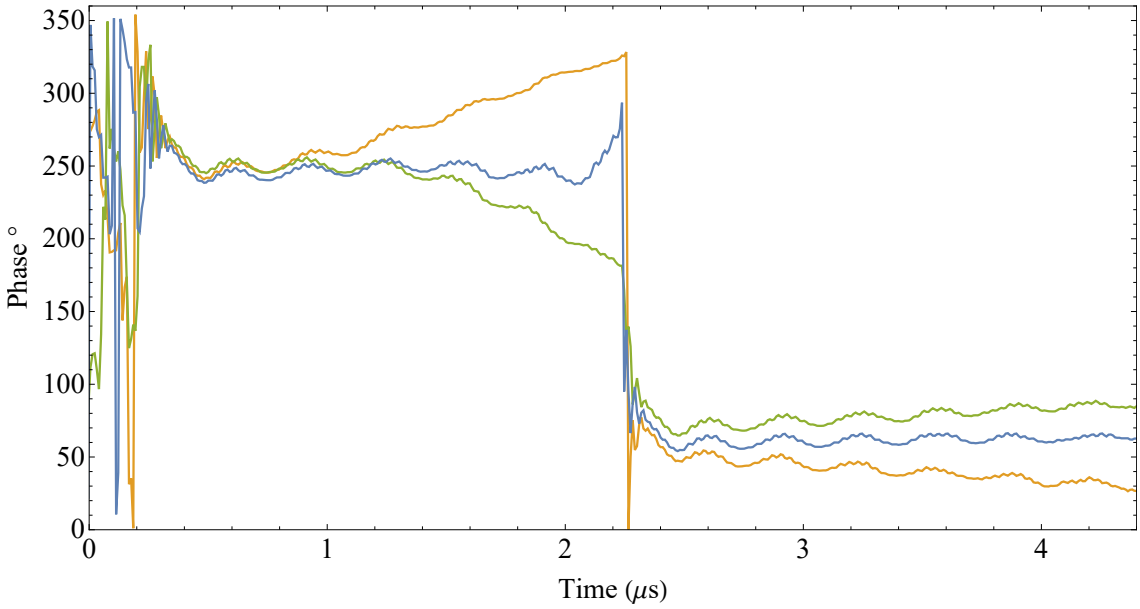

Figure 4.19: Phase variation at end of pulse length due to temperature variation of structure.

At first it was though that this effect was due to the pulsed heating in the cavity at higher power causing a change in the Q_0 of the cavity. This can happen when the resistance of the copper in the RF skin depth changes at high temperatures. However, this effect can be seen when modelling a simple equivalent circuit model of the gun, whose characteristics do not change in time, therefore the explanation is simpler than first thought.

The equivalent circuit can be built to match the S11 measurements and a single-cell resonator model is sufficient for the cavity. The coupler can be modelled by a 1:n transformer, and the power source by an AC power source with a matched impedance load. This is shown in Figure 4.20

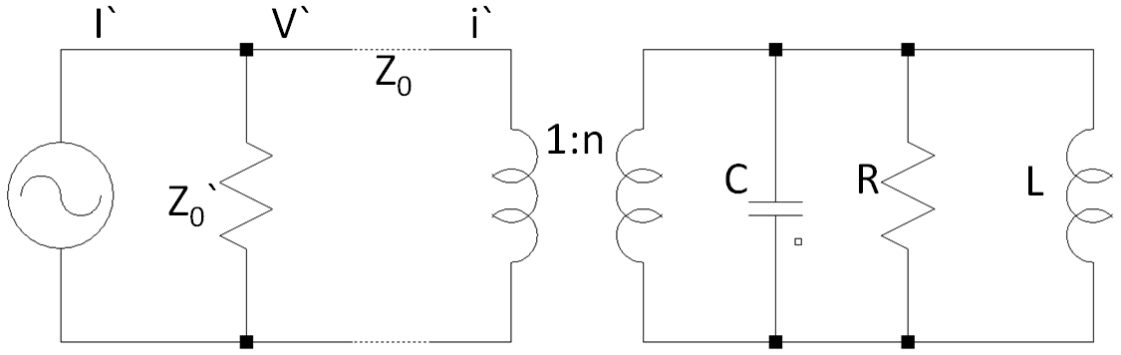

Figure 4.20: The equivalent circuit for the system

This can be converted into a simple generator circuit where the coupler and cavity is represented as a frequency dependent impedance Z_c, divided by the square of the number of turns on the 1:n transformer as shown in Figure 4.21. To transform this into cavity parameters the relations $Q_0 = (\omega_0 U)/P_C = \omega_0 RC$, and $Q_{Ext} = (\omega_0 U)/P_{Ext} = \omega_0 n^2 Z_0 C$, can be used to find that $\beta_c = Q_0/(Q_{Ext}) = R/(n^2 Z_0)$, and so $Z_C/n^2 = (\beta_c Z_0 Z_C)/R$. Here Q_0 and Q_{Ext} are the unloaded and external quality factors of the cavity, P_C and P_{Ext} are the power losses to the cavity walls and

through the coupler at steady state, and C, R, and Z_0 are the circuit capacitance, resistance and the characteristic impedance of the transmission line.

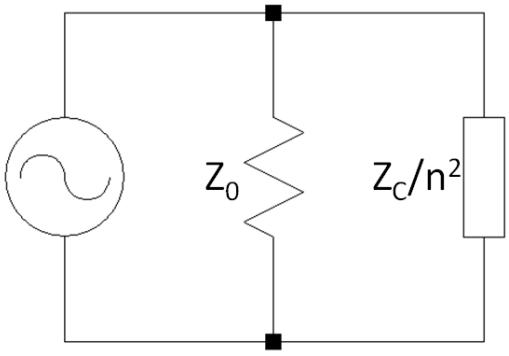

Figure 4.21: The simplified generator circuit.

The resonator impedance can be found by applying Kirchoffs 2nd Law to the RLC circuit that represents the cavity.

$$I(t) = C\dot{V} + \int \frac{V}{L}dt + \frac{V}{R} \tag{4.16}$$

Substitute in $\omega_0 = 1/\sqrt{LC}$ and $Q_0 = \omega_0 RC$, and differentiate with respect to time to give

$$\frac{\dot{I}}{C} = \ddot{V} + \frac{\omega_0 \ddot{V}}{Q_0} + \omega_0^2 V \tag{4.17}$$

Substitute alternating current and voltage signals in, $I = I_0 e^{i\omega t}$ and $V = V_0 e^{i(\omega t+\phi)}$, and solve for Z_C:

$$Z_C = \frac{V}{I} = \frac{R}{(1 - i\gamma)} \tag{4.18}$$

where

$$\gamma = Q_0 \left(\frac{\omega_0}{\omega} - \frac{\omega}{\omega_0} \right). \tag{4.19}$$

The cavity reflectance is then defined as

$$\Gamma = \frac{Z'_C - Z_0}{Z'_C + Z_0} \tag{4.20}$$

where

$$Z'_C = \frac{\beta_c Z_0 Z_C}{R} \tag{4.21}$$

Substituting in for Z_C gives

$$\Gamma = \frac{\beta_c - 1 + i\gamma}{\beta_c + 1 - i\gamma}. \tag{4.22}$$

This is the frequency dependent reflection coefficient of the cavity, S11. This, however, does not take into account the frequency dispersion in the measured S11 signal. To include this, and match the measured S11, a transmission line must be added to the model. The transmission line can be seen in Figure 4.22, where Z_0 is the characteristic impedance, Z is the impedance of the transmission line, l is the length of the line, and k is the complex wavenumber.

The S-parameter matrix

$$\begin{bmatrix} S11 & S21 \\ S21 & S22 \end{bmatrix} \tag{4.23}$$

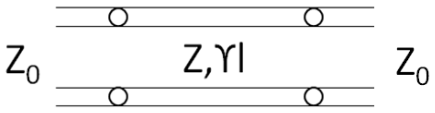

Figure 4.22: Standard transmission line.

for a transmission line is given in [78] as

$$\frac{1}{D_s}\begin{bmatrix}(Z^2-Z_0)Sh & 2ZZ_0\\ 2ZZ_0 & (Z^2-Z_0)Sh\end{bmatrix} \tag{4.24}$$

where $Sh = \sinh(kl)$, $D_s = 2ZZ_0Ch + (Z^2 - Z_0)Sh$ and $Ch = \cosh(kl)$. This matrix must then be cascaded with the S-parameter matrix for the cavity, which, as it only has one port, is the single-valued S11 parameter. The final S11 parameter is then given by

$$S11 = S11^A + \frac{S12^A S11^B S21^A}{1 - S22^A S11^B} \tag{4.25}$$

where superscript A denotes the transmission line and B denotes the cavity.

The cavity resonant frequency ω_0 can be estimated from the minimum of the measured complex S11 data. A simplex optimisation process can then be used to find exact resonant frequency, the Q_0 and β_c of the cavity, and the length, attenuation and impedance of the transition line, by matching the calculated S11 frequency dependence to the measurement. The S11 is a complex value, so in order to match both the real and imaginary parts the argument of the S11 values are chosen to for the fitting function. The fitted S11 curves are shown in Figure 4.23

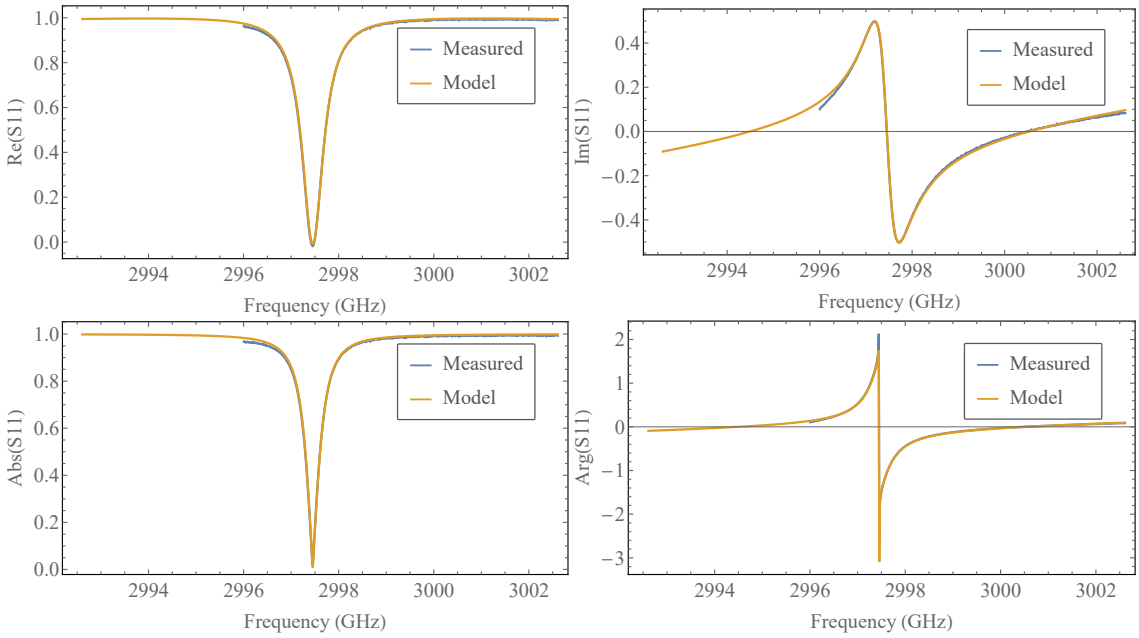

Figure 4.23: The real (top-left), imaginary (top-right), absolute (bottom-left) and argument (bottom-right) S11 as a function of frequency.

By convolving the calculated S11 signal with a Fourier transform of a real forward power pulse, the reflected signal can be calculated and the phase extracted. Figure 4.24 shows the variation in

phase for different frequency offsets between the forward pulse frequency and the cavity resonant frequency. Figure 4.25 shows a comparison between one example of measured reverse phase and the equivalent circuit model with a 25 KHz mismatch. The trend matches well however there is some superimposed oscillation with time on the measurement that is unaccounted for. This could be a dispersive effect in the coupler.

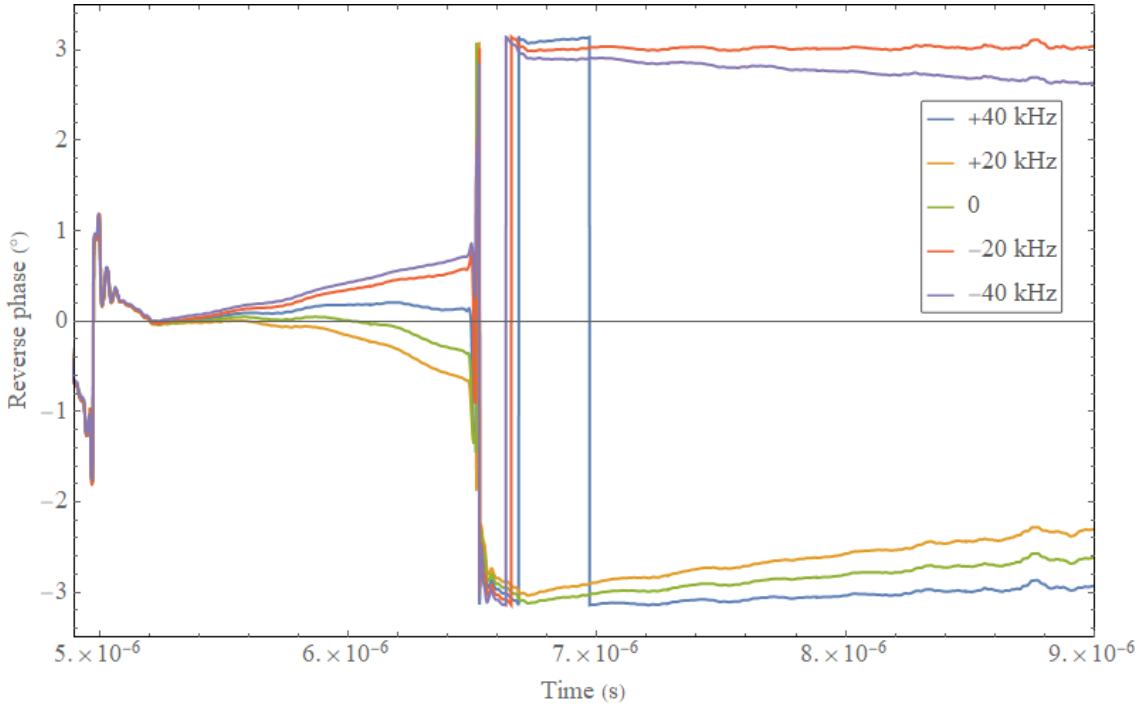

Figure 4.24: An equivalent circuit simulation of the 10 Hz photoinjector showing variation in phase for various frequency mismatches.

To explain this behaviour a simpler circuit with a coupler, but no transmission line, was used. The S11 from this model tuned to a range of RF frequencies was convolved with a rounded square forward pulse at 3 GHz. The reflected signals from the circuit model are shown in Figure 4.26.

In this less noisy model it can be seen in that when the frequency of the oscillator is detuned with respect to the forward pulse frequency the phase varies toward the end of the pulse, for small changes this tends towards a change of $\pi/2$. The reflected signal can be broken down into three parts:

1. The signal reflected from the coupler as the cavity fills
2. The signal emitted by the cavity whilst the oscillator is driven
3. The signal emitted by the cavity as the cavity empties, after the end of the forward power pulse.

These parts are easiest to see in the real and imaginary parts of the signal. Part 1 is the first peak in the real part. It is pure reflected signal from the coupler and has a phase of 0. This can be described as $A(t)\cos(\omega_0 t)$ where ω_0 is the frequency of the forward signal and $A(t)$ decreases as $e^{-(\omega_0 t)/(2Q_L)}$. Part 2 is the emitted signal from the cavity during driven operation. It can be seen on the imaginary plot as it is out of phase with part 1. This signal is zero when the cavity coupling is impedance matched, but for all other cases it can be described as $B(t)\cos(\omega_0 t + \pi + \phi)$ where ϕ is the small angular difference from π in S11 phase and $B(t)$ has the form $1 - e^{-(\omega_0 t)/(2Q_L)}$. Part

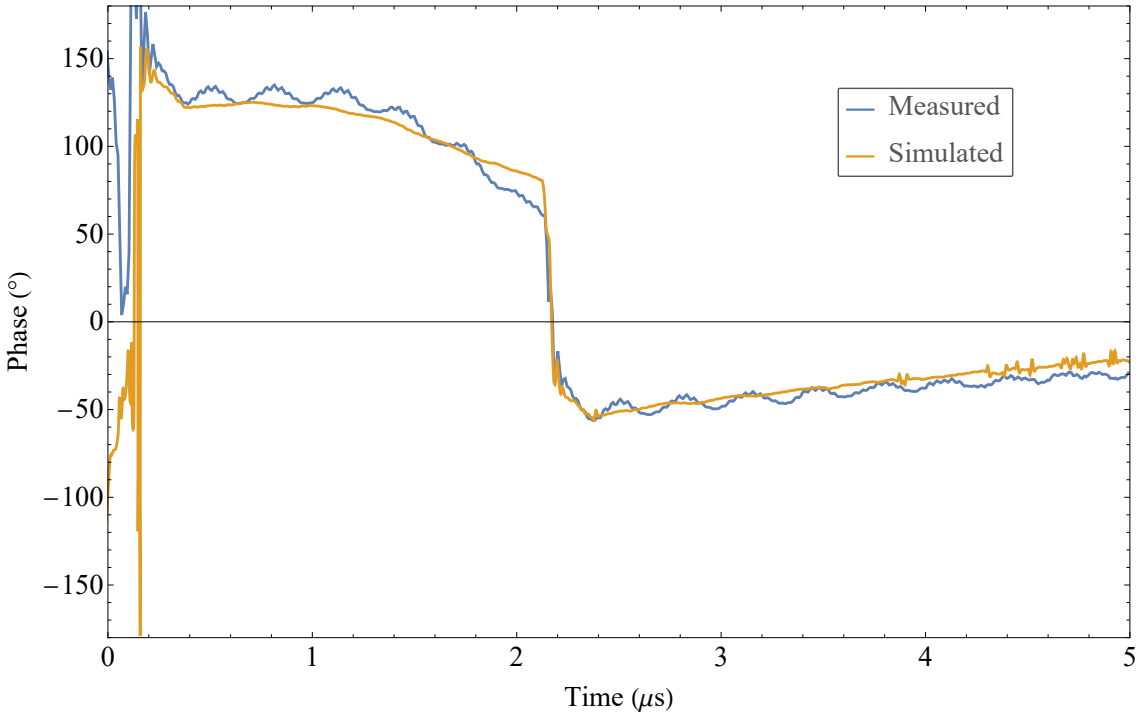

Figure 4.25: Comparison of equivalent circuit model with 25 KHz frequency mismatch to example reverse phase measurement.

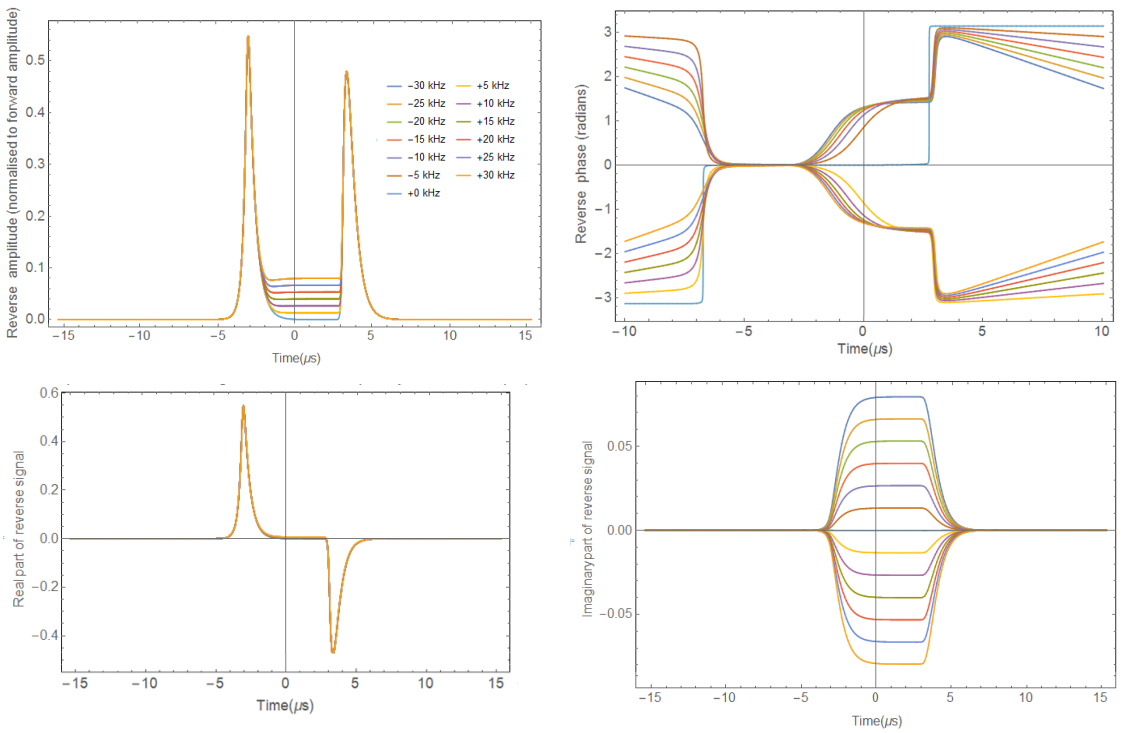

Figure 4.26: Reverse amplitude, phase, real and imaginary signals for a simplified RLC circuit for various frequency mismatches.

3 is the second peak in the real signal. It is the cavity emptying at its resonant frequency and can be described by $C\cos((\omega_0+\delta\omega)t+\pi)$ where $\delta\omega$ is the difference in frequency between the forward signal and the oscillator and $C(t)$ has the form of a decay $e^{-\omega t/(2Q_L)}$ to zero.

The phase change as the cavity fills is caused by the addition of parts 1 and 2:

$$A\cos(\omega_0 t) + B\cos(\omega_0 t+\pi+\phi) \approx A\cos(\omega_0 t) - B\cos(\omega_0 t) + B\phi\sin(\omega_0 t). \tag{4.26}$$

A and B tend towards the same value as the cavity reaches steady state, at approximately three times the cavity fill constant $\tau = 2Q_L/\omega$. We are left with $B\phi\sin(\omega_0 t)$, a small reflection that is proportional to ϕ, and 90° out of phase with the incoming signal.

It should be noted that the 400 Hz photoinjector has a much more sophisticated water stabilisation system than the 10 Hz photoinjector described here, and as such it is not anticipated that the structure temperature will vary enough to cause a similar issue on the 400 Hz photoinjector.

Solenoid effects

It was decided once conditioning had reached 0.5 µs pulse length with 1.9 MW forward cavity power that the solenoid would be required for the few days of operation before the scheduled machine shut-down. Conditioning with the solenoid on was therefore required, as previous experience had shown that a cavity conditioned to a certain gradient without an external solenoid field cannot sustain that gradient with the field.

The solenoid was switched on and the current was oscillated sinusoidally from -250 A to +250 A. The oscillation period was 100 s, the same as the time between RF steps so one oscillation was completed at each step. The aim was give the most flexibility during operation as the cavity could be run with any solenoid field, as well as de-gaussed. The RF was then switched on. Figure 4.27 shows the vacuum activity, with spikes up to 1 $\times 10^{-8}$ mBar. The background is shaded when the RF is on. The baseline vacuum without the solenoid and with the RF on previous to this was below 3 $\times 10^{-10}$ mBar. The RF was switched off again due to the vacuum activity. It is thought the program did not detect the spikes as breakdowns because the activity started as soon as the RF was turned on so a baseline vacuum could not be set, and also possibly because the program was configured to detect a breakdown in the vacuum only if a difference between successive points of 5 $\times 10^{-9}$ mBar was seen, and and these vacuum changes had a slower increase.

The solenoid was then turned on at 150 A, as this was the approximate value for operation, and the conditioning period was time-limited. The RF was tuned back on. Figure 4.28 shows the vacuum baseline increase to 2.7 $\times 10^{-9}$ mBar and then the slow recovery.

Later in the conditioning process the solenoid was oscillated again, from + 100 A to + 200 A. This would give a little more flexibility during operation. The conditioning had reached 8.5 MW at 2 µs pulse length, but the power was reduced to begin varying the solenoid. In Figure 4.29 the pressure can be seen to vary with the solenoid level. Figure 4.30 shows the improvement with time, it should be noted that the RF power was being increased during this time.

Breakdowns

A number of real breakdowns were detected during conditioning. These fall into two categories:

1. Breakdowns that occur during the time the structure is fed by the forward RF pulse- whilst the structure is filling or in steady state. These account for 70% of the total breakdowns.

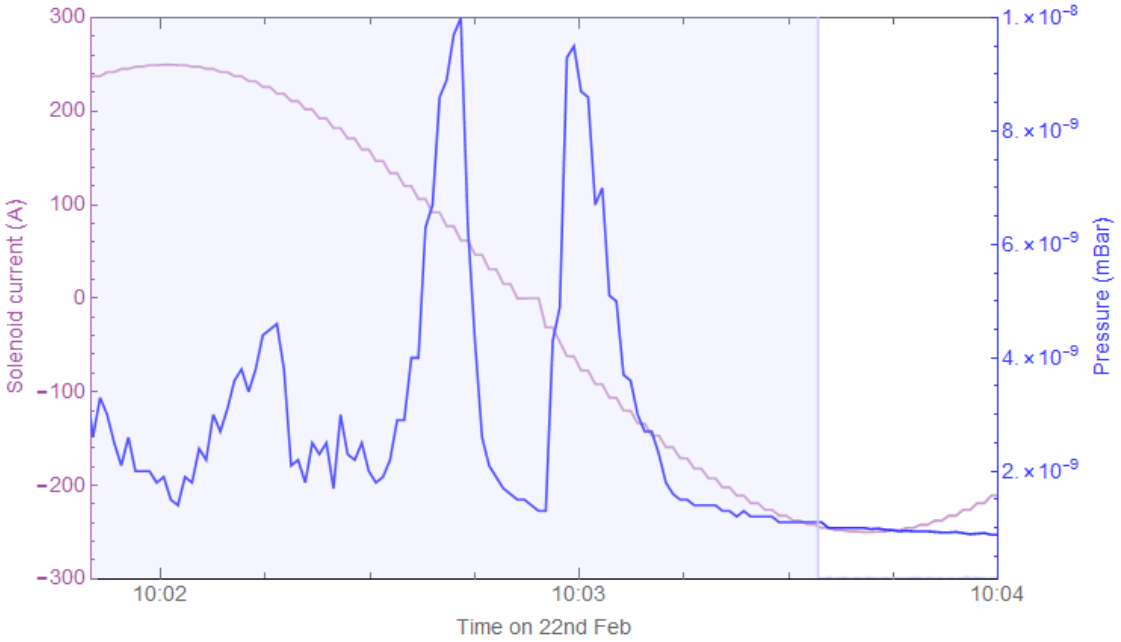

Figure 4.27: Vacuum activity at first operation with oscillating solenoid. The background is shaded purple when the RF is on.

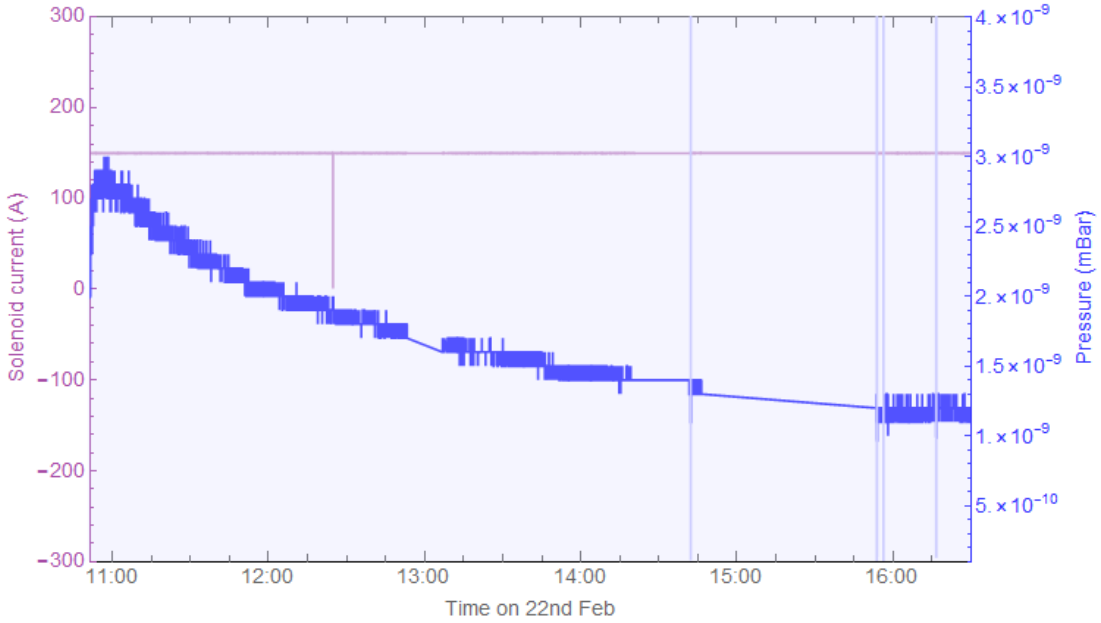

Figure 4.28: Vacuum activity with constant solenoid operation

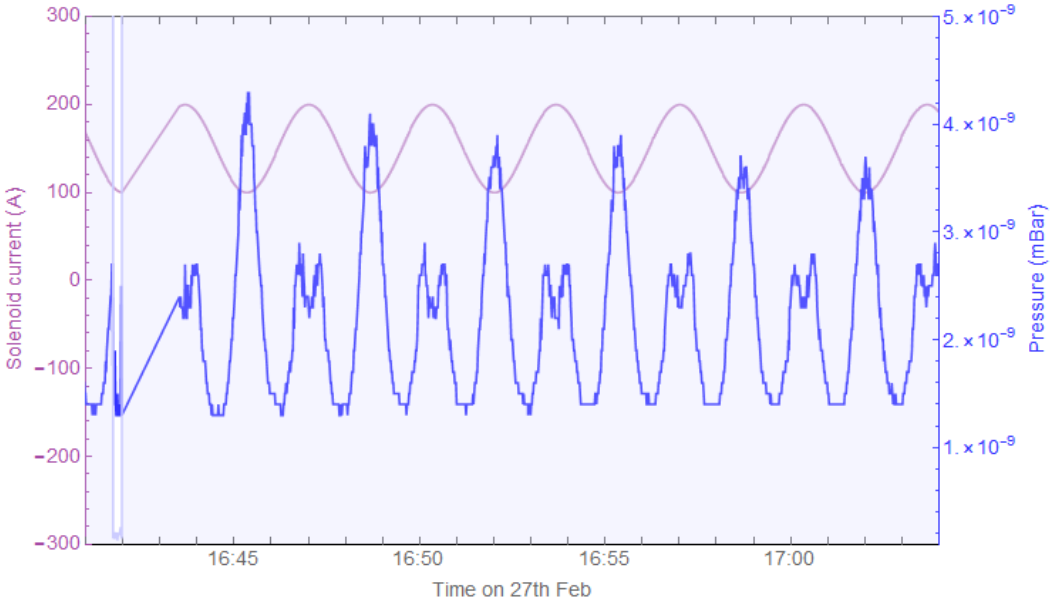

Figure 4.29: Vacuum pressure variation with solenoid level. The background is shaded purple when the RF is on.

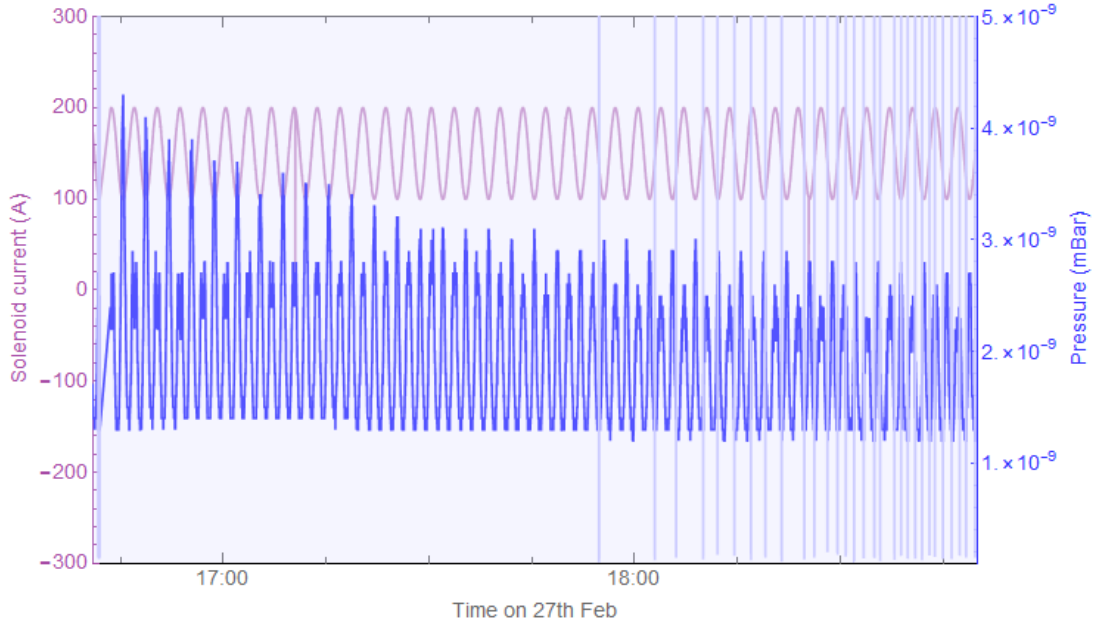

Figure 4.30: Vacuum pressure improvement over time with oscillating solenoid. The background is shaded purple when the RF is on.

These breakdowns cause a large spike in reflected power as a portion incoming RF pulse is reflected from the coupler which is now not matched. Some of the stored energy in the structure is lost to the breakdown arc, and some travels out of the coupler.

2. Breakdowns that occur as or after the forward RF pulse is switched off and the structure is emptying. These account for 30% of the total breakdowns. These breakdowns cause the reflected power to drop to zero faster than than the Q_0 of the structure would allow under normal operating conditions, as some of the stored energy has been lost in the breakdown arc.

Figure 4.31 shows an example of each of these two breakdown types. The reflected phase can be seen to vary as the cavity resonant frequency is altered by the arc. The reflected phase during the forward RF pulse is made up of the reflected power and the emitted power from the structure, and is less sensitive to the presence of an arc. The reflected phase after the end of the forward RF pulse is more sensitive to the presence of an arc as it is made up of only the emitted power. The phase change can also be seen in the phase measured at the klystron reverse coupler, indicating that some power makes it through the circulator, as well as the forward cavity and klystron couplers, indicating cross-talk between the forward and reverse signals.

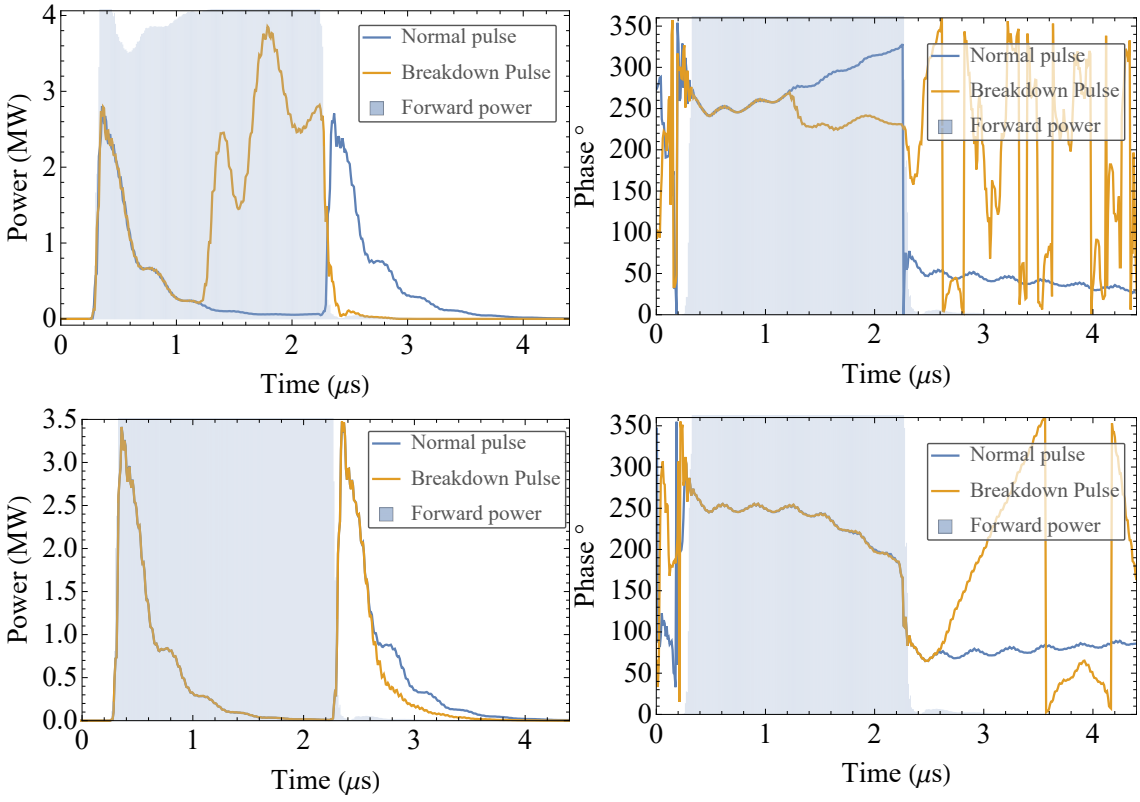

Figure 4.31: The reflected power and phase of a typical breakdown during the forward RF pulse (top) and after the end of the forward RF pulse (bottom). The forward RF pulse is shown shaded.

It was noted that many of the breakdowns occur close to the end of the forward RF pulse. As the cavity gradient is the highest at this point this is unsurprising, however many of the breakdowns seem to occur just after the end of the forward RF pulse. This is quantified in the two plots in Figure 4.32. Both plots show the time of the start of the breakdown from the end of the RF pulse, with positive values being after the pulse and negative values before the pulse. This was done to

enable comparisons with different pulse lengths in the region of interest: the end of the forward pulse. Figure 4.32a shows the time from the end of the pulse for each breakdown in chronological order. Figure 4.32b shows a histogram of the same data, with 100 ns bins. The bin immediately after the end of the forward power pulse has the most breakdowns. In both plots the colours represent the different forward pulse lengths.

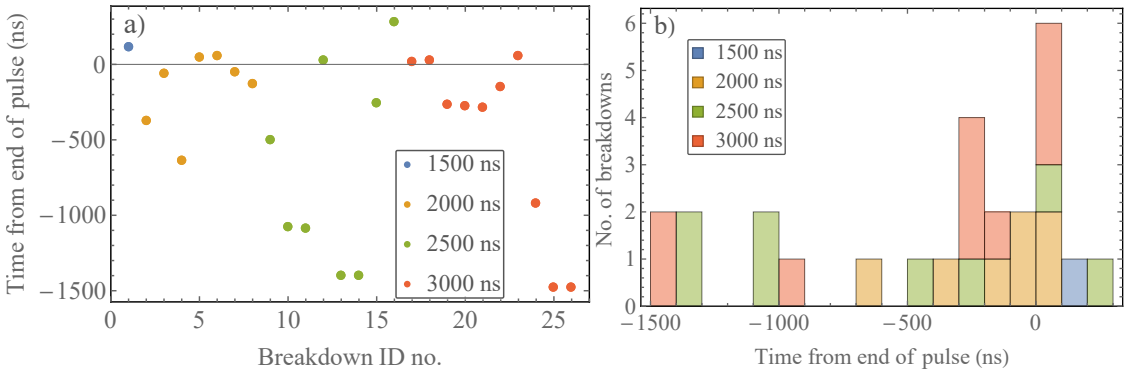

Figure 4.32: The time of the breakdown from the end of the forward RF pulse shown as a. Scatter plot in chronological order and b. Histogram with 100 ns bins. The legends in each plot give the forward power RF pulse length for each breakdown measured.

During the time immediately after the forward RF pulse ends there is similarly high gradient in the structure than the steady-state, or close to steady-state, driven structure during the last few 100 ns of the forward RF pulse. However the net active power flow in the structure is zero in steady state, but steps up as soon as the structure begins to empty after the end of the forward RF pulse. As the sample number is low it is not possible to make a definitive conclusion, however this could be evidence that active power flow is indeed a more important factor in the onset of breakdown than stored energy. The data during the 400 Hz photoinjector conditioning will increase the sample number to give a better confidence level.

Summary of beta test

The beta test was the first live test of NO-ARC to re-condition a photoinjector, and several unforeseen events occurred which NO-ARC was not able to process correctly. NO-ARC was subsequently updated to include improvements which alleviated these errors.

4.2.9 High repetition rate operation

The higher the repetition rate, the faster the cavity will condition. NO-ARC should monitor traces at the highest pulse repetition rate possible, and also should be able to switch off the high power RF before the next pulse in the event of a breakdown.

The I-tech [70] Libera system does not distribute the data for every measured RF pulse to the control system at repetition rates higher than 100 Hz, so this is the limit of the conditioning system, if we wish to be able to analyse every pulse for breakdown.

Following bench-marking tests, the I-tech Libera system was found to distribute each measured RF pulse signal trace individually, and not necessarily chronologically, and there was no method to guarantee which trace was associated with which RF pulse at high repetition rate (100 Hz). Improvements to the LLRF system were made to distribute all traces in the same numerical array, and in chronological order. With the upgraded system it is now possible to check the forward power

trace from the klystron, and disable breakdown checking if there is no forward power. Additionally, all measured pulse traces can be stored in a buffer, which is saved on detection of a breakdown, including traces after the breakdown. The breakdown can then be studied later if required, with good confidence that the traces are tagged and timestamped correctly and are chronological.

Bench-marking with the upgraded system has showed that breakdown detection can easily be operated at 100 Hz. However the disabling of the RF system after a breakdown is detected was successful for only 42% of breakdowns, with one (or very rarely two) extra pulses occurring before the RF is disabled. Of these, the extra pulses have a second breakdown in 11% of cases, leading to an overall increase in breakdowns of 4.64%. The program is currently run on a computer in the CLARA control room and relies on the CLARA network to send commands, and it is the network latency sending the signal to the LLRF system

Operational options to deal with this issue are:

a. Condition at a lower repetition rate. This will increase the overall time needed to condition.

b. Condition at 100 Hz, and accept a breakdown rate approximately 4.64% higher than it would be otherwise. Assuming the percentage of follow up breakdowns stays the same.

c. Move the software to hardware local to the Libera system. This is a longer term solution that requires more investigation.

4.3 Conditioning of 400 Hz photoinjector

4.3.1 Overview

The 400 Hz photoinjector is on the VELA beamline, and had previously seen less than 500 kW of forward power during benchmarking tests.

Conditioning of the photoinjector has been delayed since its installation on the VELA beam line in 2016 mainly due to operational constraints. The conditioning is estimated to take three months at 100 Hz with 24 hour operation, and as the VELA and CLARA gun positions share an RF source, conditioning cannot run concurrently with CLARA beam operation. Conditioning must therefore compete for time in the CLARA operational and shutdown schedule. Problems with breakdown in the SF_6 filled waveguide and switch have also meant that up-time for the system was limited.

Additionally, as can be seen in Figure 2.31, 10 MW from the klystron, leading to approximately 7 MW at the input of the structure, will not be sufficient to reach 120 MV/m. Replacement with a 20 MW klystron is planned for 2022.

In December 2018, conditioning of the 400 Hz photoinjector began. Conditioning was performed overnight and on weekends, when the CLARA beam line was not in use. It was found that at the start of each period of conditioning, the power reached at the end of the previous period could not be maintained without an increase in breakdown rate. The power was therefore re-started at a LLRF set-point estimated to give approximately 200 kW lower power. Additionally, if the klystron was not in use immediately preceding the conditioning period, it would take up approximately 40000 pulses to warm up, during which time the gain was lower than when warm, and the output power was therefore lower for a given LLRF input.

For reference, the peak electric field (which is also the gradient), peak magnetic field, and peak modified Poynting vector are plotted against input power at the structure for a range of pulse

lengths in Figure 4.33. The modified Poynting vector is calculated only for steady state operation where it consists only of the reactive power flow, and may be larger when there is active power flow during filling or emptying.

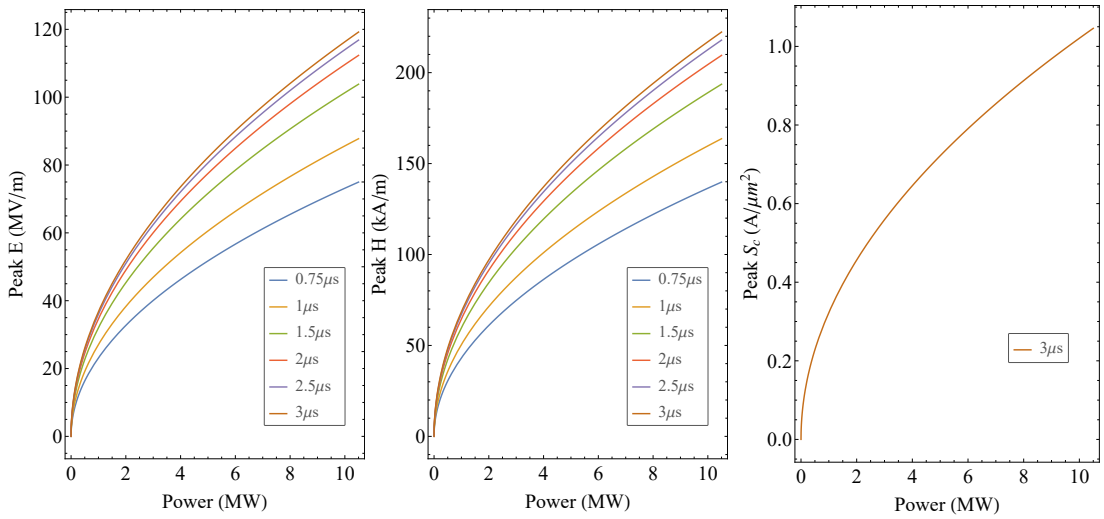

Figure 4.33: Peak E, H and S_c plotted against cavity input power for a range of input pulse lengths.

4.3.2 Conditioning progress

Conditioning began with a 750 ns pulse length from the klystron, and the power rose steadily over 64 million pulses to 2.65 MW. NO-ARC had an allowed breakdown rate of 5×10^{-5} breakdowns per pulse per metre of structure length.

Figure 4.34 shows the cavity gradient E_0 along with the cumulative number of breakdowns plotted against pulse number. For a pulse length of 750 ns the cavity is filled to 61.4% of maximum. Breakdown events can be seen where E_s briefly drops to 0.

Only a portion of the conditioning data is shown as an example of the behaviour, as for some of the conditioning period there was an error in the data saving. The data is saved in binary format due to the high memory efficiency; when parsing the data it was found that one of the data types was saved as "NoneType", and it was unknown how to parse this. Due to the binary format, this left all the data after this point un-parseable. This was discovered and fixed part way through the conditioning process. Work is ongoing to recover the data. In Figure 4.34 it can be seen that whilst progress is being made, the gradient has a "sawtooth" shape. This is caused by the power (and therefore electric field) increasing rapidly, with low numbers of breakdowns. This is then followed by multiple breakdowns, which causes NO-ARC to lower the power multiple times. This behaviour has been seen previously by Degiovanni et al [55], and can be avoided by lowering the allowed breakdown rate, thus slowing the apparently too rapid rise in power.

Figure 4.35 shows the scaled gradient, E_s, derived from Equation 4.27 [55], where

$$E_s = \frac{E_0 \tau_p^{1/6}}{\mathrm{BDR}^{1/30}} \tag{4.27}$$

along with the cumulative number of breakdowns. Scaled gradient removes the pulse length and breakdown rate dependence from the achieved gradient allowing comparison to structures conditioned with other breakdown rates and pulse lengths. This will be useful in the future once

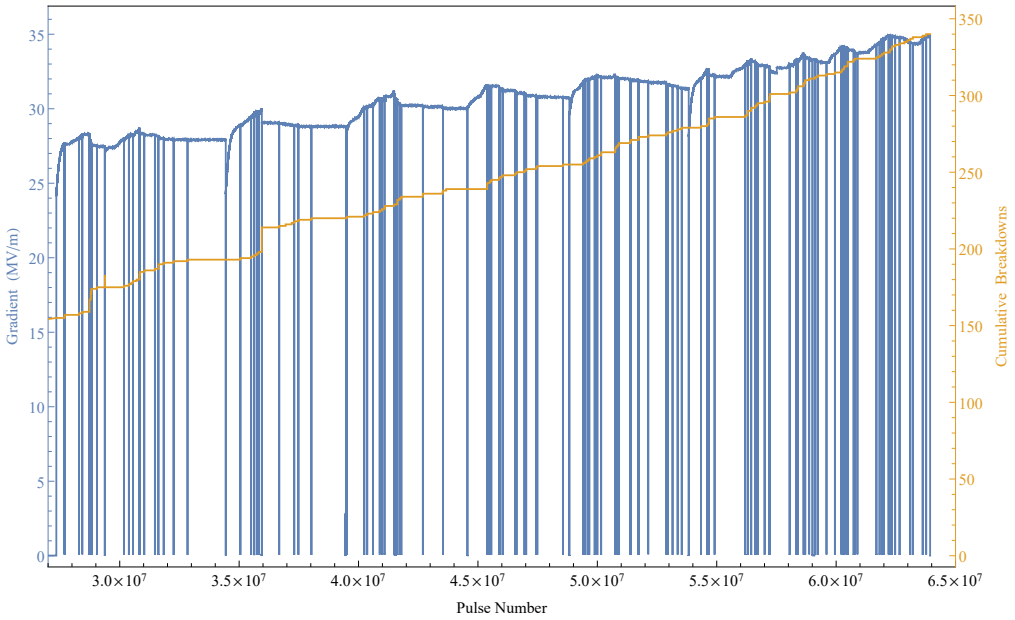

Figure 4.34: Gradient E_0 and cumulative breakdowns plotted against pulse number for a section of the conditioning run.

conditioning is complete for comparison to similar structures, or to compare conditioning with later re-conditioning of the same structure.

Figure 4.36 shows a portion of the of the conditioning process plotted against time to so that the start and end of each conditioning period can be seen . It is interesting to note that the rapid rises in power often occur at the start of a conditioning period.

Figure 4.37 shows the cavity vacuum activity along with the klystron output power. Again the power drops to zero when there is a breakdown. It can be seen that most, but not all of the breakdown events have an associated vacuum pressure spike.

The time period allocated for conditioning ended after conditioning up to klystron power 2.67 MW, E_0 (gradient) 39.24 MV/m, and E_s 5.57 MV/m. As mentioned in Section 4.2 the network delay between the LLRF system and the computer running NO-ARC is such that infrequently an extra pulse can occur between the breakdown pulse and disabling the RF. When this occurred, the extra pulse showed a breakdown in 8% of cases. This supports the finding, from high voltage DC measurements, that a breakdown causes new breakdown emission sites that substantially increase the probability of a second breakdown immediately after the first [75].

4.3.3 Low power multipactor

As described in 4.2.8, in some pulses the phase of the reflected power diverges by several hundred degrees, after the end of the forward pulse, and at low power. Gun-400 has a probe, and it can be seen that the probe phase diverges similarly, and the probe power measurement drops to zero at the same time. These effects can be seen in Figure 4.38.

The multipactor begins to affect the RF in a way that is visible in the RF signals at a probe power of approximately 550 W, corresponding to a gradient of 544 kV/m. It was only recorded in this one instance as the behaviour was identified as breakdown by NO-ARC. If there was a similar effect at higher powers it was not recorded as the breakdown detection was changed to prevent

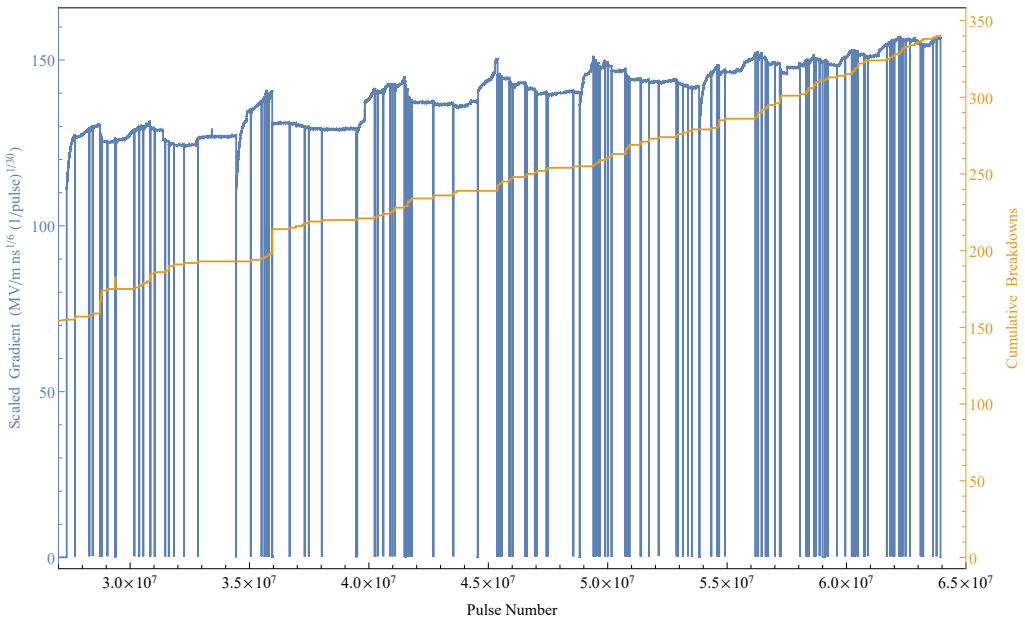

Figure 4.35: Scaled gradient E_s and cumulative breakdowns plotted against pulse number for a section of the conditioning run.

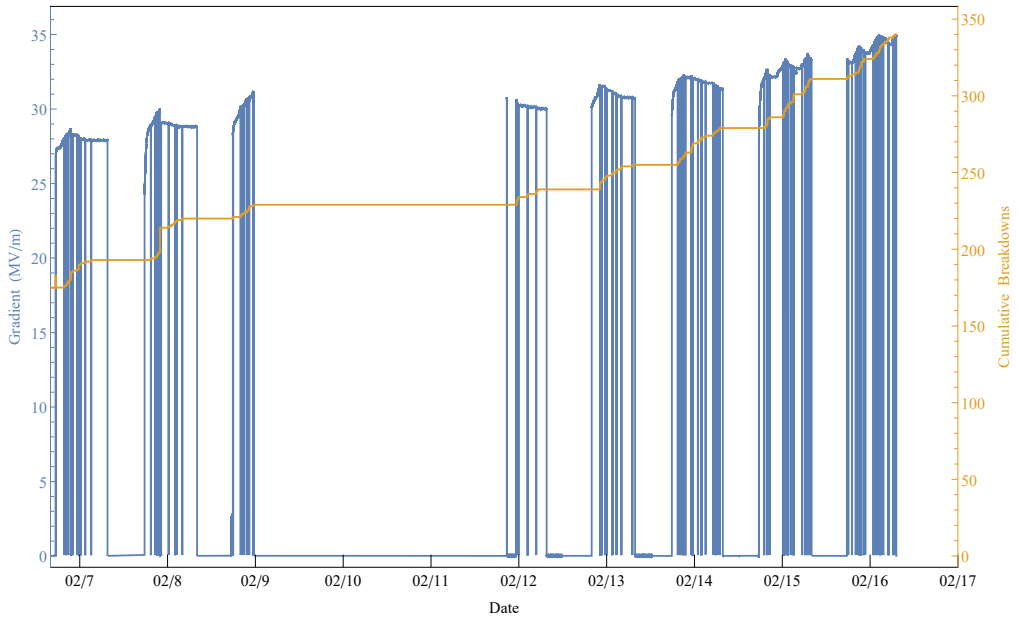

Figure 4.36: Gradient E_0 and cumulative breakdowns plotted against date for a section of the conditioning run.

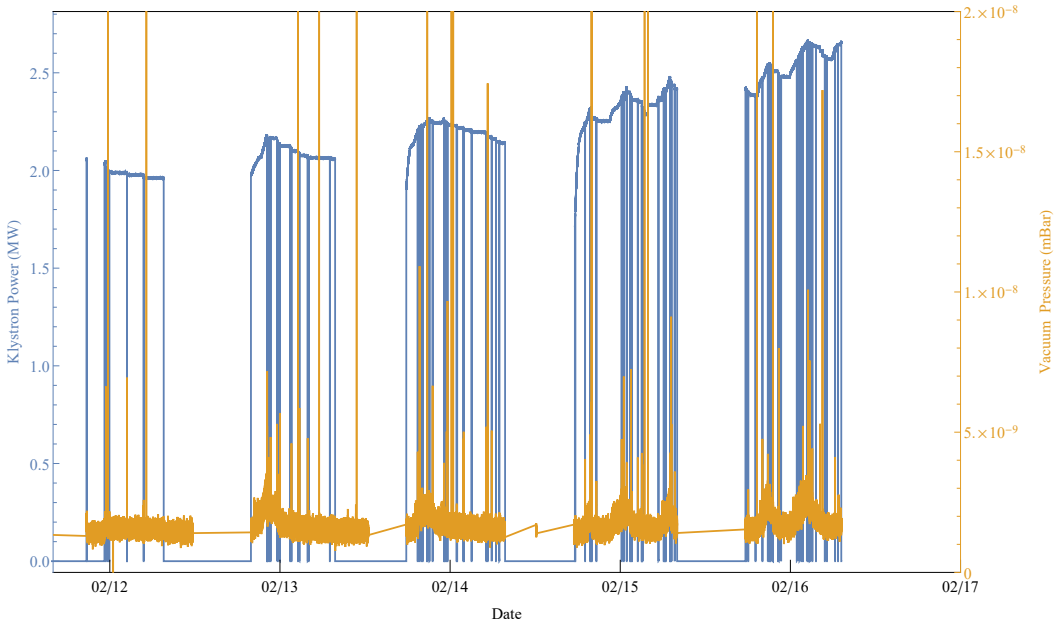

Figure 4.37: Klystron output power and vacuum level plotted against date for a section of the conditioning run.

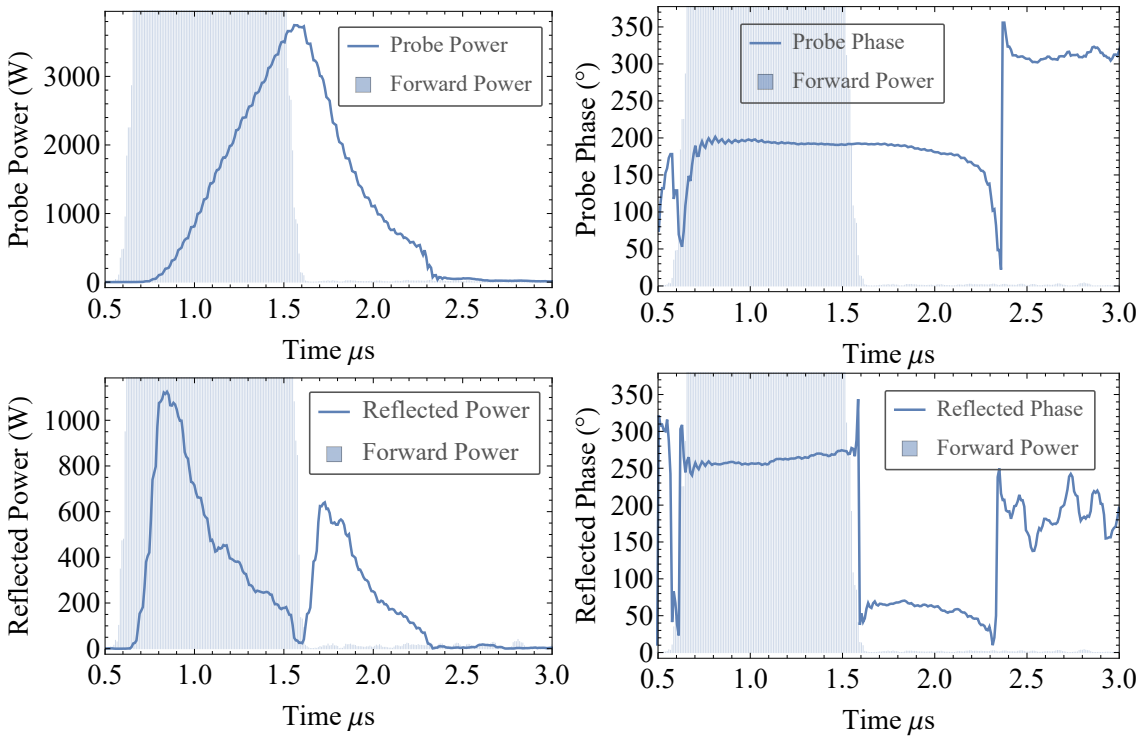

Figure 4.38: Probe power and phase and reverse power and phase showing deviation

false-positives. Again, this effect is attributed to multipactor, possibly seeded by field emission earlier in the pulse at higher field strengths.

A SPARK3D [38] simulation, started with 1000 electrons, shows multipactor between 532 and 547 kV/m. Figure 4.39 shows the electron number versus time for this range of photoinjector gradients. It can be concluded that multipactor does occur at this gradient. Figure 4.40 shows the location of the multipactor, it is in the cathode plug region.

The cavity gradient is within the multipactor band for 4 ns as the cavity fills and 33 ns as the cavity empties.

Taking the mean exponential growth rate of 4.57, the number of electrons from each seed electron can be calculated. As the cavity fills each seed electron would give rise to 6 electrons during the time in the multipactor band. This makes multipactor here unlikely, as does the fact that there would be fewer seed electrons. As the cavity empties each seed electron would give rise to 3.5×10^6 electrons.

The average impact energy from SPARK3D in the region of multipactor is 40 eV. The current required to dissipate the 550 W that can be seen to be lost in Figure 4.38 at that impact energy is 13.75 A. Assuming the current scales linearly with the increase in the number of electrons, the seed current can be estimated. For the multipactor band as the cavity empties, the current required to seed the multipactor is estimated to be 3.88 μA to reach 13.37 A after 33 ns.

For a rough order of magnitude comparison, the field emission current measured after the structure measured from the 10 Hz photoinjector is of the order of 1 mA for a 70 MV/m gradient. Scaling the current quadratically with gradient, at 1.5 MV/m a current of 0.5 μA would be expected. The seed current estimate is perhaps therefore a little higher than might be expected in the cathode plug region, but this region is close to the highest surface electric field regions in the cavity, as can be seen in Figure 4.7, and as the structure is not fully conditioned the field emission levels may be higher. Further simulations are required to discover if electrons from the cathode and surrounding high field regions can have trajectories that impact the multipactor region.

This need for seeding answers both of the questions raised in Section 4.2.8: why the low power multipactor is only seen as the cavity empties, and why it is not seen as the cavity empties for every forward power.

4.3.4 Probe measurement anomaly

A further point of interest that was seen in the saved breakdown pulses was the appearance of a deviation from the expected pulse shape of the probe amplitude signal. These took the form of "bumps" that show an increase in the probe signal. These signals with deviations persisted over minutes to hours during conditioning, hundreds of thousands of pulses. Examples of these signals can be seen in Figure 4.41, where the the first signal shown is the expected shape, and all others are deviations. The fifth plot shown appears to have two separate bumps. It can be seen in the plots that all the deviations occur within a small range of cavity gradients, between 16.6 MV/m and 19.4 MV/m, shown in purple.

This, as well as the fact that the signal eventually returned back to the expected shape, sometimes even decreasing to do so, has lead to the hypothesis that the increase in signal seen is not actually an increase in voltage, but rather an effect of electron bombardment of the probe in the second cell of the photoinjector cavity, possibly due to multipactor. It would be interesting during future operation of the photoinjector to return to this gradient and see if the effect persists, if it

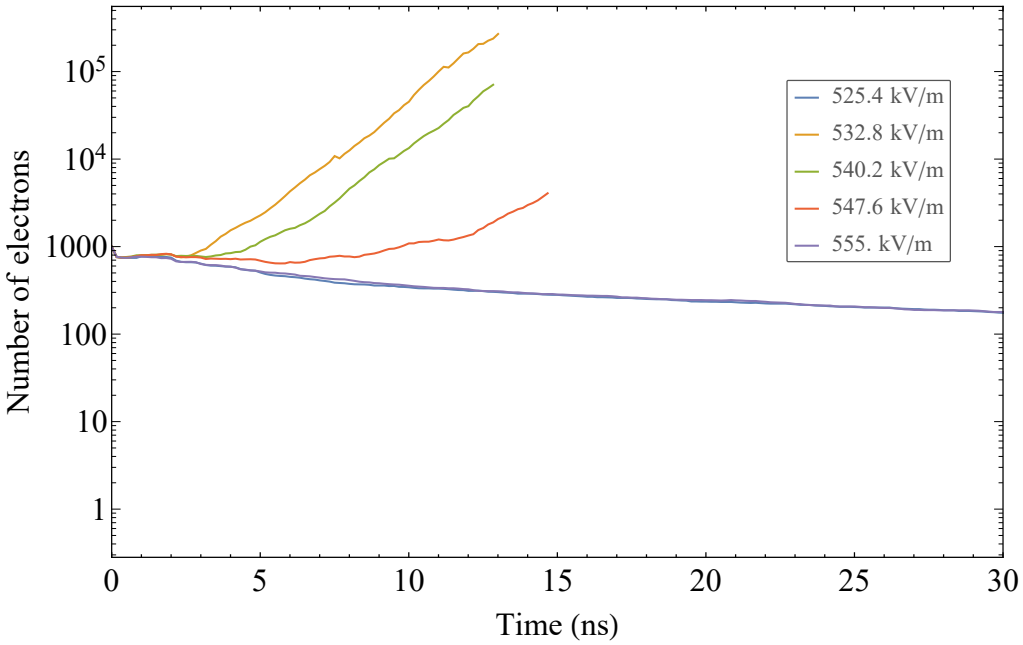

Figure 4.39: Electron number versus time for a range of photoinjector gradients. A multipactor band is seen that includes the gradient where the phase divergence was recorded.

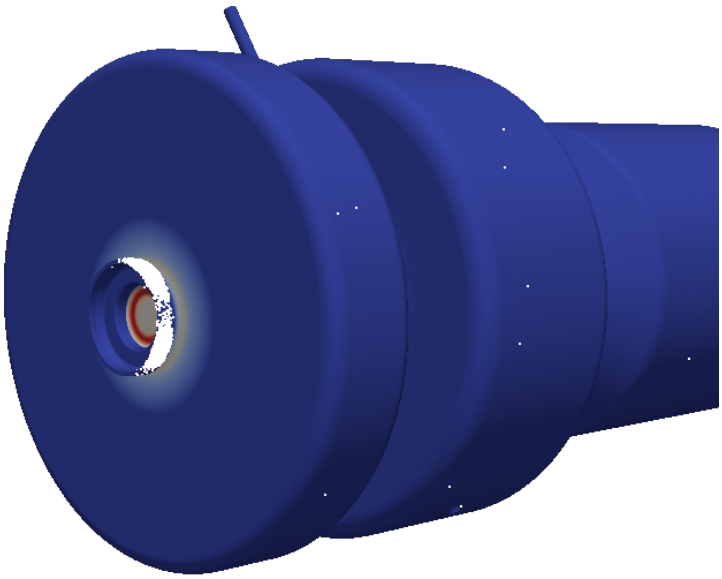

Figure 4.40: Final position of multipacting electrons in the gradient range 532.8 to 547.6 kV/m.

does not then that will be evidence this is a soft multipactor band. If this effect is seen again the solenoid could be used to disrupt the electron trajectories to give further evidence for multipactor.

A SPARK3D [38] simulation, started with 1000 electrons shows multipactor in this range of photoinjector gradients. Figure 4.42 shows the electron number versus time for a range of photoinjector gradients around 2.32 MV/m. It can be concluded that multipactor does occur at this power. Figure 4.43 shows the final positions of the multipacting electrons in this gradient range. The band is at the equator of the second cell, at the longitudinal position of the probe. Electrons can be clearly seen in the probe region, which gives credence to the theory that the signal anomaly

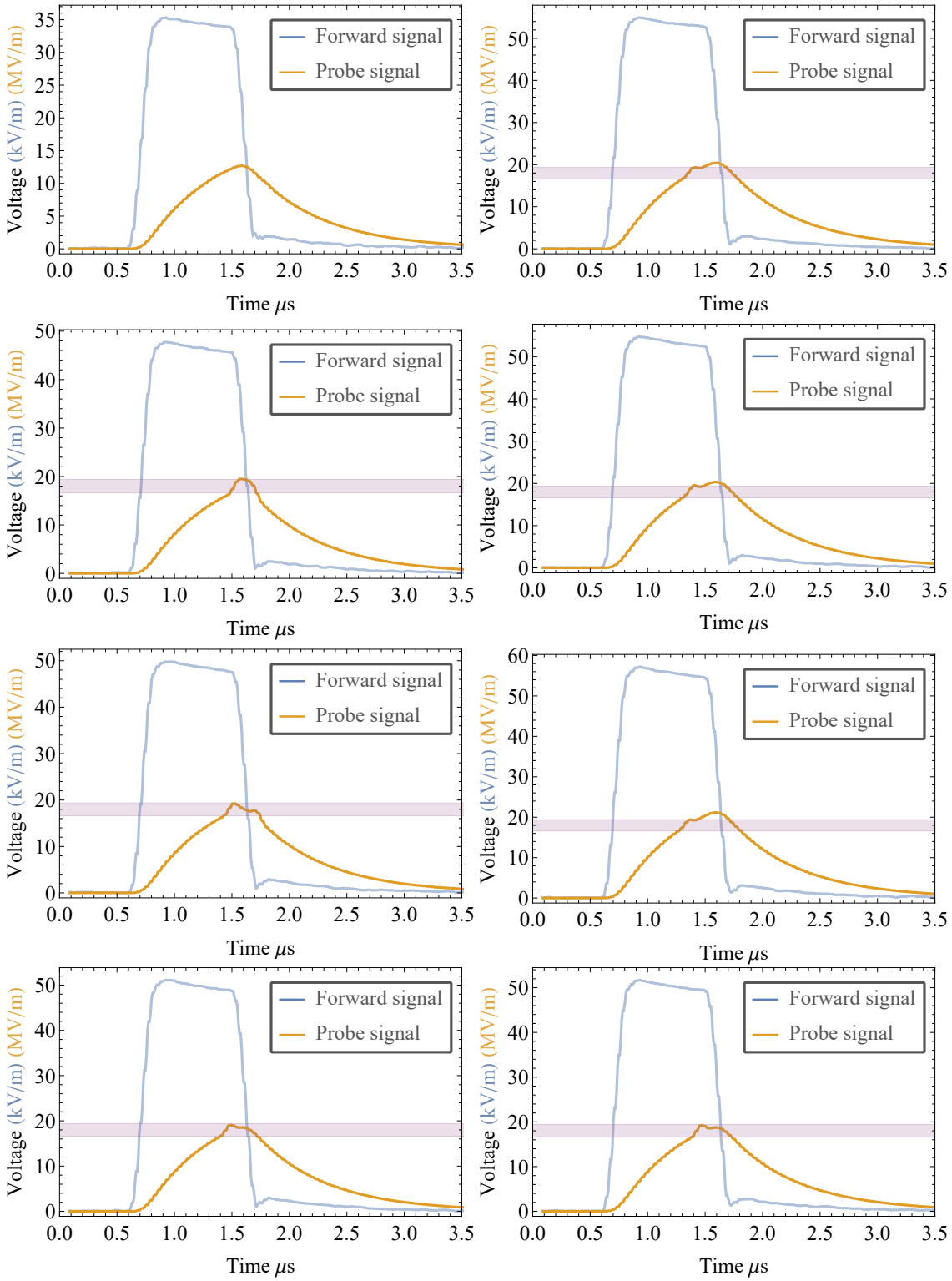

Figure 4.41: Cavity voltage measured at the probe in MV/m (orange) and forward waveguide voltage measured before the cavity in kV/m (blue).

is electrons hitting the probe.

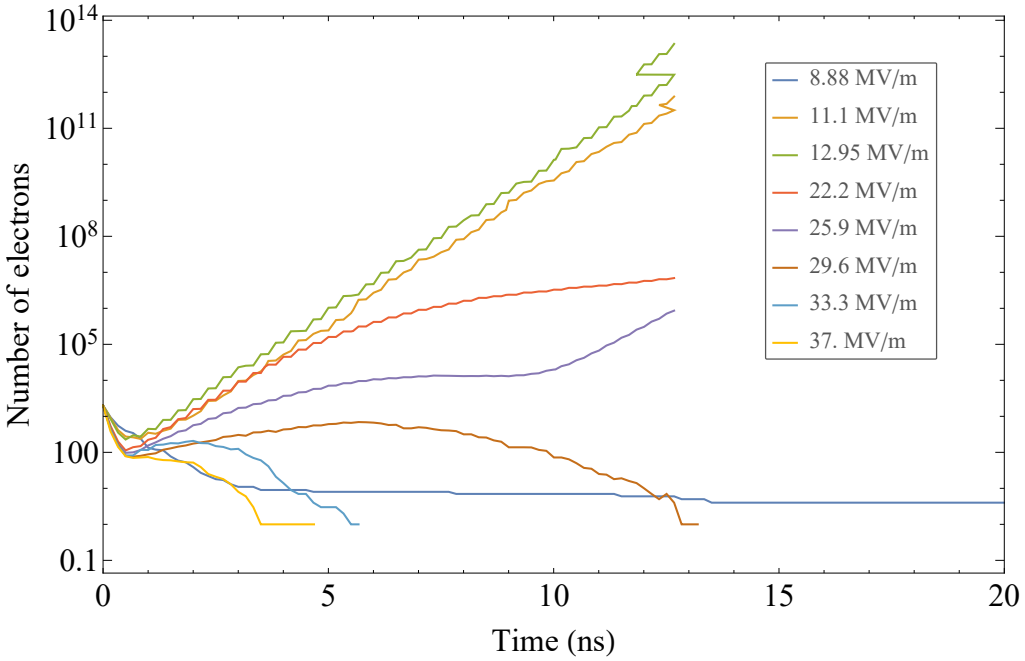

Figure 4.42: Electron number versus time for a range of photoinjector gradients. A multipactor band is seen that includes the gradient range where the probe measurement anomaly was seen.

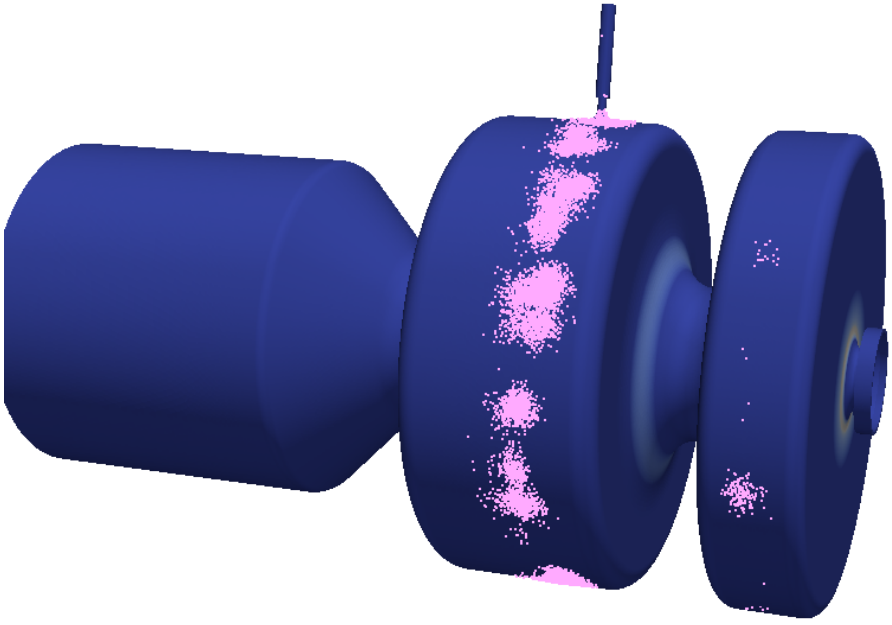

Figure 4.43: Final position of multipacting electrons in the gradient range 11.1 to 22.2 MV/m. Electrons can be seen in the probe region.

4.4 Further work

The conditioning will be re-started in spring 2022, with 6 months set aside to condition for 24 hours a day. This should remove some of the issues around re-starting the script and warming up the klystron, as well as making trends like sawtoothing easier to spot.

Some upgrades to NO-ARC are being considered. Firstly to save data as HTF5 to maintain the

memory efficiency advantage of binary whilst allowing metadata saving and data slicing. Secondly to increase the repetition rate NO-ARC can operate at. This might entail moving a portion of the program, the breakdown detection module, to run directly on the pulse measurement hardware. This would mean the network latency was no longer a factor in the time to switch off the RF after a breakdown.

Chapter 5

Analytical model of dispersion in travelling wave linacs

5.1 Introduction

Normal conducting linac technology is used worldwide to accelerate particles such as electrons to high energies whilst avoiding energy loss through synchrotron radiation. The technology is under consideration for future accelerator projects such as CLIC [79] and CompactLight [80], and the proposed UK hard X-ray FEL user facility [81]. It is important therefore to develop robust but efficient tools to validate designs. An RF pulse propagating through a travelling wave RF structure can be seen to distort due to dispersion. Each frequency of the bandwidth of the input RF pulse travels with a different phase velocity in the structure. These frequencies superimpose to distort the pulse envelope.

This effect is of particular interest in two cases. First for accelerators with a multi-bunch scheme in which each pulse is used to accelerate a train of particle bunches; each bunch must be accelerated with the same energy, and knowledge of the pulse distortion is therefore vital. The second case is that of lower group velocity structures, ie. short structures with higher losses. The low group velocity has the effect of decreasing the relative frequency bandwidth, and thus increasing the effect of dispersion. High phase advance structures have been studied for a number of facilities [82, 83] as the high phase advance allows a lower group velocity, and it has been shown that the power absorbed during an RF breakdown in the cavity is proportional to the square of the fundamental mode group velocity [84].

Calculation of the dispersion in a travelling wave linac has been previously carried out by Jones et al. [85]. They use two methods to calculate the frequency response of travelling wave linacs, which can then be convolved with the forward pulse. One method is to use and solve an equivalent circuit, and the other method uses a mode-matching code. For both methods 3D modelling of infinite periodic fiducial cells is used to establish the model inputs: the dispersion curve and loss characteristics.

The calculation described below requires no geometric model of the cavity. The inputs required are the group velocity as a function of cavity cell number and the phase advance per cell to calculate the dispersion, and the unloaded quality factor Q_0 as a function of cell number to calculate the attenuation. From these the complex wavenumber is calculated, and it is this which is used, in the frequency domain, to calculate the propagated pulse shape.

Once the pulse shape in each cell is known, the field in each cell can be calculated as a function of time, as well as the energy gain of a particle travelling through the cavity as a function of time. The filling time of the cavity can then be calculated, as well as the injection time for maximal energy or minimal timing jitter.

In this chapter, the derivation of the model and the formulas to calculate the envelope distortion is shown. The first linac of the CLARA accelerator [86], a 2 m S-band travelling wave linac is used as an example, and the complex wavenumber is calculated for this structure. A measured RF input pulse from the CLARA linac is used to demonstrate the envelope distortion, and the modelled distortion compared to measurements from CLARA operation. A method of pulse shaping to decrease the dispersion effect is shown in both model and experiment. The electron beam energy gain from the structure at different times during cavity filling and emptying is modelled for a variety of pulse shapes, and the modelled beam momentum compared to experiment with the CLARA electron beam. Good agreement is shown with the model. It is shown that beam loading can be included in the model using the analytical solutions derived by Lunin et al. [87]. In Section 5.11 the limits of the model are tested by modelling the TULIP structure [88, 89]. The model is shown to accurately predict the pulse shape evolution in a backwards travelling wave structure with negative dispersion and which does not accept the full 3 dB bandwidth of the RF pulse.

5.2 Derivation of the complex wavenumber

To begin we calculate the complex wavenumber $k = \beta - i\alpha$ as a function of z, longitudinal position in the cavity and ω, the angular frequency. Here β is the propagation constant and α the attenuation constant. As the dispersion curve is sinusoidal, we posit that any angular frequency $\omega(\beta, z)$ within the cavity bandwidth can be approximated for small angles at fixed z by

$$\omega(\beta) = a\cos(\beta(z)c_L) + b \tag{5.1}$$

evaluating at $\beta(z)c_L = \pi/2$ and $\beta(z)c_L = \pi$ to find a and b we find that

$$\omega(\beta, z) = \omega_{\pi/2}(z) - \Delta\omega(z)\cos(\beta(z)c_L) \tag{5.2}$$

where c_L is the cell length, $\omega_{\pi/2}$ is the angular frequency of the $\pi/2$ mode and $\Delta\omega$ is the difference between the angular frequency of the π-mode ω_π and that of the $\pi/2$-mode $\omega_{\pi/2}$.

It follows that

$$\frac{d\omega}{d\beta} = \Delta\omega(z)c_L\sin(\beta(z)c_L) \tag{5.3}$$

which is the group velocity. At the operating frequency ω_0, the group velocity of the structure $v_{g0}(z)$ as a function of longitudinal position, and the phase advance per cell which is constant along the structure, are known. Take for example a phase advance of $2\pi/3$, we can write

$$\frac{d\omega_0}{d\beta_0} = \Delta\omega(z)c_L\sin(2\pi/3) = v_{g0}(z) \tag{5.4}$$

Rearranging for $\Delta\omega$:

$$\Delta\omega(z) = \frac{v_{g0}(z)}{c_L\sin(\frac{2\pi}{3})} \tag{5.5}$$

Inserting Equation 5.5 into Equation 5.2 and rearranging yields the frequency of the $\pi/2$ mode in

every cell based only on the operating frequency and phase advance of the structure and the group velocity for each cell:

$$\omega_{\pi/2}(z) = \omega_0 + \frac{v_{g0}(z)}{c_L \tan(\frac{2\pi}{3})} \tag{5.6}$$

Inserting Equations 5.5 and 5.6 into Equation 5.2 yields the real part of the longitudinal wavenumber at any frequency in any cell:

$$\beta(\omega, z) = \frac{1}{c_L} \arccos\left(\frac{\omega_{\pi/2}(z) - \omega}{\Delta\omega(z)}\right) \tag{5.7}$$

where $\omega_{\pi/2}$ and $\Delta\omega$ are known from Equations 5.6 and 5.5 respectively.

The attenuation constant α can be calculated simply from

$$\alpha(z) = -\frac{dP(z)/dz}{2P(z)} = \frac{\omega}{2v_g(z)Q_0(z)} \tag{5.8}$$

where $P(z)$ is the propagating power as a function of longitudinal position, and Q_0 is the unloaded quality factor. In backwards travelling wave structures v_g is negative and therefore so is α, leading to increasing power along the structure in z as the power flow is in the opposite direction.

5.3 Calculating envelope distortion

For a given input RF pulse $A(z,t)$ travelling through a dispersive medium the pulse can be described in the frequency domain as it travels in both time (t) and longitudinal space (z) as

$$A(z,t) = \int_{-\infty}^{\infty} \hat{A}(\omega) e^{i(\omega t - k(\omega)z)} d\omega \tag{5.9}$$

To find $k(\omega)z$ at any point along z we can integrate $k(z,\omega)$ up to that point. Equation 5.9 becomes

$$A(z,t) = \int_{-\infty}^{\infty} \hat{A}(\omega) \exp\left(i\left(\omega t - \int_0^z k(z',\omega)dz'\right)\right) d\omega \tag{5.10}$$

The complex wavenumber $k = \beta - i\alpha$ can now be used to calculate the envelope distortion at any point along the structure.

5.4 RF envelope evolution in the CLARA linac

The first linac on CLARA is a 2 m 61 cell S-band travelling wave structure operating at a gradient of up to 22 MV/m. It operates with a phase advance of $2\pi/3$. The group velocity $v_g(z)$ and $Q_0(z)$ of the first CLARA linac are known from the design. The group velocity varies from 1.88 to 0.85% of the speed of light, and the Q_0 varies from 12090 to 12039, longitudinally along the structure.

The cell length c_L is 33.32 mm and the operating frequency is 2998.5 MHz. From this information and Equations 5.7 and 5.8, $k(z,\omega)$ can be calculated. A piecewise equation was used to make the attenuation dominant outside the cavity bandwidth:

$$k(\omega, z) = \begin{cases} -iN & \omega < \omega_{\pi/2} - \Delta\omega \\ \beta - i\alpha & \omega_{\pi/2} + \Delta\omega \geq \omega \geq \omega_{\pi/2} - \Delta\omega \\ -iN & \omega > \omega_{\pi/2} + \Delta\omega \end{cases} \tag{5.11}$$

where N is an arbitrarily large number. The dispersion in the structure as shown by the propagation constant as a function of ω, for different longitudinal positions along the structure can be seen in Figure 5.1. The attenuation at the operating frequency as a function of longitudinal position along the structure can be seen in Figure 5.2.

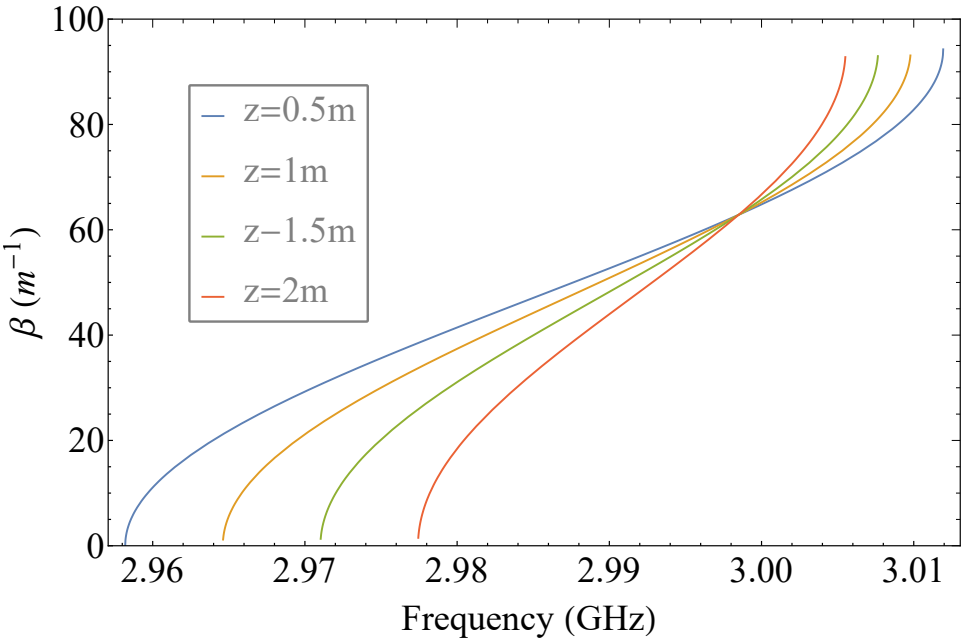

Figure 5.1: Propagation constant (β) as a function of angular frequency (ω), for different longitudinal positions along the structure (z)

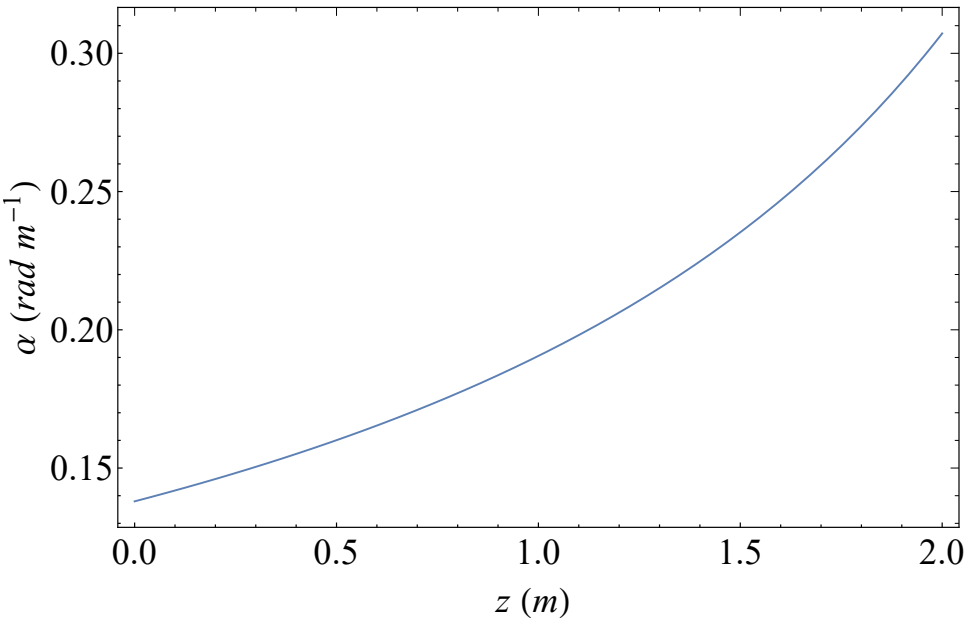

Figure 5.2: Attenuation (α) as a function of longitudinal position along the structure (z) at the operating frequency

The next step is to calculate the integral of k with respect to z, for all ω, $\int_0^z k(z,\omega)dz$. The integrated β as a function of angular frequency up to different longitudinal positions along the structure is shown in Figure 5.3, and the integrated α as a function of z is shown in Figure 5.4.

An example input pulse measured at a waveguide directional coupler before the cavity coupler

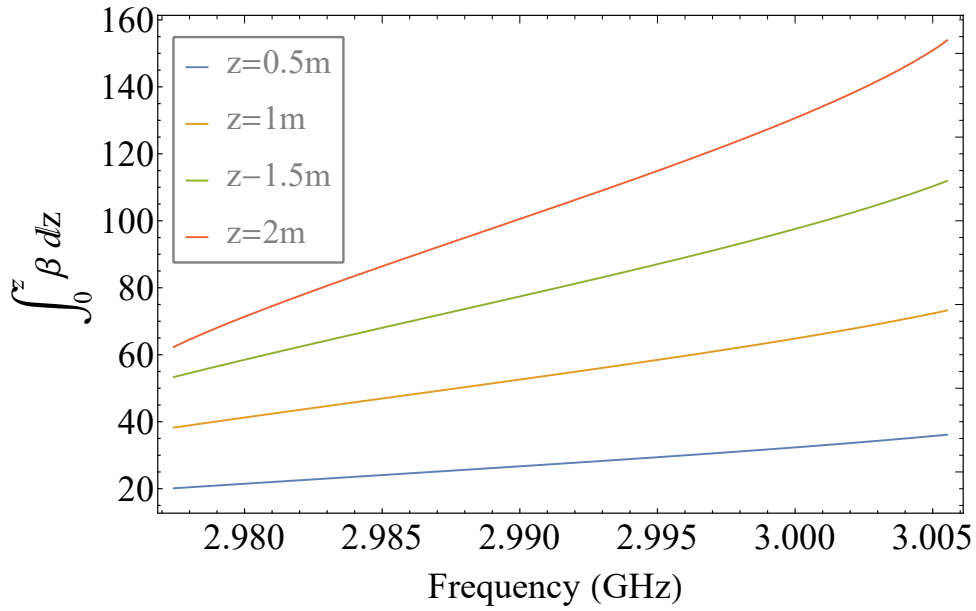

Figure 5.3: Integrated propagation constant (β) as a function of angular frequency (ω), up to different longitudinal positions along the structure (z)

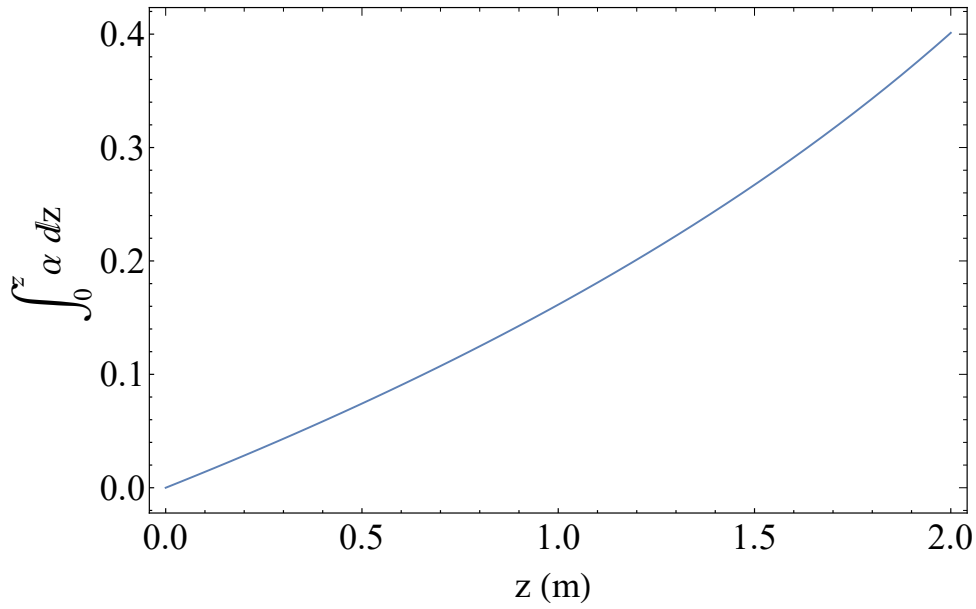

Figure 5.4: Integrated attenuation (α) up to longitudinal position along the structure (z)

is shown in Figure 5.5. The complex envelope is extracted, and then a Discrete Fourier Transform (DFT) performed on the pulse data. In the frequency domain, the pulse is multiplied by $\exp\left(i\int_0^L k(z,\omega)dz\right)$ where L is the longitudinal position at which to calculate the distortion. The evolution of the example pulse in the frequency domain is shown in Figure 5.6, at positions in the cavity and after it.

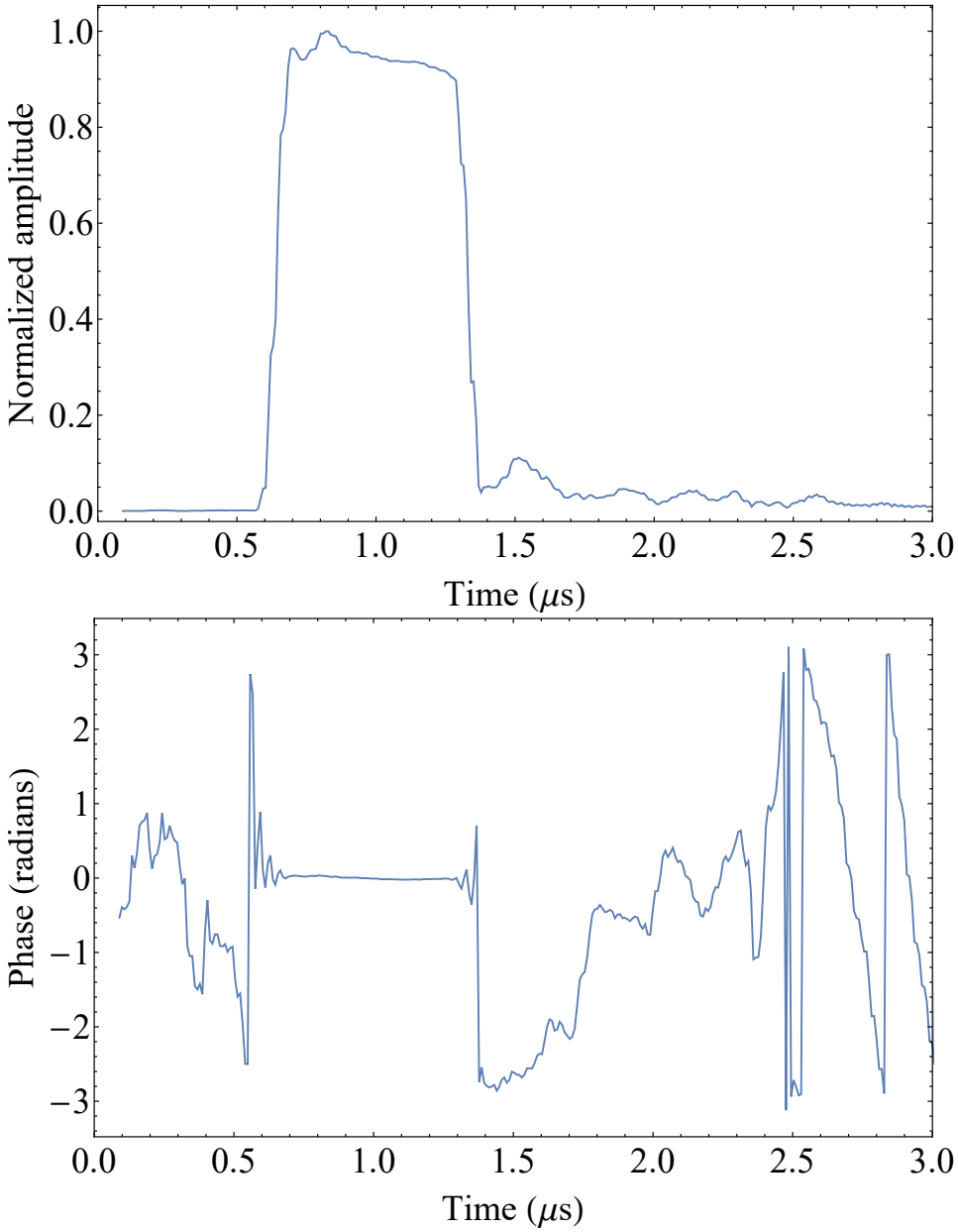

Figure 5.5: Measured amplitude (top) and phase (bottom) of example CLARA linac input pulse

An inverse DFT can be applied to recover the time domain pulses. Figure 5.7 shows the same pulse at the same locations in the time domain. The pulses decrease in amplitude along the cavity due to the attenuation, and the envelope is distorted due to the dispersion.

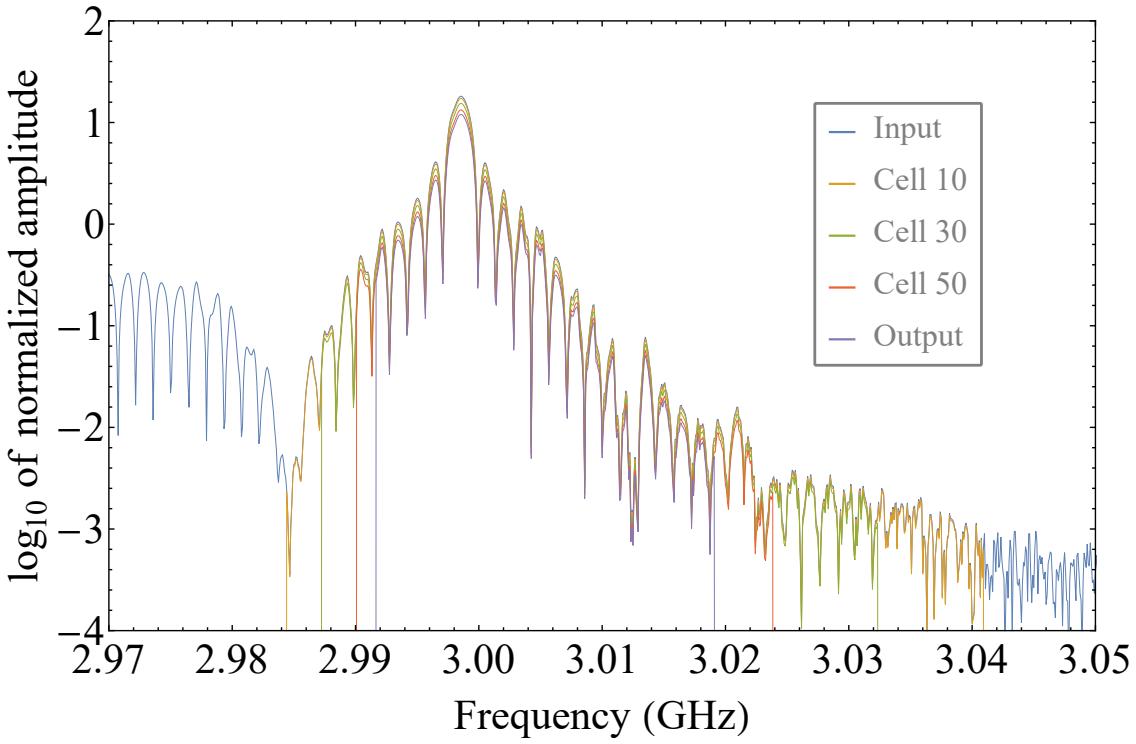

Figure 5.6: $\log_{10}$ of measured amplitude of the input pulse, and calculated pulse in cell 10, cell 30 and cell 50, and pulse at the output in frequency domain.

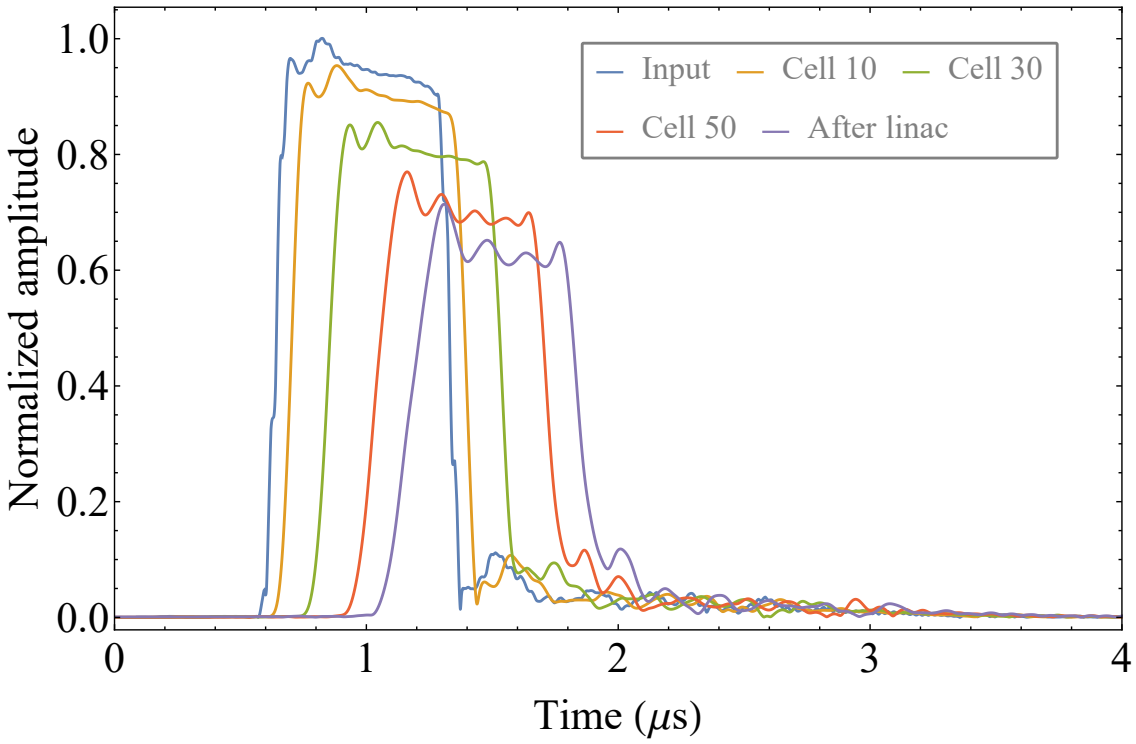

Figure 5.7: Input RF pulse and calculated envelope distortion of the RF pulse in cell 10, cell 30 and cell 50, and at the output.

5.5 Envelope distortion comparison to experiment

The CLARA linac has an RF probe in the 58th cell, as well as on each of two loads after the structure. Thus we can compare the modelled signal immediately after the last cell, and that in the 58th cell, to experimental data. The accuracy of the RF measurement calibration is estimated to be approximately 10-15%, therefore in the figures below, the amplitude of the experimental data has been linearly scaled to match the modelled result to allow better comparison. Figure 5.8 shows the pulse measured at the load after the output coupler, it is a very good match in both time and amplitude, this shows that the envelope distortion of the pulse as it travels down the cavity is well modelled.

Figure 5.9 shows the probe signal comparison. The temporal oscillation superimposed on the pulse is a very good match in time, but the amplitude of the oscillation on the measured pulse is larger. The amplitude of the oscillation is also larger than that seen after the cavity, implying it is more than simple dispersion causing the oscillations. An additional reactance in the measurement circuit could explain the discrepancy, or there may be a mismatch at the cavity output coupler (as it is only matched for the operating frequency), leading to reflections back down the cavity, and possibly a standing wave.

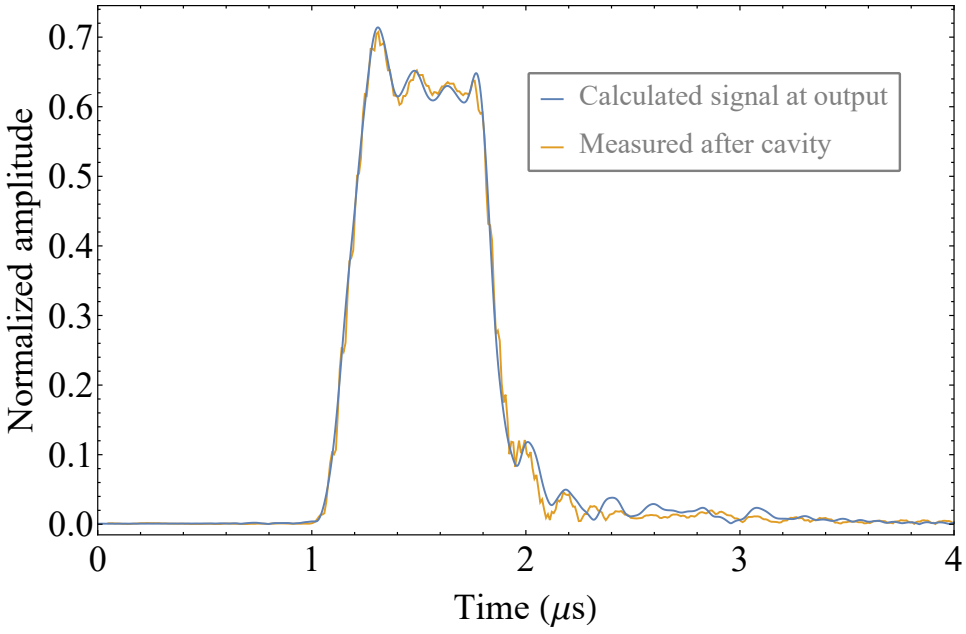

Figure 5.8: Calculated pulse after the cavity compared to measured signal.

5.6 Pulse shaping to decrease dispersion

The dispersion seen in the cavity is dependent on the frequency spectrum of the incoming RF pulse. Removing the sharp corner from the pulse front reduces the size of the side lobes and therefore the dispersion. A shaped pulse with a 200 ns ramp and 500 ns flat top is shown in Figure 5.10 and its shape in the frequency domain is shown, compared to that of the original 700 ns flat top pulse, in Figure 5.11. For the new pulse the simulated pulse shape is compared to the measured pulse at the probe in Figure 5.12. There is good agreement, and the dispersion is greatly reduced. More generally it can be calculated from the model that the amplitude of the time domain oscillations

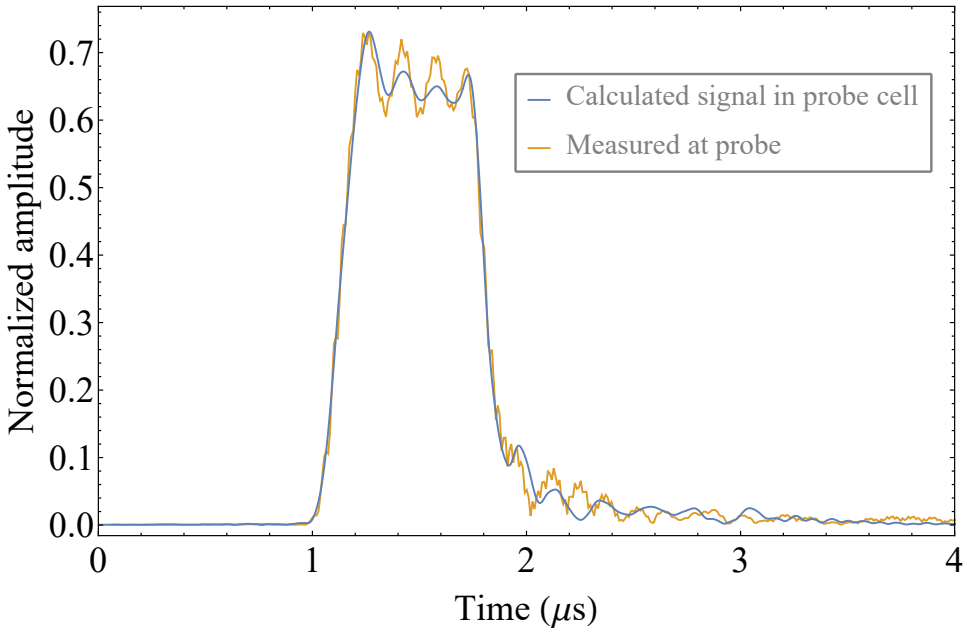

Figure 5.9: Calculated pulse at the probe compared to probe signal.

superimposed on the pulse envelope decreases by 35% for every 100 ns of linear ramp added to the forward pulse shape.

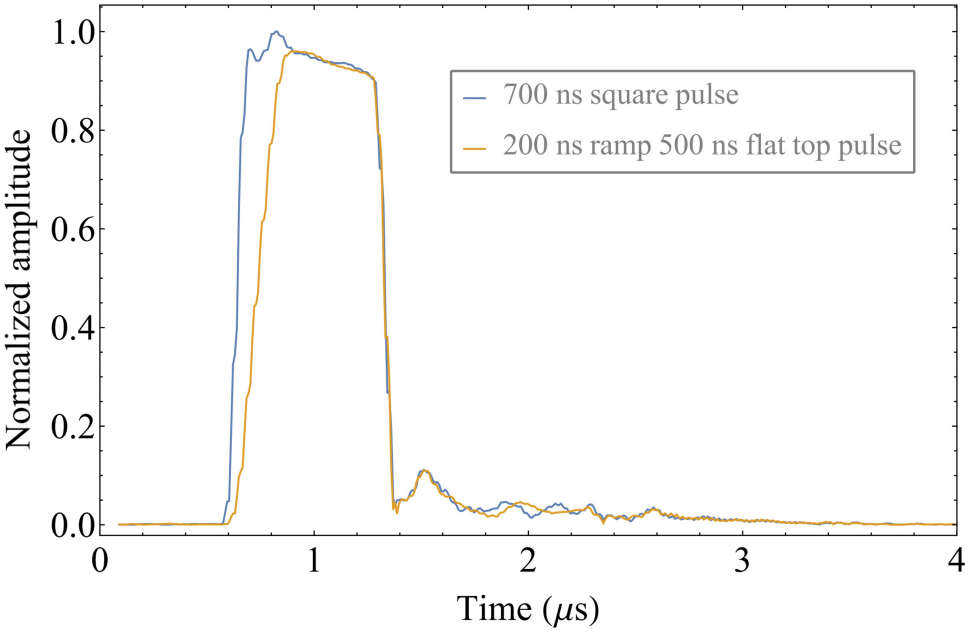

Figure 5.10: 700 ns square pulse compared with shaped pulse for dispersion reduction with 200 ns ramp and 500 ns flat top

5.7 Beam momentum gain prediction

To calculate the momentum gain of the beam we must consider that the beam must be synchronous with the RF in time: the field should be calculated in each cell at a different time due to the finite

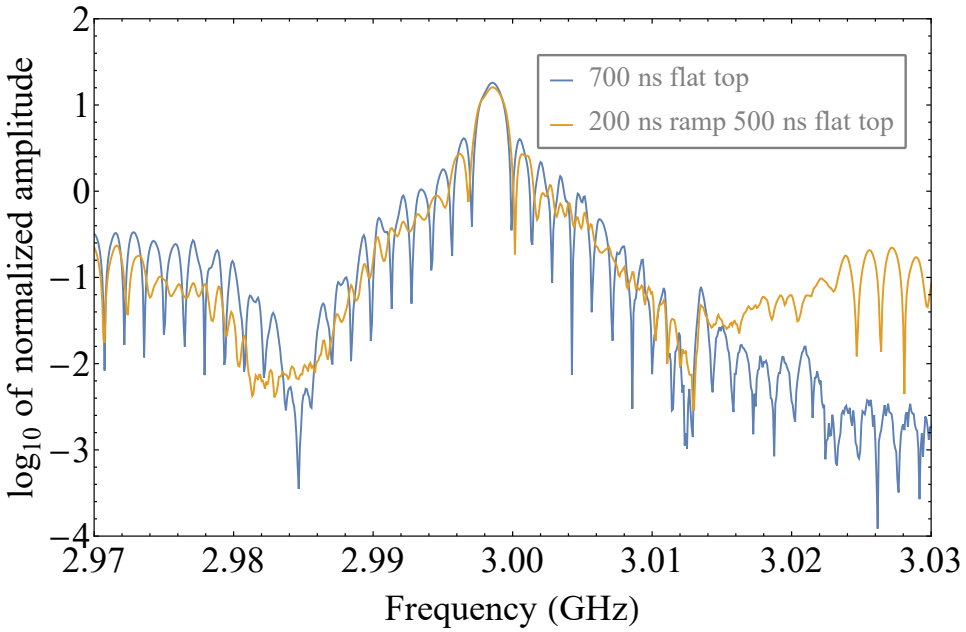

Figure 5.11: Frequency domain comparison of shaped pulse for dispersion reduction and original flat topped pulse.

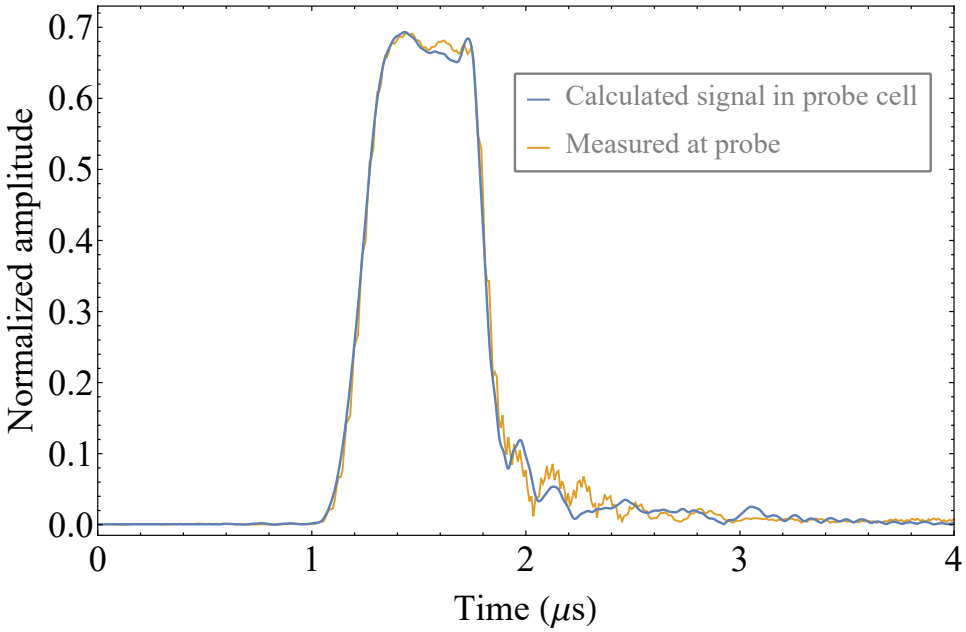

Figure 5.12: Shaped pulse for dispersion reduction simulated at the probe compared to measured at the probe.

beam velocity. To add this to the model, we modify Equation 5.9 to be a function of the cell number, n, and calculate the field in the cell only for the time that the beam arrives in each cell: $t = nc_L/c$, and take only the real part. The equation becomes

$$A(n,t) = \int_{-\infty}^{\infty} \hat{A}(\omega) \exp\left(i\left(\omega(\frac{nc_L}{c} + t) - \int_0^{nc_L} k(z,\omega)dz\right)\right) d\omega. \tag{5.12}$$

To find the electric field amplitude we can use the equation [11]

$$E_a(z) = \sqrt{\frac{\omega_0 r_L(z) P_0}{Q_0(z) v_{g0}(z)}} \tag{5.13}$$

where P_0 is the structure input power and $r_L(z)$ is the shunt impedance per unit length as a function of longitudinal position.

To add in the time dependence from the calculated envelope we take the real part of the normalized envelope $\mathrm{Re}\{A(n,t)\}$ for an input of 1 W, and multiply by the electric field amplitude to give $E_{acc}(n,t)$, the accelerating electric field that interacts with the beam in cell n.

$$E_{acc}(n,t) = E_a(nc_L)\,\mathrm{Re}\{A(n,t)\} \tag{5.14}$$

This can be simplified for calculation by replacing the $E_a(nc_L)$ term with the field in the first cell $E_a(c_L)$ and multiplying by $E_a(nc_L)/E_a(c_L)$ using the definition of E_a in Equation 5.13. For our case, r_L/Q_0 varies by 0.42% along the length of the linac, and so this term was approximated to be invariant, leaving v_{g0} as the only term that varies along the structure.

$$E_{acc}(n,t) = E_a(c_L)\sqrt{\frac{v_{g0}(c_L)}{v_{g0}(nc_L)}}\,\mathrm{Re}\{A(n,t)\}. \tag{5.15}$$

A range of RF pulse shapes used as inputs to the model are shown in Figure 5.13. Deviation from the ideal pulse shape created with the low level RF control is due to dispersion in the waveguide. The accelerating field as a function of cell number at discrete time steps for each of the pulse shapes is shown in Figure 5.14.

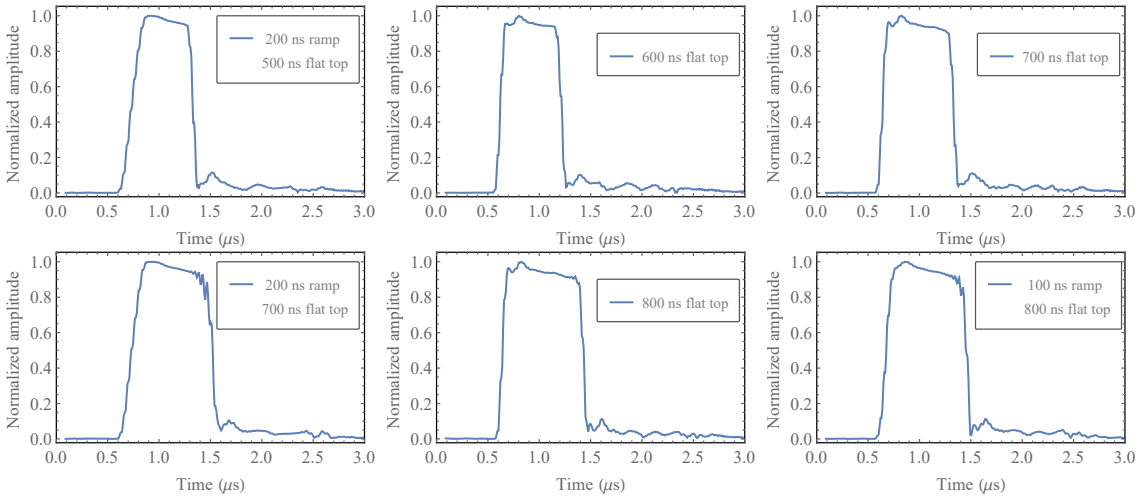

Figure 5.13: Pulse shapes measured before the linac

To calculate the kinetic energy K gained by an electron beam in the cavity we must integrate over the field in the structure to determine the peak accelerating voltage, then multiply by the

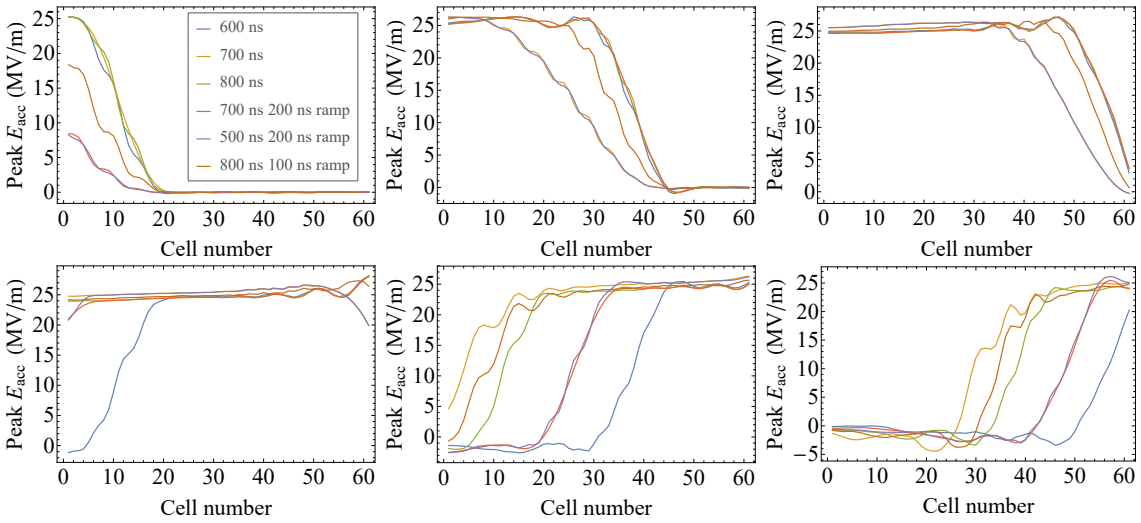

Figure 5.14: Peak fields in each linac cell at time steps 200 ns apart

transit time factor T where

$$T = \frac{\sin(\omega_0 c_L/2c)}{\omega_0 c_L/2c}, \tag{5.16}$$

The validity of this approximation is explored in the Section 5.12.

$$K(t) = T \sum_{n=1}^{N_c} E_{acc}(n,t) \tag{5.17}$$

where N_c is the number of cells. The kinetic energy gain for a relativistic beam injected into the cavity over the full range of possible filling times can be seen in Figure 5.15.

It is interesting to note that the pulse shapes with the ramp at the start have a generally similar smooth shape to those without the ramp, and the peak momentum is again very similar. This shows that the oscillation in the amplitude of the pulse envelope in the square pulse shapes has a minimal effect on the beam momentum of a single bunch. Additionally the smooth curves for all pulse shapes show that even pulses with high dispersion and large amplitude oscillations are robust to timing jitter. To illustrate this a longer pulse has been modelled, so that the "flat top" (in this case sloping due to the slope on the pulse shape) can be seen.

A 1200 ns square input pulse, and a 1200 ns input pulse with a 150 ns ramp at the start are shown in Fig 5.16, both before the structure, and in the last cell of the structure. The modelled energy gain at different beam injection times is shown in Figure5.17. The flat top pulse shows superimposed oscillations onto the pulse shape from dispersion, but the energy profile is fairly robust to the oscillations. The energy profile from the square pulse reaches a maximum energy gain that is 0.4 MeV lower than the pulse with the ramp, and shows slow deviations of up to 0.12 MeV from linear. A pulse with a ramp may therefore be optimal for multi-bunch schemes, but for CLARA's single bunch operation no pulse shaping is required.

The beam momentum after the linac $p(t)$ can be found by adding K to the kinetic energy gained in the photoinjector K_{gun} and dividing by c,

$$p(t) = \frac{1}{c}\left(K_{gun} + K(t)\right) \tag{5.18}$$

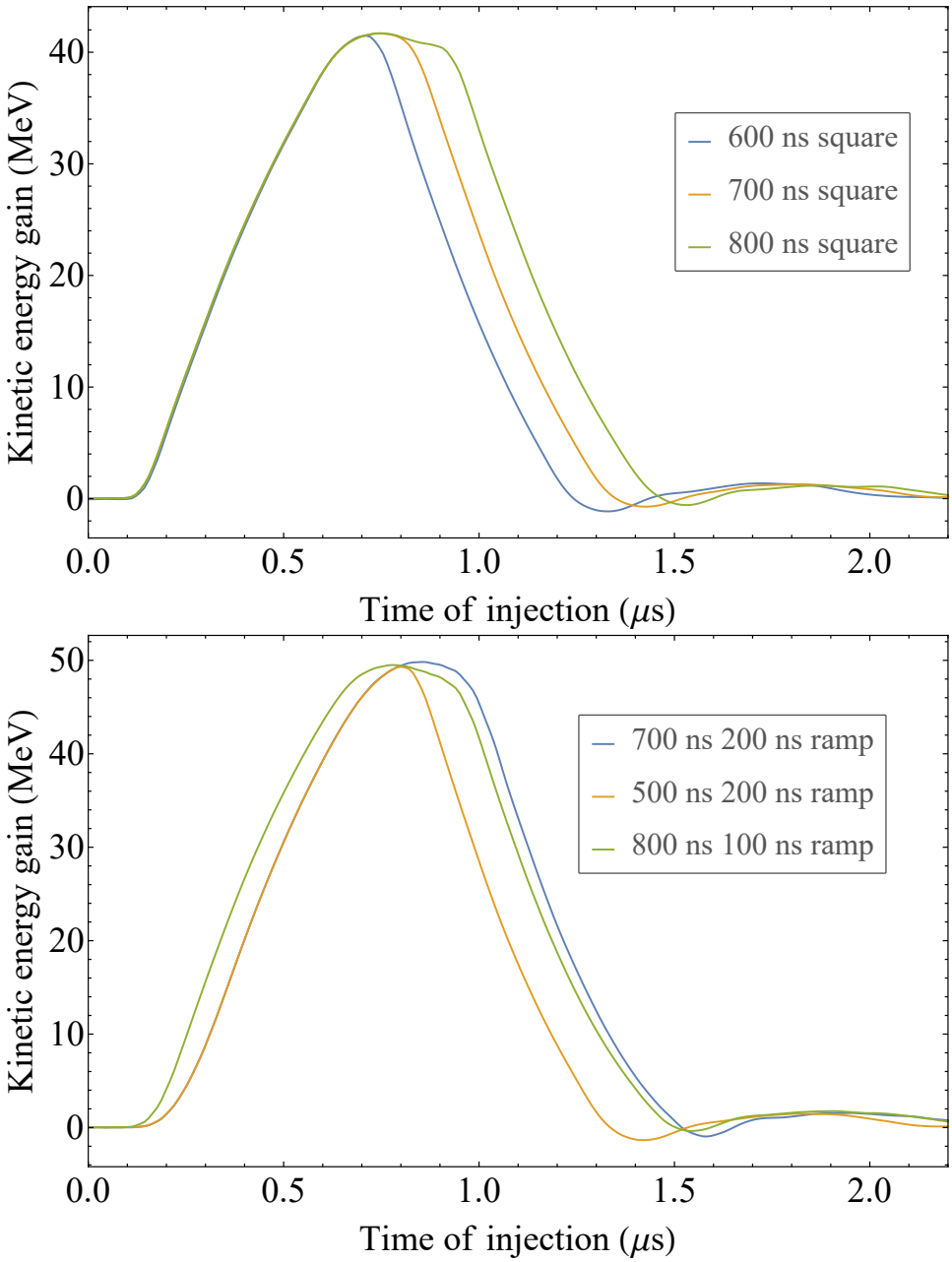

Figure 5.15: Modelled energy gain in the linac structure over the full filling range for pulses shown in Figure 5.13 for square pulses (top) and pulses with ramps (bottom).

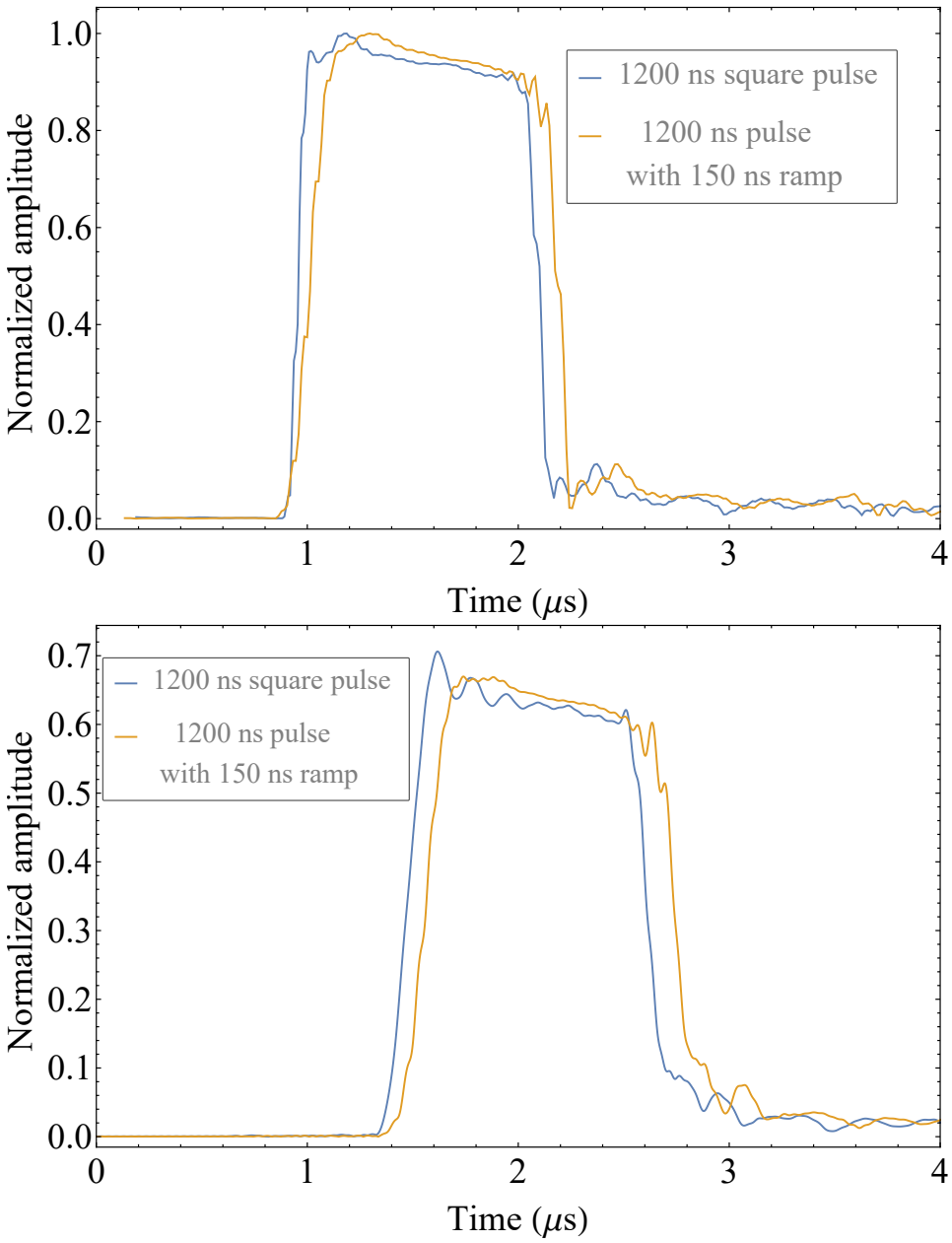

Figure 5.16: (1200 ns square pulse and 1200 ns pulse with 150 ns ramp before structure (top) and in the last cell (bottom)

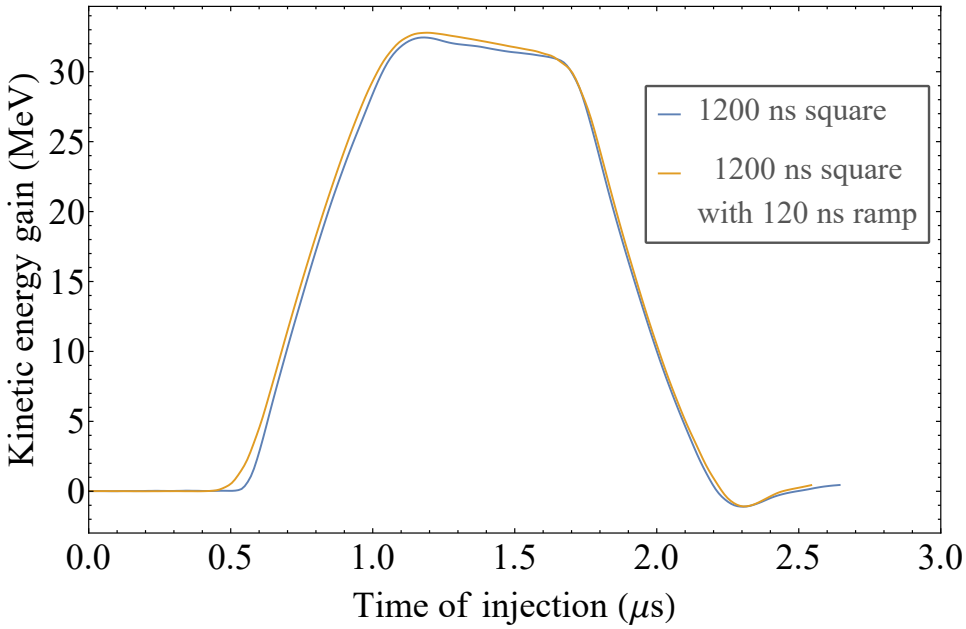

Figure 5.17: Modelled energy gain in the linac structure over the full filling range for pulses shown in Figure 5.16. The square pulse (blue) has been shifted in time

5.8 Cavity filling time

The filling time t_{fill} from the cavity design, calculated from the group velocity v_g using the equation

$$t_{fill} = \int_0^L \frac{1}{|v_g|} dz \tag{5.19}$$

is 540 ns. This calculation does not take into account the filling time of the final cell, which, due to the relatively short length of the linac (2m), is non-negligible compared to the design filling time. This can be estimated by modelling the final cell as a standing wave cavity, with fill time τ

$$\tau = \frac{Q_{ext}}{\omega} \tag{5.20}$$

which is equal to 13 ns.

The time for the RF power to reach the end of the structure plus the time for the final cell to fill to can be calculated from $t_{fill} + 3\tau$ to be 579 ns, which gives a more accurate indication of the filling time required to reach the maximum voltage. Using the model, it can be seen that the filling time required for the beam to reach maximum momentum is between 620 and 750 ns, and depends on the pulse shape. The reason for this discrepancy is that the simple methods do not take account of the filtering of the cavity. it can be seen from Figure 5.7 that the sharp front edge of the pulse becomes angled in the cavity, and the angle increases along the cavity. The method of calculation described here includes this change to the pulse shape and as such predicts a longer filling time, in good agreement with experimental results.

5.9 Beam momentum comparison to experiment

5.9.1 Measured cavity values

The amplitude and phase advance variation per cell are known from perturbation measurements and are shown in Figure 5.18. The field in each cell can be scaled according to these values by

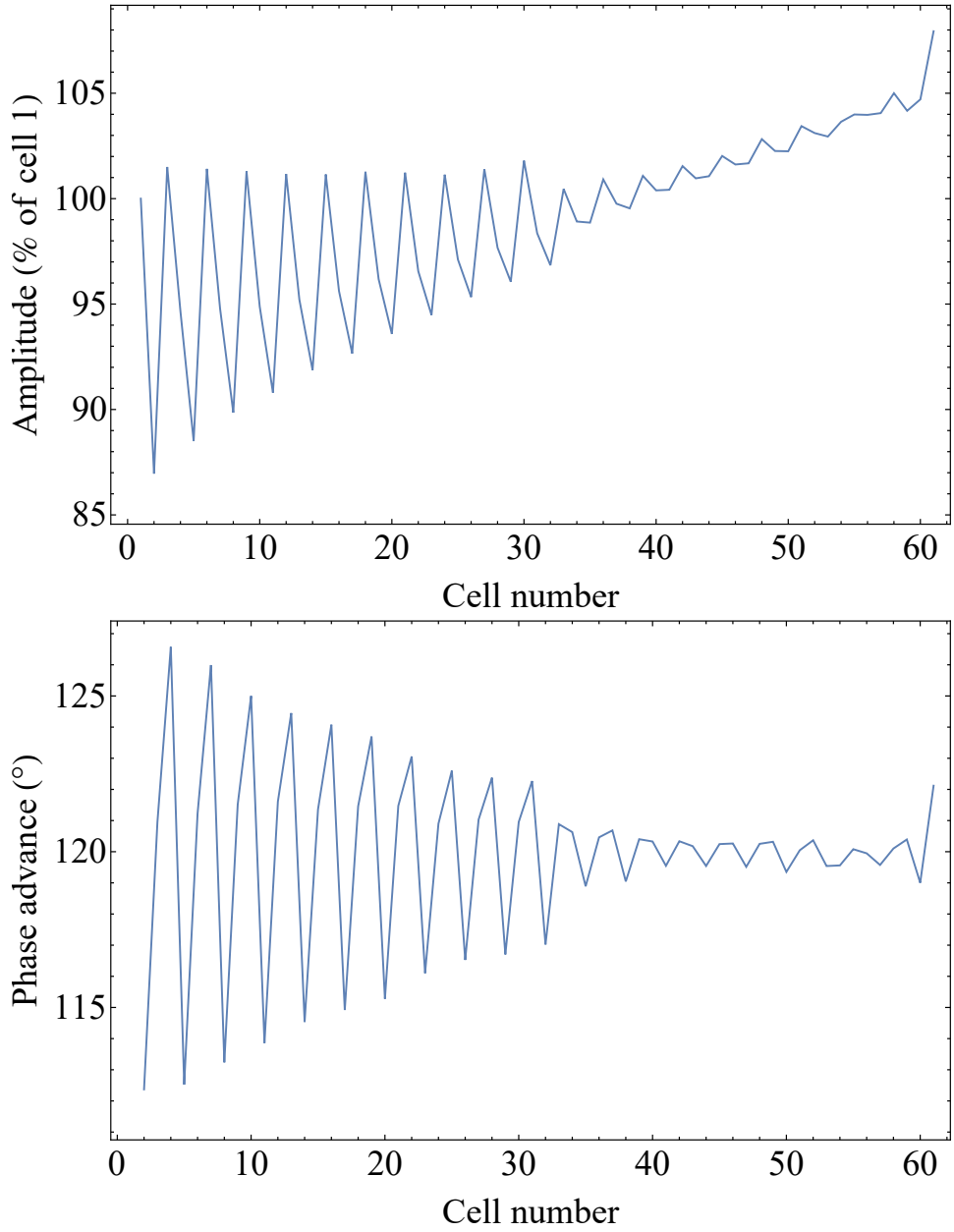

Figure 5.18: Amplitude error per cell (top) and phase advance per cell (bottom) in Linac 1

taking the real part of the complex error and adding it to Equation 5.15.

5.9.2 Momentum measurement with constant dipole current

The CLARA phase 1 beam line, along with the CLARA-to-VELA spectrometer line, is shown in Figure 5.19. The RF structures on the beam line are the RF photoinjector and Linac 1. The dipole after the linac allows deflection of the beam into the spectrometer line for momentum measurement.

All measurements of the beam momentum were performed in collaboration with J. McKenzie.

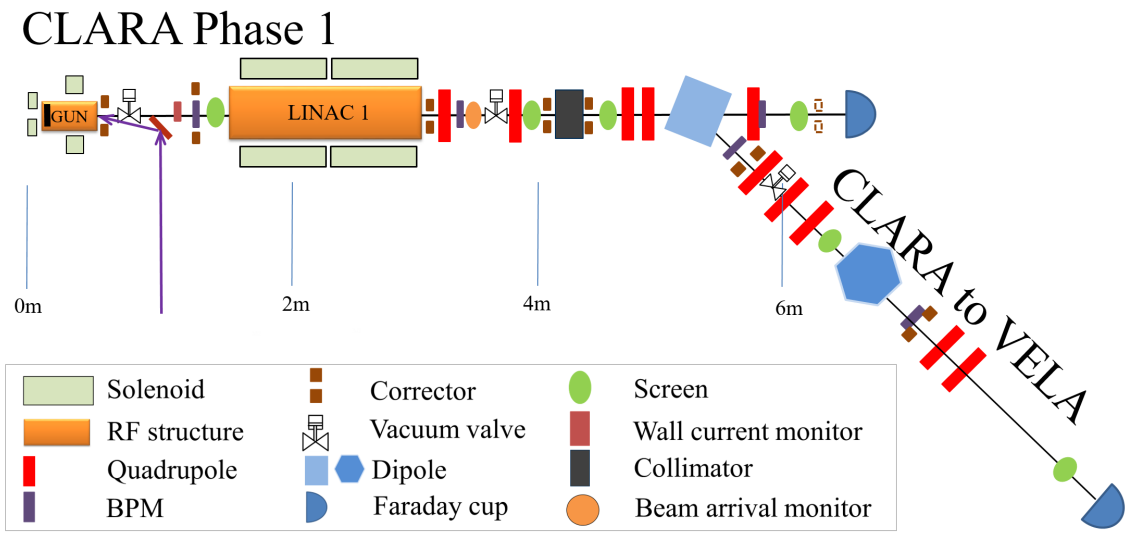

Figure 5.19: Schematic of CLARA front end including linac and dipole

The photoinjector was operated at the phase of maximum momentum gain, with the beam momentum measured as 4.14 MeV/c. The linac was also operated at the phase of maximum energy gain, with a square 700 ns pulse. The beam was steered with the dipole down the spectrometer line to the first beam position monitor (BPM) in that line. The beam was centred horizontally on the BPM using the dipole. The current was 64.46 A.

The timing of the linac pulse with respect to the injected beam was scanned in 12 ns steps either side of the nominal, as this is the granularity of the low level RF system timing. At each step the beam position was measured on the BPM over 100 shots and the mean recorded. This was performed for the full range of timing for which the BPM picked up a real signal. This procedure was then repeated for five of the pulse shapes shown in Figure 5.13.

The beam momentum p was calculated from the bending angle θ calculated from the BPM position of the beam, and the dipole current I.

$$p = cI_s\theta \tag{5.21}$$

where I_s is the integrated magnet strength, defined as the power series

$$I_s = k_0 + k_1 I + k_2 I^2 + k_3 I^3 + k_4 I^4 + k_5 I^5 \tag{5.22}$$

Where k_n are the field integral coefficients for the magnet, defined from the experimentally measured excitation curve [90].

The measured momentum is shown in Figure 5.20 compared to the simulated momentum for the same pulse shape. It can be seen that the model accurately predicts the beam momentum when the beam passes through the linac at different stages of filling and emptying. The mean absolute errors (MAE) on the prediction from the model are given in Table 5.9.2.

Table 5.1: Table showing the Mean Absolute Error of the prediction from the model when compared to experimental data.

Pulse Shape	Mean absolute error (MeV/c)
600 ns square	0.178
600 ns square	0.162
600 ns square	0.163
500 ns with 200 ns ramp	0.215
700 ns with 200 ns ramp	0.118

5.9.3 Momentum measurement with varying dipole current

To measure the beam momentum over the entire range of timings where the RF pulse interacts with the beam, the dipole current had to be varied to ensure the beam was still passing through the BPM. This was performed for the 700 ns square pulse. For each time step the dipole current was changed to centre the beam on the spectrometer BPM. The momentum was then calculated from this current.

The measured momentum is compared to the modelled momentum in Figure 5.21.

The fit is very good, with a MAE of 0.561 MeV/c. Changing the dipole current will always introduce the risk of hysteresis errors to the measurement. Additionally at the lowest energies the beam size was very large, several millimeters in diameter. Some clipping of the beam on an aperture on the high energy side could explain the slight deviation at 1.5-1.8 μs.

5.10 Beam loading

Whilst the CLARA linac has negligible beam loading, this method may be of use in facilities where, due to high bunch charge and multi-bunch regimes, beam loading must be considered. To add beam loading to the model we use the analytical calculation for the transient beam loading described in [87]. This calculation would require generalisation before application to a structure with negative dispersion. The beam loading gradient, G, as a function of z and t is given by

$$G(z,t) \;=\; g(z)\int_0^z I_b[t \,-\, \tau_d(z) \,+\, \tau_d(z')]H[t \,-\, \tau_d(z) \,+\, \tau_d(z')]\frac{\omega r_s(z')}{2g(z')v_g(z')Q_0(z')}dz' \quad (5.23)$$

where $I_b(t)$ is the time dependent beam current and H is the Heaviside function. τ is the signal time delay,

$$\tau_d(z) = \int_0^z \frac{1}{v_g(z')}dz' \quad (5.24)$$

and $g(z)$ describes the steady state longitudinal variation of the cavity gradient, which can be obtained evaluating E_{acc} from Equation 5.15 when the cavity is fully filled and normalizing to the first cell.

To incorporate the beam loading gradient in the model we modify Equation 5.15 by subtracting the beam loading gradient. Once known, the beam loading can be compensated by changes to the

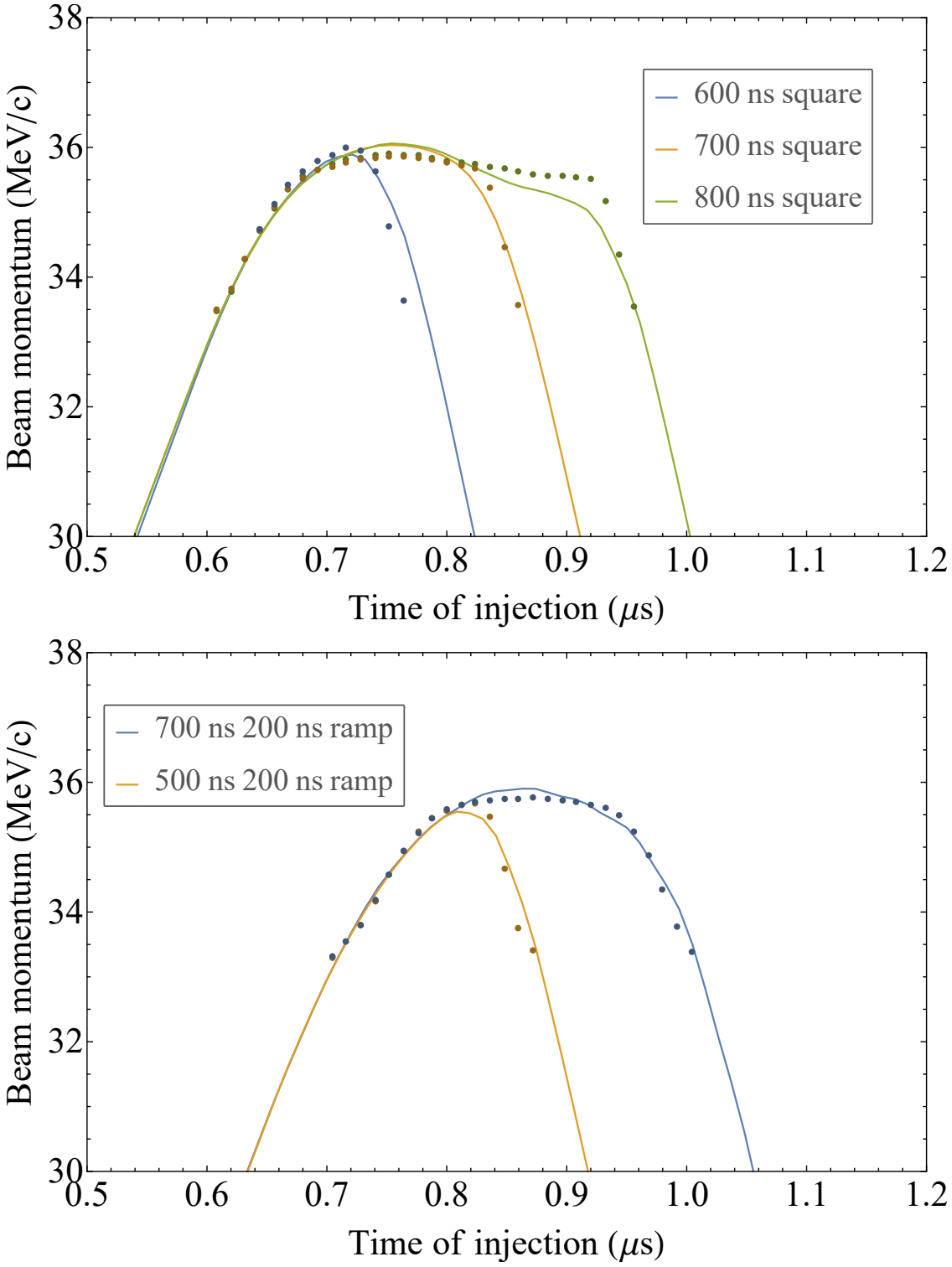

Figure 5.20: Measured momentum (points) at different beam injection times compared to model (lines) for square pulses (top) and ramped pulses (bottom).

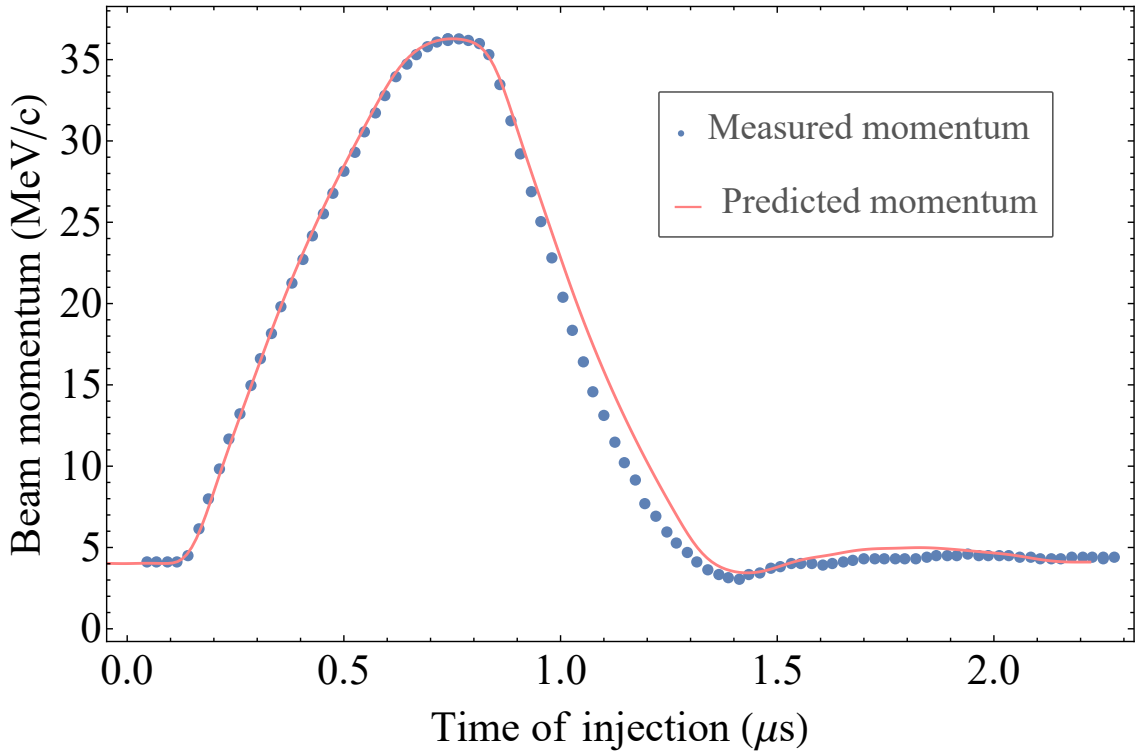

Figure 5.21: Measured momentum at different beam injection times compared to model over the full range of timings for a 700 ns square pulse.

input RF pulse shape.

$$E_{acc}(n,t) = \frac{\sqrt{aP_{in}}}{L}\sqrt{\frac{v_{g0}(c_L)}{v_{g0}(nc_L)}}\,\mathrm{Re}\{A(n,t)\} - G(t,nc_L) \tag{5.25}$$

To show an example, let us increase the CLARA beam load to a train of 15 bunches, each of charge 3 nC, with a bunch separation of 10 ns, introduced into the CLARA linac 650 ns after the start of the 800 ns pulse. The beam current $I_b(t)$ is a rectangular function 150 ns long with maximum value 300 mA.

The modelled beam loading gradient, unloaded cavity gradient and the loaded gradient as a function of time for the start, middle and end cells can be seen in Figure 5.22. The time dependent momentum is then found as before from Equation 5.18, and is shown in Figure 5.23, compared with the momentum from the unloaded cavity and the momentum loss through beam loading.

5.11 Testing the limits of the model

The CLARA linac has positive dispersion, and accepts the full 3 dB bandwidth of the input pulses shown.

To test the limits of the model the pulse shape evolution of another structure was modelled. The TULIP structure [88, 89] is a backwards travelling wave structure with negative dispersion, and it has a passband that does not accept the full 3 dB bandwidth of the input pulse. Equation 5.10, with k given by the piecewise function in Equation 5.11 was used to model the shape of a given real input pulse at the end of the structure. The measured input RF pulse and the transmitted pulse are shown in Figure 5.24 . Also shown is S21 calculated from the ratio of each measurement, the

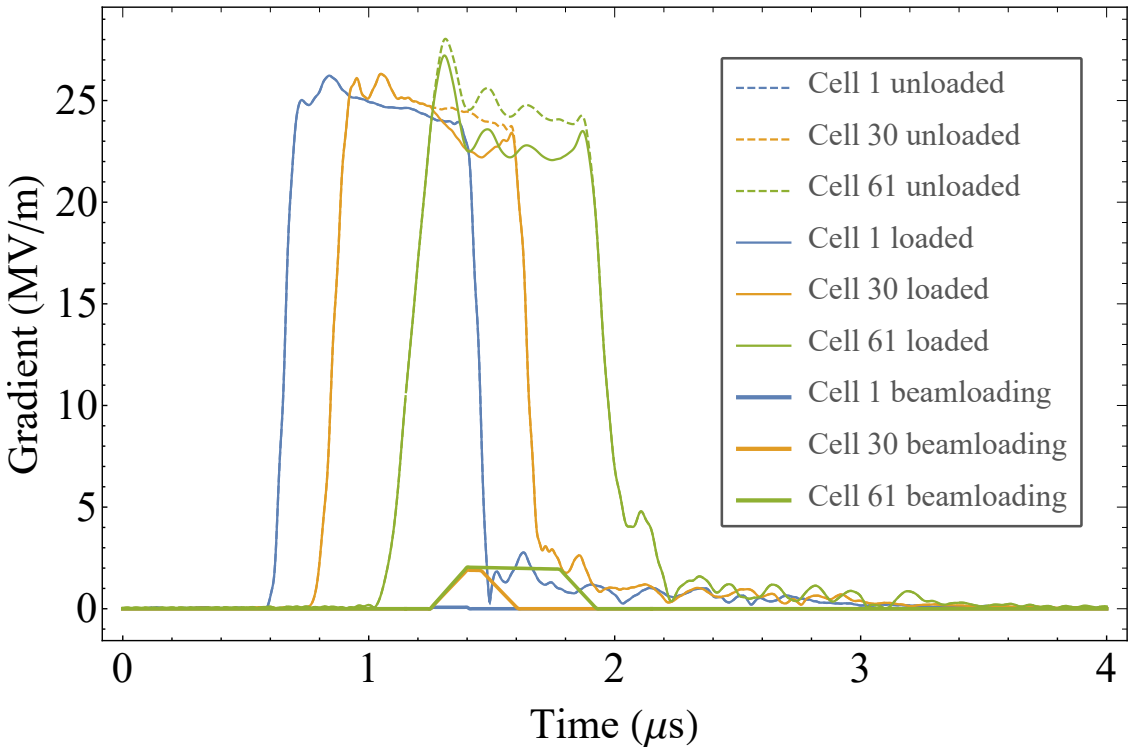

Figure 5.22: Unloaded, loaded and beam-loading gradients in the start middle and end cells as a function of time.

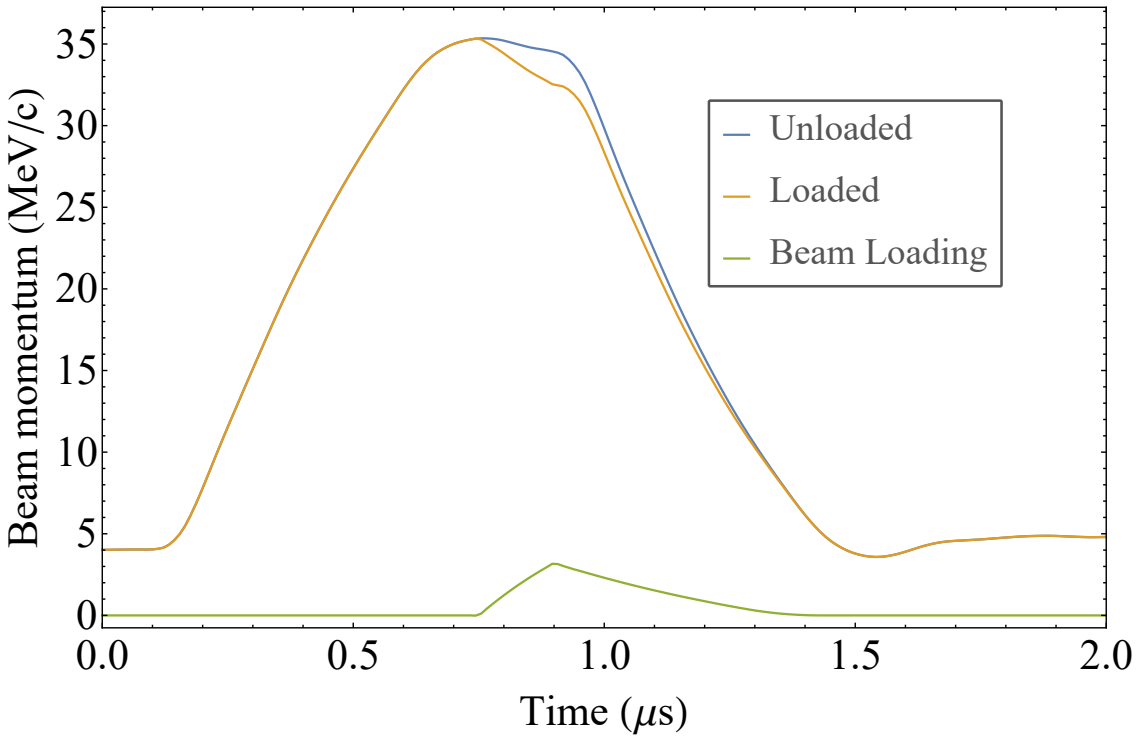

Figure 5.23: Modelled momentum with and without beam loading and beam loading momentum loss at different beam injection times for an 800 ns square pulse.

S21 calculated in this way is inaccurate in regions of low amplitude, such as between the side-bands, due to the signal-to-noise ratio. The region that is highly attenuated by the piecewise function in Equation 5.11 is shown shaded. It can be seen that the high frequency end of the passband has a sharp cut-off, which matches the model well. The lower frequency end shows some transmission in the region highly attenuated by the model, but the maximum transmitted amplitude in this region is 0.6% of the peak input amplitude.

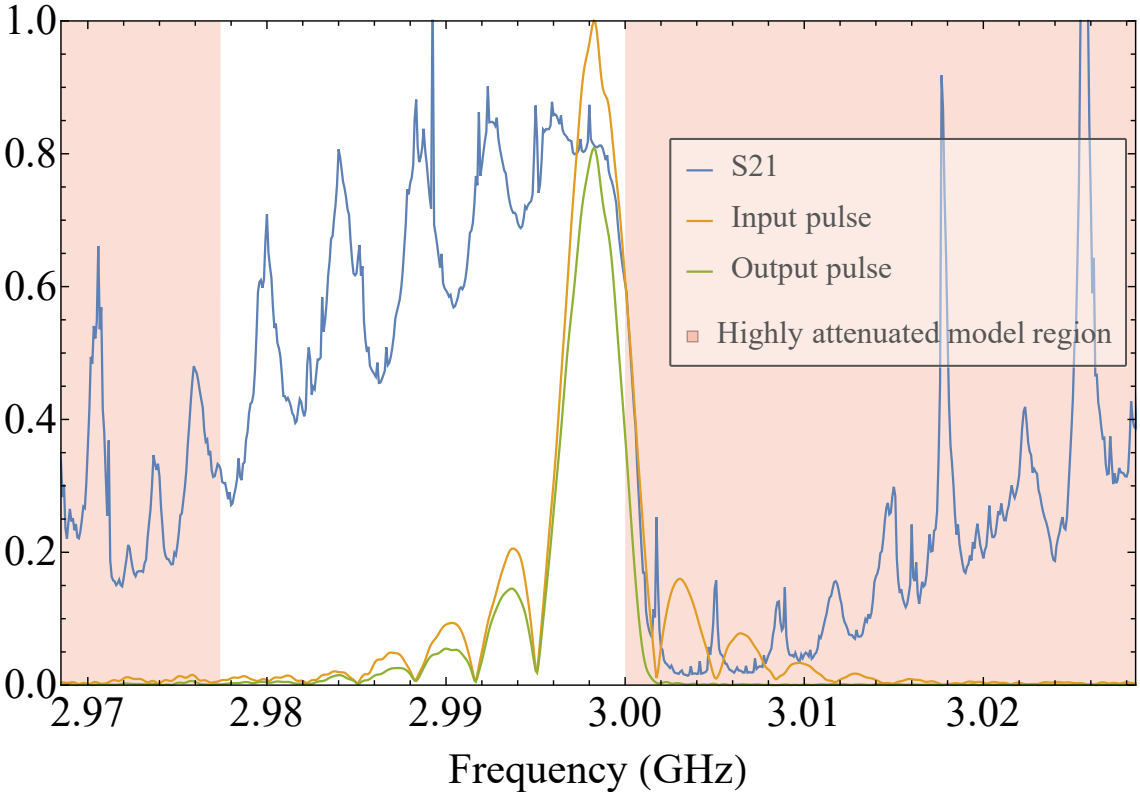

Figure 5.24: The measured incident and transmitted pulses from the TULIP cavity [89] and the S21 transmission parameter calculated from the measured pulses, compared to the region highly attenuated in the model by the piecewise equation.

Figure 5.25 shows the comparison to the measured transmitted pulse data. The shape of the pulse matches well, however the attenuation in the structure is more than expected from the design Q_0 value. This could be explained by error on the input and output power measurements, or the Q_0 of the fabricated structure being lower than the design. Modelled using a Q_0 of 80% of the design value, the MAE is 24.52 kW.

It can be concluded that the pulse shape evolution works well on both structures with negative dispersion, and those with small passbands with respect to the incoming RF pulse bandwidth. No data was available to test the accuracy of beam momentum predictions in these cases. In the small passband case, is possible that reflected RF in the structure may interact with the beam, something which is not included in the model, however these reflections are unlikely to be synchronous.

5.12 Validity of the transit time factor approximation

Equation 5.16 gives a simple approximation, which we will call Approximation 1, for the transit time factor that does not take into account variation in the structure parameters such as aperture

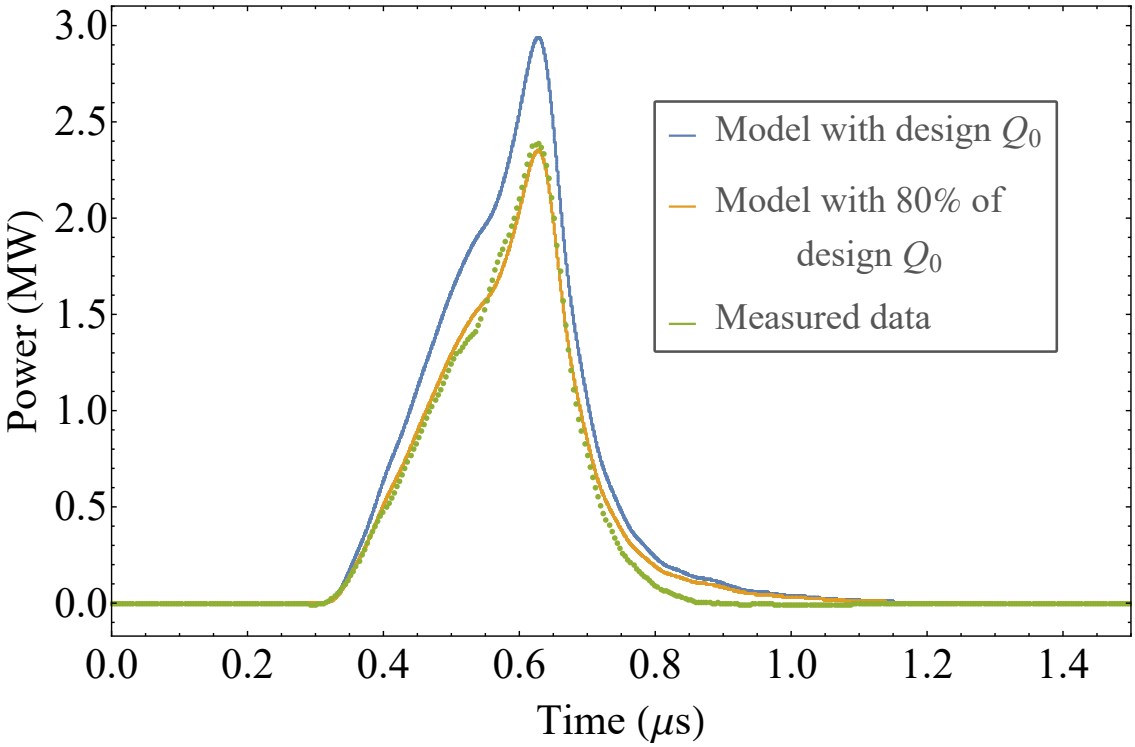

Figure 5.25: Comparison of the measured transmitted pulse in the TULIP cavity [89] to the modelled pulse with Q_0 at design value and with Q_0 at 80% design value.

radius and iris thickness. This could be varied to include the effect of iris thickness by replacing the cell length, c_L, with the gap length, g, given as $g = c_L - i_L$, where i_L is the iris length (or diaphragm thickness). The equation, which we will call Approximation 2, becomes

$$T = \frac{\sin(\omega_0 g/2c)}{\omega_0 g/2c}. \tag{5.26}$$

A further refinement to the transit time factor approximation, which we will call Approximation 3, is given by Wangler [11]

$$T = J_0(a\omega/c)\frac{\sin(\omega_0 g_c/2c)}{\omega_0 g_c/2c}. \tag{5.27}$$

where a is the coupling aperture radius, and $g_c = g + 0.85\rho_c$ is an empirical correction for the gap size which takes into account the rounding of the aperture to remove the sharp edge, ρ_c being the rounding radius.

A 3D simulation model of a single cell with periodic boundary conditions was constructed in CST Studio Suite [38], and used to calculate the transit time factor for varying aperture using the equation

$$T = \frac{\int_{-cL/2}^{cL/2} E(z)\cos(\omega_0 z/c)dz}{\int_{-cL/2}^{cL/2} E(z)dz}. \tag{5.28}$$

In Figure 5.26 the effect of iris length on the transit time factor is shown for the different approximations and the 3D model result, at the nominal aperture radius of 9.44 mm. It can be seen that the approximation used in the Section 5.7 method, Approximation 1, gives a value of 0.827 for the transit time factor. The deviation of the transit time factor from the 3D simulation at the nominal iris length of 5 mm is 0.037, but the deviation becomes as large as 0.046 for a 9 mm

iris length. This error would propagate to give the same percentage error on the cavity voltage and the beam momentum, for example a beam momentum of 40 MeV/c would have an error of 1.48 MeV/c for the nominal iris length.

Approximations 2 and 3 appear to overestimate the effect of the iris length. Approximation 2 however does give a closer value to the 3D simulation, and could be considered for use if the iris length was known. Approximation 3 gives a significantly lower result for transit time factor due to the the overestimated effect of the aperture-dependent factor.

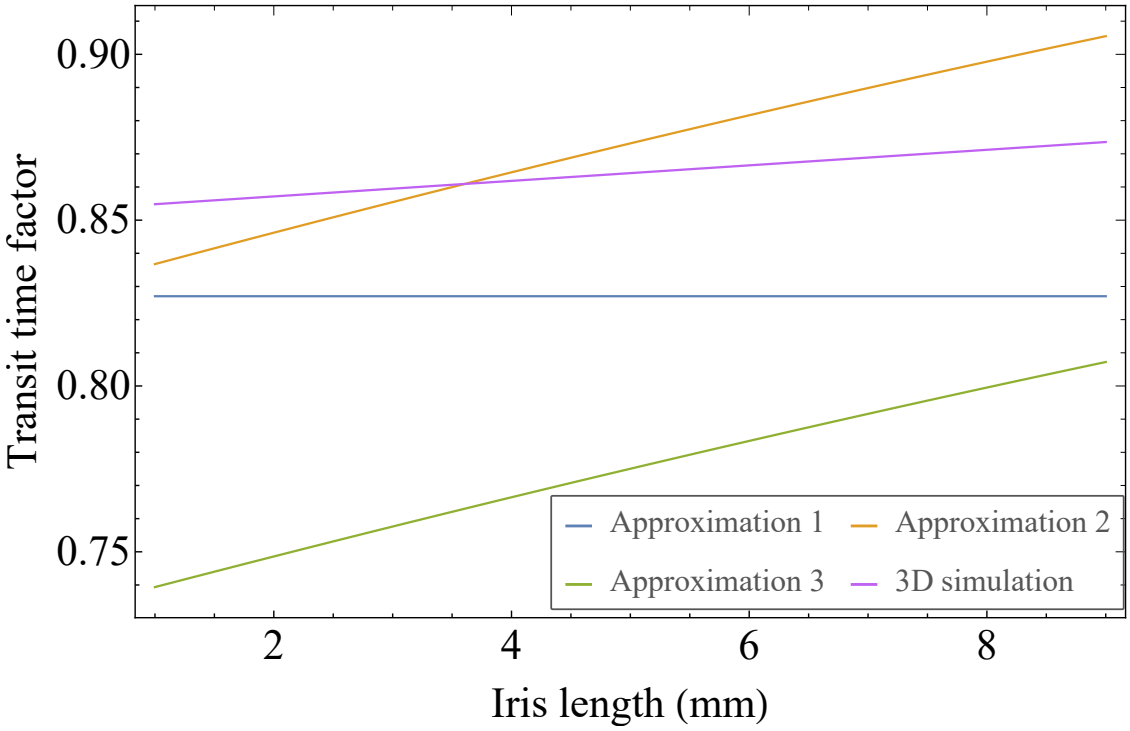

Figure 5.26: Comparison of 3 approximation methods for transit time factor with result from 3D simulation of single cell for varying iris length with a fixed aperture size of 9.44 mm. Approximation 1 was used in the beam momentum model in Section 5.7

In Figure 5.27 the effect of aperture radius on the transit time factor is shown for the different approximations and the 3D model result, at the nominal iris length of 5 mm. It can be seen that the variation in transit time factor from the 3D simulation with aperture size is minimal, varying by less than 0.008 across the range. The aperture size of the linac varies from 9.43 mm to 11.85 mm, giving a deviation from the transit time factor value given for Approximation 1, which is 0.827, of 0.038 to 0.035 along the structure. Approximation 2, which is again independent of aperture radius, gives the closest result to the 3D simulation, with a maximum deviation of 0.013. Approximation 3 appears to again overestimate the effect of the aperture.

The average error, for CLARA linac 1 parameters, obtained by comparing the approximation used in Section 5.7 (Approximation 1) to the 3D simulation, is 0.0363. This is a 4.4 % error on the transit time factor, so the approximation will propagate to give a 4.4 % error on the voltage and beam momentum.

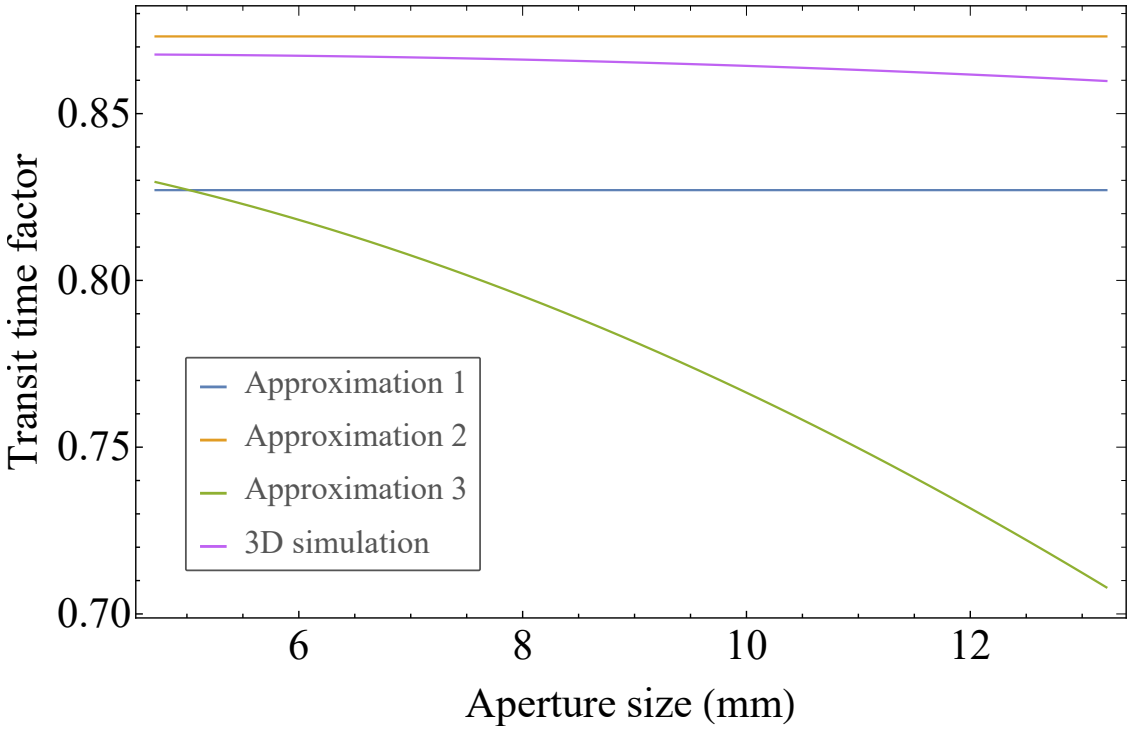

Figure 5.27: Comparison of 3 approximation methods for transit time factor with result from 3D simulation of single cell for varying aperture radius with a fixed iris length of 5 mm. Approximation 1 was used in the beam momentum model in Section 5.7

5.13 Conclusion

A mathematical method of calculating the pulse envelope distortion due to dispersion in travelling wave linacs has been developed. No simulations are required, and the only inputs needed are the group velocity as a function of cell number, the phase advance, and the unloaded quality factor Q_0. However, the model can be made more accurate using low power RF measurements such as perturbation test results. Beam loading can be added to the model using an analytical transient beam loading solution. The model is a fast, simple method to accurately predict fine details of the pulse evolution, and will make it possible for purchasers of turn-key linacs, who may not have the full 3D design of the structure they have purchased, to accurately model the dispersion and acceleration in their cavity.

The model accurately predicts the pulse envelope distortion due to dispersion in the first CLARA linac. The model can predict the filling time of the linac more accurately than standard calculations. It was shown that the model can be used to calculate the beam momentum gain from a linac, at any point during filling or emptying, making it easy to predict the flat top region where timing jitter would have the lowest effect on the beam momentum. A synchronism condition term can be added to calculate only the voltage experienced by a particle beam. The model was tested against beam measurements on CLARA, and in the high energy region the Mean Average Error on the prediction is, on average for all pulse shapes, 0.167 MeV/c, and over the full pulse the the Mean Average Error is 0.561 MeV/c.

To further test the model, it was used to predict the pulse evolution in a backwards travelling wave linac with negative dispersion, which also had a passband that was small with respect to the bandwidth of the incoming RF pulse. The pulse shape distortion was accurately predicted.

5.13.1 Further work

To further test the model without the inaccuracies that come from experimental measurements the model could be tested against a 3D time domain simulation of a travelling linac with a realistic input pulse.

Chapter 6

Dipole-mode cavity tuning method comparison

6.1 Introduction

CLARA requires a dipole-mode transverse deflecting cavity to be used with a YAG screen as a longitudinal beam diagnostic. A 9-cell normal conducting RF structure has been designed to provide the equivalent of a 10 MV/m transverse deflection to the electron bunch, converting longitudinal electron position to a transverse offset. The longitudinal structure can then be analysed via imaging with a yttrium aluminium garnate scintillator screen. This transverse kick will allow resolution of 10 fs to be reached at the full CLARA beam energy of 250 MeV [91].

The RF structure design is similar to a geometry used by Tsinghua University [92] and SPARC [93]. It is a multi-cell disk-loaded geometry, with coupling apertures between the cavities. The coupling apertures lift the frequency degeneracy of the orthogonal dipole mode polarisations, allowing the lowest to be chosen as the operating mode. The coupling apertures are at the low-field of the dipole mode, the deflecting mode is coupled through the iris. The input power is coupled through a waveguide coupler into the middle cell to prohibit the excitement of the even pass-band modes. A symmetric compensating slot is included on the opposite side of the middle cell to minimise the field distortion. The structure was optimised to minimise transverse beam displacement. A full description of this can be found in [91]. The structure design is shown in Figure 6.1.

The deflecting mode is a hybrid of the TE and TM modes, causing it to split into a HE mode and an EH mode. This means that both the electric and magnetic components of the mode will contribute to the bunch deflection. The cavity fields can be seen in Figure 6.2.

To reach a 10 MV kick, the structure requires 10 MW of forward power. To limit surface damage due to thermal stress, the temperature rise limit on the surface was chosen conservatively to be 20° C, (as the threshold for thermal stress damage is 40° C) [41] which at a 3 μs pulse length gives a surface magnetic field limit of 364 kA/m. The peak surface magnetic field of the structure as designed at 10 MW input power is 284 kA/m.

The surface electric field limit was chosen based on the empirical limit in [94], with a safety factor of 20%. This is an updated fit calculated in a similar fashion to the Kilpatrick limit discussed in Section 4.1.2. This limit for the TDC is 254 MV/m. The peak surface electric field as designed at 10 MW input power is 80 MV/m.

It is clear that the peak magnetic field is closer to the prescribed limit than the electric field.This

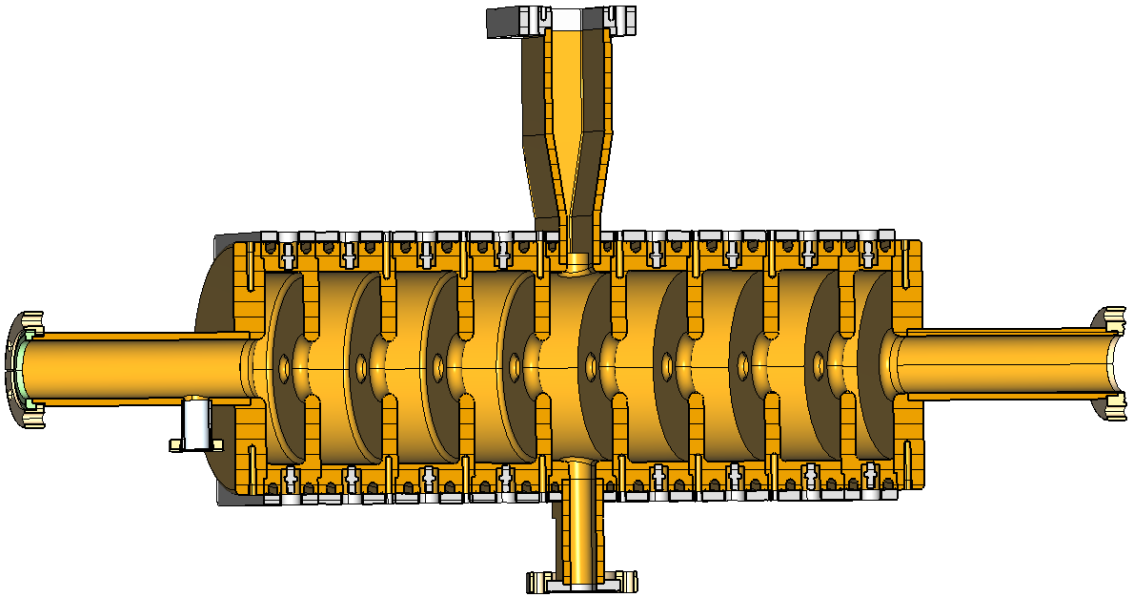

Figure 6.1: Cut-through model of TDC structure.

is due to the high magnetic field on the irises. The structure was therefore optimised to be field-flat, ie. to have the same peak field in each cell, in magnetic field rather than electric. It is not possible to have the structure be field flat in both. The field profiles for H_y on axis, E_z 5 mm off axis, and E_x on axis can be seen in Figure 6.3.

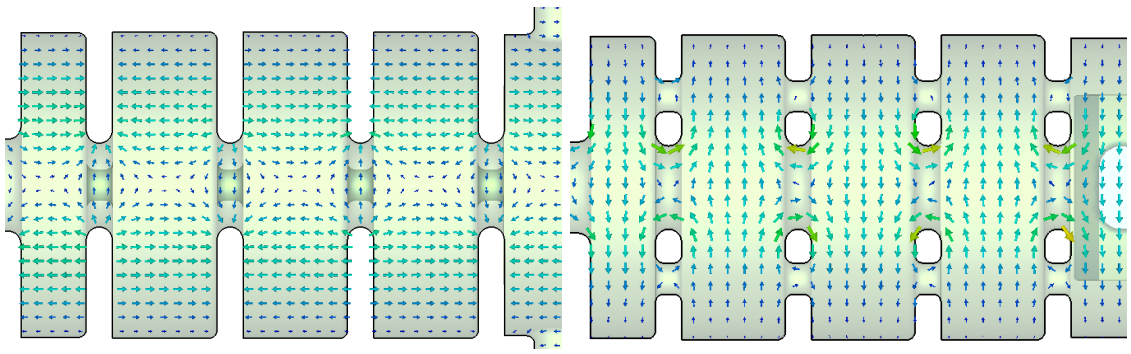

(a) Electric field in x-z plane

(b) Magnetic field in y-z plane

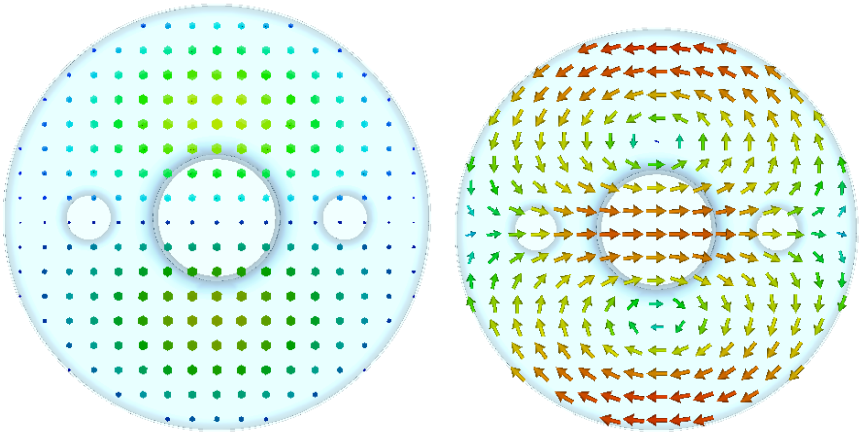

(c) Electric fields in longitudinal centre of a cell in x-y plane

(d) Magnetic fields in longitudinal centre of a cell in x-y plane

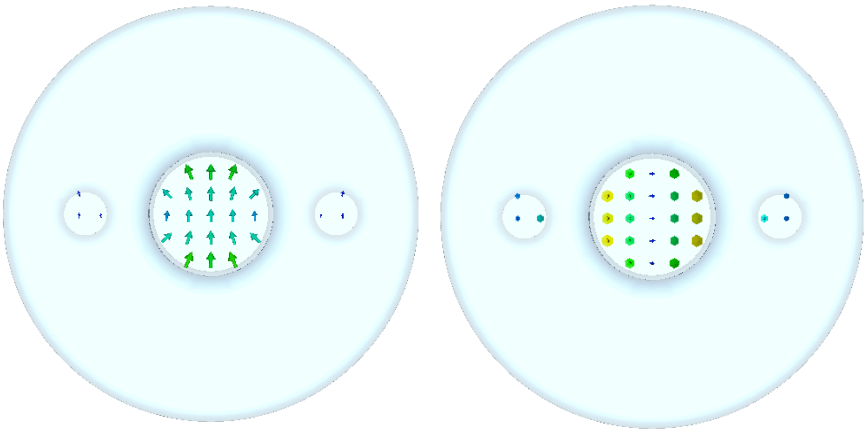

(e) Electric fields in longitudinal centre of an iris in x-y plane

(f) Magnetic fields in longitudinal centre of an iris in x-y plane

Figure 6.2: Electric (left) and magnetic (right) fields in the TDC. Where arrowheads cannot be seen, the dark and light colours represent fields pointing into and out of the plane of the page respectively

Due to manufacturing errors, for which the tolerance is ±10 µm on the radius, the structure will require tuning to achieve the modelled field flatness. The mechanical design includes two tuning studs on each cell for this purpose, an example of which can be seen in Figure 6.4. The tuning

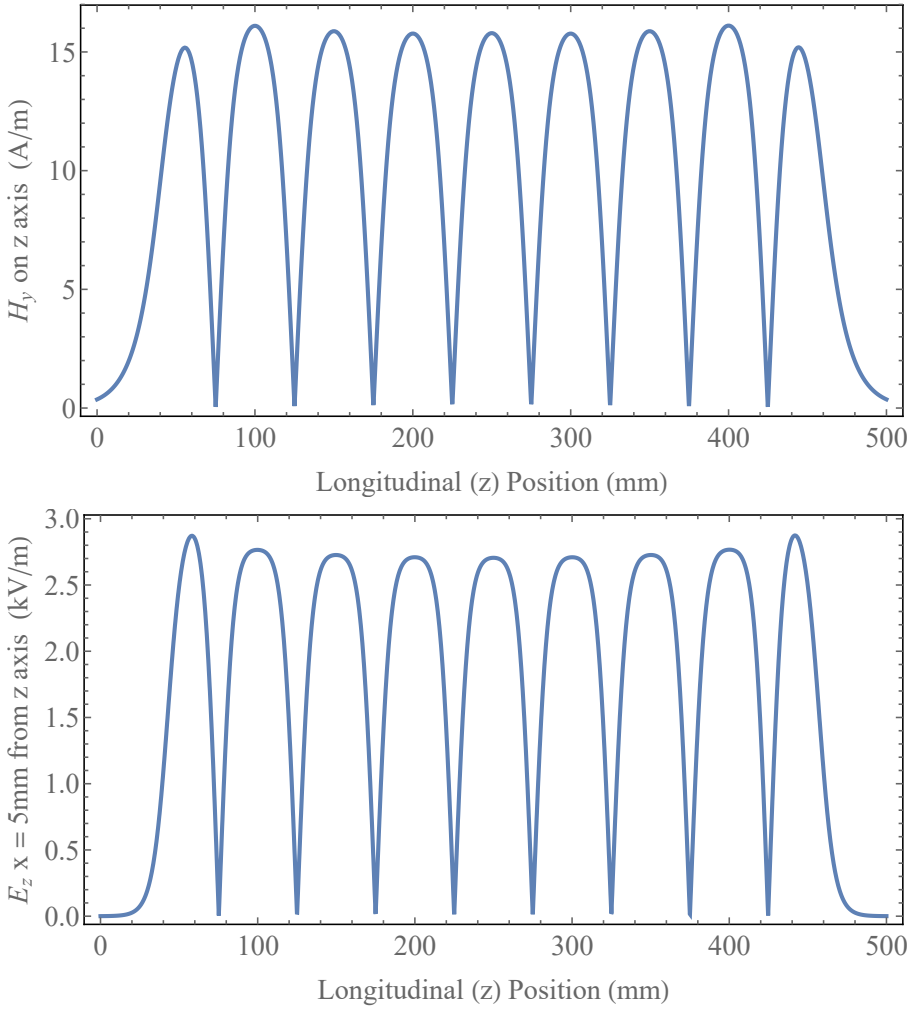

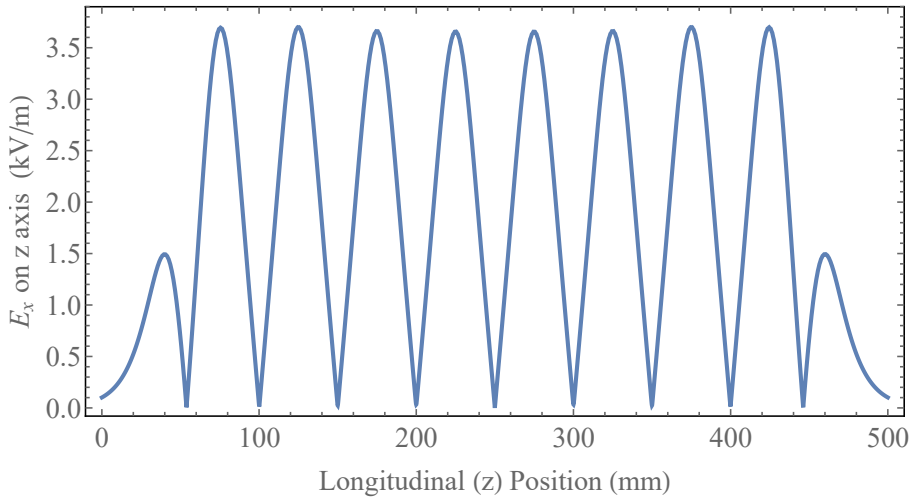

Figure 6.3: Field profiles of H_y on axis, E_z 5 mm off axis, and E_x on axis.

studs can be tapped or pulled to deform a small region of the cell and increase or decrease the cell frequency. The tuning is performed with a slide-hammer to increase repeatability, but there is no calibration between tap force and frequency change. The copper in the tuning region has been found to work harden [95] after successive taps, so any calibration would change over time. For these reasons the tuning must be done iteratively, tapping or pulling the most out-of-tune cell and then re-measuring to find the next. The studs will be used to tune the field profile only, any overall frequency correction will be done by changing the operating temperature.

This chapter will define and test different methods to find the out-of-tune cells and the amount and direction of tuning required. The inputs to these methods must consist only of structure RF parameters that can be measured at low power. A CST Studio Suite [38] model has been used to test these models as the fabrication of the structure has not yet been completed.

6.2 Literature review

6.2.1 Tuning a multicell structure

The classic method for tuning a multi-cell RF structure is that described in Padamsee, Knobloch and Hays [52]. This models the cells as capacitively coupled LC oscillators. The equivalent circuit is shown in Figure 6.5. Here L and C are the characteristic inductance and capacitance for each cell, C_k are apacitances that model the cell-to-cell coupling, and C_b are capacitances that model the beam-tubes. Kirchoff's loop rule, that the sum of all potential differences in any circuit loop must add to zero, is applied to each circuit loop I_j. This finds for the first cell

$$\left(\frac{1}{i\omega C_b} + i\omega L\right) I_1 + \left(\frac{1}{i\omega C}\right) I_1 + \left(\frac{1}{i\omega C_k}\right) (I_1 - I_2) = 0, \tag{6.1}$$

and for the middle cells $1 < j < N$ of an N cell structure

$$\left(\frac{1}{i\omega C_k}\right) (I_j - I_{j-1}) + \left(i\omega L + \frac{1}{i\omega C}\right) I_j + \left(\frac{1}{i\omega C_k}\right) (I_j - I_{j+1}) = 0, \tag{6.2}$$

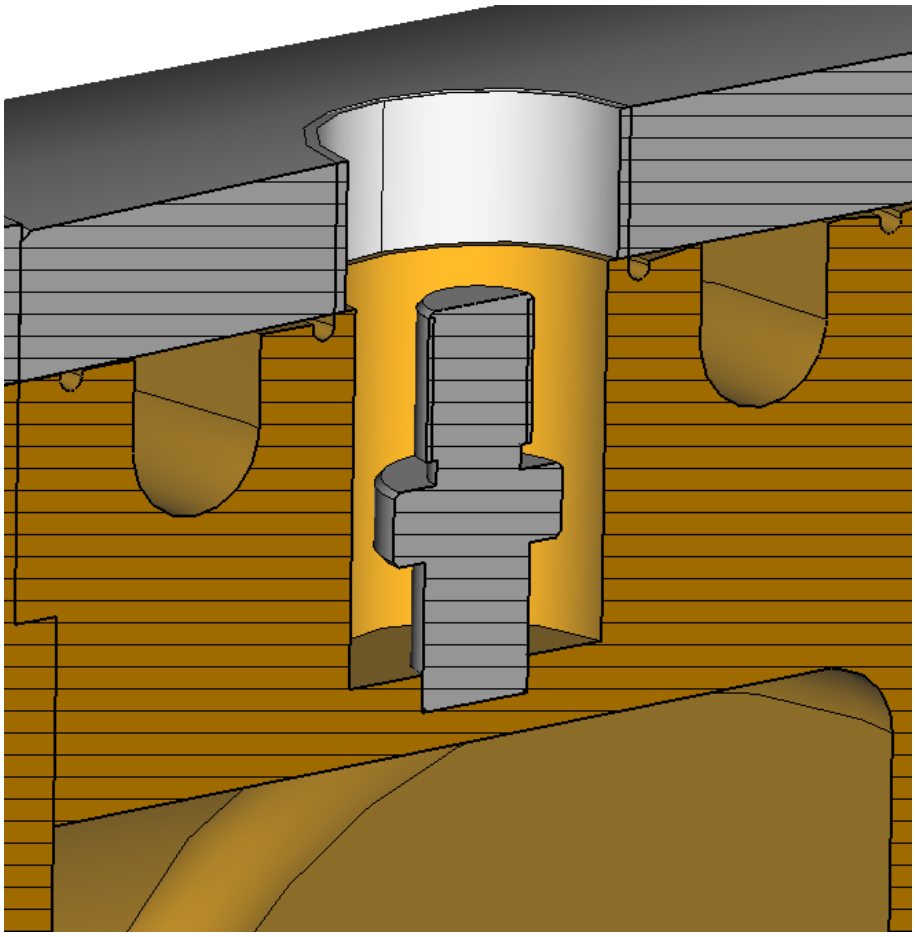

Figure 6.4: Cut-through view of mechanical model showing tuning pin on TDC cell.

and for the end cell j_N of an N cell structure

$$\left(\frac{1}{i\omega C_k}\right)(I_N - I_{N-1}) + \left(i\omega L + \frac{1}{i\omega C}\right) I_N + \left(\frac{1}{i\omega C_b}\right) I_N = 0. \tag{6.3}$$

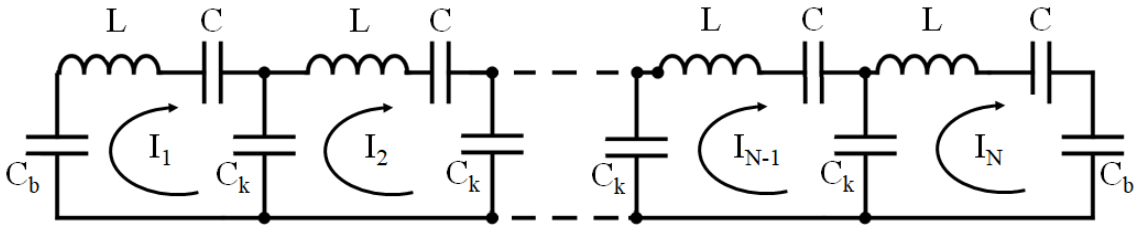

Figure 6.5: Equivalent circuit model of an N- cell structure

Defining structure resonant angular frequency $\omega_0^2 = 1/(LC)$, coupling factor $k = C/C_k$ and beam pipe additional coupling $\gamma = C/C_b$, and $\Omega = \omega^2/\omega_0^2$, as well as multiplying through by $i\omega C$ creates the tridiagonal matrix equation

$$\mathbf{A}\vec{v} = \Omega\vec{v} \tag{6.4}$$

where

$$\mathbf{A} \equiv \begin{pmatrix} 1+k+\gamma & -k & 0 & \dots & 0 \\ -k & 1+2k & -k & & \vdots \\ 0 & & \ddots & & 0 \\ \vdots & & -k & 1+2k & -k \\ 0 & \dots & 0 & -k & 1+k+\gamma \end{pmatrix} \tag{6.5}$$

where the $\vec{v}$ notation is used to imply that instead of I_j in the circuits we use cell voltages v_i in an RF structure.

For the π mode to be field-flat (have the same maximum field in each cell) the Nth normalised vector is

$$\vec{v}^{(N)} = \frac{1}{\sqrt{N}} \begin{pmatrix} 1 \\ -1 \\ 1 \\ \vdots \end{pmatrix} \tag{6.6}$$

By substituting this into the first two rows of the matrix in Equation 6.4 it is shown that $\gamma = 2k$.

The eigenvector solution to Equation 6.5 is

$$v_j^{(m)} = \sqrt{(2-\delta_{mN})/N} \sin\left[m\pi\left(\frac{2j-1}{2N}\right)\right] \tag{6.7}$$

for cell number $j = 1...N$ represented by subscripts, and mode number $m = 1...N$ represented by superscripts. This notation will be used from here on.

The eigenvalue of mode m is found to be

$$\Omega^{(m)} = \left(\frac{f_m}{f_0}\right)^2 = 1 + 2k\left[1 - \cos\left(\frac{m\pi}{N}\right)\right] \tag{6.8}$$

And for an RF structure with badly tuned cells, let the capacitance on that each cell become

$$C_j = \frac{C}{1+e_j} \tag{6.9}$$

where $|e_j| << 1$. The matrix equation becomes

$$\begin{pmatrix} 1+3k+e_1 & -k & 0 & \dots & 0 \\ -k & 1+2k+e_2 & k & & \vdots \\ 0 & & \ddots & & 0 \\ \vdots & & -k & 1+2k+e_{N-1} & -k \\ 0 & \dots & 0 & -k & 1+3k+e_N \end{pmatrix} \vec{v'} = \Omega' \vec{v'}, \tag{6.10}$$

which can be expressed as

$$(\mathbf{A} + \mathbf{E})\vec{v'} = \Omega' \vec{v'} \tag{6.11}$$

where $\mathbf{E}_{ij} = \delta_{ij} e_j$.

Using a first order perturbation approach (the full treatment can be found in Padamsee,

Knobloch and Hays [52]), the eigenvalue change for the perturbed eigensystem can be found from

$$\begin{aligned}\delta\Omega^{(m)} &= \Omega'^{(m)} - \Omega^{(m)} \\ &= \left(\vec{v}^{(m)}\right)^T \mathbf{E}\vec{v}^{(m)} \\ &= \sum_{j,k} v_j^{(m)} \delta_{jk} e_j v_k^{(m)} \\ &= \sum_j v_j^{(m)} e_j v_j^{(m)}.\end{aligned} \tag{6.12}$$

For predicting the amplitude errors the perturbation approach gives

$$\begin{aligned}\delta\vec{v}^{(m)} &= \vec{v}'^{(m)} - \vec{v}^{(m)} \\ &= \sum_{n\neq m} \frac{1}{\Omega^{(m)} - \Omega^{(n)}} \sum_j v_j^{(m)} e_j v_j^{(n)} \vec{v}^{(n)}.\end{aligned} \tag{6.13}$$

Next a transformation matrix $\mathbf{H}$ is required to relate the perturbations in field $\delta\vec{v}^{(m)}$, which can be indirectly measured, to the capacitance errors $\vec{e}$, the vector of the components e_j.

$$\delta\vec{v}^{(m)} = \mathbf{H}\vec{e}. \tag{6.14}$$

$\mathbf{H}$ can be found by rearranging the summation in Equation 6.13

$$\begin{aligned}H_{lk}^{(m)} &= \sum_{j\neq m} \frac{v_l^{(j)} v_k^{(j)} v_k^{(m)}}{\Omega^{(m)} - \Omega^{(j)}} \\ &= \sum_{j\neq m} \frac{v_l^{(j)} v_k^{(j)} v_k^{(m)}}{2k[\cos(j\pi/N) - \cos(m\pi/N)]}\end{aligned} \tag{6.15}$$

The π mode, where the fields in neighbouring cells are π radians out of phase with each other, is the $m = N$ mode. This is the mode we want to tune. $\mathbf{H}$ for this mode is

$$\begin{aligned}H_{lk}^{(m)} &= \sum_{j\neq N} \frac{v_l^{(j)} v_k^{(j)} v_k^{(N)}}{\Omega^{(N)} - \Omega^{(j)}} \\ &= \sum_{j\neq N} \frac{v_l^{(j)} v_k^{(j)} v_k^{(N)}}{2k[\cos(j\pi/N) + 1]}\end{aligned} \tag{6.16}$$

A bead-pull technique can be used to measure the change in cavity frequency in response to a perturbation of the already out-of-tune structure $\delta f_j'^{(N)}$ when perturbed by a bead in the centre of each cell j. To use Equation 6.14 these must be converted to $\delta v_j^{(N)}$. Again modelling as a first order perturbation for the π mode, and using primes to represent the out-of-tune solution, it can be found that

$$\delta\Omega_j'^{(N)} = (v_j'^{(N)})^2 e_{\text{bead}} \tag{6.17}$$

and from Equation 6.17 and the definition $\Omega = \omega^2/\omega_0^2$

$$\begin{aligned} \delta f_j'^{(N)} &= \frac{1}{2}\frac{\delta\Omega_j'^{(N)}}{\Omega'^{(N)}} f^{(N)} \\ &= \frac{1}{2}\frac{f'^{(N)}}{\Omega'^{(N)}}(v_j'^{(N)})^2 e_{\text{bead}} \end{aligned} \tag{6.18}$$

Expanding the $(v_j'^{(N)})^2$ term for small perturbations allows us to express it in terms of the unperturbed modes

$$(v_j'^{(N)})^2 = \left(v_j^{(N)}\right)^2 \left(1 + \frac{\delta v_j^{(N)}}{v_j^{(N)}}\right)^2 \simeq \left(v_j^{(N)}\right)^2 \left(1 + \frac{2\delta v_j^{(N)}}{v_j^{(N)}}\right) \tag{6.19}$$

this can be substituted in Equation 6.18, and then solve for $\delta v_j^{(N)}$ to find

$$\delta v_j^{(N)} = \left(\frac{\delta f_j'^{(N)}}{\left(v_j^{(N)}\right)^2} \left[\frac{2\Omega'^{(N)}}{e_{\text{bead}} f'^{(N)}}\right] - 1 \right) \frac{v_j^{(N)}}{2} \tag{6.20}$$

To find the term in square brackets consider the average of the frequency shifts, recalling that the $\vec{v}$ are normalised

$$\begin{aligned} < \delta f' > &= \frac{1}{N}\sum_j \delta f_j'^{(N)} \\ &= \frac{1}{2}\frac{f'^{(N)}}{\Omega'^{(N)}}\frac{e_{\text{bead}}}{N}\sum_j (v_j'^{(N)})^2 \\ &= \frac{1}{2}\frac{f'^{(N)}}{\Omega'^{(N)}}\frac{e_{\text{bead}}}{N} \end{aligned} \tag{6.21}$$

Substituting this and Equation 6.6 into Equation 6.20 we find

$$\delta v_j^{(N)} = \left(\frac{\delta f_j'^{(N)}}{< \delta f' >} - 1 \right) \frac{v_j^{(N)}}{2} \tag{6.22}$$

which expresses $\delta v_j^{(N)}$ in terms of only the unperturbed mode and the measured frequency shifts.

To use Equation 6.14 to calculate $\vec{e}$ we must invert $\mathbf{H}$. However $\mathbf{H}$ is singular and cannot be inverted. Information is lost in the transformation of absolute capacitance errors into amplitude changes. To make up for the missing information we assume the last cell of the structure is has $e_j = 0$, and strip off the last column of $\mathbf{H}$ to give a reduced matrix $\mathbf{H_r}$. Similarly we construct vectors $\vec{e_r}$ and $\delta\vec{v_r}$ of length $N-1$ and then

$$\vec{e_r} = (\mathbf{H_r})^{-1}\delta\vec{v_r}. \tag{6.23}$$

To use $\vec{e_r}$ to correct all the cells would tune the frequency of all cells to the last cell. To avoid this and produce no net change in frequency a corrected vector $\vec{e_c}$ is constructed.

$$\begin{aligned} (\vec{e_c})_j &= -\left[(\vec{e_r})_j - < \vec{e_r} >\right] \text{ for 1,...,(N-1)} \\ (\vec{e_c})_N &= < \vec{e_r} > \end{aligned} \tag{6.24}$$

where

$$< \vec{e_r} >= \frac{1}{N} \sum_{j=1}^{N-1} (\vec{e_r})_j \tag{6.25}$$

The capacitance errors ($\vec{e_c}$) can be converted to π-mode frequency corrections using

$$\delta \vec{f_c} = \vec{e_c} \frac{f^{\pi}}{2N} \tag{6.26}$$

To construct the model a value for k is required. This can be found by combining Equation 6.8 at two modes m and p and solving for k

$$k = \frac{\frac{1}{2}[(f^{(p)})^2 - (f^{(m)})^2]}{(f^{(m)})^2(1 - \cos(p\pi/N)) - (f^{(p)})^2(1 - \cos(m\pi/N))}. \tag{6.27}$$

6.2.2 Two-chain model of a dipole mode structure

The circuit model for a monopole mode described in subsection 6.2.1 was extended by Bane and Gluckstern [96] to model a dipole mode. This model consists of two parallel chains, one representing a TE mode, and the other a TM mode, with the modes modelled as travelling waves moving antiparallel to each other. The two chains couple with each other to model the behaviour of the hybrid of the TE and TM modes. The circuit model can be seen in Figure 6.6.

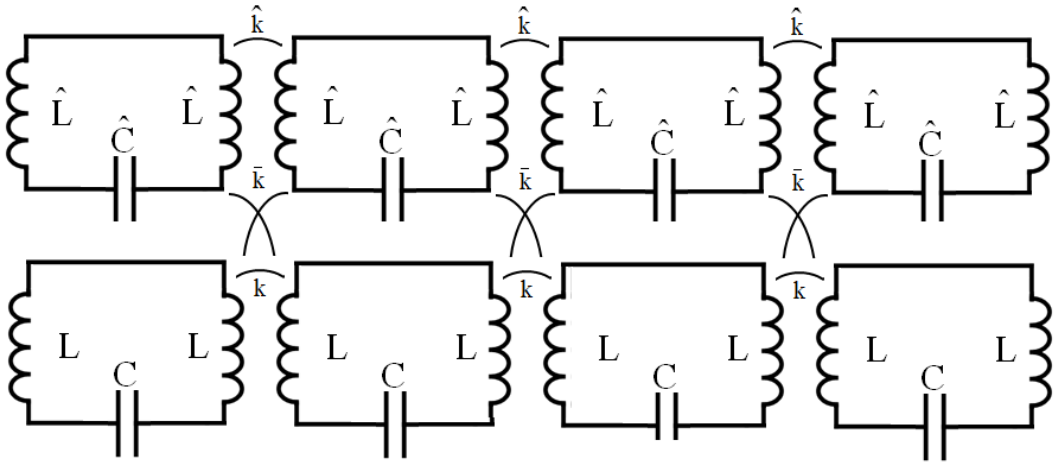

Figure 6.6: Two-chain circuit model of dipole mode.

The model was found to more accurately predict the dispersion curve of a dipole mode in a multicell structure than the monopole circuit model.

This model has been successfully used to model dipole modes as unwanted higher order modes in RF structures [85, 97], where the result of interest is the dispersion relation in order to predict the frequencies of these modes, but no record of its use in tuning a dipole mode deflecting cavity has been found.

Whilst the circuit equations for the two-chain model can be constructed in a similar way to to monopole mode model, the result is a much larger number of variables. Consider for example that there are now three coupling factors, one for each of: the TE mode, the TM mode, and the cross-coupling between the two modes. It is due to this complexity and large number of variables

for which to solve that a similar treatment to the method described in subsection 6.2.1 to find the frequency errors on each cell has not been attempted.

6.2.3 Singular Value Decomposition and the Pseudoinverse

Any real $m \times n$ matrix $\mathbf{A}$ can be factorised into a Single Value Decomposition (SVD) [98]:

$$\mathbf{A} = \mathbf{U}\mathbf{\Sigma}\mathbf{V}^{\mathbf{T}} \tag{6.28}$$

where the right singular vector of $\mathbf{A}$ is $\mathbf{U}$, an $m \times m$ real orthogonal matrix. $\mathbf{\Sigma}$ is an $m \times n$ rectangular diagonal matrix, whose diagonal consists of non-negative real numbers, which are the singular values of $\mathbf{A}$. The left singular vector of $\mathbf{A}$ is $\mathbf{V}$, an $n \times n$ real orthogonal matrix.

One of the applications of the SVD is that it allows the calculation of the pseudoinverse, a generalisation of the matrix inverse. As the SVD can be found for any matrix, the pseudoinverse allows the inversion of any matrix, including those that are singular, non-square or ill-conditioned.

The pseudoinverse (Moore-Penrose inverse), denoted by the + superscript, is given by

$$\mathbf{A}^{+} = \mathbf{V}\mathbf{\Sigma}^{+}\mathbf{U}^{\mathbf{T}} \tag{6.29}$$

where the $n \times m$ pseudoinverse of $\mathbf{\Sigma}$ is found by taking the reciprocal of each non-zero element of the diagonal and then transposing the matrix.

6.2.4 Singular Value Decomposition for tuning of an RF quadrupole

In 2016 Koubek et al [99] used a method involving SVD and the pseudoinverse to successfully tune a 750 MHz 4-vane RF quadrupole (RFQ).The RFQ has 8 sets of 4 tuners along its length, with each set having one tuner in each quadrant.

Bead-pulling was used to measure the fields in each quadrant, B_i with $i = 1..4$. These were then aligned to each other and and the quadrupolar, Q, and dipolar, Ds and Dt, components calculated via

$$\begin{aligned} Q &= (B_1 - B_2 + B_3 - B_4)/4 \\ Ds &= (B_1 - B_3)/2 \\ Dt &= (B_2 - B_4)/2 \end{aligned} \tag{6.30}$$

In the ideal case the quadrupolar component should be constant along the structure, and the dipolar components should be zero. The relative values are sufficient so Q is defined to be 100% on average. The requirement is for an equation system which can be solved for the ideal tuner settings based on the values of Q,Ds and Dt at a 11 longitudinal points in the structure.

A response matrix $\mathbf{M}$ was created by varying each tuner in turn and measuring the field distribution. The derivative of each field component at each measurement location could then be found. $\mathbf{M}$ was defined with elements

$$m_{i,j} = \frac{\partial V_i}{\partial T_j} \tag{6.31}$$

where i are the measurement locations and j is the number of tuners. The relation between the

change in the field distribution $\vec{V}$ and the change in tuner settings $\vec{T}$ is then

$$\vec{V} = \mathbf{M} \cdot \vec{T} \tag{6.32}$$

By inverting the matrix $\mathbf{M}$ the required change in tuner settings $\vec{T}'$ required to produce a desired change in the field components $\vec{V}'$ could be found

$$\vec{T}' = \mathbf{M}^{-1} \cdot \vec{V}' \tag{6.33}$$

The equation is over-determined therefore $\mathbf{M}$ is non-square and ill-conditioned. By using the SVD the pseudoinverse of $\mathbf{M}$ can be found and thus the $\vec{T}'$. The tuners can then be adjusted as prescribed. In practice the procedure was iterative due to errors in the tuner adjustment and the system not being perfectly linear. After six iterations the field distribution of all components was in an acceptable range. The results of the iterative tuning can be seen in Figure 6.7.

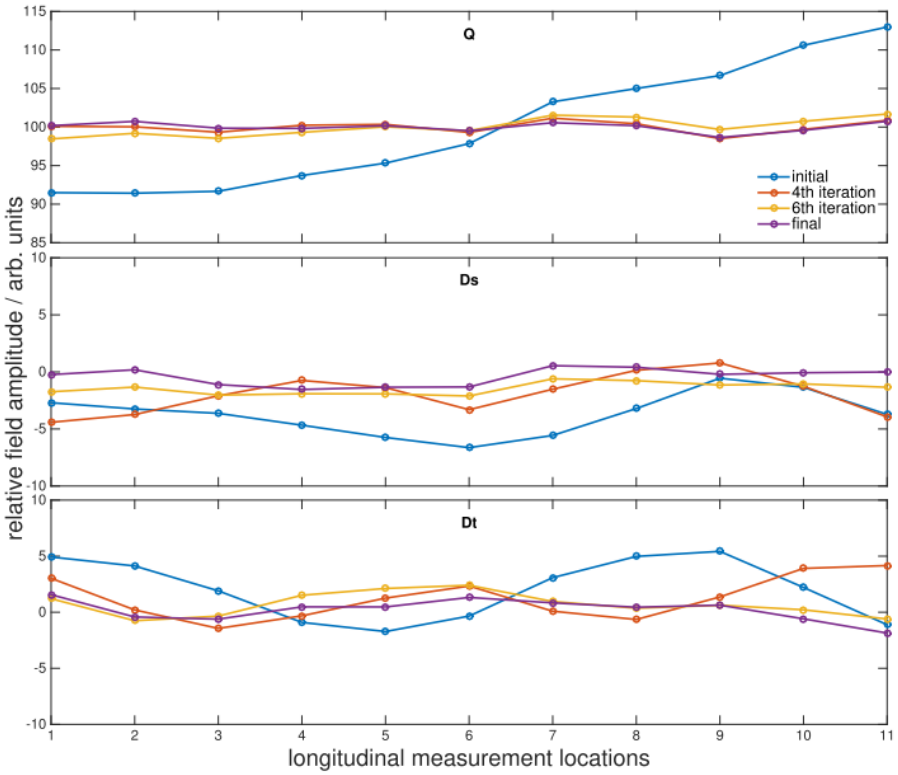

Figure 6.7: Results of iterative tuning on amplitude of Q,Ds and Dt. Figure reproduced from [99].

6.3 Methods for comparison

The methods of predicting the error in each cell from the field profile results that will be used for comparison will be referred to as Unmodified Circuit Model, Modified Circuit Model, Pseudoinverse, and Pseudoinverse with Coupling.

6.3.1 Unmodified Circuit Model

The Unmodified Circuit Model is the tuning method described in subsection 6.2.1.

For a dipole mode structure, the fields of note for deflection are the transverse electric field on axis E_x, the transverse magnetic field on axis H_y. E_x is maximal in the irises between cells, which makes it a poor fit for this tuning method. The axial electric field off axis by an arbitrary (but consistent) distance, E_z is the closest analogue to the on-axis E_z measured for the monopole mode. This field component was chosen to use with this method, measured at 5 mm vertically off-axis.

The value for the coupling constant k was calculated from Equation 6.27, using the π mode and the $8\pi/9$ mode. The frequency of the $8\pi/9$ mode was calculated in CST using a periodic single cell model. For $N = 9$ cells, k becomes

$$k = \frac{\frac{1}{2}[(f^{(N)})^2 - (f^{(8)})^2]}{2(f^{(8)})^2) - (f^{(N)})^2(1 - \cos(8\pi/N))} = -0.01211. \tag{6.34}$$

It is important to note that this k value is negative, signifying inductive coupling.

The matrix $\mathbf{A}$ is constructed just as in Equation 6.5. The relation $\gamma = 2k$ is used, but is now an approximation, as the structure is not field flat in E_z. From the matrix, the eigenvalues for the unperturbed system $\Omega^{(m)}$ can be found.

A CST simulation was used to find the dispersion curve for the unperturbed structure. To compare this to the frequency of each mode f_m from the calculated eigenvalues we use

$$f_m = f_0\sqrt{\Omega^{(m)}} \tag{6.35}$$

where f_0 is the frequency of the 0th mode in the pass-band. To find this we use the frequency of the π mode from the unperturbed CST simulation and rearrange Equation 6.8 to find

$$f_0 = f_m\sqrt{2k[1 - \cos(N\pi/N)]}. \tag{6.36}$$

As the eigenvalues range from 1 to $1 + 4k$, and the f_m are not used in the model, it is arbitrary to choose this method or to use the simulated value for the frequency of the 0th mode from a periodic single cell 3D simulation. As some variation from the simulated dispersion curve is expected this option was chosen so that the dispersion curves will match at the operating frequency. The two curves are shown in Figure 6.8. It can be seen that the curves diverge, which, as the calculated frequency errors will have contributions from all modes, may cause some inaccuracy in the predictions of the model.

As the field components can be extracted from a CST model without the need for a perturbation "bead-pull" measurement, Equation 6.22 can be altered to take the field component measurement for each cell directly:

$$\delta v_j^{(N)} = \left(\frac{(E_z)_j'^{(N)}}{< (E_z)' >} - 1\right)\frac{v_j^{(N)}}{2}, \tag{6.37}$$

where the values of $(E_z)_j'^{(N)}$ are measured at the centre of each cell longitudinally. The matrix $\mathbf{H}$ was constructed and the reduced matrix $\mathbf{H_r}$ produced as described in subsection 6.2.1, as well as the reduced $\delta\vec{v_r}$. The frequency errors $\delta\vec{f_c}$ to bring the cells in tune without changing the frequency of the operating mode were then calculated as as described in subsection 6.2.1.

As the structure was designed to be field-flat in H_y, E_z is not field-flat. This method gives the $\delta\vec{f_c}$ required to give a field-flat structure in the given component. Therefore the model was first run with input values from the ideally tuned structure which is field flat in H_y. This gives the $\delta\vec{f_{ideal}}$ between the ideal model and one that would be field flat in E_z. The model is then run

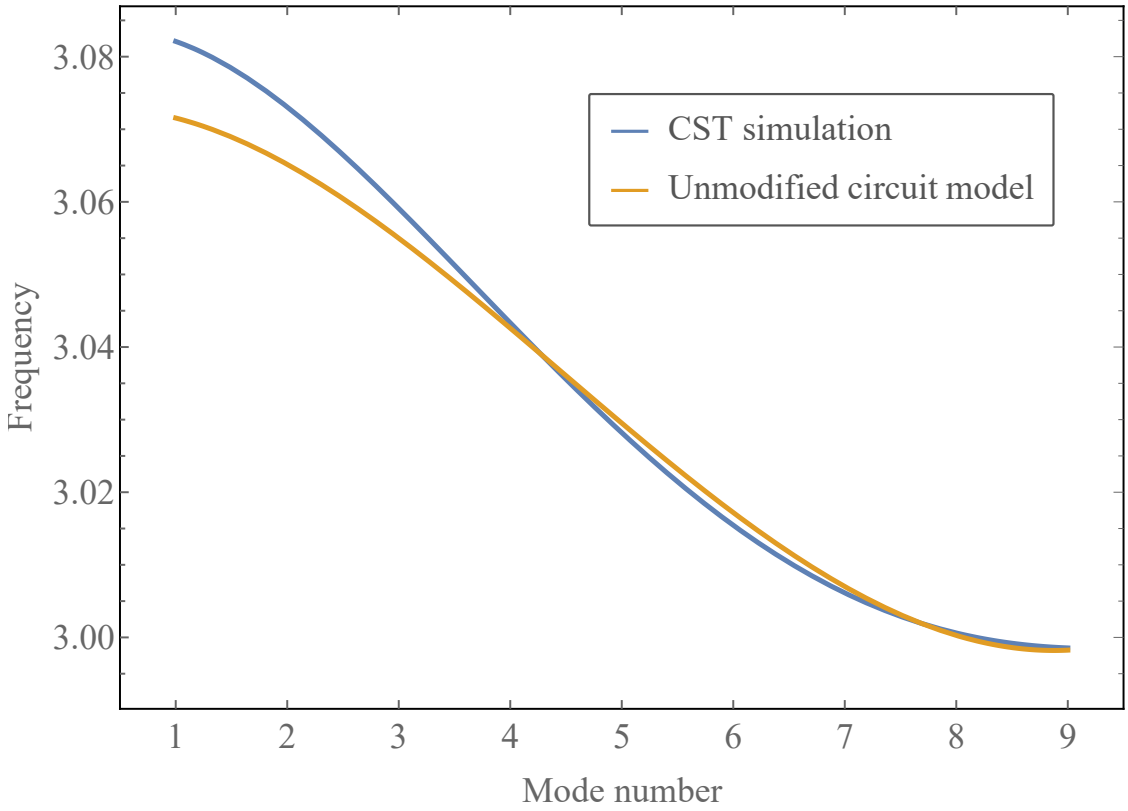

Figure 6.8: Comparison of dispersion curve from CST simulation (blue) and Unmodified Circuit Model (orange).

again with the test input model that has errors to give $\delta \vec{f_{test}}$. The required $\delta \vec{f_{req}}$ for tuning is then

$$\delta \vec{f_{req}} = \delta \vec{f_{test}} - \delta \vec{f_{ideal}}. \tag{6.38}$$

As the aim is to tune for the field profile only, and not frequency correction, this is the required result. However to enable comparison to known errors we can add a frequency correction. The average frequency correction required is divided by $2\vec{\hat{E}_z}$

$$\delta \vec{f^{(\pi)}} = \frac{f^{(\pi)}_{desired} - f^{(\pi)}_{measured}}{2 \times 9 \vec{\hat{E}_z}} \tag{6.39}$$

where $\vec{\hat{E}_z}$ is the vector of the peak E_z in each cell normalised to the mean value of $(E_z)_j$, and the factor of 2 is due to the dipole mode. The $\vec{\hat{E}_z}$ factor is required as cells with more field have a larger effect on frequency when tuned.

The required $\delta \vec{f_{full}}$ for frequency and field profile correction is then

$$\delta \vec{f_{full}} = \delta \vec{f_{req}} - \delta \vec{f^{(\pi)}}. \tag{6.40}$$

6.3.2 Modified Circuit Model

As there is a resonant mode in the irises between the cells of the structure, the structure could be modelled as a set of resonantly coupled LC circuits, as shown in Figure 6.9. The coupling factor would then be

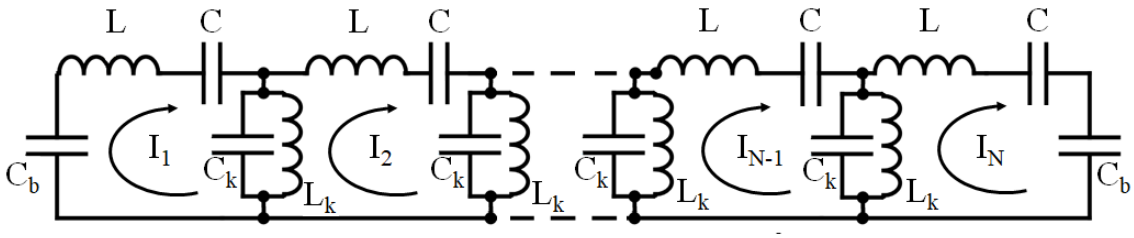

Figure 6.9: Resonantly coupled circuit model.

$$k = \frac{CL_k}{C_k(L_k - 1/(\omega^2 C_k))} \tag{6.41}$$

where C is the cell capacitance, and L_k and C_k are the coupler inductance and capacitance. k now has a frequency dependence, which is shown in Figure 6.10.

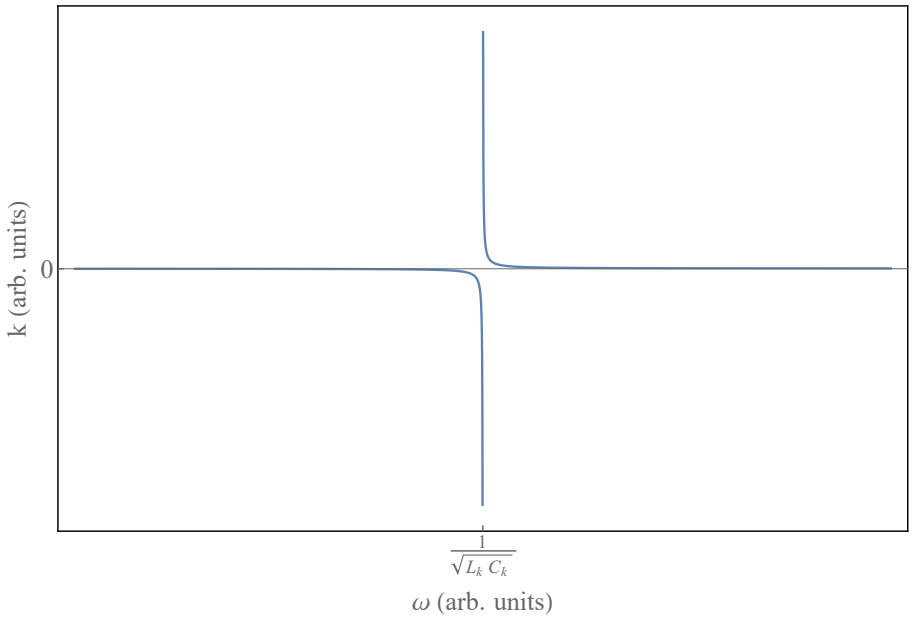

Figure 6.10: The frequency dependence of the resonant coupling factor k.

For the perturbation theory method we need an eigenmatrix whose eigenvalues are defined as $\Omega = \frac{\omega^2}{\omega_0^2}$, therefore a frequency dependent k cannot be used inside the matrix.

The resonance frequency of the mode in the iris is higher than the cavity frequency. The inductor dominates, as is clear from the negative k value as in Equation 6.34. However the inductor strength varies symmetrically along the cavity, as shown in Figure 6.11, and therefore k varies in the same way. This is modelled by letting each symmetric pair of inductors have a different k value k_j, where k_0 are the beam pipe coupling strengths and j increments by 1 along the circuit up to $j = 4$ for the inductors either side of the middle cell, and then decrements back to $j = 0$. Matrix $\mathbf{A}$ becomes

$$\mathbf{A} \equiv \begin{pmatrix} 1+k_0+k_1 & -k_1 & 0 & \dots & 0 \\ -k_1 & 1+k_1+k_2 & -k_2 & \vdots & \\ 0 & & \ddots & & 0 \\ \vdots & & -k_2 & 1+k_1+k_2 & -k_1 \\ 0 & \dots & 0 & -k_1 & 1+k_0+k_1 \end{pmatrix}. \tag{6.42}$$

Recalling that

$$\mathbf{A}\vec{v} = \Omega\vec{v} \tag{6.43}$$

and solving the jth eigenvalue equation for v_{j+1} we find

$$\begin{aligned} v_2 &= \left(\frac{1+k_0+k_1-\Omega}{k_1}\right) v_1 \\ v_j &= \left(\frac{1+k_{j-2}+k_{j-1}-\Omega}{k_{j-1}}\right) v_{j-1} - \left(\frac{k_{j-2}}{k_{j-1}}\right) v_{j-2},\ 2<j<4 \\ v_6 &= \left(\frac{1+2k_4-\Omega}{k_4}\right) v_5 - v_4 \\ v_j &= \left(\frac{1+k_{N-j+1}+k_{N-j+2}-\Omega}{k_{N-j+1}}\right) v_{j-1} - \left(\frac{k_{N-j+2}}{k_{N-j+1}}\right) v_{j-2},\ 6<j<9 \\ v_9 &= \left(\frac{k_1}{1+k_0+k_1-\Omega}\right) v_8. \end{aligned} \tag{6.44}$$

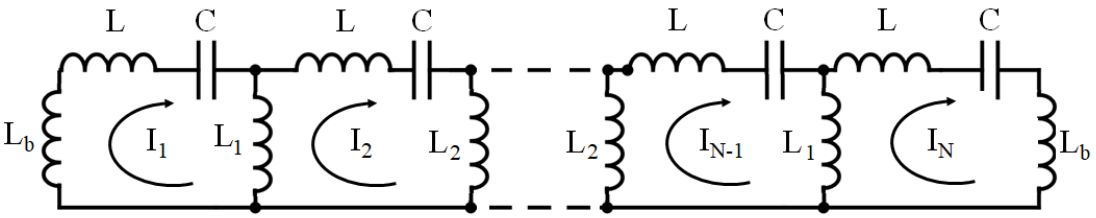

Figure 6.11: Inductively coupled circuit model with symmetrically varying coupling inductor strength.

Setting $v_1 = 0$, we now have a system of equations that give the relative voltages for the tuned structure. A simplex optimisation process [100] was used to find the k_j by minimising the fitting function $g(\vec{k})$

$$g(\vec{k}) = \sqrt{\sum_j |v_j(\vec{k})| - (\tilde{E_z})_j^{(N)})^2} \tag{6.45}$$

at the frequency of the π mode, where the $(\tilde{E_z})_j^{(N)}$ were taken from the simulation of the π mode in the tuned structure and normalised to the first cell. The initial values used were and $k_0 = 2k$ and $k_j = k$ for $j < 0$ where $k = -0.01211$ is the unmodified circuit coupling factor.

The optimised value of $\vec{k} = (-0.0248147, -0.0120203, -0.0120606, -0.0120747, -0.0121017)$, minor changes from the initial values.

The optimised $v_j(\vec{k})$ and $(\tilde{E_z})_j^{(N)}$ are shown in Figure 6.12. The residuals are all below 10^{-13}, so the points on the plot are overlaid.

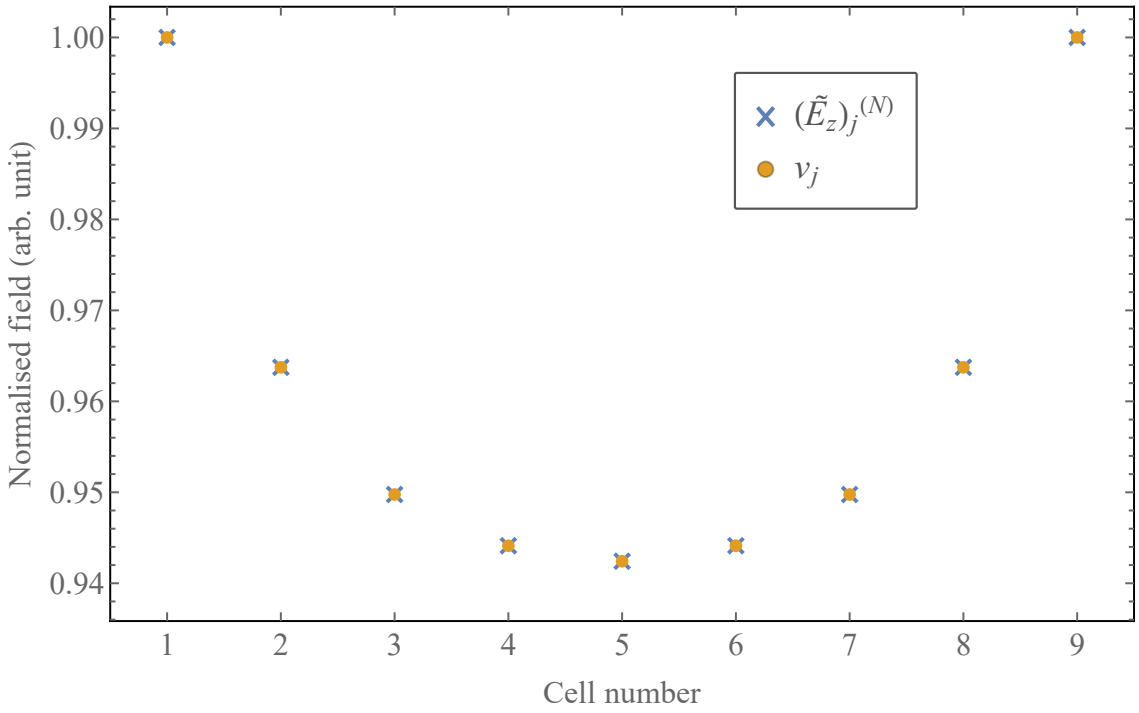

Figure 6.12: Comparison of field profile from CST simulation $(\tilde{E_z})_j^{(N)}$ and optimised $v_j(\vec{k})$.

Finding f_m from the eigenvalues as in Section 6.3.1, the dispersion curve can be found. It is shown in Figure 6.13 compared to the curve from the CST simulation and the curve from the unmodfied circuit. There is little change from the unmodified model. Again the divergence of these curves may cause some inaccuracy in the predictions of the model. Now the new matrix $\mathbf{A}$ has been constructed we can find $\delta\vec{f_{freq}}$ and $\delta\vec{f_{full}}$ in the same way as in Section 6.3.1.

6.3.3 Pseudoinverse

There are three field components of interest: E_x and H_y on axis and E_z at 5mm off axis. These can all be measured with a bead-pull perturbation measurement. In the ideal case each field component will match that of the optimised CST model. To form a response matrix, 9 CST Studio Suite [38] Frequency Domain solver simulations were performed of the 3D TDC model, each with a 10 µm larger radius of one cell than the optimised design.

From each simulation the peak field in each cell was extracted for H_y on axis and E_z at 5mm off axis, and the peak field in each iris (including the beam-pipe irises) for E_x on axis. This totalled $9 + 9 + 10 = 28$ values, V_i, each found for the 9 cases of an error on each of the cells. The ideally tuned model was also simulated to find the same 28 values in the unperturbed case, $V_{i(0)}$. The normalised difference between the tuned and each untuned model ∂V_i was found from

$$\partial V_i = \frac{V_{i(0)} - V_i}{V_{i(0)}}. \tag{6.46}$$

The response matrix $\mathbf{M}$ was constructed with elements

$$m_{i,j} = \frac{\partial V_i}{\partial R_j} \tag{6.47}$$

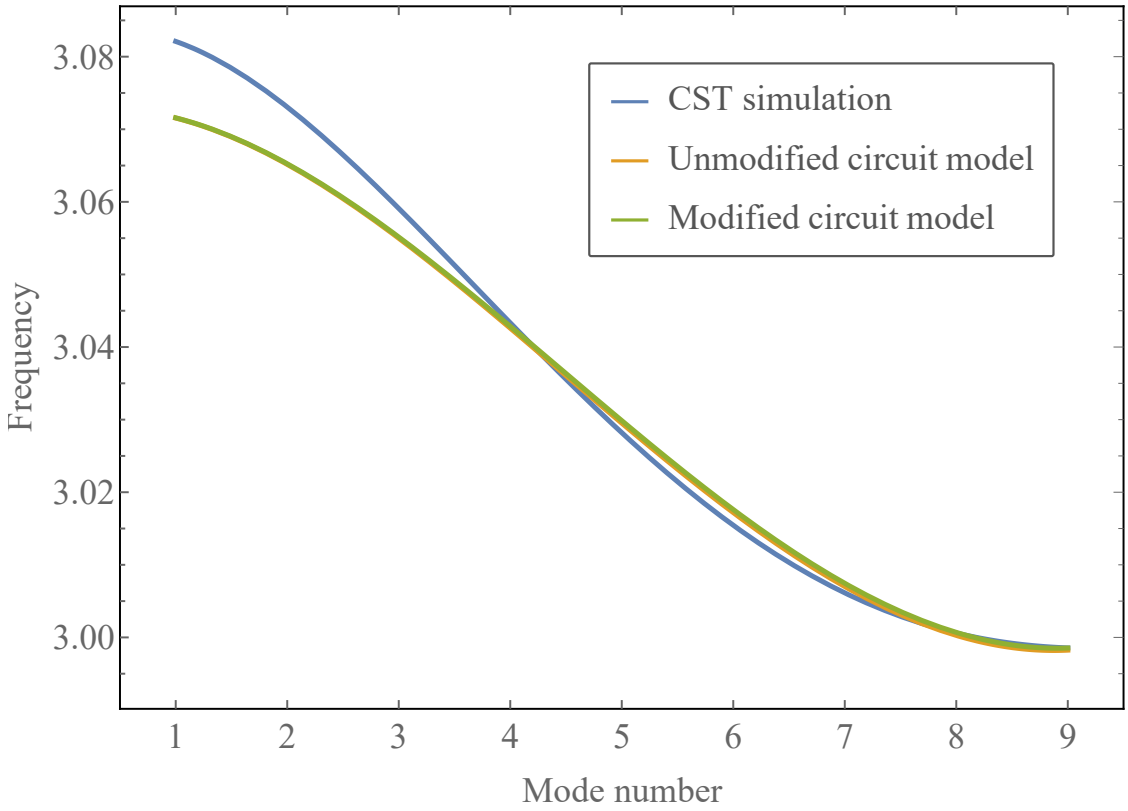

Figure 6.13: Comparison of dispersion curve from CST simulation (blue), Unmodified Circuit Model (orange), and Modified Circuit Model (green).

where the i are the 28 field measurement indices and ∂R_j is the radius change on cell j. We have a 28×9 response matrix which shows the relation between the desired change in the 3 field profiles and the change of the cell radius:

$$\vec{V} = \mathbf{M} \cdot \vec{R} \tag{6.48}$$

where

$$\mathbf{M} = \begin{pmatrix} \frac{\partial (E_x)_1}{\partial R_1} & \frac{\partial (E_x)_1}{\partial R_2} & \cdots & \frac{\partial (E_x)_1}{\partial R_9} \\ \vdots & \vdots & \ddots & \cdots \\ \frac{\partial (E_x)_{10}}{\partial R_1} & \frac{\partial (E_x)_{10}}{\partial R_2} & \cdots & \frac{\partial (E_x)_{10}}{\partial R_9} \\ \frac{\partial (E_z)_1}{\partial R_1} & \frac{\partial (E_z)_1}{\partial R_2} & \cdots & \frac{\partial (E_z)_1}{\partial R_9} \\ \vdots & \vdots & \ddots & \cdots \\ \frac{\partial (E_z)_9}{\partial R_1} & \frac{\partial (E_z)_9}{\partial R_2} & \cdots & \frac{\partial (E_z)_9}{\partial R_9} \\ \frac{\partial (H_y)_1}{\partial R_1} & \frac{\partial (H_y)_1}{\partial R_2} & \cdots & \frac{\partial (H_y)_1}{\partial R_9} \\ \vdots & \vdots & \ddots & \cdots \\ \frac{\partial (H_y)_9}{\partial R_1} & \frac{\partial (H_y)_9}{\partial R_2} & \cdots & \frac{\partial (H_y)_9}{\partial R_9} \end{pmatrix}. \tag{6.49}$$

Figure 6.14 shows $\frac{\partial V_i}{\partial R_j}$ for $1 < j < 5$, split into the three field components. The remaining R_j

are symmetric about the structure centre.

By inverting the matrix $\mathbf{M}$ the required change in cell radius $\vec{R'}$ required to produce a desired change in the field components $\vec{V'}$ could be found

$$\vec{R'} = \mathbf{M}^{-1} \cdot \vec{V'} \tag{6.50}$$

The matrix cannot be inverted as it is non-square and ill-conditioned; the system is overdetermined. The pseudoinverse of the matrix $\mathbf{M}^{+}$was calculated using the Wolfram Mathematica [36] function PseudoInverse, which is based on SVD. Then we may use

$$\vec{R'} = \mathbf{M}^{+} \cdot \vec{V'} \tag{6.51}$$

with any measured field vector $\vec{V'}$ to find the required cell radii changes to reach the ideal field profile. As previously this is the required result tune for the field profile only, without frequency correction. However to enable comparison to known errors we can alter the model to contain a frequency correction by adding an extra value to the end the field component vector $\vec{V}$, adding a new row to the matrix $\mathbf{M}$

$$m_{29,j} = \frac{\partial f}{\partial R_j} \tag{6.52}$$

where

$$\partial f = w\frac{f_0 - f}{f_0}, \tag{6.53}$$

where f_0 is the ideal frequency, f is the measured frequency for each detuned model, and w is a weighting that is used to ensure ∂f does not dominate, as ∂f is much larger than any of the $\partial \vec{V_i}$. Then a test $\vec{V'}$ must have $\partial f'$ as the last value to find $\vec{R'}$

6.3.4 Pseudoinverse with Coupling

It was noted that the radial change of the middle cell, cell 5, of the structure had the smallest effect on the field profile compared to radial errors on the other cells, as can be seen in Figure 6.14. This is due to the symmetry of the structure. This could cause uncertainty in the radial change prediction for cell 5. To increase the robustness of the Pseudoinverse method, we can use the input coupling factor, β_c, which is most sensitive to changes in the radius of cell 5:

$$\begin{aligned} \beta_c &= \frac{1 - \Gamma_{min}}{1 + \Gamma_{min}} (\text{Undercoupled case}) \\ \beta_c &= \frac{\Gamma_{min} + 1}{\Gamma_{min} - 1} (\text{Overcoupled case}) \end{aligned} \tag{6.54}$$

where Γ_{min} is the minimum value of the reflected (S11) resonance curve. Over- or under-coupledness was determined from the Polar Plot. β_c was calculated for each detuned model. The normalised difference from the ideal β_c β_{c0} is

$$\partial\beta_c = \frac{\beta_{c0} - \beta_c}{\beta_{c0}}, \tag{6.55}$$

where f_0 is the ideal frequency and f is the measured frequency for each detuned model. $\partial\beta_c$ was added as an extra value at the end the field component vector $\vec{V}$, adding a new row to $\mathbf{M}$

$$m_{30,j} = \frac{\partial\beta_c}{\partial R_j} \tag{6.56}$$

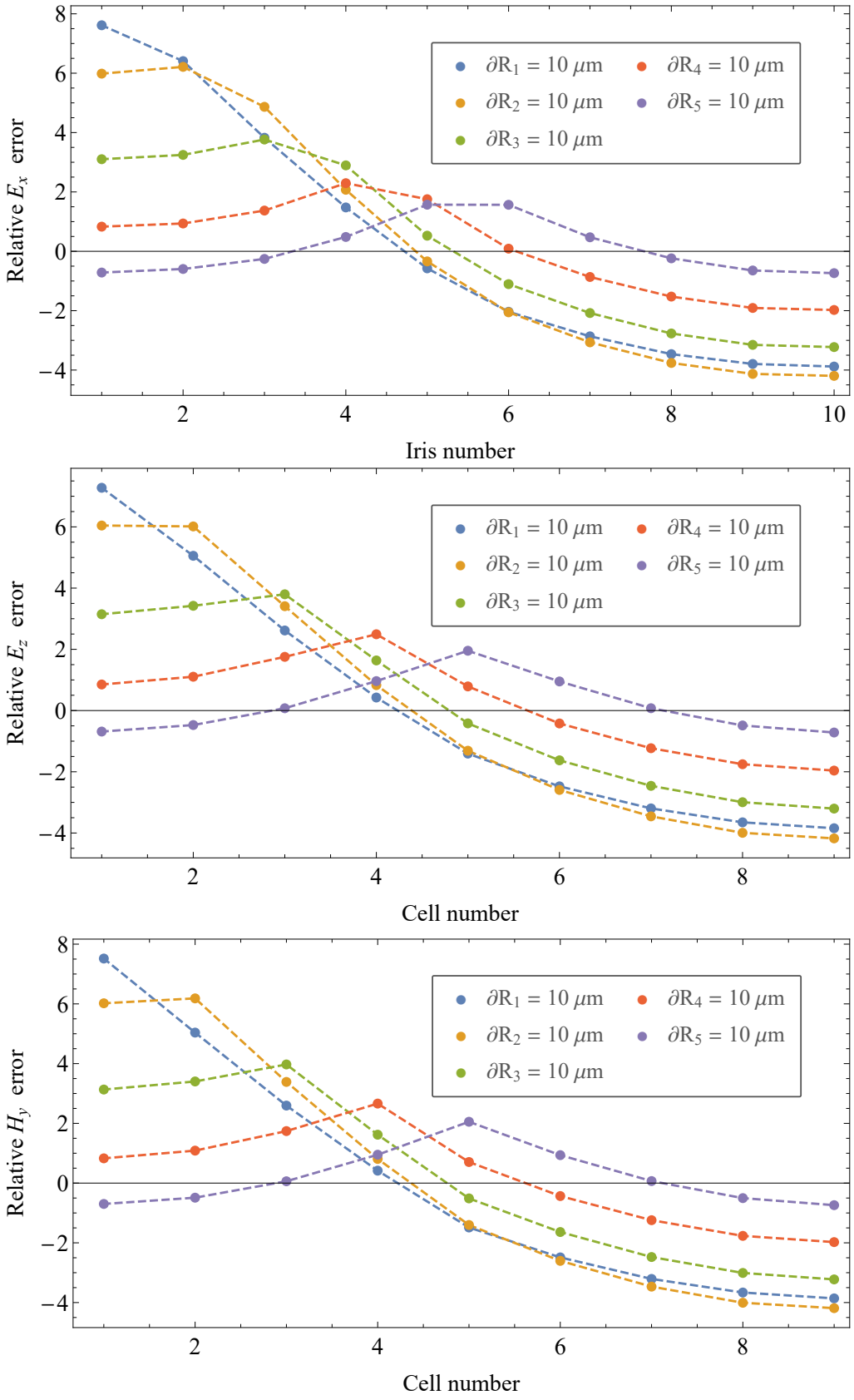

Figure 6.14: $\frac{\partial V_i}{\partial R_j}$ for $1 < j < 5$ split into the three field components E_x on-axis, measured at the irises, E_z 5 mm off-axis, measured at the longitudinal centre of each cell, H_y on-axis, measured at the longitudinal centre of each cell.

This can be inverted in the same way, $\mathbf{M}$ now requiring a vector $\vec{V}'$ with the last element β_c to find the required radii changes $\vec{R}'$ to reach the ideal field profile (and coupling).

6.4 Testing and results

To test each method, a random number generator was used to assign a radial cell error, e_j where j is the cell number, of between -20 μm and +20 μm to up to 5 different cells of the structure. This was repeated to create 20 structures in CST Studio Suite that each had small errors. The fabrication tolerance on the cell radius is ± 10 μm, so the tests have reasonable expectations of the possible errors.

Table 6.1 shows the parameters that were extracted from the simulation of each test, and the methods that use each parameter.

Table 6.1: Parameters and number of values extracted from simulation, and the methods which take them as inputs. The methods are: 1 = Unmodified Circuit Model, 2= Modified Circuit Model, 3= Pseudoinverse, and 4= Pseudoinverse with Coupling.

Parameter	No. of values	1	2	3	4
Peak E_x on-axis in irises	10			x	x
Peak H_y on-axis in cells	9			x	x
Peak E_z 5 mm off-axis in cells	9	x	x	x	x
Resonant frequency of π mode	1	x	x		
Minimum of S11 (Γ_{min})	1				x
Coupledness	1				x

Each method was performed on each of the 20 tests. The H_y on axis for each test is compared to the unperturbed case in Figure A.1 in Appendix A.

The two methods that use the pseudoinverse return the result as an "effective radial error", R'_j for each cell which would cause the detuned field profile. These can be compared to the input parameters, R_j directly. The weighting w from Equation 6.53 must be found to optimise the frequency correction.

The value δR, the mean of the residuals, that is the mean of the difference between the input radial errors and the predicted radial errors, was found for each test, as a function of the weighting w,

$$\delta R(w) =< R_j - R'_j(w) > . \tag{6.57}$$

This value can be seen plotted against the resonant frequency of the test structure for a range of w in Figure 6.15, for both pseudoinverse based methods. It can be seen that there is a frequency dependence to δR with no frequency correction ($w = 0$) which weakens as w is switched on. To find the optimum we use the standard deviation of $\delta R_{abs}(w)$ where

$$\delta R_{abs}(w) =< |R_j - R'_j(w)| > . \tag{6.58}$$

This can be seen in Figure 6.16 for both pseudoinverse based models. The value of w is chosen as 505 for the Pseudoinverse method and 650 for Pseudoinverse with Coupling method.

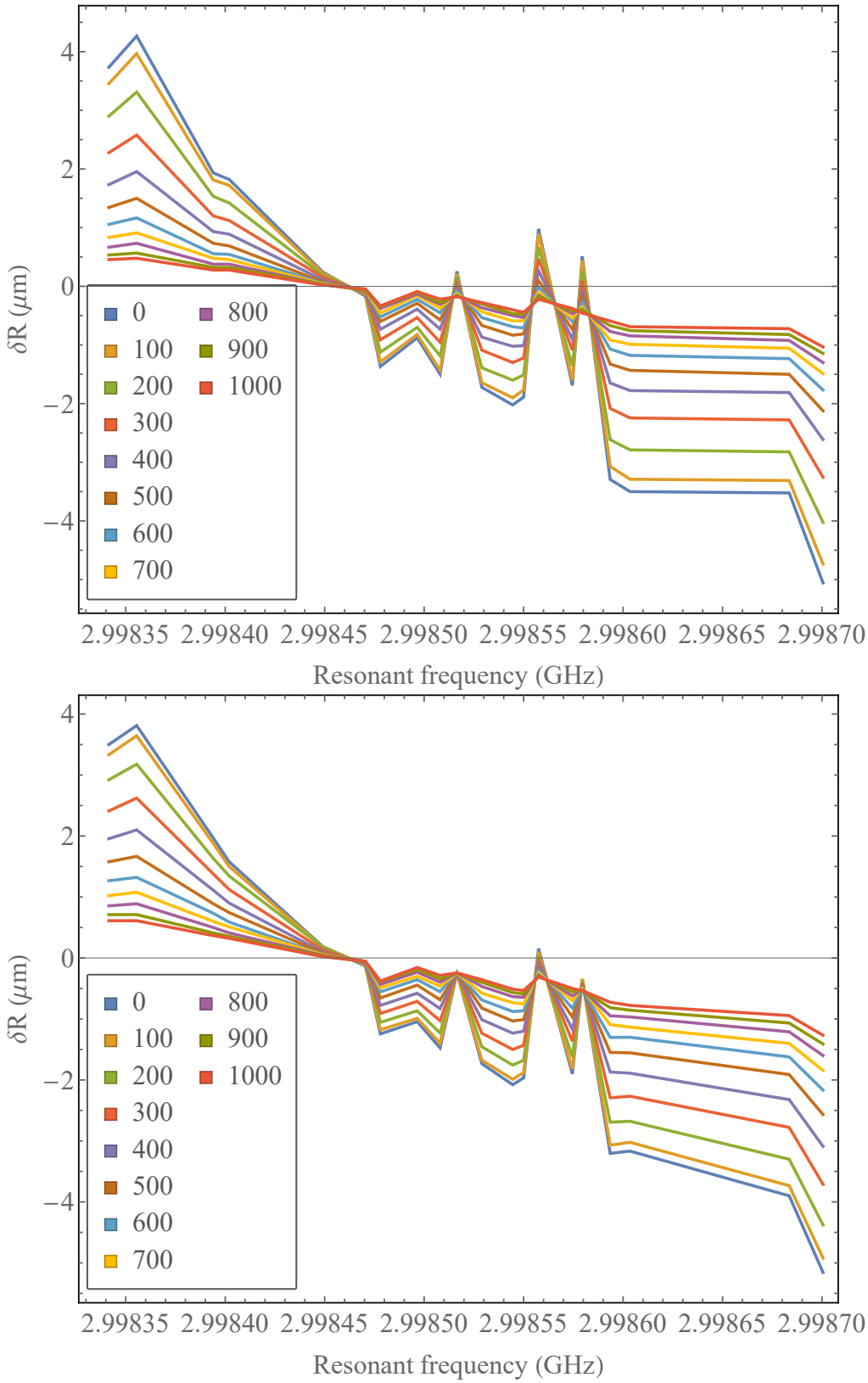

Figure 6.15: $\delta R(w)$ versus structure frequency for a range of w for the Pseudoinverse (top) and Pseudoinverse with Coupling (bottom)models.

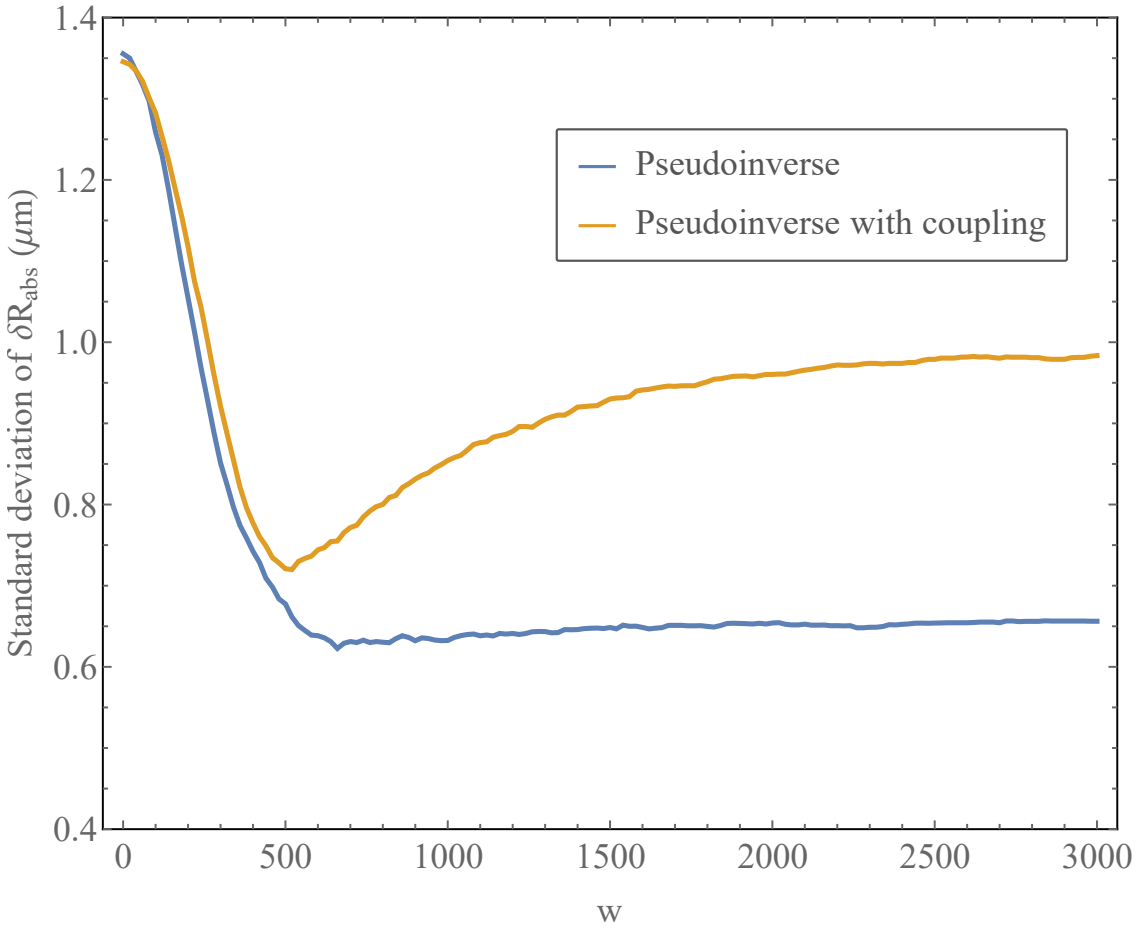

Figure 6.16: Variation in $\delta R_{abs}(w)$ with w for the Pseudoinverse and Pseudoinverse with Coupling models.

The equivalent circuit models based methods return the result as a change in frequency $\delta\vec{f_{full}}$ for each cell which would cause the detuned field profile. To compare to the input parameters a scaling factor is required. A single cell simulation found that the scaling factor between radius and frequency $dr/df = -2.09 \times 10^{-8}$ mm/Hz, however this was found to produce effective radial errors far smaller than the input values. Pragmatically, a new scaling factor s was found that gave the minimum value for a fitting function

$$s = \text{Min}\left[\sum_{N}^{20}\sum_{j}^{9} |R_j - s\delta(f_{full})_j|\right] \tag{6.59}$$

where N is the number of tests. We can then use $R'_j = sdf'_j$ to find the effective radial errors. The factor s has a value of -3.85×10^{-7} mm/Hz and is the same for both equivalent circuit models. The reason for this discrepancy is unknown. As the tuners on the TDC are not calibrated, the absolute size of the cell errors is only of interest for comparison purposes.

Figure 6.17 has 20 plots, each plot compares the input radial errors to the radial errors from the 4 models for the 20 examples.

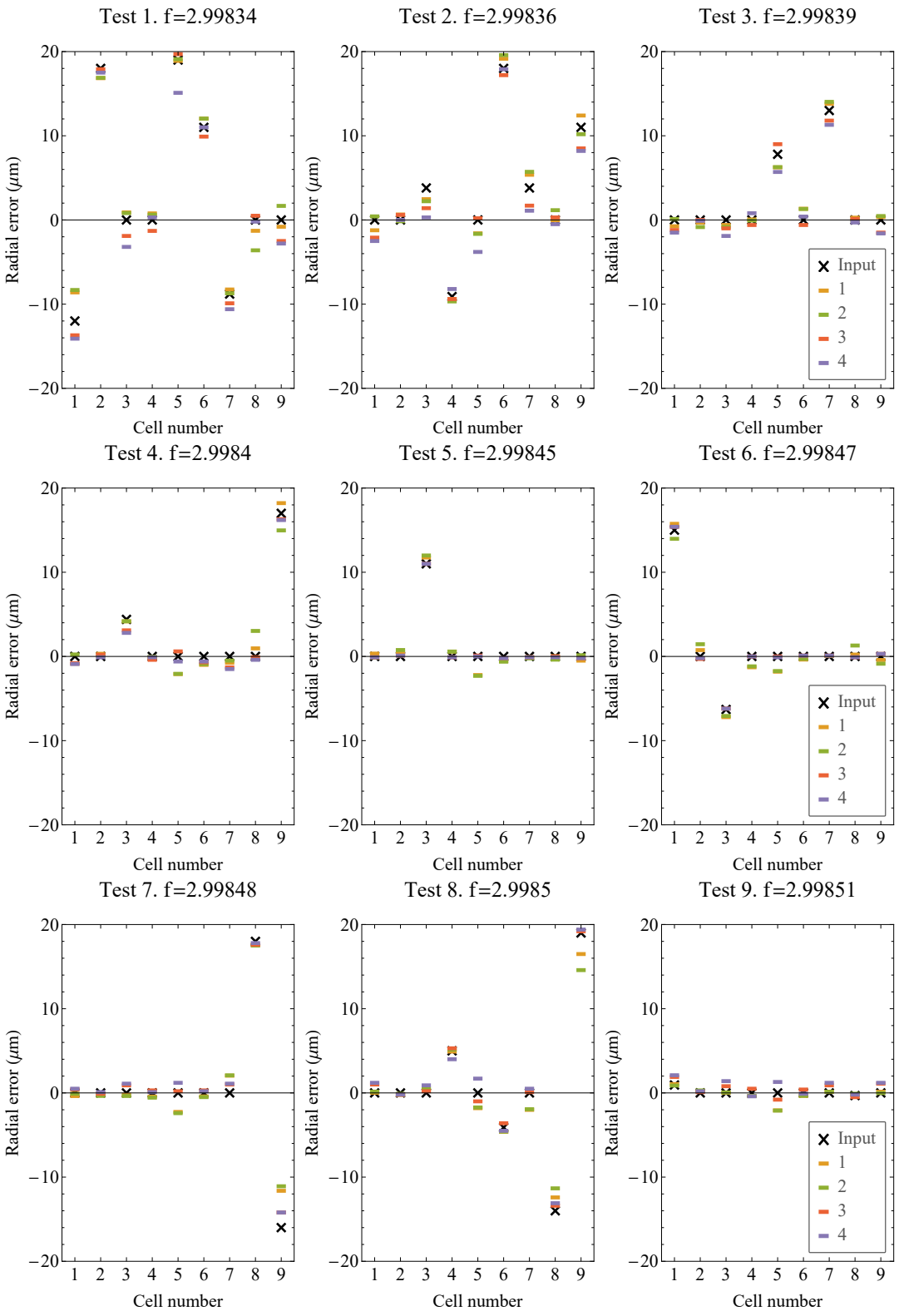
Test 1. f=2.99834
Test 2. f=2.99836
Test 3. f=2.99839
Test 4. f=2.9984
Test 5. f=2.99845
Test 6. f=2.99847
Test 7. f=2.99848
Test 8. f=2.9985
Test 9. f=2.99851
Radial error (μm)
Cell number
Input
1
2
3
4

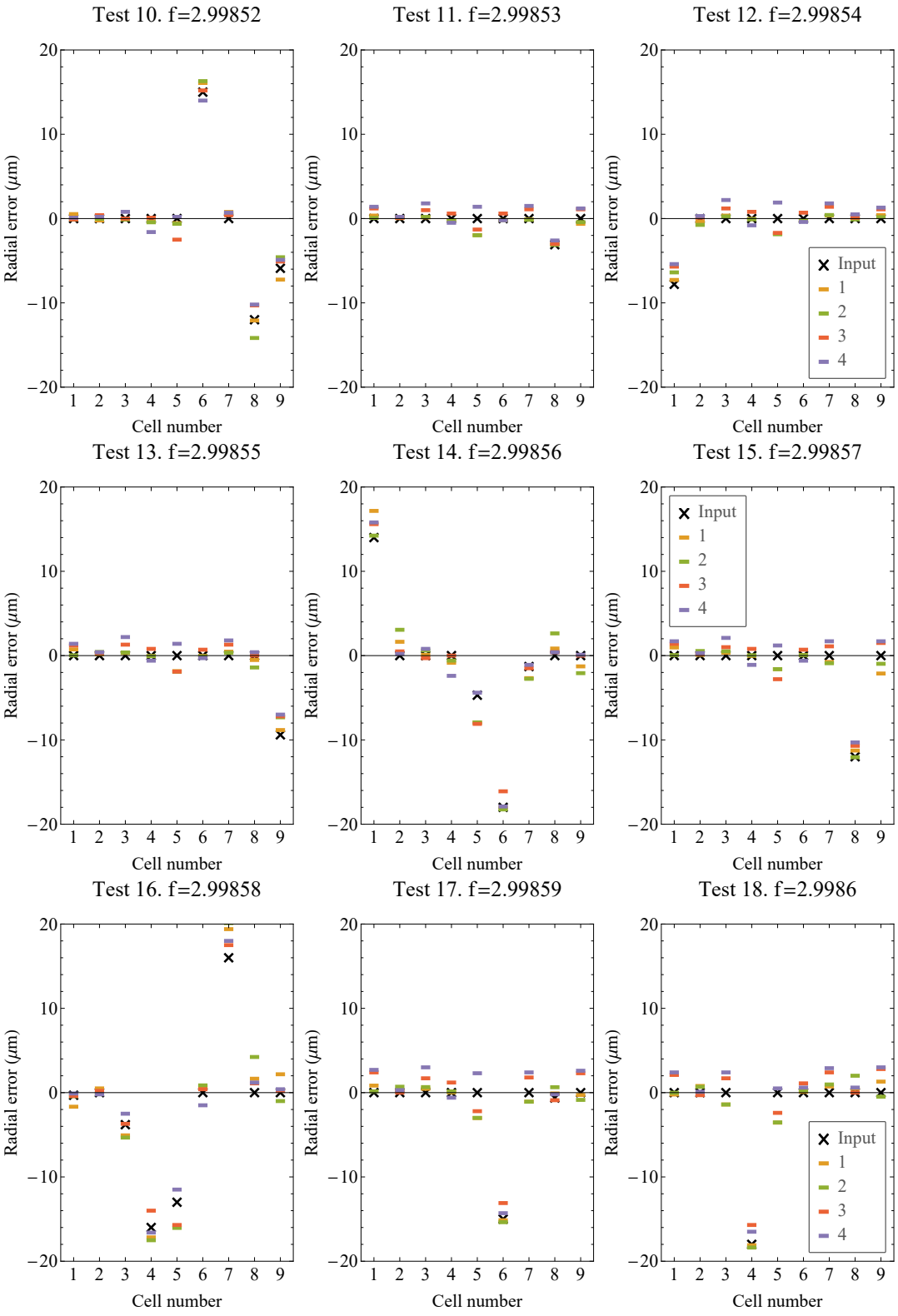
Test 10. f=2.99852
Test 11. f=2.99853
Test 12. f=2.99854
Test 13. f=2.99855
Test 14. f=2.99856
Test 15. f=2.99857
Test 16. f=2.99858
Test 17. f=2.99859
Test 18. f=2.9986
Radial error (μm)
Cell number
Input
1
2
3
4

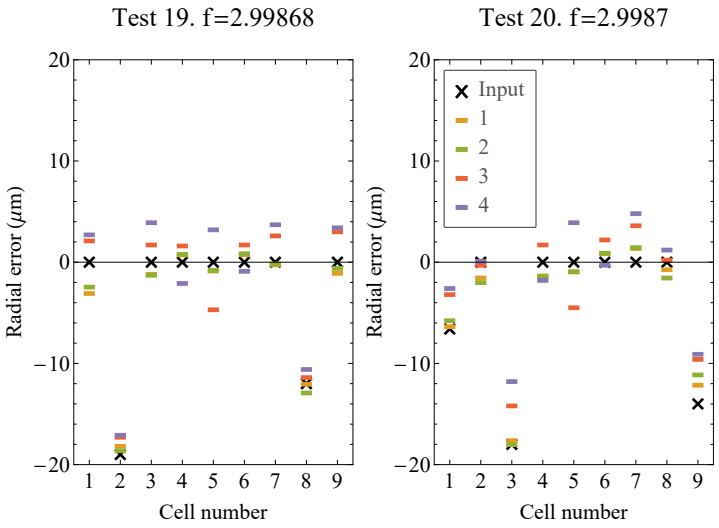

Figure 6.17: Predicted radial error from each method compared to the input radial error for the 20 test cases. The methods are: 1 = Unmodified Circuit Model, 2= Modified Circuit Model, 3= Pseudoinverse, and 4= Pseudoinverse with Coupling.

The most important test of the methods, given the planned iterative nature of the tuning, is whether each method correctly predicts the most out of tune cell for each detuned model test. This is summarised in Table 6.2.

Table 6.2: Number of tests for which each method incorrectly predicted the most out-of-tune cell, and the number identifier of the tests in which the most out-of-tune cell was not correctly predicted. The methods are: 1 = Unmodified Circuit Model, 2= Modified Circuit Model, 3= Pseudoinverse, and 4= Pseudoinverse with Coupling.

Method	Number of failed tests	Failed test ID numbers
1	1	9
2	1	9
3	0	-
4	1	1

Method 3, Pseudoinverse performs the best in these tests. Test 9 has input radial changes, in μm, $\vec{R} = [0.94, 0, 0, 0, 0, 0, 0, -0.31, 0]$. These are relatively small errors. It can be concluded that the circuit model based methods, 1 and 2, might be less accurate for small errors, but more data would be required to know for sure. Figure 6.18 shows comparisons of both tests with the unperturbed case for the profile of the main deflecting field, H_y. It can be seen that the change in field profile from both tests are small, and if the structure had this field profile it would not be tuned at all. The failures of the circuit based methods for these tests are therefore not that significant. Test 1 has input radial changes $\vec{R} = [-12, 18, 0, 0, 19, 11, -8.8, 0, 0]$. The same comparison of H_y field profile is shown for test 1 in Figure 6.19. The change in field profile is much larger. Method 4, Pseudoinverse with Coupling failed on this test, due to the error in cell 5 being under-estimated. This is interesting considering the coupling was added to the matrix to give more input data to determine the error in cell 5. This is discussed further in Section 6.5. Method 4 gave cell 2 as the most out-of-tune. In practise this may not have caused significant issue as this cell is also very out of tune. It seems likely the order of tuning would have been changed, with perhaps some error left in cell 5 at the end.

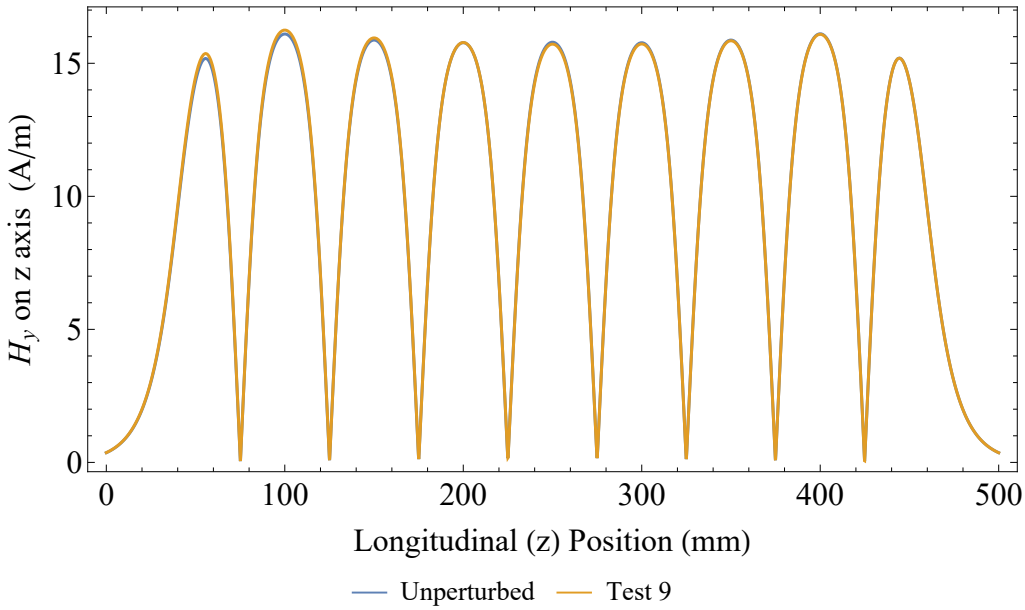

Figure 6.18: H_y on axis for test 9 compared to unperturbed case.

The root mean squared error ($RMSE$) and the R^2 value for each method are given in Table 6.3, where

$$RMSE = \sqrt{\frac{\sum_{i=1}^{N_{tot}} (R_i - R_i')^2}{N}} \tag{6.60}$$

and

$$R^2 = \sqrt{\frac{\sum_{i=1}^{N_{tot}} (R_i - R_i')^2}{\sum_{i=1}^{N_{tot}} (R_i - < R >)}} \tag{6.61}$$

where we calculate across all cells and all tests i, up to a total of $N_{tot} = 180$ values. $< R >$ is the mean of the input radial errors R_i and R_i' are the model result radial errors.

Table 6.3: $RMSE$ and R^2 for each method. The methods are: 1 = Unmodified Circuit Model, 2= Modified Circuit Model, 3= Pseudoinverse, and 4= Pseudoinverse with Coupling.

Method	$RMSE$ (μm)	R^2
1	1.183	0.9663
2	1.393	0.9522
3	1.421	0.9468
4	1.666	0.9250

The $RMSE$ gives us an estimate for the average error on each of the R_j' for each method. It is lowest for method 1 and highest for method 4. R^2 is a measure of the correlation of $\vec{R}'$ to $\vec{R}$. It is highest for method 1 and lowest for method 4.

Method 3 predicted the most out-of-tune cell for every test, however using these statistical figures of merit it is not the best model, that is method 1. To explain this, graphical residual analysis has been used.

Figure 6.20 shows the residuals ($\vec{R} - \vec{R}'$) for each method plotted against the frequency of the detuned model. The pattern is random for the two circuit model based methods, but a heteroscedastic bow-tie shape can be seen for both pseudoinverse based methods. This could be a

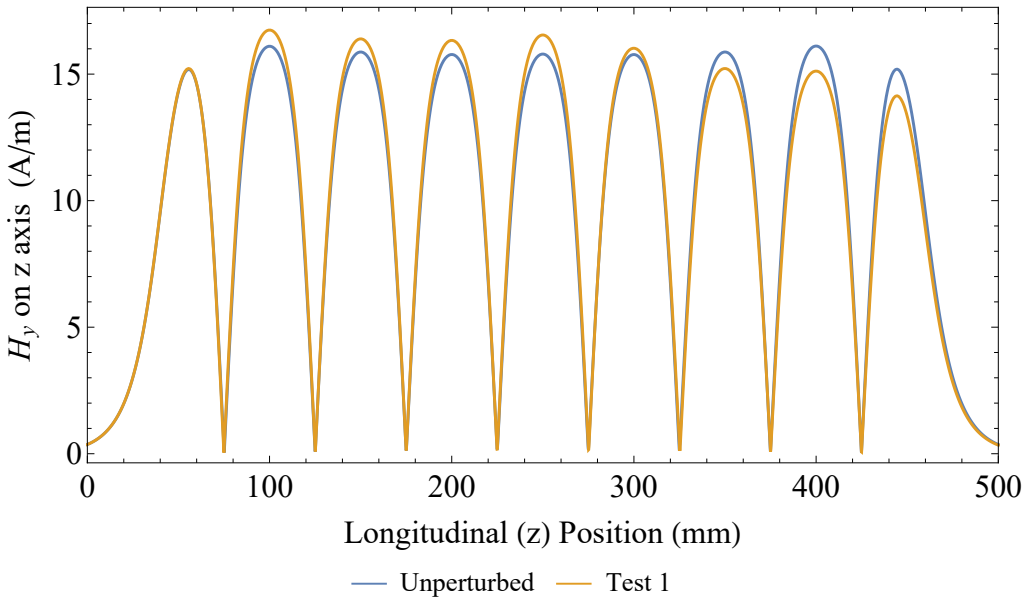

Figure 6.19: H_y on axis for test 1 compared to unperturbed case.

relationship with frequency itself, or it could be that frequency error is a predictor of the size of the perturbation. Figure 6.21 shows the residuals plotted against the sum of all the input errors on the detuned model, $\sum_j R_j$ which is used here as an analog for the size of the perturbation. The same heteroscedastic pattern is seen as for frequency. This implies the pattern seen is due to the size of the perturbation. The pseudoinverse methods assume linearity for the matrix equation Equation 6.47, and that assumption is less valid as the perturbation increases, leading to larger residuals at larger perturbations. That the minimum variance does not occur at $\sum_j R_j = 0$ or $f = 2.9985$ GHz warrants further investigation, and as there is an offset for both plots this could be related to the CST simulation results. It should be noted that the equivalent circuit model based methods also assume a small perturbation as the modelling includes a first order perturbation technique. From Figure 6.21 it appears that the validity of this assumption does not vary appreciably in the range of perturbations tested.

Overall the Pseudoinverse method seems the optimum for small perturbations, but for larger perturbations the Unmodified Circuit Model method may give more accurate results. Tests with a larger range of $\vec{R}$ would need to be performed to confirm this.

6.5 Further work

More consideration of the models is required before using one to tune the CLARA TDC. One area that has not been considered is the robustness of each method to measurement error. Random and systematic errors could be added to the CST results to test this. It is likely that the pseudoinverse methods input data will have the highest error, as the absolute value of the field is required to compare to the unperturbed solution, and the calibration of the size and material of the beads used in the bead-pull measurement will be critical. It should be noted that it is impossible to create a new inverted matrix $\mathbf{M}$ from the physical TDC, as the tuning pins cannot be used repeatably. Therefore were one these models to be used for tuning, the matrix $\mathbf{M}$ already constructed from the CST simulations would be used. Conversely the circuit model methods require only the relative field values which will have a lower measurement error.

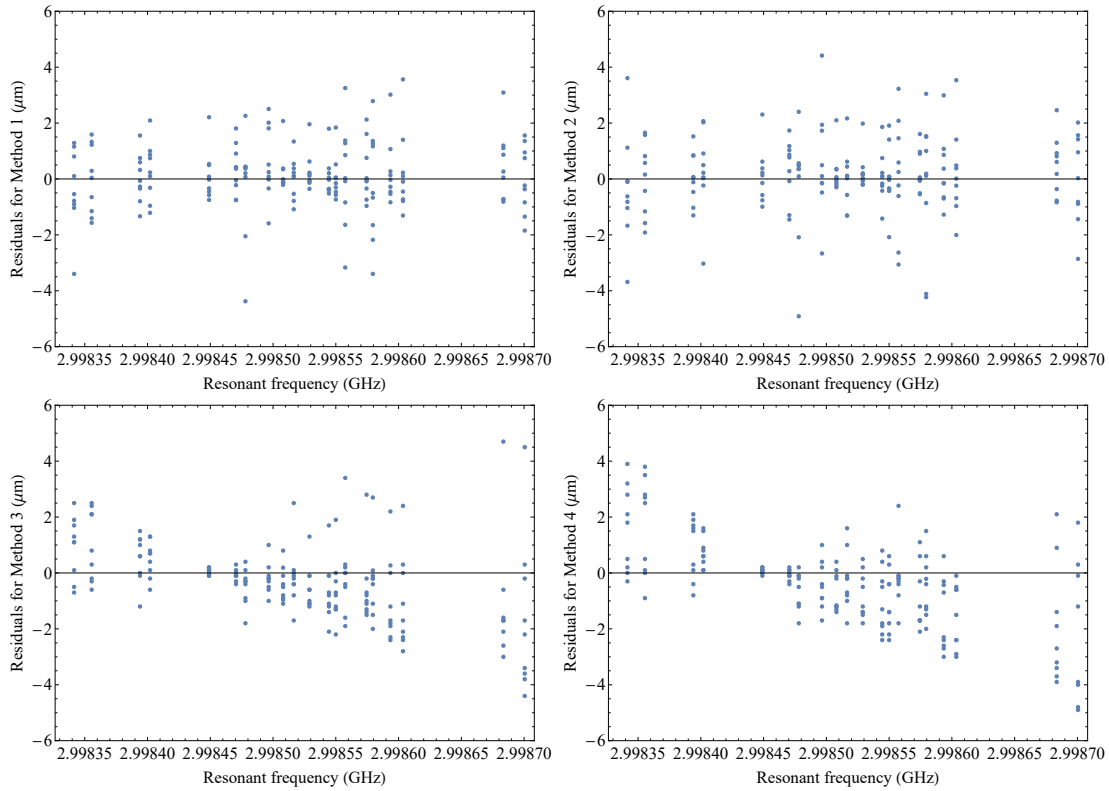

Figure 6.20: Residuals for each method plotted against the resonant π-mode frequency of each detuned structure. The methods are: 1 = Unmodified Circuit Model, 2= Modified Circuit Model, 3= Pseudoinverse, and 4= Pseudoinverse with Coupling.

It may be that whilst Pseudoinverse with Coupling performed poorer than the Pseudoinverse method in the perfect measurement scenario, the addition of $\partial\beta_c$ may make the Pseudoinverse with Coupling method more robust to measurement error. Weighting of the $\partial\beta_c$, as was done for ∂f in Section 6.4 has not been explored and may increase the performance of the Pseudoinverse with Coupling method.

As mentioned in Section 6.4, more tests would give better statistics for comparing the methods on finding the most out-of-tune cell. Additionally, testing with larger input radius errors $\vec{R}$ is required to test if the circuit model based methods perform better at larger perturbations. More statistics may help to find the cause of the asymmetry in the residuals analysis.

Additionally the methods should be tested on a model with detuned irises, to see if they correctly predict cell changes that compensate for the iris detuning.

When one model has been chosen and optimised, the TDC will have been delivered and can be tuned.

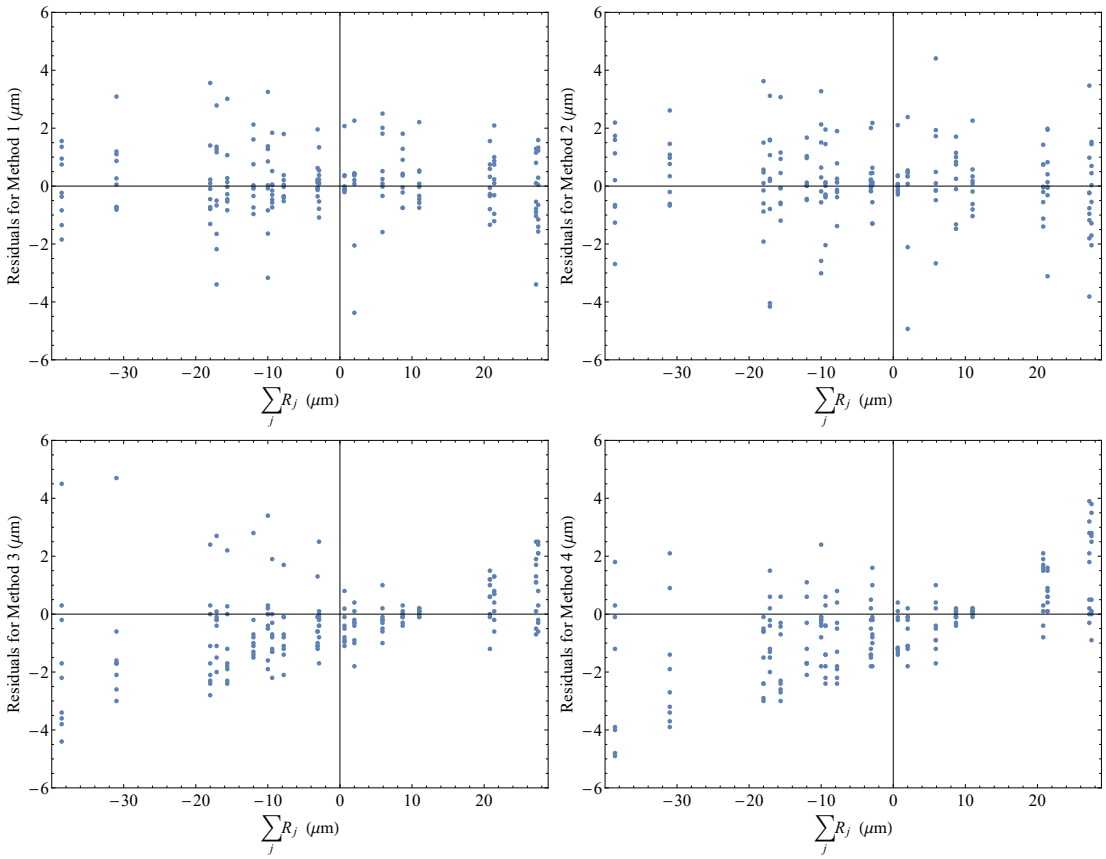

Figure 6.21: Residuals for each method plotted against resonant $\sum_j R_j$. The methods are: 1 = Unmodified Circuit Model, 2= Modified Circuit Model, 3= Pseudoinverse, and 4= Pseudoinverse with Coupling.

Chapter 7

Conclusion

7.1 CLARA 400 Hz photoinjector

The new 400 Hz photoinjector for CLARA has been designed and tuned, as described in Chapters 2 and 3. The photoinjector design meets all the specification criteria, including the stringent average power handling requirement, however the klystron currently available does not provide sufficient power to reach 120 MV/m. This will be rectified by a new klystron, to be installed in spring 2022. The tuning was very successful, performed by trimming the length of each cell to tune the frequency and field flatness. A field flatness of 98±1% was achieved and the frequency will require only a 0.2°C change in cooling water temperature to reach the specified frequency of 2.9985 GHz. The Q_0 was the only parameter which changed significantly between the design and the fabricated structure, decreasing by 1772±400.

A completely automated program that can run unmanned safely was designed to condition all the RF structures on CLARA, but particularly the 400 Hz photoinjector, as described in Chapter 4. This is due to the high gradient, which means there would be a risk of surface damage if the power were to be increased too quickly, allowing too many breakdowns during manual conditioning. The program, called NO-ARC, has been tested on the current CLARA 10 Hz photoinjector. Several occurrences of interest were noted, such as the effect of external solenoids on breakdown rate, and possible multipactor at low power affecting the phase of the reflected RF as the power in the cavity decayed. Conditioning was started on the 400 Hz photoinjector, but could not be completed in the time available. Unfortunately much of the data saved during this conditioning period was corrupted. During the conditioning period, a similar low power multipactor effect was seen as in the 10 Hz photoinjector. The multipactor was simulated and found to be in the cathode plug region, and to require seeding with field emission from earlier in the RF pulse. Additional multipactor simulations revealed the provenance of a "bump" seen on the cavity probe amplitude signal to be from multipactor electrons in the probe region.

The main piece of further work on the photoinjector is to complete the conditioning, which is planned for spring 2022. Additionally several upgrades to NO-ARC are planned for the future, which are detailed in Chapter 4, and include a change to the data saving format to avoid the loss of data in the future.

7.2 RF dispersion modelling of the first CLARA linac

A new simple and fast analytical method to model RF dispersion in travelling wave linacs is described in Chapter 5. The model requires only the group velocity and phase advance along the structure to model the dispersion. The addition of the Q_0 allows the attentuation to be added to the model. The model was shown to accurately model the dispersion in the first CLARA linac, allowing accurate calculation of the pulse evolution along the structure, and the structure filling time. A synchronism condition was added to calculate only the voltage experienced by a particle beam, and the model was used to calculate the momentum gain for an electron bunch for a range of injection times for several pulse lengths. This was compared to beam momentum measurements from CLARA and again showed a good agreement. The model makes it easy to predict the beam momentum gain for the linac, and also to predict the optimal beam injection time for robustness to timing jitter. In the future the model can be added to the CLARA virtual machine to allow beam operators to easily simulate the effect of changes to the RF pulse and the injection time on the beam, as well as be adapted for the other CLARA linacs.

7.3 Comparision of tuning methods for the CLARA transverse deflecting cavity

The CLARA transverse deflecting cavity (TDC) will require field flatness tuning after fabrication. Chapter 6 describes four methods to find the detuning of each cell from RF measurements. The first is standard method for calculating the detuning on each cell of a multi-cell structure using perturbation theory, and the second is a modificatio of it to better fit the cell-to-cell coupling of the TDC. A new method for tuning dipole mode cavities is suggested, which uses singular value decomposition to find the pseudoinverse of a matrix of RF measurement information. The third and fourth methods described are two versions of this method with slightly different measurement matrices. The methods are tested using 20 randomly detuned simulations of the TDC and using each method to find the detuning of each cell. All the methods predict the cell errors well. The results are discussed, and with the data used the optimum method for small perturbations is a pseudoinverse based method, but for larger perturbations the modified perturbation theory based method may give better results.

The further work required to compare these methods is detailed in Chapter 6. It includes testing the robustness of each method to error, using additional simulated test structures to get better statistics, and testing the methods on structures with a detuned iris. After one method is chosen, the TDC will be tuned, conditioned using NO-ARC, and will then be operational on the CLARA beam line.

7.4 Summary

This thesis covers development work on three RF structures for CLARA. The CLARA photoinjector design, tuning and the gradient achieved through conditioning will determine the bunch emittance and energy spread for the machine, which are crucial to a future free electron laser test facility. The first CLARA linac increases the beam momentum to 50 MeV/c, and simple, fast simulation tools can be used to easily predict the effect of changes to the pulse length, shape or injection time on the CLARA electron beam. The dispersion modelling method can easily be

adapted for the second, third and fourth linacs to find the optimum RF parameters for the beam up to 250 MeV/c. The transverse deflecting cavity will then be used to measure and optimise the longitudinal profile and length of the electron bunch. Each structure is required to meet its specification to achieve the CLARA beam parameters that will be needed to test novel free electron laser schemes in the future. The work in this thesis has brought CLARA closer towards that goal.

References

[1] E. A. Seddon et al. “Short-wavelength free-electron laser sources and science: a review”. In: *Reports on progress in physics* 80.11 (2017).

[2] Philip H. Bucksbaum and Nora Berrah. “Brighter and faster: The promise and challenge of the x-ray free-electron laser”. In: *Physics Today* 68.7 (2015), p. 26.

[3] N. Huang et al. “Features and futures of X-ray free-electron lasers”. In: *The Innovation* 2.2 (2021), p. 100097.

[4] J. A. Clarke et al. “CLARA conceptual design report”. In: *Journal of Instrumentation* 9.5 (2014).

[5] K. Batchelor et al. “Development of a High Brightness Electron Gun for the Accelerator Test Facility at Brookhaven National Laboratory”. In: *Proceedings of the 1st European Particle Accelerator Conference (EPAC1988)* (1988), pp. 954–957.

[6] W. Decking and H. Weise. “Commissioning of the European XFEL Accelerator”. In: *Proceedings of the 8th International Particle Accelerator Conference (IPAC2017)* (2017), pp. 1–6.

[7] L. Serafini. “The short bunch blow-out regime in RF photoinjectors”. In: *AIP Conference Proceedings*. Vol. 413. 1. 2008, pp. 321–334.

[8] P. Musumeci et al. “Experimental generation and characterization of uniformly filled ellipsoidal electron-beam distributions”. In: *Physical Review Letters* 100.24 (2008), pp. 1–4.

[9] Z. Huang et al. “Uncorrelated energy spread and longitudinal emittance of a photoinjector beam”. In: *Proceedings of the IEEE Particle Accelerator Conference (PAC2005)* (2005), pp. 3570–3572.

[10] T. Rao and D. H. Dowell. *An Engineering Guide to Photoinjectors*. CreateSpace Independent Publishing, 2013. eprint: 1403.7539.

[11] T. Wangler. *RF Linear Accelerators*. 2nd Edition. Wiley-VCH, 2008.

[12] K. T. McDonald. “Design of the Laser-Driven RF Electron Gun for the BNL Accelerator Test Facility”. In: *IEEE Transactions on Electron Devices* 35.11 (1988), pp. 2052–2059.

[13] D. Alesini. “Power Coupling”. In: *CERN Yellow Report CERN-2011-007* (2011).

[14] D.T. Palmer et al. “Microwave measurements of the BNL / SLAC / UCLA 1.6 cell photocathode RF gun”. In: *Proceedings of the IEEE 1995 Particle Accelerator Conference (PAC1995)* (1995), pp. 982–984.

[15] T. Kobayashi et al. “Performance Study of High Current Photo-Cathode RF-Gun with New Laser System”. In: *International Journal of Applied Electromagnetics and Mechanics* 14 (2001), pp. 143–150.

[16] L. Palumbo and J. Rosenzweig. *Technical Design Report for the SPARC Advanced project.* Tech. rep. INFN, 2004, pp. 1–138.

[17] S. Telfer et al. “Commissioning of the UCLA PEGASUS Photoinjector Laboratory”. In: *Proceedings of the IEEE 2001 Particle Accelerator Conference (PAC2001)* 3 (2001), pp. 2263–2265.

[18] D.T. Palmer. “The Next Generation Photoinjector”. PhD thesis. Stanford University, 1998.

[19] C. Limborg et al. *RF Design of the LCLS Gun.* Tech. rep. LCLS-TN-05-3. 2005, pp. 1–12.

[20] J. Raguin et al. “The Swiss FEL RF Gun : RF Design and Thermal Analysis”. In: *Proceedings of the 26th International Linear Accelerator Conference (LINAC2012)* (2012), pp. 442–444.

[21] J. Hong et al. “New RF-Gun Design for The PAL-XFEL”. In: *Proceedings of 34th International Free Electron Laser Conference (FEL2012)* (2012).

[22] B. Dwersteg et al. “RF gun design for the TESLA VUV free electron laser”. In: *Nucl .Instrum. Meth. A* 393 (1997), pp. 93–95.

[23] Y. Chen et al. “Coaxial Coupler RF Kick in the PITZ RF Gun”. In: *Proceedings of the 38th International Free Electron Laser Conference (FEL2017).* 2017, pp. 1–3.

[24] M. Ferrario et al. *Conceptual Design of the XFEL Photoinjector.* Tech. rep. TESLA FEL Report. 2001.

[25] J. Rodier et al. “Construction of the Alpha-X Photo-Injector Cavity”. In: *Proceedings of the 10th European Particle Accelerator Conference (EPAC2006)* (2006), pp. 6–8.

[26] D. H Dowell et al. “The Development of the Linac Coherent Light Source RF Gun”. In: *SLAC-PUB-13401* September (2008), pp. 1–33. eprint: 1503.05877.

[27] C. Travier and J. Gao. “LAL (Orsay) RF Gun Project”. In: *Proceedings of the 2nd European Particle Accelerator Conference (EPAC1990)* (1990), pp. 706–708.

[28] J. H. Han et al. “Design of a high repetition rate S-band photocathode gun”. In: *Nucl .Instrum. Meth. A* 647.1 (2011), pp. 17–24.

[29] W. H. Huang et al. “Design and beam dynamics simulation for the photoinjector of Shanghai soft X-ray free electron laser test facility”. In: *33rd International Free Electron Laser Conference (FEL 2011).* 2011, pp. 299–301.

[30] R. Ganter et al. “SwissFEL cathode load-lock system”. In: *Proceedings of the 35th International Free-Electron Laser Conference (FEL2013).* 2013, pp. 259–262.

[31] F. Stephan et al. “New experimental results from PITZ”. In: *Proceedings of the 24th Linear Accelerator Conference (LINAC 2008).* 2009, pp. 474–476.

[32] J. H. Han et al. “Conditioning and High Power Test of the RF Guns at PITZ”. In: *Proceedings of the 9th European Particle Accelerator Conference (EPAC2004)* June (2004), pp. 357–359.

[33] S. S. Kurennoy et al. “Normal-conducting high current RF photoinjector for high power CW FEL”. In: *Proceedings of the IEEE 2005 Particle Accelerator Conference (PAC2005)* 2005 (2005), pp. 2866–2868.

[34] D.J. Dunning et al. “FEL considerations for CLARA: a UK test facility for future light sources”. In: *Proceedings of the ICFA Workshop on Future Light Sources 2012* (2012).

[35] J. W. McKenzie et al. “High repetition rate S-band photoinjector design for the CLARA FEL”. In: *Proceedings of the 36th International Free Electron Laser Conference, (FEL2014)* (2014), pp. 889–892.

[36] Wolfram Research Inc. *Mathematica 12.3.1*. Champaign, Illinois, 2021.

[37] R. Holsinger and K. Halbach. *Poisson Superfish*. https://laacg.lanl.gov/laacg/services/download_sf.phtml.

[38] Dassault Systemes. *CST Studio Suite*. www.3ds.com. 2021.

[39] G. Burt et al. *CLARA 400 Hz photoinjector design report*. Tech. rep. 2014.

[40] V. Paramonov, A. Skasyrskaya, and B. L. Militsyn. “Evaluations of parameters stability for S-band RF gun cavity due to effects of pulsed RF heating”. In: *Proceedings of the 26th Russian Particle Accelerator Conference (RuPAC2018)* (2018), pp. 100–102.

[41] D. P. Pritzkau. “RF Pulsed Heating”. PhD thesis. Stanford University, 2001.

[42] S. B. van der Geer and de Loos M. J. *General Particle Tracer*. http://www.pulsar.nl/gpt.

[43] B. Kyle. *GPT Simulations into the Effects of HRRG Coupler Offsets on CLARA*. Tech. rep. 2016.

[44] E. Somersalo, P. Yla-Oijala, and D. Proch. “Analysis of multipacting in coaxial lines”. In: *Proceedings of the 1995 IEEE Particle Accelerator Conference (PAC1995)* (1995), pp. 1500–1502.

[45] *Research Instruments GmbH*. https://research-instruments.de, Bergisch Gladbach, Germany.

[46] W. Boyes. *Instrumentation Reference Book*. Elsevier Inc., 2010.

[47] R. Fandos, W. Wuensch, and A. Grudiev. *Measurement of S Parameters of an Accelerating Structure with Double-Feed Couplers*. Tech. rep. CERN-OPEN-2007-012. 2006.

[48] B. Keune. *Tuning and FAT- HRRG*. Tech. rep. Research Instruments GmbH. 2016.

[49] T. G. Lucas. “High Field Phenomenology in Linear Accelerators for the Compact Linear Collider”. PhD thesis. University of Melbourne, 2018.

[50] A Grudiev and W Wuensch. “A new local field quantity describing the high gradient limit of accelerating structures”. In: *Proceedings of the 24th Linear Accelerator Conference (LINAC2008)*. 2009, pp. 936–938.

[51] F. Jackson et al. “Dark current studies in the CLARA front-end injector”. In: *Proceedings of the 8th International Particle Accelerator Conference (IPAC2017)*. 2017.

[52] H. Padamsee, J. Knobloch, and T. Hays. *RF superconductivity for accelerators*. Wiley-VCH, 2008, p. 521.

[53] K. N. Sjøbæk. “Avoiding vacuum arcs in high gradient normal conducting RF structures”. PhD thesis. University of Oslo, 2016.

[54] V. A. Dolgashev et al. “Study of basic rf breakdown phenomena in high gradient vacuum structures”. In: *Proceedings of the 25th Linear Accelerator Conference, (LINAC2010)*. 2011, pp. 1043–1047.

[55] A. Degiovanni, W. Wuensch, and J. Giner Navarro. “Comparison of the conditioning of high gradient accelerating structures”. In: *Physical Review Accelerators and Beams* 19.3 (2016), p. 032001.

[56] D. Alesini et al. “High Power Test Results of the ELI-NP S-Band Gun Fabricated with the New Clamping Technology Without Brazing”. In: *Proceedings of the 8th International Particle Accelerator Conference (IPAC2017)* (2017), pp. 3–6.

[57] T. Argyropoulos et al. “Design, fabrication, and high-gradient testing of an X -band, traveling-wave accelerating structure milled from copper halves”. In: *Physical Review Accelerators and Beams* 21.6 (2018), p. 061001.

[58] H. Timko et al. “Mechanism of surface modification in the plasma-surface interaction in electrical arcs”. In: *Physical Review B* 81.18 (2010), p. 184109.

[59] T. J. Boyd Jr. *Kilpatrick’s criterion*. Tech. rep. Los Alamos Group AT-1 report. 1982.

[60] W Wuensch. *The Scaling of the Traveling-Wave RF Breakdown Limit*. Tech. rep. CLIC Note 649. 2006.

[61] J. Paszkiewicz. “Studies of Breakdown and Pre-Breakdown Phenomena in High Gradient Accelerating Structures”. PhD thesis. University of Oxford, 2020.

[62] R A Marsh et al. “Performance of a second generation X -band rf photoinjector”. In: *Physical Review Accelerators and Beams* 21.7 (2018).

[63] A. E. Wheelhouse et al. “The commissioning of the EBTF S-band photo-injector gun at Daresbury Laboratory”. In: *Proceedings of the 4th International Particle Accelerator Conference (IPAC13)* (2013), pp. 2845–2847.

[64] A. Moretti et al. “Effects of high solenoidal magnetic fields on rf accelerating cavities”. In: *Phys. Rev. ST Accel. Beams* 8.7 (2005), pp. 1–6.

[65] J. Norem et al. “Dark current, breakdown, and magnetic field effects in a multicell, 805 MHz cavity”. In: *Physical Review Special Topics - Accelerators and Beams* 6.7 (2003), pp. 11–31.

[66] R. B. Palmer et al. “Rf breakdown with external magnetic fields in 201 and 805 MHz cavities”. In: *Physical Review Special Topics - Accelerators and Beams* 12.3 (2009).

[67] J. Spradlin, A. M. Valente-Feliciano, and O. Trofimova. “Surface preparation of metallic substrates for quality SRF thin films”. In: *Proceedings of the 15th International Conference on RF Superconductivity (SRF2011)* (2011), pp. 936–939.

[68] N. Shipman et al. *Effect of an externally applied magnetic field on the breakdown rate in ultra-high vacuum measured in the ”large electrode system” at CERN*. Tech. rep. CLIC Note 1078. 2017.

[69] *Experimental Physics and Industrial Control System*. http://www.aps.anl.gov/epics/.

[70] Instrumentation Technologies. www.i-tech.si, Solkan, Slovenia.

[71] B. Woolley. “High power X-band RF test stand development and high power testing of the CLIC crab cavity”. PhD thesis. Lancaster University, 2015.

[72] National Instruments. www.ni.com, Austin, Texas, USA.

[73] A. Degiovanni et al. “Diagnostics and Analysis Techniques for High Power X-Band Accelerating Structures”. In: *Proceedings of the 27th Linear Accelerator Conference (LINAC14)* (2014).

[74] H. Kockelbergh, D. J. Scott, and L. S. Cowie. “RF Breakdown Detection and Characterisation using Neural Networks”. In: *PITZ collaboration meeting May 2019* (2019).

[75] W. Wuensch et al. “Statistics of vacuum breakdown in the high-gradient and low-rate regime”. In: *Physical Review Accelerators and Beams* 20.1 (2017).

[76] M. Furmaniak. “Simulations and Measurements of Dark Current from Upgraded 10 Hz Gun at CLARA”. In: *PITZ Collaboration meeting June 2020* (2020).

[77] A. Alexandrova et al. “Optical Beam Loss Monitors Based on Fibres for the CLARA Phase 1 Beam-Line”. In: *Proceedings of the 9th International Particle Accelerator Conference (IPAC2018)* (2018).

[78] K. C. Gupta, R. Garg, and R Chadha. *Computer-Aided Design of Microwave Circuits*. Artech, 1981.

[79] M Aicheler et al. *A Multi-TeV Linear Collider Based on CLIC Technology: CLIC Conceptual Design Report*. CERN Yellow Reports: Monographs. CERN, 2012.

[80] A. Latina et al. “Compactlight design study”. In: *Proceedings of the 60th ICFA Advanced Beam Dynamics Workshop on Future Light Sources (FLS2018)* (2018).

[81] Science and Technology Facilities Council. UK XFEL Science Case. 2020.

[82] V. F. Khan et al. “A high phase advance damped and detuned structure for the main linacs of CLIC”. In: *Proceedings of the 25th Linear Accelerator Conference, (LINAC2010)* (2010).

[83] Z. Li et al. “Traveling wave structure optimization for the NLC”. In: *Proceedings of the IEEE 2001 Particle Accelerator Conference (PAC2001)* (2001).

[84] C. Adolphsen et al. “Processing studies of X-band accelerator structures at the NLCTA”. In: *Proceedings of the IEEE 2001 Particle Accelerator Conference (PAC2001)* (2001).

[85] R. M. Jones et al. “Influence of fabrication errors on wake function suppression in NC X-band accelerating structures for linear colliders”. In: *New Journal of Physics* 11.3 (2009), p. 033013.

[86] D. Angal-Kalinin et al. “Design, specifications, and first beam measurements of the compact linear accelerator for research and applications front end”. In: *Physical Review Accelerators and Beams* 23.4 (2020), p. 44801.

[87] A. Lunin, V. Yakovlev, and A. Grudiev. “Analytical solutions for transient and steady state beam loading in arbitrary traveling wave accelerating structures”. In: *Phys. Rev. ST Accel. Beams* 14 (5 2011), p. 052001.

[88] S. Benedetti et al. “RF Design of a Novel S-Band Backward Travelling Wave Linac for Proton Therapy”. In: *Proceedings of LINAC’14, Geneva, Switzerland*. 2014.

[89] S. Benedetti. “High-gradient and high-efficiency linear accelerator for hadron therapy”. PhD thesis. École Polytechnique Fédérale de Lausanne, 2018, p. 256.

[90] B. Shepherd. personal communication. Jan. 3, 2020.

[91] J. Mckenzie. “Longitudinal Beam Characterisation on VELA using a Transverse Deflecting Cavity”. PhD thesis. University of Liverpool, 2019, pp. 56–58.

[92] J. R. Shi et al. “RF deflecting cavity design for bunch length measurement of photoinjector at Tsinghua University”. In: *Chinese Physics C* 32.10 (2008), p. 837.

[93] D. Alesini et al. “RF deflector design and measurements for the longitudinal and transverse phase space characterization at SPARC”. In: *Nucl .Instrum. Meth. A* 568.2 (2006), pp. 488–502.

[94] J. W. Wang and G. A. Loew. *Field Emission and RF Breakdown in High-Gradient Room-Temperature Linac Structures*. Tech. rep. SLAC-PUB-7684. 1997.

[95] P. A. Goudket et al. “Prototype Refinement of the VELA Transverse Deflecting Cavity Design”. In: *Proceedings of the 4th International Particle Accelerator Conference (IPAC2013)* (2013), pp. 2842–2844.

[96] K. Bane and R. L. Gluckstern. “The transverse wakefield of a detuned X-band accelerator structure”. In: *Particle Accelerators* 42 (1993), pp. 123–169.

[97] M. Dehler et al. “X-band rf structure with integrated alignment monitors”. In: *Physical Review Special Topics - Accelerators and Beams* 12.6 (2009).

[98] A. Ben-Israel and T. Greville. *Generalized Inverses: Theory and Applications*. 2001, pp. 175–183.

[99] B. Koubek, A. Grudiev, and M. Timmins. “Rf measurements and tuning of the 750 MHz radio frequency quadrupole”. In: *Physical Review Accelerators and Beams* 20.8 (2017).

[100] J. K. Jones. “Design of a Novel Stacked Storage Ring for Low Emittance Light Sources”. PhD thesis. University of Manchester, 2015, pp. 102–104.

Appendix A

Comparison of TDC test fields to unperturbed fields

Figure A.1 shows the H_y field on axis for each test case discussed in 6.4.

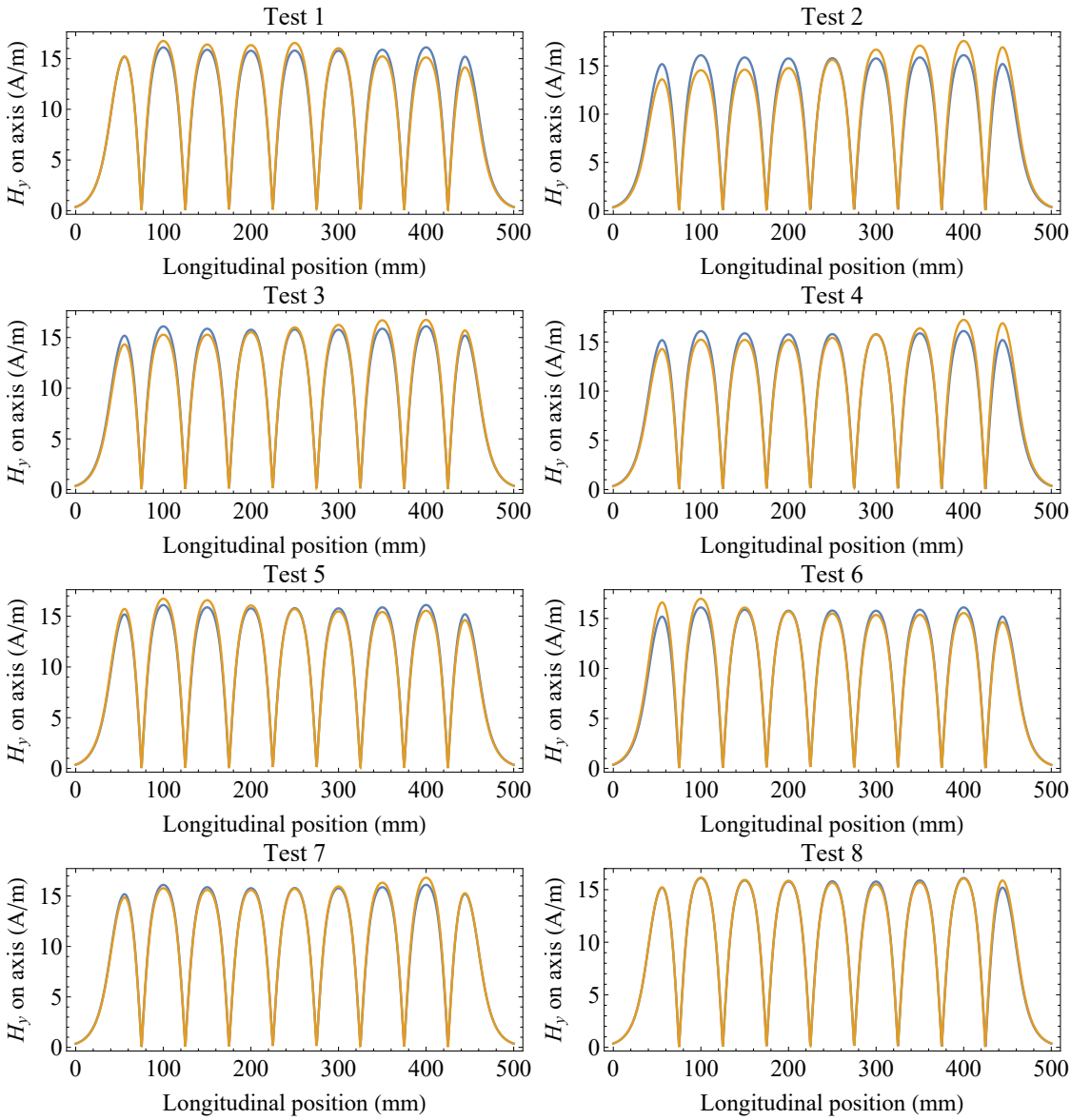

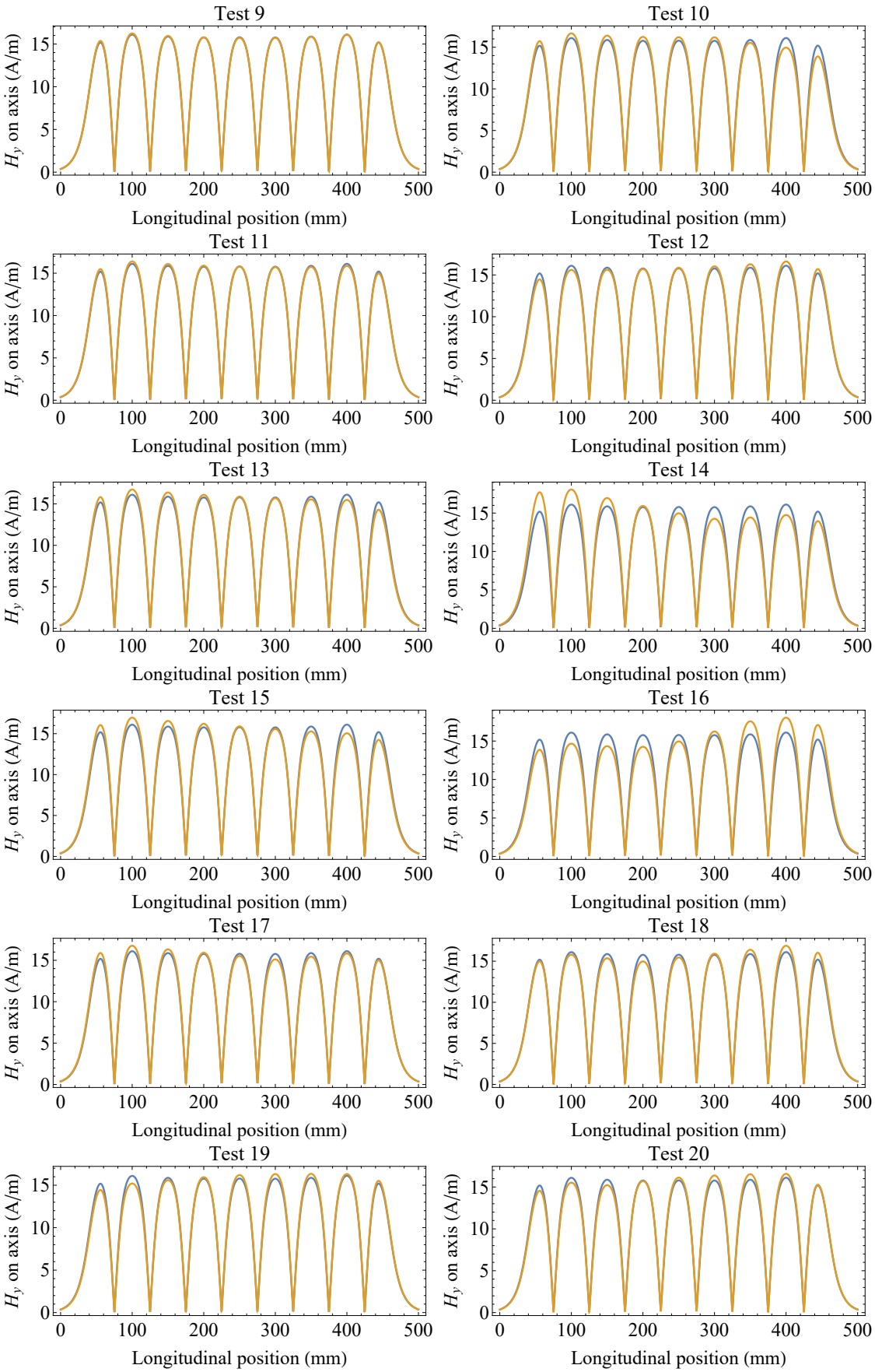

Figure A.1: Comparision of H_y on axis for each test (orange) case to the unperturbed case (blue).